

The Hidden Universe: Investigating the evolution of dusty star formation and gas consumption across cosmic time

Author:
Tracy GARRATT

Supervised by:
Prof. K. E. K. Coppin
Prof. J. E. Geach
Dr. M. Franco (Year 2-3)
Dr. M. P. Koprowski (Year 1)

Centre for Astrophysics Research
School of Physics, Astronomy and Mathematics
University of Hertfordshire

Submitted to the University of Hertfordshire in partial fulfilment of the requirements of the degree of Doctor of Philosophy.

January 2023

Abstract

Half a century has now passed since the first observations of the Universe at infrared wavelengths, revealing a population of dust-enshrouded galaxies, many of which were too faint to be detected in the optical surveys of the time. Along with observations at ultra-violet and optical wavelengths, these observations support a picture of a star-formation rate density, which rises rapidly to a peak at $z \approx 2$ and then declines to the present day. However, a key outstanding question remains: what drives this evolution of the star-formation rate density? Is the peak of the star-formation rate density driven by a larger supply of molecular gas in galaxies or because galaxies are able to form stars more efficiency, or both?

Observations of the infrared sky also laid the ground work for the discovery of a population of distant, highly infrared luminous galaxies detected at submillimetre wavelengths (Submillimetre Galaxies). Whilst we now have a good understanding of the physical properties of the ‘canonical’ $z \approx 2$ submillimetre population, the study of the intrinsically rare, high-redshift, bright-end tail of this population is far from complete. With only a few detections of bright ($S_{850\mu\text{m}} > 15 \text{ mJy}$) submillimetre sources the single-dish number counts and the redshift distribution of this population are poorly constrained. It is also commonly accepted that bright sources detected in single-dish submillimetre surveys are either gravitationally lensed, intrinsically bright or blends of multiple galaxies, but the relative contribution of each of these sub-populations to the bright end of the single-dish submillimetre counts is currently unknown. Current models struggle to reproduce the abundance and redshift distribution of the bright-end of the submillimetre population, hampered by a lack of robust observational data. To better inform these models we not only need accurate submillimetre number counts and a robust redshift distribution for the bright-end of the submillimetre population (single-dish sources with fluxes $S_{850\mu\text{m}} > 15 \text{ mJy}$), but also a clear picture of the contribution of lensed and blended galaxies to the over-abundance of bright submillimetre galaxies observed.

In this thesis we use data from the two largest extragalactic surveys at $850\mu\text{m}$ with JCMT to date; the SCUBA-2 Cosmology Legacy Survey and the SCUBA-2 Large eXtragalactic Survey, as well as recent data from an ALMA follow-up survey of the SCUBA-2 Large eXtragalactic Survey XMM-LSS field.

We employ a statistical approach to explore the cosmological evolution of the molecular gas mass density (ρ_{H_2}) measuring the average observed $850\mu\text{m}$ flux density of near-infrared selected galaxies as a function of redshift. The redshift range considered corresponds to a span where the $850\mu\text{m}$ band probes the Rayleigh-Jeans tail of thermal dust emission in the rest-frame, and can therefore be used as an estimate of the mass of the interstellar medium (ISM). With a sample approximately 2 orders of magnitude larger than in previous works we significantly

reduce statistical uncertainties on ρ_{H_2} to $z \approx 2.5$. Our measurements are in broad agreement with recent direct estimates from blank field molecular gas surveys, finding that the epoch of molecular gas coincides with the peak epoch of star formation with $\rho_{\text{H}_2} \approx 2 \times 10^7 \text{ M}_\odot \text{ Mpc}^{-3}$ at $z \approx 2$. We demonstrate that ρ_{H_2} can be broadly modelled by inverting the star-formation rate density with a fixed or weakly evolving star-formation efficiency. This “constant efficiency” model shows a similar evolution to our statistically derived ρ_{H_2} , indicating that the dominant factor driving the peak star formation history at $z \approx 2$ is a larger supply of molecular gas in galaxies rather than a significant evolution of the star-formation rate efficiency within individual galaxies.

We use data from the SCUBA-2 Large eXtragalactic survey of the XMM-LSS field to investigate the abundance of sources at the bright-end of the $850 \mu\text{m}$ number counts. The S2LXS XMM-LSS survey maps an area of 9 deg^2 , reaching a moderate depth of $1\sigma \simeq 4 \text{ mJy beam}^{-1}$. This is the largest contiguous area of extragalactic sky mapped by JCMT at $850 \mu\text{m}$ to date. The wide area of the S2LXS XMM-LSS survey allows us to probe the ultra-bright ($S_{850\mu\text{m}} \gtrsim 15 \text{ mJy}$), yet rare submillimetre population. We present the S2LXS XMM-LSS catalogue, which comprises 40 sources detected at $>5\sigma$ significance, with deboosted flux densities in the range of 7 mJy to 48 mJy. We robustly measure the bright-end of the $850 \mu\text{m}$ number counts at flux densities $>7 \text{ mJy}$, reducing the Poisson errors by a factor ≈ 2 compared to existing measurements. The S2LXS XMM-LSS observed number counts show the characteristic upturn at bright fluxes, expected to be motivated by local sources of submillimetre emission and high-redshift strongly lensed galaxies. We find that the observed $850 \mu\text{m}$ number counts are best reproduced by model predictions that include either strong lensing or source blending from a 15 arcsec beam, indicating that both may make an important contribution to the observed over-abundance of bright single-dish $850 \mu\text{m}$ selected sources.

We explore the multiplicity fraction of bright single-dish $850 \mu\text{m}$ selected sources using data from a follow up ALMA survey of 17 single-dish detected submillimetre sources from the S2LXS XMM-LSS field. Our ALMA maps reach a median sensitivity of $1\sigma = 0.11 \text{ mJy}$, with a median synthesised beam size of $0.59'' \times 0.50''$. In our deep ALMA maps we detect 22 sources at a significance of $>5\sigma$, finding a multiplicity fraction of 54% at $S_{850\mu\text{m}} > 12 \text{ mJy}$. Our initial results suggest that source blending does not significantly contribute to the abundance of bright sources observed in single-dish $850 \mu\text{m}$ surveys. This is an unexpected result given that the S2LXS XMM-LSS number counts are broadly reproduced by models that incorporate source blending, and further work is required to confirm this.

Declaration

I declare that no part of this work is being submitted concurrently for another award of the University or any other awarding body or institution. This thesis contains a substantial body of work that has not previously been submitted successfully for an award of the University or any other awarding body or institution.

The following parts of this submission have been published previously and/or undertaken as part of a previous degree or research programme:

1. Chapter 2: this has been published as Garratt et al., 2021, *The Astrophysical Journal*, **912**, 62.
2. Chapter 3: this has been published as Garratt et al., 2023, *Monthly Notices of the Royal Astronomical Society*, **520(3)**, 3669.

Except where indicated otherwise in the submission, the submission is my own work and has not previously been submitted successfully for any award.

Acknowledgements

I would like to thank everyone who has helped and supported me over the past few years at Hertfordshire, you have all contributed to making my PhD an amazing experience. Firstly I would like to thank my supervisor Kristen Coppin for your unwavering support throughout my PhD. The journey hasn't been without its hurdles (a global pandemic and a baby make for a slightly unusual PhD journey) but you have always been there to guide me through, and to keep me on track. I would also like to thank my supervisor Jim Geach for giving your time and your invaluable guidance. In addition I'd like to thank Maciej Koprowski and Max Franco. I am incredibly lucky to have had you both as 'bonus' supervisors in my supervisory team, and I am very grateful for your support and words of encouragement.

Thank you to my fellow postgraduate students who have made my time at Hertfordshire a really enjoyable experience. Thank you for the interesting (and often off topic) office chats, the many laughs and the (often) much needed trips to the pub. I would particularly like to thank Ben Law, Calum Morris, Jaime Vargas González, John Tolladay, Kasia Nowak, Luke Fleming, Maddie Burchard, Matt Doherty, Mike Smith, Ryan Jackson, Soumyadeep Das and Will Cooper. I have been very lucky to share my PhD journey with such incredible friends and I couldn't have done this without your support.

I would also like to thank my family. My brother who kindly let me move into his house for almost 2 years so that I had a much shorter commute to campus, and my parents for your support, you have always been there for me when I needed you.

And last, but certainly not least, I'd like to thank my husband Chris for supporting my decision to follow my lifelong passion, even when that took me 200 miles away from our home. Thank you for listening to me ramble on about my research and always being there for me when I have needed reassurance.

Finally I wish to recognise and acknowledge the very significant cultural role and reverence that the summit of Maunakea has always had within the indigenous Hawaiian community. We are most fortunate to have the opportunity to conduct observations from this mountain.

Contents

Abstract	i
Acknowledgements	iv
Contents	v
List of Figures	viii
List of Tables	xi
List of Abbreviations	xii
1 Introduction	1
1.1 Galaxy Formation and Evolution	1
1.1.1 Λ Cold Dark Matter Model	1
1.1.2 Galaxy structure	2
1.2 Far-infrared and Submillimetre Astronomy	5
1.3 Identifying multi-wavelength counterparts to Submillimetre Galaxies	13
1.3.1 Radio interferometry	15
1.3.2 Optical and near-infrared colour selection	17
1.3.3 Submillimetre interferometry	18
1.4 Tracing Molecular Gas Mass Density	20
1.5 Overview	24
2 Cosmic evolution of the H₂ mass density and the epoch of molecular gas	27
2.1 Introduction	27
2.2 Data	29
2.2.1 SCUBA-2 Cosmology Legacy Survey	29
2.2.2 UKIDSS-UDS ultraviolet–optical–mid-infrared imaging and catalogue	29
2.3 Methods	30
2.4 Results	37
2.4.1 Estimating molecular gas mass: Rayleigh-Jeans luminosity-to-gas mass relation	37
2.4.2 Deriving molecular gas mass density from the halo mass function.	42
2.4.3 Estimating molecular gas mass density using a “constant efficiency” model	42
2.5 Discussion	43
2.5.1 Evolution of cosmic molecular gas mass density at $0 \leq z \leq 2.5$	43

2.5.1.1	The impact of the mass-metallicity relation	43
2.5.1.2	Bright SMGs undetected in the K -band	45
2.5.2	Comparison of the evolution of molecular gas mass density to other studies in the literature	46
2.5.3	Contribution of the brightest submillimetre sources to the cosmic evolution of the molecular gas mass density	48
2.5.4	Additional constraints on the evolution of molecular gas mass density	49
2.5.5	The epoch of molecular gas	51
2.5.6	Estimating the evolution of cosmic molecular gas mass density at $z \gtrsim 2.5$	51
2.6	Conclusions	52
3	The SCUBA-2 Large eXtragalactic Survey: 850 μm map, catalogue and the bright-end number counts of the XMM-LSS field	54
3.1	Introduction	54
3.2	The SCUBA-2 Large eXtragalactic Survey	55
3.2.1	Observations	56
3.2.2	Data reduction	58
3.2.3	Astrometric refinement and registration	64
3.3	Analysis	66
3.3.1	Area Coverage	66
3.3.2	Source extraction	67
3.3.3	Simulated SCUBA-2 maps	70
3.3.4	Flux boosting	72
3.3.5	Completeness	73
3.3.6	Positional uncertainty	75
3.3.7	False detection rate	78
3.4	Discussion	79
3.4.1	Bright-end number counts of the 850 μ m population	79
3.4.2	Comparison to models	87
3.5	Summary	91
4	ALMA follow-up of the SCUBA-2 Large eXtragalactic Survey XMM-LSS field: Source catalogue and first results	93
4.1	Introduction	93
4.2	Pinpointing the position of 850 μ m selected sources from S2LXS XMM-LSS with ALMA	94
4.2.1	ALMA observations and data reduction	96
4.2.2	Source extraction	97
4.2.3	Multiplicity Fraction	99
4.2.4	Redshift distribution	101
4.2.5	Summary	102
5	Conclusions	105
5.1	Evolution of the molecular gas mass density	105
5.2	The bright-end of the single-dish 850 μ m selected submillimetre population	106
6	The future of submillimetre astronomy	108
6.1	Future Infrared/Submillimetre Instruments	108

6.1.1	Atacama Large Aperture Submillimetre Telescope	109
6.1.2	James Webb Space Telescope	109
6.1.3	Third generation 850 μ m camera on the JCMT	110
6.1.4	Origins	110
6.1.5	TolTEC camera for the Large Millimeter-wave Telescope	111
6.1.6	Large Latin American Millimeter Array	111
6.1.7	Cerro Chajnantor Atacama Telescope - prime	111
6.2	Summary	112

A	Multi-wavelength imaging for sources in the SCUBA-2 Large eXtragalactic Survey main catalogue	113
----------	------------------------------------------------------------------------------------------------------	------------

	Bibliography	135
--	---------------------	------------

List of Figures

1.1	Λ Cold Dark Matter Model	2
1.2	The Hubble galaxy morphological classification scheme	3
1.3	Typical spectral energy distributions for four main galaxy types; spiral, elliptical, AGN and starburst.	4
1.4	Extragalactic Background Light	6
1.5	Star-forming main sequence	8
1.6	Negative K correction in submillimetre astronomy.	10
1.7	S2CLS number counts for $850\mu\text{m}$ sources	11
1.8	Gravitational Lensing	12
1.9	RGB image illustrating the multiple potential optical counterparts to a single-dish selected submillimetre source.	14
1.10	VLA and RGB images illustrating that radio interferometry reduces the number of potential optical counterparts to a single-dish selected submillimetre source.	16
1.11	Colours of a sample of SMGs compared to a sample of K -band selected galaxies, showing that SMGs are typically redder than galaxies selected at K -band.	18
1.12	Frequency range of ALMA receiver bands overplotted with the observed frequency of ^{12}CO lines ($J_{\text{up}} = 2-9$) for $1 < z < 5$, illustrating that submillimetre interferometers are an effective means to measure precise redshifts for SMGs.	20
1.13	The cosmic star formation rate density	22
1.14	Estimates of the molecular gas mass density from direct measurements of CO line emission	24
2.1	Graphical representation showing how we bin an individual galaxy according to its position in the observed map and redshift probability distribution	32
2.2	One- and two-dimensional posterior distributions for the average observed flux density in μJy of galaxies in each redshift bin for $\Delta z(0.25)-\Delta z(4.75)$	34
2.3	One- and two-dimensional posterior distributions for the average observed flux density in μJy of galaxies in each redshift bin for $\Delta z(5.25)-\Delta z(9.75)$	35
2.4	Two-dimensional posterior distributions for the average observed flux density in μJy of galaxies in each redshift bin for $\Delta z(0.25)-\Delta z(4.75)$ and $\Delta z(5.25)-\Delta z(9.75)$	36
2.5	Flux density and number density of galaxies in redshift intervals.	38
2.6	Estimates of $\rho_{\text{H}_2}(z)$ derived using a 3D stacking method and the RJ luminosity-to-gas mass ratio of Scoville et al. (2016).	44
2.7	Marginalised stellar mass estimates for our sample of galaxies, demonstrating that at high redshifts we are only sensitive to the most massive galaxies.	46
3.1	Layout of the S2LXS XMM-LSS map	58
3.2	Distribution of the zenith opacity at 225 GHz for the S2LXS observations.	59

3.3	Stages of DIMM data reduction	60
3.4	Flux density map for a PONG tile	63
3.5	Representative $0.5 \text{ deg} \times 0.5 \text{ deg}$ cutout of the S2LXS XMM-LSS matched filtered signal-to-noise ratio map.	64
3.6	S2LXS XMM-LSS matched filtered instrumental noise map overplotted with the positions of the $40 > 5\sigma$ sources detected in the S2LXS XMM-LSS field.	65
3.7	Cumulative area of the S2LXS XMM-LSS map as a function of instrumental noise.	68
3.8	Distribution of pixel values in the matched-filtered signal-to-noise ratio jackknife map compared to the distribution of pixel values in the matched-filtered signal-to-noise ratio science map	71
3.9	Flux boosting measured by comparing the recovered flux density to the injected flux density for each source in the fake source catalogue.	74
3.10	Distribution of injected (true) flux densities of sources in the fake source catalogue in bins of S_{obs} and $\sigma_{\text{inst}} = 4 \text{ mJy}$	75
3.11	Completeness measured by comparing the number of sources injected into our fake maps to the number recovered at a detection threshold of 5σ	76
3.12	Positional offset estimated by calculating the difference between the injected and recovered coordinates for each source in the fake catalogue.	77
3.13	Purity rate estimated by comparing the number of sources in the S2LXS XMM-LSS science map to the number of spurious detections in the jackknife map above a signal-to-noise threshold.	79
3.14	A comparison of the recovered number counts to the ‘true’ number counts in the simulated maps, before and after corrections.	85
3.15	Number counts of single-dish $850 \mu\text{m}$ selected sources measured from the S2LXS XMM-LSS survey 5σ catalogue	88
4.1	Multi-wavelength images for three sources in the S2LXS XMM-LSS $>5\sigma$ catalogue. We show the position of the ALMA counterparts illustrating the difficulty in identifying true multi-wavelength counterparts to single-dish sources without the finer resolution of ALMA.	95
4.2	ALMA signal-to-noise ratio maps.	99
4.3	Redshift distribution for ALMA counterparts to the brightest submillimetre sources in the S2LXS XMM-LSS $>5\sigma$ catalogue.	101
A.1	Multi-wavelength image cutouts centred on source S2LXSJ021831-053131	114
A.2	Multi-wavelength image cutouts centred on source S2LXSJ022700-052405	114
A.3	Multi-wavelength image cutouts centred on source S2LXSJ021735-054854	115
A.4	Multi-wavelength image cutouts centred on source S2LXSJ022548-041751	116
A.5	Multi-wavelength image cutouts centred on source S2LXSJ021520-053222	116
A.6	Multi-wavelength image cutouts centred on source S2LXSJ022252-042412	117
A.7	Multi-wavelength image cutouts centred on source S2LXSJ022324-042602	117
A.8	Multi-wavelength image cutouts centred on source S2LXSJ022735-051558	118
A.9	Multi-wavelength image cutouts centred on source S2LXSJ022322-033747	118
A.10	Multi-wavelength image cutouts centred on source S2LXSJ022614-045616	119
A.11	Multi-wavelength image cutouts centred on source S2LXSJ022854-042445	119
A.12	Multi-wavelength image cutouts centred on source S2LXSJ021826-041900	120
A.13	Multi-wavelength image cutouts centred on source S2LXSJ022342-044501	120

A.14 Multi-wavelength image cutouts centred on source S2LXSJ022332-042948	. .	121
A.15 Multi-wavelength image cutouts centred on source S2LXSJ022649-035146	. .	121
A.16 Multi-wavelength image cutouts centred on source S2LXSJ021938-042930	. .	122
A.17 Multi-wavelength image cutouts centred on source S2LXSJ022400-034623	. .	123
A.18 Multi-wavelength image cutouts centred on source S2LXSJ022042-053806	. .	123
A.19 Multi-wavelength image cutouts centred on source S2LXSJ021943-052436	. .	124
A.20 Multi-wavelength image cutouts centred on source S2LXSJ022256-051816	. .	124
A.21 Multi-wavelength image cutouts centred on source S2LXSJ022044-044641	. .	125
A.22 Multi-wavelength image cutouts centred on source S2LXSJ022508-045914	. .	125
A.23 Multi-wavelength image cutouts centred on source S2LXSJ022122-042315	. .	126
A.24 Multi-wavelength image cutouts centred on source S2LXSJ022426-042736	. .	127
A.25 Multi-wavelength image cutouts centred on source S2LXSJ021501-050817	. .	127
A.26 Multi-wavelength image cutouts centred on source S2LXSJ021536-045218	. .	128
A.27 Multi-wavelength image cutouts centred on source S2LXSJ021921-045651	. .	128
A.28 Multi-wavelength image cutouts centred on source S2LXSJ022039-053937	. .	129
A.29 Multi-wavelength image cutouts centred on source S2LXSJ021957-053406	. .	129
A.30 Multi-wavelength image cutouts centred on source S2LXSJ022032-053615	. .	130
A.31 Multi-wavelength image cutouts centred on source S2LXSJ021938-052502	. .	130
A.32 Multi-wavelength image cutouts centred on source S2LXSJ022134-053558	. .	131
A.33 Multi-wavelength image cutouts centred on source S2LXSJ021907-052202	. .	131
A.34 Multi-wavelength image cutouts centred on source S2LXSJ021910-051532	. .	132
A.35 Multi-wavelength image cutouts centred on source S2LXSJ021939-052315	. .	132
A.36 Multi-wavelength image cutouts centred on source S2LXSJ022122-051113	. .	133
A.37 Multi-wavelength image cutouts centred on source S2LXSJ022018-051124	. .	133
A.38 Multi-wavelength image cutouts centred on source S2LXSJ022150-052835	. .	134
A.39 Multi-wavelength image cutouts centred on source S2LXSJ022133-051558	. .	134
A.40 Multi-wavelength image cutouts centred on source S2LXSJ022003-052000	. .	135

List of Tables

2.1	Average observed $850\mu\text{m}$ flux density as a function of redshift	39
2.2	Average rest-frame $850\mu\text{m}$ luminosity, average molecular gas mass and co-moving molecular gas mass density as a function of redshift	40
3.1	Ancillary multi-wavelength data for the S2LXS XMM-LSS field	57
3.2	S2LXS XMM-LSS catalogue containing 40 sources detected at a significance of $>5\sigma$	80
3.3	Differential (dN/dS) and cumulative ($N > S'$) $850\mu\text{m}$ number counts measured from the S2LXS XMM-LSS survey.	89
4.1	AS2LXS catalogue containing 22 sources detected at a significance of $>5\sigma$. .	100

List of Abbreviations

ΛCDM	Λ Cold Dark Matter model
AS2UDS	ALMA survey of the S2CLS UKIDSS/UDS field
AGN	Active Galactic Nuclei
ALESS	ALMA survey of the LABOCA Extended Chandra Deep Field South Submillimetre Survey
ALMA	Atacama Large Millimeter/submillimeter Array
ASPECS	ALMA Spectroscopic Survey
ASPECS LP	ASPECS Large Program
CFHT CLAUDS	Canada-France-Hawaii Telescope Large Area <i>U</i> -band Deep Survey
CIB	Cosmic Infrared Background
CMB	Cosmic Microwave Background
COLDZ	CO Luminosity Density at High <i>z</i> Survey
COSMOS	Cosmic Evolution Survey
Deep Drill	<i>Spitzer</i> survey of the Deep Drilling fields
DIMM	Dynamical Iterative Map-Maker
DRC	Distant Red Core
DXS	Deep eXtragalactic Survey
E-COSMOS	Extended COSMOS
FCF	Flux conversion factor
FRC	Far-Infrared-Radio Correlation
FWHM	Full width half maximum
GOODS	Great Observatories Origins Deep Survey
H-ATLAS	<i>Herschel</i> Astrophysical Terahertz Large Area Survey
HerMES	<i>Herschel</i> Multi-tiered Extragalactic Survey
HSC-SSP	Hyper Suprime-Cam Subaru Strategic Program

IRAC	Infrared Array Camera
ISM	Interstellar Medium
JCMT	James Clerk Maxwell Telescope
LABOCA	Large Apex Bolometer Camera Array
LOFAR	Low Frequency Array
MAMBO	Max-Planck Millimeter Bolometer
MCMC	Markov Chain Monte Carlo
MIGHTEE	MeerKAT International GigaHertz Tiered Extragalactic Explorations
NOEMA	Northern Extended Millimeter Array
PSF	Point spread function
RJ	Rayleigh-Jeans
SCUBA	Submillimeter Common User Bolometer Array
SCUBA-2	Submillimeter Common User Bolometer Array 2
S2CLS	SCUBA-2 Cosmology Legacy Survey
S2COSMOS	SCUBA-2 COSMOS
S2LXS	SCUBA-2 Large eXtragalactic Survey
SED	Spectral Energy Distribution
SEDS	<i>Spitzer</i> Extended Deep Survey
SERVS	<i>Spitzer</i> Extragalactic Representative Volume Survey
SFR	Star formation rate
sSFR	Specific star formation rate
SMA	Submillimetre Array
SMG	Submillimetre Galaxy
SMURF	Submillimetre Common User Reduction Facility
SNR	Signal-to-noise ratio
SPIRE	Spectral and Photometric Imaging Receiver
SpUDS	<i>Spitzer</i> UKIDSS-UDS
SPT	South Pole Telescope
SPT-SZ	SPT Sunyaev Zel'dovich survey
STUDIES	SCUBA-2 Ultra Deep Imaging East Asian Observatory Survey
SWIRE	<i>Spitzer</i> Wide-area Infrared Extragalactic Survey
UDS	Ultra-Deep Survey
UKIRT	UK Infrared Telescope

UKIDSS	UKIRT Infrared Deep Sky Survey
ULIRG	Ultra Luminous Infrared Galaxy
UV	Ultra-Violet
VISTA VIDEO	Visible and Infrared Survey Telescope for Astronomy Deep Extragalactic Observations survey
VLA	Very Large Array
WFCAM	UKIRT Wide Field Camera
XMM-LSS	X-Ray Multi-Mirror Large Scale Structure Survey

Chapter 1

Introduction

1.1 Galaxy Formation and Evolution

1.1.1 Λ Cold Dark Matter Model

The Λ Cold Dark Matter (Λ CDM) model (see Bull et al., 2016, for a review) underpins our current understanding of galaxy formation and evolution (see Figure 1.1 for an illustration). The early Λ CDM Universe was hot, dense and radiation-dominated, and consisted of a nearly homogeneous plasma of photons and baryons (Jones and Lambourne, 2004). In its first moments the Universe underwent a period of exponential expansion, termed inflation, during which microscopic quantum fluctuations in the plasma were expanded to macroscopic scales (Baumann, 2012). The perturbations in the cold dark matter density grew through gravitational collapse in over-dense regions to form dark matter ‘halos’ (Jones and Lambourne, 2004).

As the Universe expanded it cooled, and electrons and baryons combined for the first time to form atoms – mostly neutral hydrogen. In this period (referred to as the ‘epoch of recombination’) the Universe was matter-dominated. As the photon scattering rate dropped below the rate of Hubble expansion, photons ceased to interact with electrons and the Universe became transparent (Ryden, 2016). Shortly after came the epoch of the ‘last scattering’, when typical Cosmic Microwave Background (CMB) photons were scattered for the last time by electrons. The density fluctuations that existed in the Universe at this time are imprinted on the CMB (Baumann, 2012).

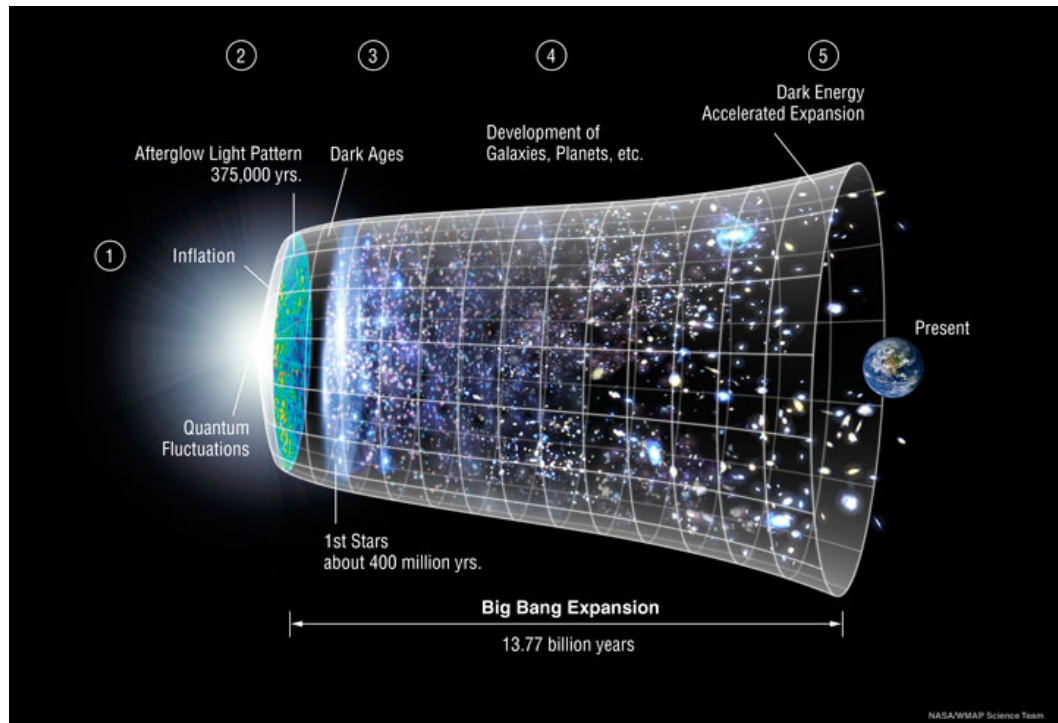


FIGURE 1.1: Illustration showing the evolution of the Universe as predicted by the Λ Cold Dark Matter model. Figure from https://lambda.gsfc.nasa.gov/education/graphic_history/univ_evol.cfm (National Aeronautics and Space Administration, 2015).

The framework of Λ CDM favours a ‘bottom-up’ model of galaxy formation (White and Rees, 1978). Following recombination baryons (in the form of gas) ‘fell’ into the gravitational wells of dark matter halos (Benson, 2010). Over time the gas cooled and condensed in the central regions of these dark matter halos, eventually settling to form rotationally supported disc-like structures (Fall and Efstathiou, 1980; Mo et al., 1998). Within these discs clumps of gas collapsed to form stars (Somerville and Davé, 2015). These primeval galaxies merged, and through further mergers over time, formed the massive galaxies we see in the local Universe today (White and Rees, 1978; Cole et al., 2000).

1.1.2 Galaxy structure

Over the course of the 20th century astronomers developed several approaches to classify external galaxies (e.g., Wolf, 1908; Hubble, 1926, 1936; de Vaucouleurs, 1959; Sandage, 1961; Sandage et al., 1975). These early attempts to study the structure of galaxies relied on their apparent visual morphology at optical wavelengths. Arguably the most well known of these classification schemes is the Hubble sequence (see Figure 1.2), a morphological classification

that divides galaxies into two main types; spiral and elliptical, with a further division of spiral galaxies into those with or those without bars. (Hubble, 1926, 1936).

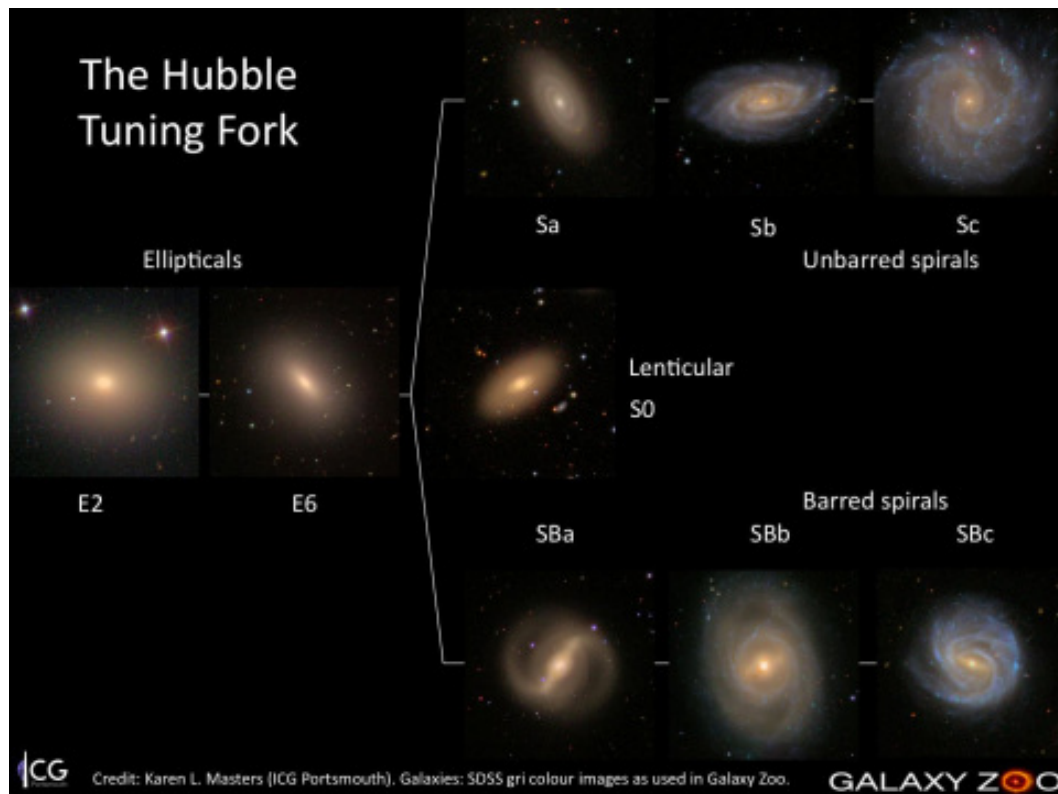


FIGURE 1.2: Hubble’s morphological classification scheme for galaxies, often referred to as ‘Hubble’s Tuning Fork’. This figure defines two main galaxy types; spiral and elliptical, with a further division of spiral galaxies into those with or those without bars. Figure from <https://blog.galaxyzoo.org/2011/02/23/the-hubble-tuning-fork/> (Masters, 2011).

Around the same time as morphological classification schemes were being developed, astronomers also began to correlate morphology with other physical properties, finding that in the local Universe elliptical galaxies are generally massive, red and show little evidence for current star formation, whilst spiral galaxies are less massive, blue and show evidence of ongoing star formation (e.g., Holmberg, 1958). This simplistic description of galaxy structure can often be applied in the local Universe, where massive galaxies can generally be described as spirals or ellipticals. However, the picture is not so straightforward in the high-redshift Universe ($z > 2$), where the galaxy population is dominated by irregular and peculiar galaxies that often have a very different structure to the galaxies we observe locally (e.g., Driver et al., 1995; Conselice et al., 2005). We also cannot simply link the colour of galaxies to star-forming activity, because, for example, the presence of an Active Galactic Nuclei (AGN) or dust extinction can affect the colours we observe (see Figure 1.3). Therefore, to build on our current understanding of galaxy evolution we

must study the physical properties of galaxies (i.e., stellar mass, star formation rate, gas mass) rather than relying on their visual morphology.

A spectral energy distribution (SED) shows the energy output of a galaxy across the electromagnetic spectrum. In Figure 1.3 we show template spectral energy distributions for four main galaxy types; spiral, elliptical, AGN and starburst, to illustrate how the different components of galaxies can affect their brightness at different wavelengths. Young stars typically emit most of their light at ultra-violet and optical wavelengths, and so we see a peak at these wavelengths in the spiral galaxy SED. For the starburst galaxy we also see a strong peak at $100\mu\text{m}$, which is caused by dust absorbing UV light from young stars and re-emitting this in the infrared part of the spectrum. Elliptical galaxies typically consist of old red stars, which emit most of their light at optical and near-infrared wavelengths, and so we see a dip in the SED of the elliptical galaxy at shorter wavelengths. We see a dip in the SEDs of typical star forming galaxies (i.e., the Sc and starburst galaxies in Figure 1.3) between a rest frame wavelength of $1.6\mu\text{m}$ (the stellar bump) and $100\mu\text{m}$ (the peak of star formation heated dust emission). In contrast AGN heated dust typically radiates at near- and mid-infrared wavelengths, effectively filling in this dip in the galaxy SED (e.g., Donley et al., 2012; Ivison et al., 2004).

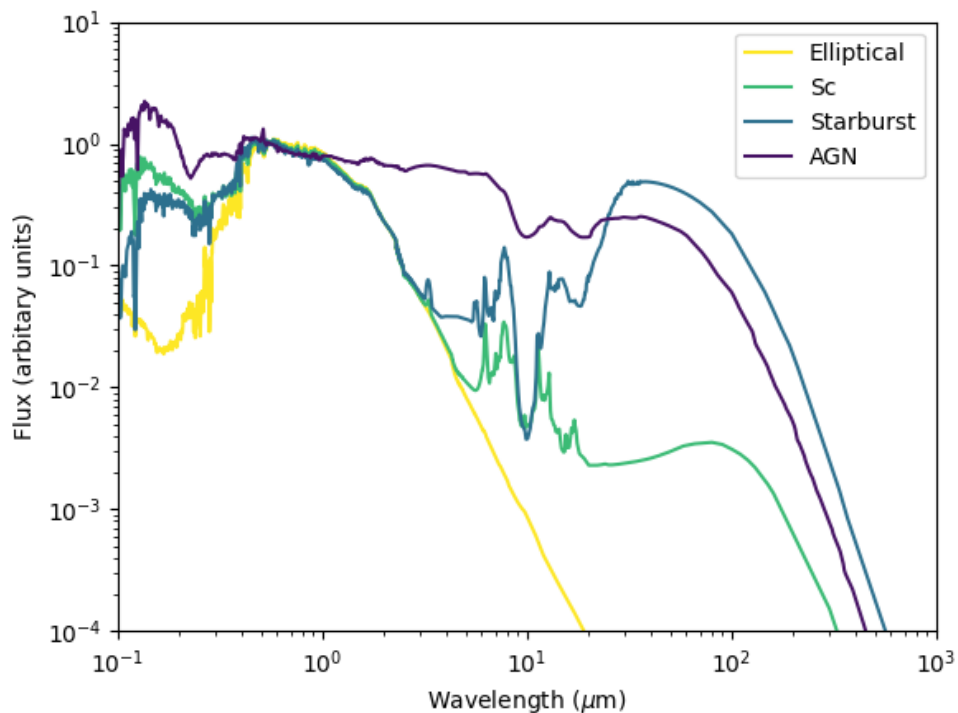


FIGURE 1.3: Typical spectral energy distributions for four main galaxy types; spiral (Sc), elliptical, AGN and starburst. The SED templates are taken from the SWIRE template library (Polletta et al., 2007).

It is common practice in astronomy to measure a galaxy's physical properties by fitting spectral energy distributions of model galaxies to data obtained from observations. Spectral energy distribution fitting can be used to estimate many fundamental galaxy properties such as star formation rate, stellar mass, photometric redshift, dust and gas mass, and luminosity.

1.2 Far-infrared and Submillimetre Astronomy

Historically our knowledge of how galaxies form and evolve has been driven by observations made at optical wavelengths. However, over the past 50 years, helped by the boom in infrared/millimetre facilities (both ground-based and in space), the study of the Universe at infrared/millimetre wavelengths has quickly gained momentum. The first infrared observations targeted a small number of known extragalactic sources revealing that some galaxies emit the same amount of energy in the infrared as at optical wavelengths (e.g., Low and Kleinmann, 1968; Kleinmann and Low, 1970). Over the course of the following decade the scale of infrared surveys dramatically expanded, with the first all-sky infrared survey (the *Infrared Astronomical Satellite* mission; Neugebauer et al., 1984) detecting $\sim 20,000$ local starburst galaxies, the majority of which were too faint to be included in previous optical catalogues (Beichman et al., 1988). In the 1990's the NASA *Cosmic Background Explorer* (Boggess et al., 1992) gave us the first measurements of the Cosmic Infrared Background (CIB; the integrated infrared emission from all galaxies in the history of the Universe). These data (e.g. Puget et al., 1996; Fixsen et al., 1998; Hauser et al., 1998), along with measurements of the CIB at mid-infrared wavelengths (e.g., Papovich et al., 2004; Dole et al., 2006) revealed that the Extragalactic Background Light has comparable intensities at optical ($\lambda < 8\mu\text{m}$) and infrared ($\lambda > 8\mu\text{m}$) wavelengths (see Figure 1.4), meaning that around half the optical and ultra-violet emission from galaxies is absorbed by interstellar dust and re-emitted in the far-infrared (e.g., Dole et al., 2006; Hauser and Dwek, 2001).

The most luminous infrared galaxies are known as Ultra Luminous Infrared Galaxies (ULIRGs) and Hyper Luminous Infrared Galaxies (HyLIRGs) with integrated infrared luminosities of $L_{\text{IR}} > 10^{12}L_{\odot}$ and $L_{\text{IR}} > 10^{13}L_{\odot}$ respectively, and star formation rates commonly in excess of $50M_{\odot}\text{yr}^{-1}$ (e.g., Sanders and Mirabel, 1996; Casey et al., 2014). In these dusty star-forming galaxies light from young, short-lived, massive stars is absorbed by the surrounding dust and re-radiated at infrared wavelengths.

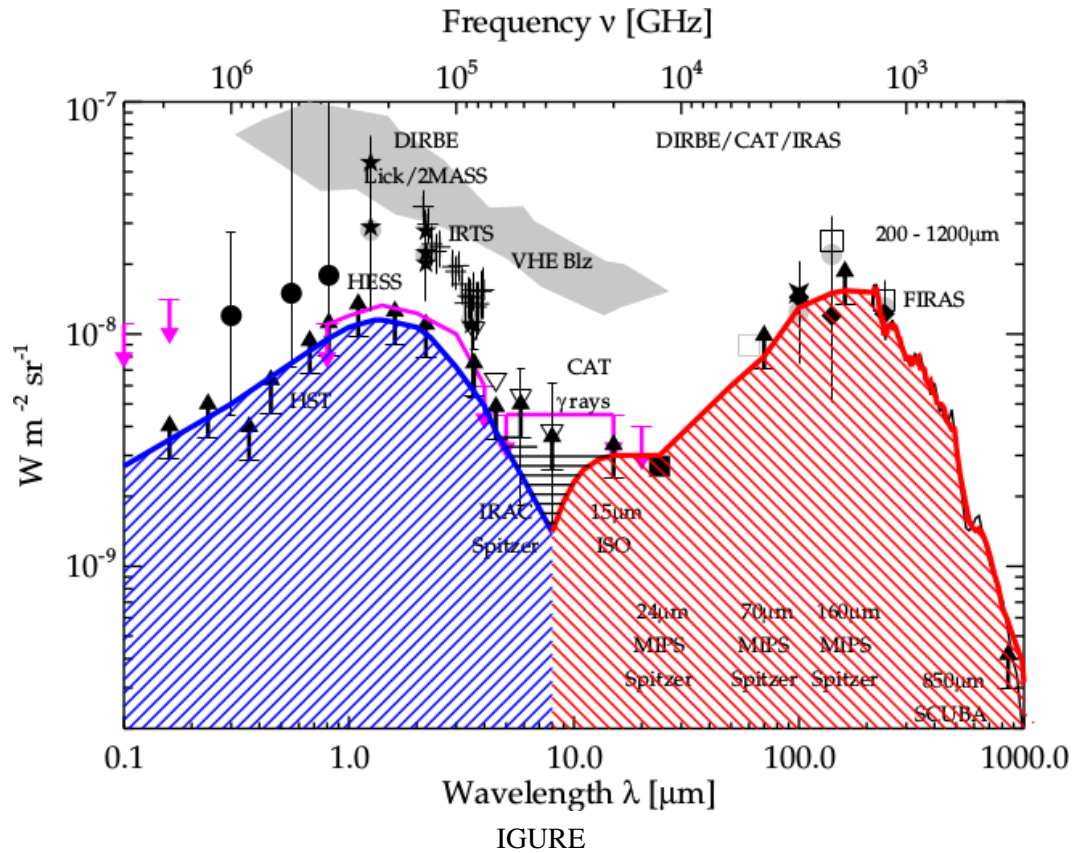


FIGURE 1.4: Estimates of the Cosmic Optical Background (blue-shaded) and Cosmic Infrared Background (red-shaded), illustrating that the Extragalactic Background Light has comparable intensities at optical and infrared wavelengths. Figure from Dole et al. (2006).

Dusty star-forming galaxies detected at submillimetre wavelengths are commonly known as Submillimetre Galaxies (SMGs). Since the first observations of SMGs in the late 1990's (e.g., Smail et al., 1997; Barger et al., 1998; Hughes et al., 1998) there has been considerable progress in our understanding of their physical properties and cosmological significance in the context of galaxy evolution (see Casey et al., 2014; Hodge and da Cunha, 2020, for detailed reviews). We now know that SMGs selected at $850\mu\text{m}$ are intrinsically highly infrared luminous ($L_{\text{IR}} > 10^{12}L_{\odot}$) with star formation rates in excess of $100M_{\odot}\text{yr}^{-1}$ (e.g., Chapman et al., 2005; Magnelli et al., 2012; Swinbank et al., 2014; Ikarashi et al., 2015; Michałowski et al., 2017; Miettinen et al., 2017), have a number density which peaks at $\langle z \rangle \approx 2-3$ (e.g., Chapman et al., 2005; Pope et al., 2005; Wardlow et al., 2011; Simpson et al., 2014; Chen et al., 2016; Miettinen et al., 2017), have high stellar masses (e.g., Swinbank et al., 2004; Hainline et al., 2011; Michałowski et al., 2012; Da Cunha et al., 2015; Michałowski et al., 2017), are gas-rich (e.g., Frayer et al., 1998; Greve et al., 2005; Tacconi et al., 2006; Ivison et al., 2011; Thomson et al., 2012; Bothwell et al., 2013), often host Active Galactic Nuclei (e.g., Alexander et al., 2005; Johnson et al., 2013; Pope et al., 2008; Wang et al., 2013), and with a volume density three orders of magnitude greater than

that of local ULIRGS (e.g., Smail et al., 1997; Chapman et al., 2005) contribute approximately 20% of the total star formation rate density over a redshift range 1 to 4 (e.g., Casey et al., 2013; Swinbank et al., 2014). These properties make SMGs excellent candidates for the progenitor population of massive elliptical galaxies seen in the local Universe today.

SMGs are observed to have (on average) higher star formation rates than local ULIRGs/HyLIRGs (e.g., Sanders and Mirabel, 1996; Casey et al., 2014; Swinbank et al., 2014; Michałowski et al., 2017), and so are sometimes considered to be ‘scaled-up’ versions of these local infrared-luminous galaxies (e.g., Swinbank et al., 2014). However, when placed in the context of the star-forming main-sequence (the tight correlation between star formation rate and stellar mass for star forming galaxies at a given redshift, e.g., Daddi et al., 2007), this picture of SMGs as ‘extreme’ ULIRGs/HyLIRGs is challenged. Equation 1.1 defines the main sequence with respect to the age of the Universe, where t is the age of the Universe in Gyr, SFR is the star formation rate in $M_{\odot}\text{yr}^{-1}$ and M_* is stellar mass in units of M_{\odot} (Speagle et al., 2014).

$$\log(\text{SFR}) = (0.84 - 0.026 \times t) \times \log(M_*) - (6.51 - 0.11 \times t) \quad (1.1)$$

In Figure 1.5 we show the star-forming main sequence from Speagle et al. (2014) corresponding to redshifts at the mid-point of four redshift bins ($z = 0.25$, $z = 1.25$, $z = 2.75$ and $z = 4.25$). We also show a factor of 3 offset above and below this main sequence to highlight any outliers. We over-plot a sample of ULIRGs (with $z < 0.5$) from Kilerci Eser et al. (2014) and SMGs (with $z > 0.5$) from the ALMA follow-up survey of the SCUBA-2 Cosmology Legacy Survey UDS field (Dudzevičiūtė et al., 2019). In this figure all the ULIRGS from the Kilerci Eser et al. (2014) sample lie above the main sequence and so are classified as outliers (i.e., starbursts), compared to just 25% of the SMG sample. We note that the majority of SMGs ($\approx 60\%$) reside on the star-forming main sequence.

Whilst many of the physical properties of SMGs are now well constrained, their formation mechanism remains widely debated. It has been suggested that similar to their low redshift analogues (ULIRGs) SMGs form via major mergers of gas-rich discs, which trigger star formation and black hole growth (e.g., Baugh et al., 2005). There is observational evidence to support this merger-driven scenario, with observations of some SMGs revealing irregular or interacting morphologies (e.g., Chapman et al., 2003; Chen et al., 2015) and/or complex gas kinematics (e.g., Tacconi et al., 2008; Engel et al., 2010). In contrast, recent results from cosmological

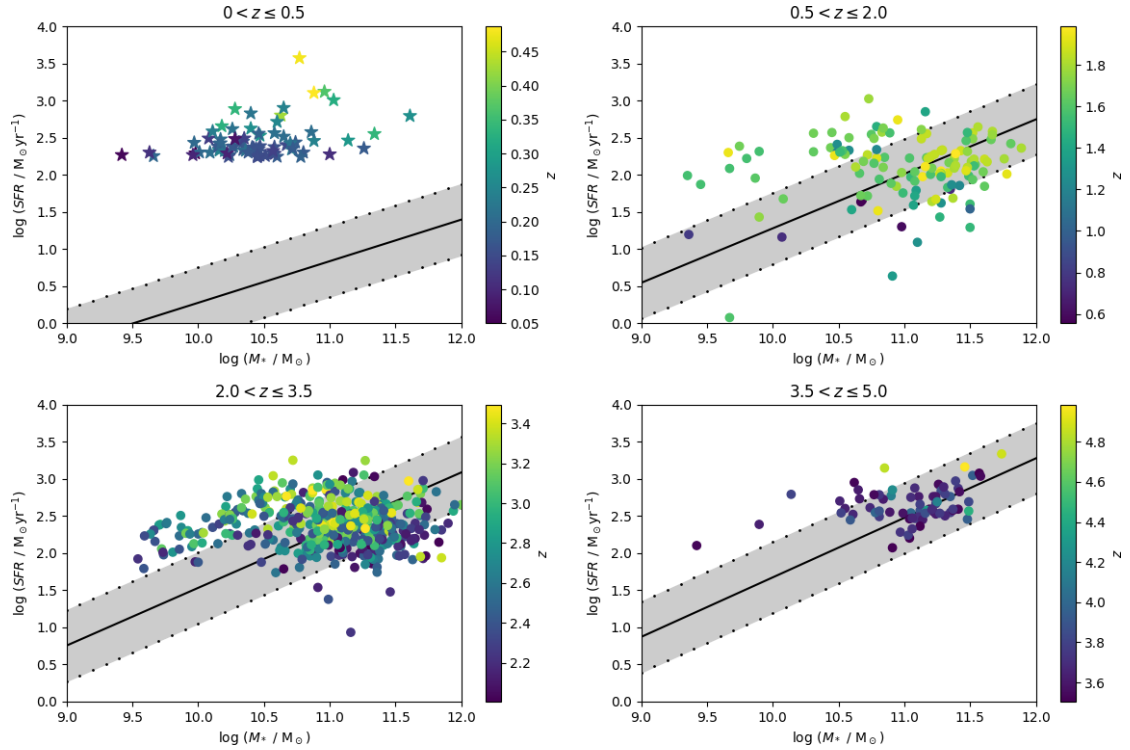


FIGURE 1.5: We show the star-forming main sequence (black line) from Speagle et al. (2014) corresponding to redshifts at the mid-point of four redshift bins ($z = 0.25$, $z = 1.25$, $z = 2.75$ and $z = 4.25$). The dashed black line shows a factor of 3 offset from this main sequence to highlight any outliers. We also show a sample of ULIRGs (filled stars) from Kilerci Eser et al. (2014) and SMGs (filled circles) from Dudzevičiūtė et al. (2019). All the ULIRGs are clear outliers above the main sequence. Conversely the majority ($\approx 60\%$) of the SMGs lie on the main sequence, with only 25% classified as outliers above the main sequence.

hydrodynamic simulations hint at an opposing formation mechanism, with the intense star formation rates of SMGs being fuelled through prolonged gas accretion over ≈ 1 Gyr (e.g., Davé et al., 2010; Narayanan et al., 2015). It is also quite possible that sub-populations of SMGs form via different processes, with SMGs seen to have distinct irregular or disk morphologies in ultraviolet imaging, indicating that these populations may have different formation histories (e.g., Miettinen et al., 2017). This is consistent with some semi-analytical models in which galaxy starbursts can be triggered by either disk (and bars if present) instabilities or galaxy mergers (Lacey et al., 2016; Cowley et al., 2019; Lagos et al., 2019), illustrating that various formation mechanisms may be responsible for the enhanced star formation rates we observe in SMGs.

As light from distant astronomical objects travels through space the wavelength at which the radiation is originally emitted is lengthened due to the expansion of the Universe. Consequently when we observe astronomical objects that lie at different redshifts in a particular filter/waveband we are sampling different rest-frame wavelengths. Equation 1.2 shows the relationship between redshift and wavelength,

$$\frac{\lambda_o}{\lambda_e} = 1 + z, \quad (1.2)$$

where λ_o is the wavelength of the observation and λ_e is the rest-frame wavelength. A K correction is used to transform the measurement of an object's observed flux (or magnitude) to an equivalent measurement in the rest-frame of the object. Submillimetre astronomy benefits from a strong negative K correction that arises from the shape of the intrinsic spectral energy distribution (SED) of a typical star-forming galaxy, which peaks at $100\ \mu\text{m}$. When we observe emission from a local star-forming galaxy at a wavelength of $850\ \mu\text{m}$ we are probing the Rayleigh Jean's tail (the rest-frame cold dust continuum emission) of the galaxy's intrinsic SED, and so, as we observe star-forming galaxies at increasing cosmological distances the rest-frame emission we observe at $850\ \mu\text{m}$ moves up the Rayleigh Jeans tail, closer to the peak of the intrinsic SED. This increasing power of rest-frame emission with increasing cosmological distance compensates for cosmological dimming. This means that SMGs of equal luminosity that lie at $1 < z < 8$ will have similar observed fluxes at $850\ \mu\text{m}$, making SMGs a useful probe of the early Universe (see Figure 1.6).

The first extragalactic submillimetre surveys were conducted with the Submillimeter Common User Bolometer Array camera (SCUBA; Holland et al., 1999) mounted on the James Clerk Maxwell telescope (JCMT), providing the first census of dust-obscured star formation in distant galaxies at submillimetre wavelengths (Smail et al., 1997; Hughes et al., 1998; Barger et al., 1998). Subsequent extragalactic submillimetre surveys built on the success of these early observations, and aided by the development of new submillimetre/millimetre instruments such as the Large Apex BOLometer Camera Array (LABOCA; Siringo et al., 2009), AzTEC (Wilson et al., 2008) and the MAX-Planck Millimeter BOLometer (MAMBO Kreysa et al., 1998), the scale of extragalactic surveys at submillimetre/millimetre wavelengths expanded (e.g., Coppin et al., 2006; Eales et al., 2000; Scott et al., 2008; Weiß et al., 2009). However, the limited field of view and sensitivity of the early submillimetre/millimetre instruments made it difficult to map large areas of the sky (i.e., $> 1\ \text{deg}^2$), with the largest and deepest of these surveys detecting around 100 sources (Coppin et al., 2006; Weiß et al., 2009), insufficient numbers for robust statistical studies of this cosmologically important population of galaxies.

A breakthrough in single-dish submillimetre astronomy came with the introduction of SCUBA-2 (Holland et al., 2013), the second generation bolometer array on the JCMT. SCUBA-2 is a dual wavelength camera with two arrays of 5120 pixels that simultaneously map the sky at

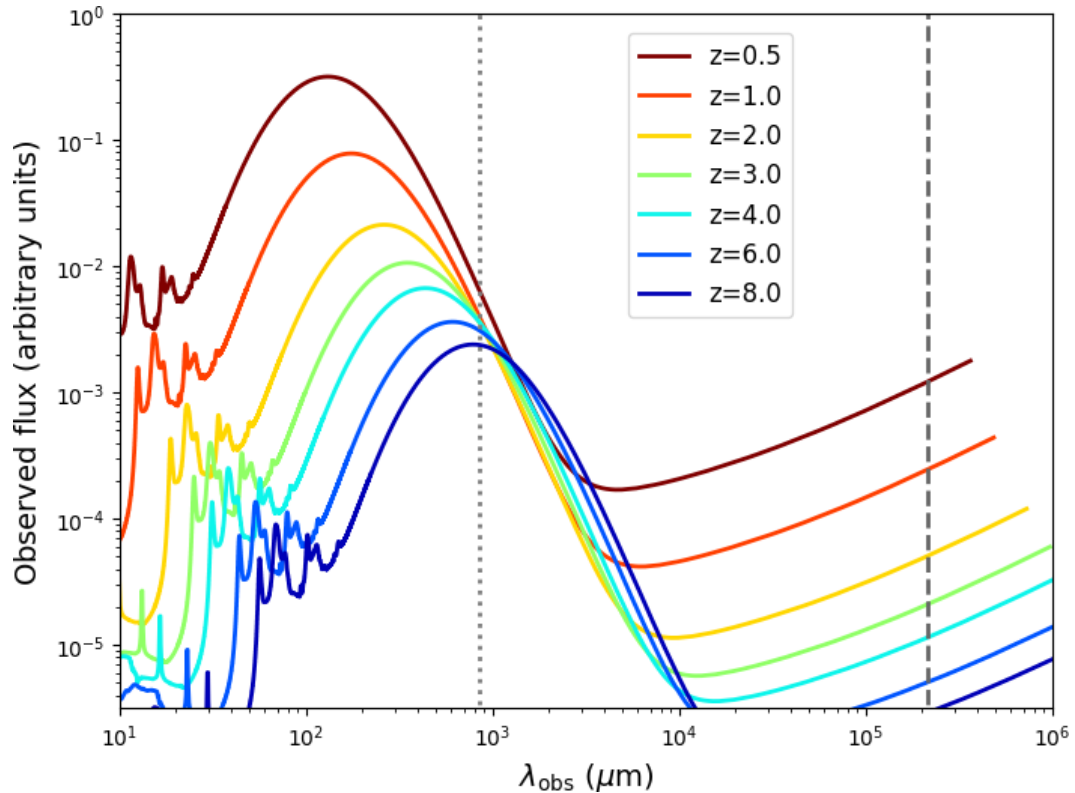


FIGURE 1.6: The average ultraviolet-to-radio intrinsic SED of galaxies detected in the ALMA survey of SMGs in the Extended Chandra Deep Field South (ALESS; Da Cunha et al., 2015), redshifted to show the observed flux (in arbitrary units) for the redshift range $0.5 < z < 8$. At a wavelength of $850\mu\text{m}$ (light grey dotted line) the flux densities of galaxies are nearly unchanged between $1 < z < 8$ due to the very negative K correction. However, at a wavelength of 0.21 m (corresponding to a frequency of 1.4 GHz , i.e., within the frequency range of the Very Large Array), shown as the dark dashed line, the observed flux is fainter with increasing redshift (i.e., a positive K correction).

wavelengths of $450\mu\text{m}$ and $850\mu\text{m}$, covering a field of view of 8 arcmin^2 . With a mapping speed that is over an order of magnitude faster than that of its predecessor (at equivalent depth), SCUBA-2 opened the door for wide area (i.e., $> 1\text{ deg}^2$) surveys at submillimetre wavelengths. The first such survey was the SCUBA-2 Cosmology Legacy Survey (S2CLS; Geach et al., 2017), which began shortly after the commissioning of SCUBA-2. This survey, the largest of the seven original legacy surveys undertaken with JCMT, mapped a total area of 5 deg^2 over seven extragalactic fields to a median depth (at $850\mu\text{m}$) of $1\sigma \simeq 1\text{ mJy beam}^{-1}$. Owing to the wide-area and depth of S2CLS, this survey detected almost 3000 sources at a significance of $> 3.5\sigma$ in the $850\mu\text{m}$ maps, a sample an order of magnitude larger than in previous submillimetre surveys, allowing the single-dish $850\mu\text{m}$ number counts to be measured to unprecedented accuracy. The S2CLS $850\mu\text{m}$ number counts are well fit by a Schechter (1976) function of the form

$$\frac{dN}{dS} = \left(\frac{N_0}{S_0}\right) \left(\frac{S}{S_0}\right)^{-\gamma} \exp\left(-\frac{S}{S_0}\right), \quad (1.3)$$

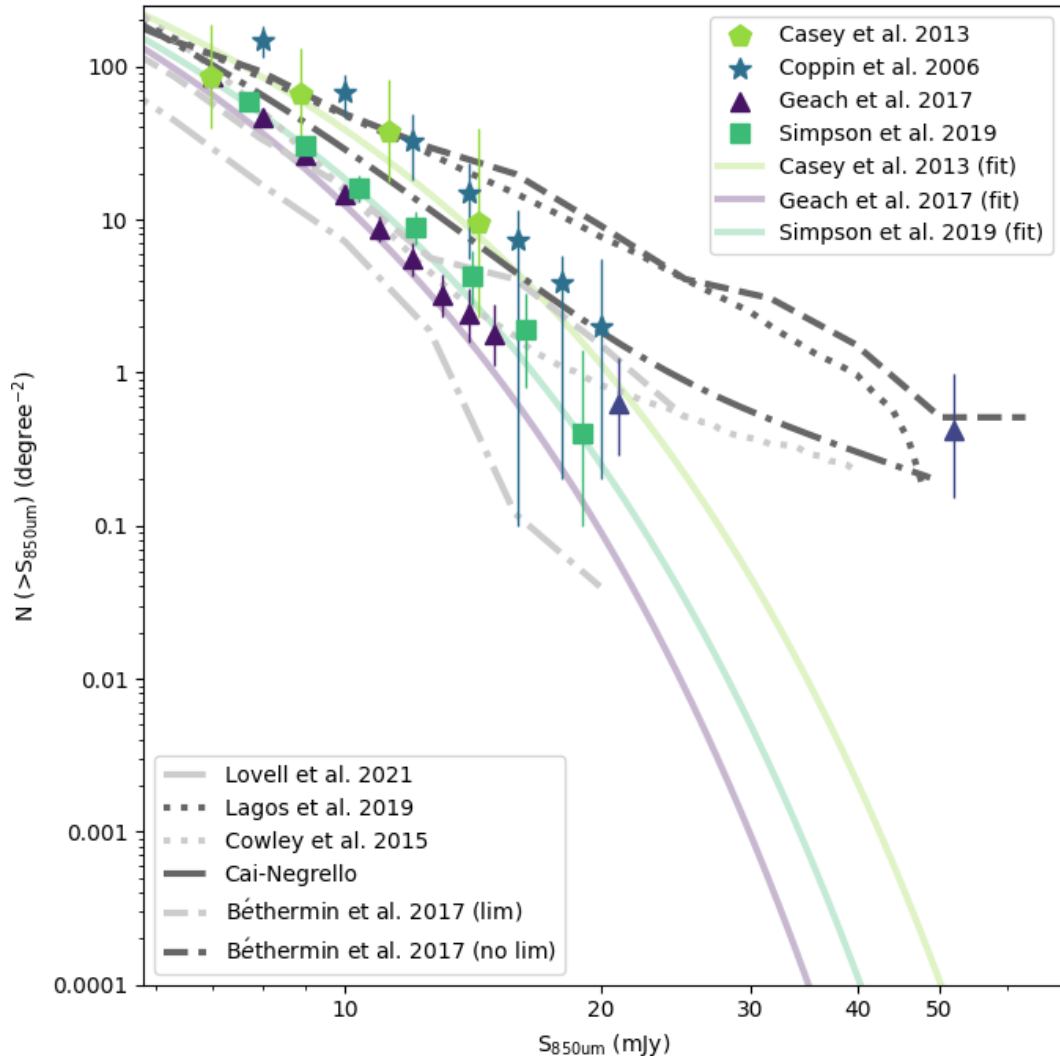


FIGURE 1.7: Cumulative number counts of single-dish $850\mu\text{m}$ selected sources measured from the S2CLS survey $>3.5\sigma$ catalogue (purple triangles; Geach et al., 2017). The error bars show Poisson uncertainties (Gehrels, 1986). We also show the observational constraints from S2COSMOS (Simpson et al., 2019), Casey et al. (2013) and Coppin et al. (2006), and the $850\mu\text{m}$ number counts from semi-analytic models (Cowley et al., 2015; Lagos et al., 2019), empirical models (Béthermin et al., 2017; Cai et al., 2013; Negrello et al., 2017) and the cosmological hydrodynamical simulation SIMBA (Lovell et al., 2021). At flux densities above 15 mJy there is a clear upturn in the S2CLS source counts, which lie above the Schechter (1976) function fit (purple line).

with $N_0 = 7180 \pm 1200 \text{ deg}^{-2}$, $S_0 = 2.5 \pm 0.4 \text{ mJy beam}^{-1}$ and $\gamma = 1.5 \pm 0.4$ (see Figure 1.7). However, at intrinsic fluxes above 15 mJy there is a clear upturn in the S2CLS source counts, which lie above the Schechter (1976) function fit.

An over-abundance of bright sources is also seen at far-infrared wavelengths in the *Herschel* Astrophysical Terahertz Large Area Survey (H-ATLAS; Eales et al., 2010; Negrello et al., 2010) and the *Herschel* Multi-tiered Extragalactic Survey (HerMES; Oliver et al., 2012; Wardlow et al.,

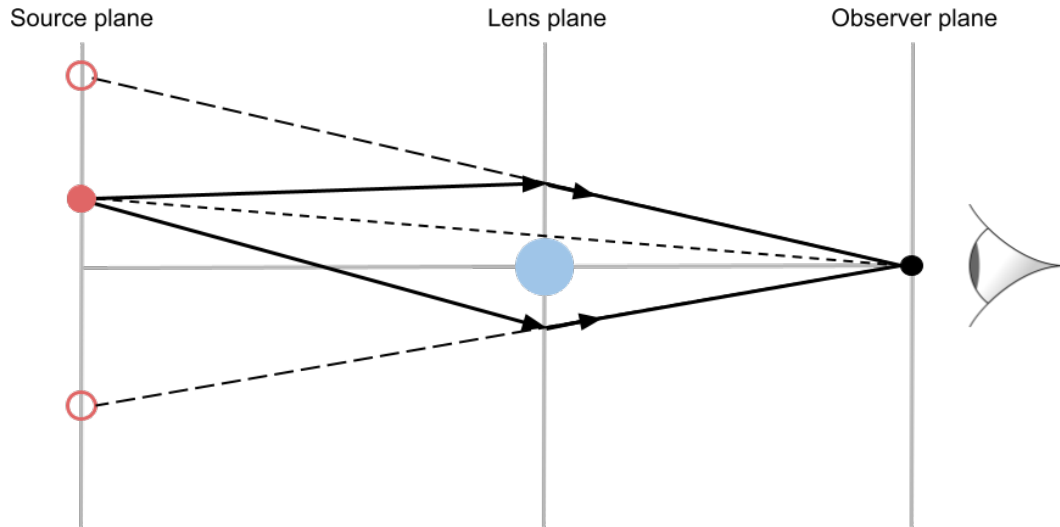


FIGURE 1.8: An illustration of gravitational lensing. As the light from a distant source (i.e., a galaxy) passes a foreground massive object the path of the light is curved. This causes the image of the galaxy to be distorted, and as there are multiple light paths connecting the source and the observer, this gives rise to multiple images of the same galaxy.

2013), and at millimetre wavelengths (but only at high flux densities, $S_{1.4\text{mm}} \gtrsim 10\text{mJy}$, corresponding to $S_{850\mu\text{m}} \gtrsim 40\text{mJy}$) in the South Pole Telescope Sunyaev Zel’dovich survey (SPT-SZ; Vieira et al., 2010; Mocanu et al., 2013), and is attributed to the presence of local objects and high-redshift gravitationally lensed sources. Gravitational lensing occurs when light from a distant source (i.e., a galaxy) passes a massive foreground object (i.e., a galaxy cluster), causing the path of light to curve (see Figure 1.8). The deflection of light by massive objects is predicted by Einstein’s General Theory of Relativity and arises because the gravity of these massive objects can curve spacetime. Through gravitational lensing the image of a distant source will be distorted, and if there are multiple light paths connecting a source and an observer, this will also give rise to multiple images of the same galaxy. Gravitational lensing magnifies the image of the background source which allows us to observe light from distant galaxies that would otherwise be too faint for us to detect.

It has been demonstrated that a simple flux cut at 100mJy in the *Herschel* $500\mu\text{m}$ band is almost 100 per cent effective at selecting strongly lensed galaxies, after local ($z < 0.1$) sources of emission have been removed (Negrello et al., 2010; Wardlow et al., 2013). S2CLS (Geach et al., 2017) provides tentative evidence that a flux cut at $850\mu\text{m}$ may yield a similar result – the brightest $850\mu\text{m}$ selected sources in this survey are a lensed high-redshift galaxy (‘Orochi’; Ikarashi et al., 2011) and a well-known Galactic object (the Cat’s Eye Nebula). However, with only six $850\mu\text{m}$ selected sources in S2CLS with intrinsic fluxes above 15mJy , the bright-end of the number counts remains poorly constrained and the potential of a flux cut at this wavelength

to select strongly lensed galaxies barely explored. The brightest SMGs selected at $850\ \mu\text{m}$ are also observed to be the most distant (e.g., Stach et al., 2019; Simpson et al., 2020; Chen et al., 2022), but with so few single-dish selected $850\ \mu\text{m}$ sources with flux densities $S_{850\ \mu\text{m}} > 15\ \text{mJy}$ the redshift distribution of sources in this flux regime is poorly constrained, and the trend of increasing redshift with submillimetre flux density is untested for these ultra-bright sources. Current galaxy formation models struggle to reproduce the number of ultra-bright SMGs observed (e.g., Béthermin et al., 2017; Cowley et al., 2015; Lagos et al., 2019; Lovell et al., 2021) and also vary in their predictions of the redshift distribution for these bright submillimetre galaxies (e.g., Béthermin et al., 2017; Lacey et al., 2016; Lagos et al., 2020; Lovell et al., 2021), and so observing a sufficient number of highly infrared luminous galaxies for robust statistical studies, is key to provide strong constraints for these models. Intrinsically bright submillimetre sources are rare, with abundances for sources with flux densities $>20\ \text{mJy}$ currently estimated to be only $\approx 0.5\text{--}5$ galaxies per square degree (e.g., Béthermin et al., 2012; Geach et al., 2017), and so a moderate depth survey at $850\ \mu\text{m}$ with an area $> 10\ \text{deg}^2$ is needed to properly probe this far-infrared luminous, and potentially high redshift population of galaxies.

1.3 Identifying multi-wavelength counterparts to Submillimetre Galaxies

Accurately identifying the true multi-wavelength counterpart/counterparts to a single-dish detected submillimetre source is important, since multi-wavelength photometry can be used to derive a galaxy’s physical properties such as photometric redshift, stellar mass and star formation rate via spectral energy distribution (SED) fitting. However, identifying the unambiguous multi-wavelength counterpart/counterparts to a single-dish submillimetre source is difficult due to the poor resolution of single-dish telescopes. Whilst the typical resolution of ultra-violet (UV) and optical surveys is sub-arcsecond (e.g., the Hyper Suprime-Cam Subaru Strategic Program r -band wide tier image has a resolution of $0.67\ \text{arcsec}$; Aihara et al., 2018), the resolution of single-dish surveys at a wavelength of $850\ \mu\text{m}$ is around $15''$ (i.e., the beam size of SCUBA-2 on the James Clark Maxwell Telescope; Holland et al., 2013). This means that there are usually multiple potential UV/optical counterparts for a single-dish selected submillimetre source within the single-dish beam (see Figure 1.9). The emission from a single-dish detected source may also come from either an individual submillimetre galaxy, or from multiple SMGs blended in the single-dish beam. These multiple components can be detected at the finer resolution of submillimetre

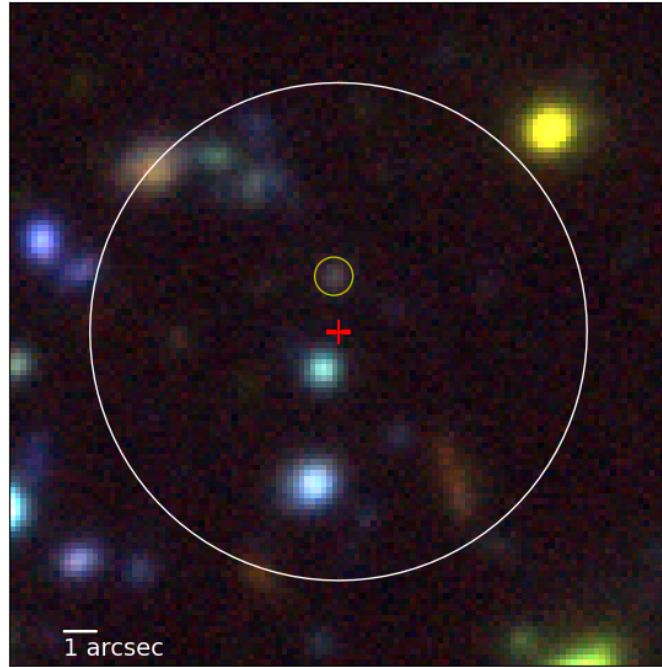


FIGURE 1.9: Red-Green-Blue colour image ($20'' \times 20''$) centred on the position of a single-dish $850\mu\text{m}$ selected source – S2LXSJ021939-052315 from the SCUBA-2 Large eXtragalactic Survey (S2LXS; Chapter 3). The colour image is made using y -, i - and g -band data from the Hyper Suprime-Cam Subaru Strategic Program (HSC-SSP; Aihara et al., 2018). The white circle shows the SCUBA-2 beam size ($15''$). The red cross marks the position of the S2LXS source and the yellow circle marks the position of the counterpart from the ALMA survey of the S2CLS UKIDSS/UDS field (AS2UDS; Stach et al., 2019). This images illustrates that there may be multiple potential optical counterparts for a single-dish selected submillimetre source within the SCUBA-2 beam.

interferometers (see section 1.3.3 for details), with surveys finding that approximately 44% of single-dish sources with flux densities $S_{850\mu\text{m}} > 9\text{ mJy}$ and 28% of single-dish sources with flux densities $S_{850\mu\text{m}} > 5\text{ mJy}$ are blends of multiple SMGs with flux densities $S_{850\mu\text{m}} \geq 1\text{ mJy}$ (e.g., Stach et al., 2018). This means that there may be more than one multi-wavelength counterpart to a single-dish selected submillimetre source. This picture is complicated further as for around 20% of single-dish selected sources the true optical counterpart/counterparts are too faint to be detected (e.g., Dudzevičiūtė et al., 2019). If the true multi-wavelength counterpart is too faint to be seen then either no multi-wavelength counterpart will be found, or a neighbouring galaxy may be incorrectly classified as the true counterpart to a single-dish selected $850\mu\text{m}$ source. Over the past few decades several methods have been developed to tackle the challenge of correctly identifying multi-wavelength counterparts to single-dish selected submillimetre sources; the various approaches are discussed in the following subsections.

1.3.1 Radio interferometry

Many of the early attempts to identify unambiguous multi-wavelength counterparts to single-dish selected submillimetre sources (e.g., Ivison et al., 2002, 2007; Pope et al., 2006; Chapin et al., 2009) exploited the tight linear relationship between radio and far-infrared emission in star-forming galaxies, known as the far-infrared-radio correlation (FRC; Helou et al., 1985; Condon, 1992). This correlation arises because both far-infrared and radio emission are effective tracers of star formation, specifically the formation and destruction of massive stars. Massive, young stars emit most of their energy at UV wavelengths, which is absorbed by the surrounding dust and re-emitted in the far-infrared part of the electromagnetic spectrum. At the end of their (short) lives these same massive stars explode as supernovae and cosmic rays are accelerated in the supernova remnants emitting non-thermal radio continuum radiation. The FRC is often described by the parameter q_{IR} , defined as the logarithmic ratio between L_{IR} and $L_{1.4\text{GHz}}$

$$q_{\text{IR}} = \log_{10} \left(\frac{L_{\text{IR}}/L_{\odot}}{L_{1.4\text{GHz}}/L_{\odot} \times 3.75 \times 10^{12} \text{Wm}^{-2}} \right), \quad (1.4)$$

with surveys typically measuring a median value of q_{IR} in the range $q_{\text{IR}} = 2.2\text{--}2.7$ for star-forming galaxies (e.g., Ivison et al., 2010; Sargent et al., 2010; Thomson et al., 2014; Algera et al., 2020).

One of the advantages of using deep radio observations to identify counterparts to single-dish selected submillimetre sources is that the surface density of radio sources is much less than in the optical, and so the probability that a radio source is randomly associated with a submillimetre source is low (e.g., Ivison et al., 2002; Pope et al., 2006). The low surface density of radio sources also means that it is unlikely that a single-dish selected submillimetre source will have multiple possible radio counterparts, with approximately 10% of submillimetre sources expected to have 2 possible radio counterparts (e.g., Ivison et al., 2002; Chapman et al., 2005). The resolution of surveys conducted with radio interferometers is also typically finer than single-dish submillimetre surveys; the LOw Frequency ARray (LOFAR) survey of the XMM-LSS field has an angular resolution of $7.5 \times 8.5''$ (Hale et al., 2019); the VLA survey of the XMM-LSS field has an angular resolution of $4.5''$ (Heywood et al., 2020); and the MeerKAT International Gigahertz Tiered Extragalactic Explorations survey of the XMM-LSS field has an angular resolution

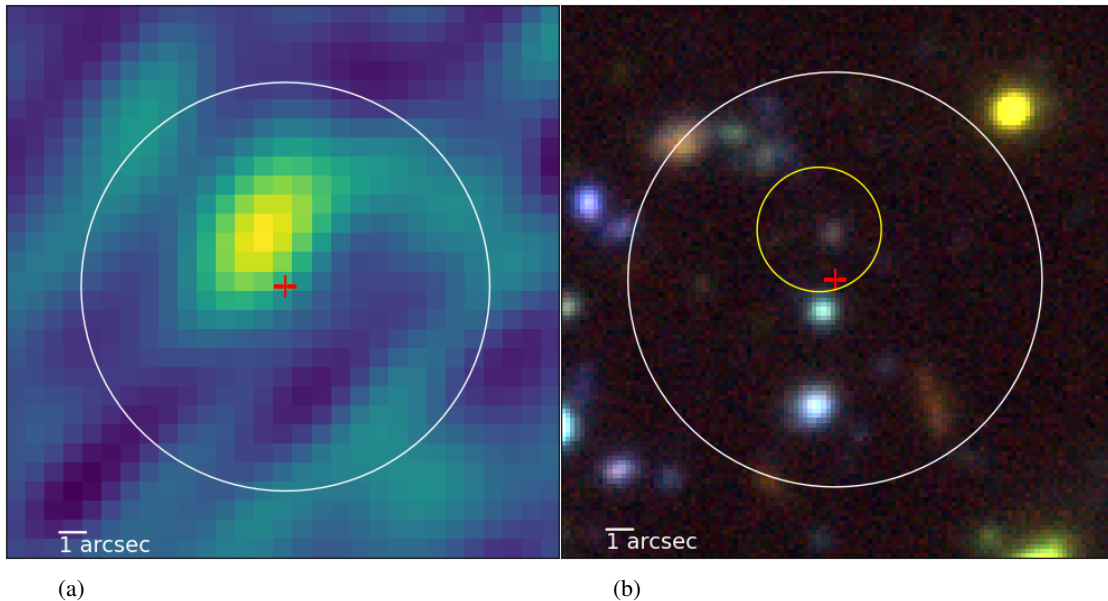


FIGURE 1.10: (a) Image cutout ($20'' \times 20''$) from the VLA 1-2 GHz survey of the XMM-LSS field total intensity mosaic (Heywood et al., 2020). This cutout is centred on the position of a single-dish $850 \mu\text{m}$ selected source – S2LXSJ021939-052315 from S2LXS (Chapter 3). The white circle shows the SCUBA-2 beam ($15''$) centred on the position of the S2LXS source (red cross) (b) Red-Green-Blue colour image ($20'' \times 20''$) also centred on the position of the single-dish $850 \mu\text{m}$ selected source S2LXSJ021939-052315 from S2LXS. The colour image is made using y -, i - and g -band data from the Hyper Suprime-Cam Subaru Strategic Program (HSC-SSP; Aihara et al., 2018). The white circle shows the SCUBA-2 beam ($15''$) centred on the position of the S2LXS source (red cross). The yellow circle is centred on the position of the radio counterpart from the VLA survey of the XMM-LSS field (Heywood et al., 2020) and shows the resolution of the VLA image ($4.5''$). There is only one radio source within the SCUBA-2 beam (sub-figure a) compared to multiple optical sources (sub-figure b) illustrating that the source density in the deep radio survey is much less than in the optical. These images also clearly show how the finer resolution of the radio detection (assuming that this is not randomly associated with the submillimetre source) reduces the number of potential UV/optical counterparts for the S2LXS source.

of $8.2''$ (e.g., Heywood et al., 2022), and so once a radio counterpart to a single-dish submillimetre source is identified it is much simpler to identify the corresponding UV/optical counterpart from the position of the radio source (see Figure 1.10 for illustration).

In submillimetre astronomy it became common practice (e.g., Ivison et al., 2007; Pope et al., 2006; Chapin et al., 2009; Biggs et al., 2011) to use the method of Downes et al. (1986) to calculate the probability that a radio source of an observed flux density at an observed distance from a submillimetre source is a random association ($'P'$). This method applies a correction factor to the raw Poisson probability to account for the given search radius and the limiting depth of the radio observations. As this approach takes into account the surface density of radio sources as a function of flux density, if there are two (or more) possible radio counterparts at the same distance from a submillimetre source, the brighter (and so rarer) object will have the lower

value of ‘ P ’. Typically in submillimetre surveys a radio counterpart is considered to be secure if it has $P < 0.05$.

Unfortunately using radio identifications as a route to identifying multi-wavelength counterparts to SMGs is not without its limitations: approximately 25-60% of submillimetre sources do not have secure radio counterparts (e.g., Ivison et al., 2002; Pope et al., 2006; Ivison et al., 2007; Biggs et al., 2011; Cowie et al., 2017)¹; around 10% of submillimetre sources will have multiple possible radio counterparts (e.g., Ivison et al., 2002; Pope et al., 2006; Ivison et al., 2007), and assuming a value $P < 0.05$ means that approximately 5% of matches will be spurious identifications. In addition, in contrast to submillimetre observations that benefit from a strong negative K correction, radio observations are hindered by a positive K correction (see Figure 1.6), thus for a fixed luminosity and observer-frame wavelength, as the cosmological distance of a galaxy increases, the rest-frame galaxy spectrum sampled is intrinsically fainter. This means that with the sensitivity of existing radio facilities it is very difficult to detect radio emission for galaxies at redshifts $z > 3.5$ (Casey et al., 2014), and so this method preferentially selects counterparts for SMGs at $z < 3.5$.

1.3.2 Optical and near-infrared colour selection

SMGs are typically red in optical-near-infrared colours (e.g., Smail et al., 2002; Ivison et al., 2002; Frayer et al., 2004; Yun et al., 2008). This characteristic has motivated several surveys to use some form of optical-near-infrared colour selection to identify multi-wavelength counterparts to single-dish selected submillimetre sources (e.g., Yun et al., 2008; Biggs et al., 2011; Yun et al., 2012; Alberts et al., 2013; Chen et al., 2016; An et al., 2019; Shim et al., 2022). In Figure 1.11 we compare the colours of a sample of SMGs from the ALMA follow up survey of the S2CLS UDS field (Dudzevičiūtė et al., 2019) to a sample of K -band selected galaxies from the UKIRT Infrared Deep Sky Survey UDS data release 11 catalogue (Lawrence et al., 2007, Alamaini et al. in prep.). We show the colours from the optical-near-infrared triple colour selection of Chen et al. (2016) to illustrate that SMGs are typically redder than K -band selected galaxies, thus allowing counterparts to be identified via a colour selection approach. Since single-dish submillimetre surveys are commonly conducted in fields with extensive multi-wavelength coverage, using solely a colour selection takes advantage of existing data and negates the need for further follow-up (i.e., interferometry) observations. However, a number of surveys use more

¹We note that fraction of secure radio counterparts to submillimetre sources found likely varies between surveys due to the sensitivity of the radio maps, the chosen search radius and the size of the single-dish beam.

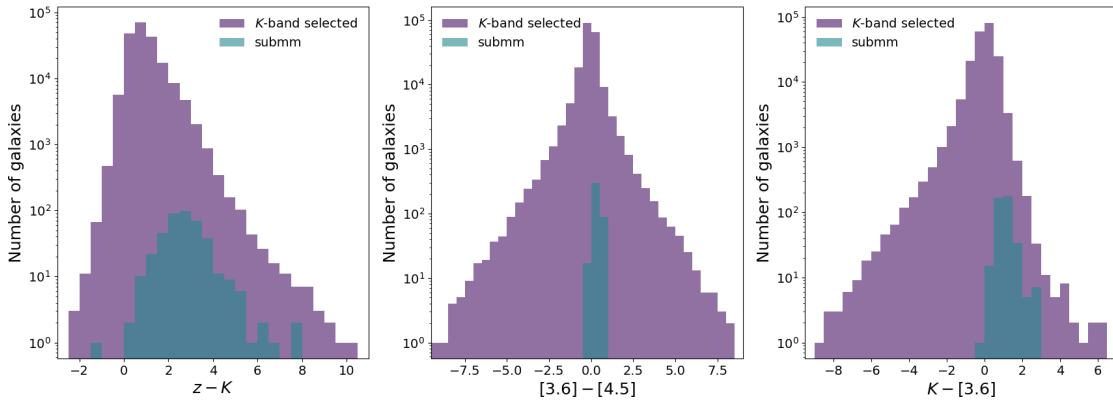


FIGURE 1.11: We compare the colours of a sample of SMGs (teal histogram) to a sample of K -band selected galaxies (purple histogram). The sample of SMGs is taken from the ALMA follow up survey of the S2CLS UDS field (Dudzevičiūtė et al., 2019) and the sample of K -band selected galaxies are from the UKIRT Infrared Deep Sky Survey UDS data release 11 catalogue (Lawrence et al., 2007, Almaini et al. in prep). The colours shown are from the optical-near-infrared triple colour selection of Chen et al. (2016), illustrating that SMGs are typically redder than K -band selected galaxies.

than one technique to identify multi-wavelength counterparts to single-dish selected submillimetre sources, combining the results obtained via radio interferometry (Biggs et al., 2011; Yun et al., 2012; Chen et al., 2016; An et al., 2019; Shim et al., 2022) and/or $24\mu\text{m}$ emission (Biggs et al., 2011; Yun et al., 2012) with a colour selection. Using several different methods to identify counterparts can be an effective way to reduce the biases inherent in these approaches. Employing radio interferometry to locate robust counterparts to SMGs preferentially identifies counterparts for brighter (at FIR/submillimetre wavelengths) and lower redshift galaxies. This is expected given the known far-infrared-radio correlation and the positive K correction at these wavelengths. However, in contrast to radio interferometry follow up, colour selections are able to successfully identify counterparts for fainter and higher redshift SMGs (e.g., Chen et al., 2016; Shim et al., 2022). By using both a colour selection technique and radio interferometry to identify multi-wavelength counterparts to single-dish selected submillimetre sources the completeness of identifications can be boosted to 70–80% (e.g., Chen et al., 2016; An et al., 2019; Shim et al., 2022), which is compatible with the expectation that $\sim 20\%$ of SMGs will be undetected at optical/near-infrared wavelengths (e.g., Dudzevičiūtė et al., 2019).

1.3.3 Submillimetre interferometry

Arguably the simplest way to effectively identify unambiguous multi-wavelength counterparts to single-dish selected submillimetre sources is through deep follow up observations conducted with submillimetre interferometers, with the obvious advantage that these follow up surveys are

sampling the same frequency range as the initial detection. There are currently several large submillimetre interferometers; the Submillimeter Array (SMA); the Northern Extended Millimeter Array (NOEMA); and the Atacama Large Millimeter/submillimeter Array (ALMA), all offer sub-arcsecond resolution and continuum sensitivities equivalent to S2CLS within reasonable integration times. Taking ALMA as an example, for a continuum observation centred on a frequency of 343.50 GHz ($\lambda \approx 870 \mu\text{m}$) reaching a sensitivity of $1\sigma = 0.2 \text{ mJy}$ only requires approximately 1 minute of integration time on source (excluding overheads). Over the past decade submillimetre interferometry has successfully been used to conduct follow up observations for a number of single-dish submillimetre surveys (e.g., Hodge et al., 2013; Brisbin et al., 2017; Cowie et al., 2017; Stach et al., 2019; Simpson et al., 2020), with more than 1000 SMGs detected in these follow up observations. Submillimetre interferometers also offer the opportunity for spectroscopic follow up of single-dish selected submillimetre sources, often targeting bright CO lines to spectroscopically measure precise redshifts (see Figure 1.12) and to estimate molecular gas masses (e.g., Frayer et al., 1998, 1999; Coppin et al., 2007; Tacconi et al., 2010; Ivison et al., 2011; Thomson et al., 2012; Bothwell et al., 2013; Riechers et al., 2013; Walter et al., 2016; Decarli et al., 2019; Riechers et al., 2019; Riechers et al., 2020). The sub-arcsecond resolution of these facilities allows UV/optical counterparts to SMGs to be easily pin-pointed (e.g., Brisbin et al., 2017; Cowie et al., 2017; Miettinen et al., 2017; Dudzevičiūtė et al., 2019; Simpson et al., 2020) and simple confirmation of whether the emission from a single-dish selected submillimetre source comes from an individual submillimetre galaxy or is a blend of multiple SMGs (e.g., Hodge et al., 2013; Stach et al., 2018; Simpson et al., 2020).

It is simply not possible to follow up all single-dish selected submillimetre sources with submillimetre interferometers, as these facilities are very over-subscribed and whilst continuum follow up of an individual submillimetre galaxy only requires approximately 1 minute of integration time on source, given the narrow field of view of these interferometers (i.e. the field of view of ALMA at a frequency of 300 GHz is $19''$) extending this to the 1000s of sources detected in single-dish submillimetre surveys (e.g., Geach et al., 2017; Simpson et al., 2019) is just not practical. Therefore, identifying counterparts via other means (i.e., the methods described in subsection 1.3.1 and 1.3.2) is necessary to fully exploit the data from single-dish submillimetre surveys.

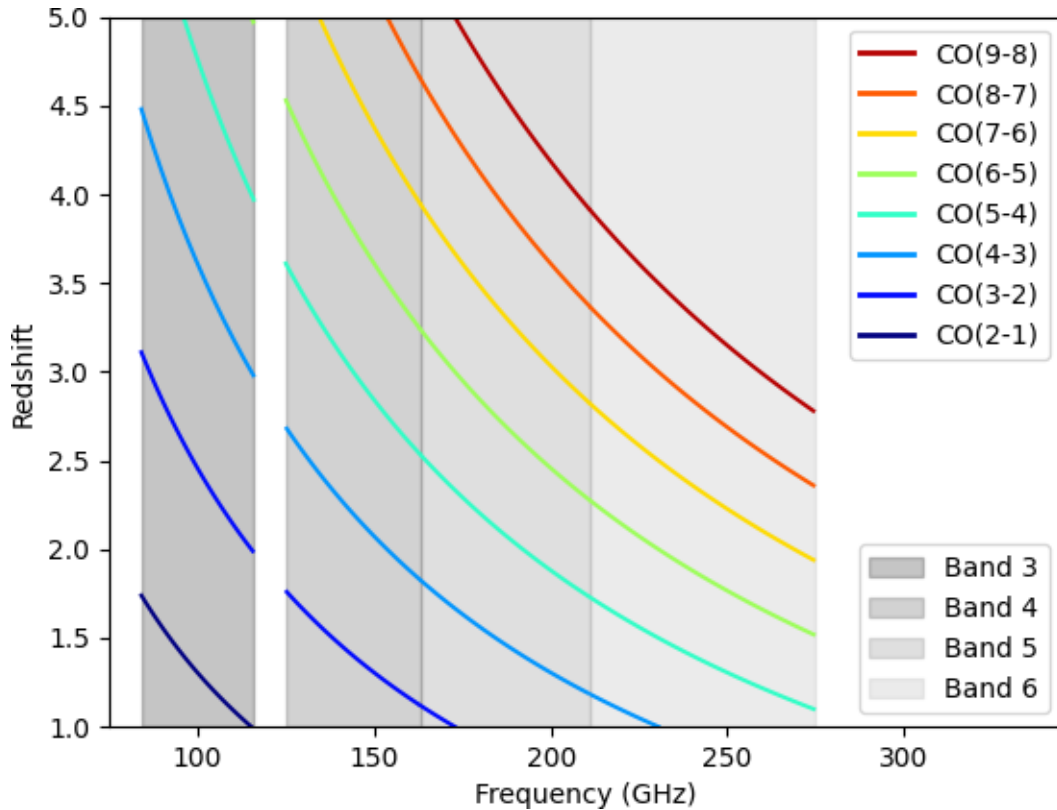


FIGURE 1.12: Frequency range of ALMA receiver bands 3, 4, 5 and 6 (grey shading), overlaid with the observed frequency of ^{12}CO lines ($J_{\text{up}} = 2-9$) across a redshift range $z = 1-5$, illustrating that submillimetre interferometers are an effective means to measure precise redshifts for SMGs.

1.4 Tracing Molecular Gas Mass Density

Submillimetre surveys are not limited to telling us about the dust properties of galaxies, we can also use the data from these surveys to explore the molecular gas content in galaxies. This is possible because the dust-to-gas mass ratio is relatively constant for galaxies with high stellar masses $M_{\text{stellar}} = (2 - 40) \times 10^{10} M_{\odot}$ (Tremonti et al., 2004, e.g.). When we observe emission from a $z \lesssim 3$ star-forming galaxy at a wavelength of $850 \mu\text{m}$ we are probing the Rayleigh-Jean's tail (the rest-frame cold dust continuum emission) of the galaxy's intrinsic SED. Since the Rayleigh-Jeans tail is nearly always optically thin and in light of the tight correlation between dust and gas mass, this means that measurements of dust emission can be used as a direct probe of molecular gas mass (e.g., Eales et al., 2012; Magdis et al., 2012; Scoville et al., 2007). An important caveat to this approach is that the mass-metallicity relation (MZR) evolves with redshift, so that for a fixed stellar mass the metallicity decreases towards higher redshifts. Therefore, whilst a $10^{10} M_{\odot}$ galaxy in the local Universe is likely to have near-solar metallicity (e.g., Tremonti et al., 2004), at the redshifts probed by SMGs ($z \approx 2$) the metallicity of a $10^{10} M_{\odot}$

galaxy is likely to be less (e.g., Sanders et al., 2021; Zahid et al., 2013). This means that methods assuming a constant dust-to-gas ratio may under-estimate the gas mass for galaxies that lie at higher redshifts.

Molecular gas mass density $\rho_{M_{\text{H}_2}}(z)$, star formation rate density $\rho_{\dot{M}_*}(z)$ and the stellar mass density $\rho_{M_*}(z)$ are three intimately linked observational tracers that broadly characterise the cosmic evolution of galaxies. Our current understanding of galaxy evolution is largely driven by comprehensive measurements of the latter two (see Madau and Dickinson, 2014, for a review), with a clear empirical picture emerging of an evolution of star formation, which rises rapidly to a peak around $z \approx 2$ and then decays to the present day (see Figure 1.13). Completing the triptych is important since the evolution of the molecular gas content of galaxies encodes several important pieces of astrophysics: gas consumption in star formation; gas recycling via feedback; and fresh gas accretion. Ultimately, it is the evolution of molecular gas that drives galaxy evolution as it is the fuel from which stars are assembled. Measurements of molecular gas in galaxies are therefore needed to complete the picture, and to resolve a key outstanding question: *Was the peak of star formation history driven by a larger supply of molecular gas or because galaxies formed stars more efficiently (e.g., driven by galaxy mergers/instabilities etc.), or both?*

The bulk of the cold gas reservoir in the Universe is comprised of hydrogen gas in the form of atomic hydrogen (H_I) and molecular hydrogen (H_2). In the current model of galaxy formation gas is delivered into galaxies via hot- or cold-mode accretion (e.g., Birnboim and Dekel, 2003). The cooling gas must form H_2 for star formation to occur. The two main routes to H_2 formation in galaxies are via the gas phase reaction $\text{H} + \text{e}^- \rightarrow \text{H}^- + \gamma$, $\text{H}^- + \text{H} \rightarrow \text{H}_2 + \text{e}^-$, and via a dust phase, where H_2 forms on the surface of dust grains via efficient three-body reactions (Gould and Salpeter, 1963).

H_2 radiates poorly in typical interstellar medium (ISM) conditions due to the lack of a permanent dipole moment and a minimum rotational excitation temperature that is significantly higher (≈ 500 K) than typical temperatures of the cold star-forming ISM (Wakelam et al., 2017). However, H_2 can be indirectly traced through its interactions with CO, which traces the same cold, dense ISM and has a low dipole moment enabling its excitation in regions of low density ($n_{\text{crit}} \sim 10^2 \text{ cm}^{-3}$). Consequently, ^{12}CO , the second most abundant molecule in the ISM, is commonly used as a tracer of the available reservoir of molecular gas in galaxies (e.g., Solomon and Vanden Bout, 2005; Carilli and Walter, 2013). The ground state transition $\text{CO}(J = 1 \rightarrow 0)$ is a reliable tracer of total molecular gas, with the conversion factor from CO luminosity to H_2

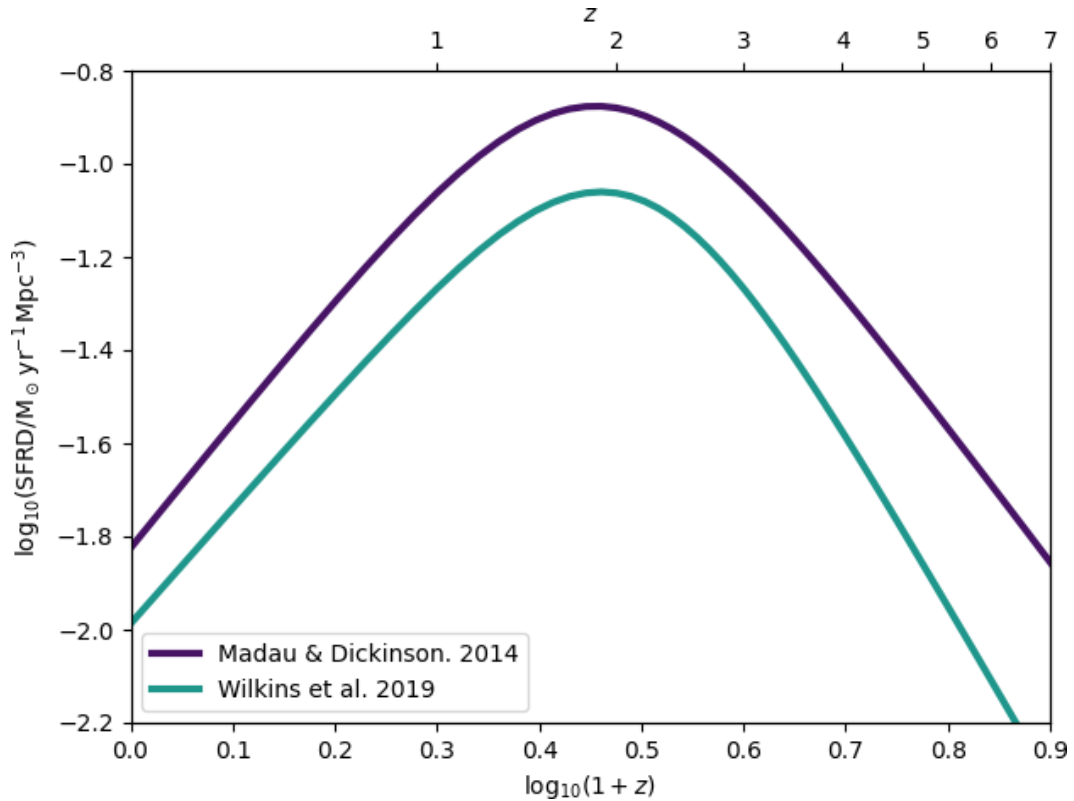


FIGURE 1.13: We show the best fit star formation rate density of Madau and Dickinson (2014) measured from ultra-violet and infrared luminosities (purple line) and the best fit star formation rate density of Wilkins et al. (2019), a recalibration of the Madau and Dickinson (2014) cosmic star formation rate density (teal line), showing the peak of the star formation history at $z \approx 2$.

gas mass ($\alpha_{\text{CO}} = M_{\text{H}_2}/L'_{\text{CO}}$) calibrated locally (see Bolatto et al., 2013, for a review). Observing the ground-state transition line avoids additional uncertainties inherent in observations of higher- J CO transitions, which require a correction for gas excitation to derive the equivalent CO ($J = 1 \rightarrow 0$) luminosity.

Until recently measurements of the cosmological molecular gas mass density were hampered by a paucity of observational data. Over the past few years direct measurements of the cold molecular gas reservoirs of individual galaxies have increased rapidly, with surveys primarily targeting star-forming and lensed galaxies (e.g., Frayer et al., 1998, 1999; Coppin et al., 2007; Tacconi et al., 2010; Ivison et al., 2011; Thomson et al., 2012; Bothwell et al., 2013; Riechers et al., 2013; Stach et al., 2017; Oteo et al., 2018; Gómez-Guijarro et al., 2019; Lenkić et al., 2019). However, as these surveys rely on observationally-expensive detections of faint spectral lines, measurements of molecular gas mass are still dwarfed in number in comparison to samples of galaxies with measurements of star formation rate (SFR) and/or stellar mass. Moreover, to properly assess the cosmological evolution of the cold gas content of galaxies a blank field survey approach is required to measure the gas mass function, rather than targeted (and therefore

biased) observations of high- z galaxies as has generally been the case for cold gas observations outside the local volume.

Recently surveys using a blank field molecular line scan strategy have emerged as an alternative to targeted observations. These surveys evade many of the biases towards massive star-forming galaxies inherent in targeted approaches. The inaugural blank field CO survey was conducted with the Plateau de Bure Interferometer observing the *Hubble* Deep Field North (Walter et al., 2014; Decarli et al., 2014). This was followed more recently by the ALMA Spectroscopic Survey in the *Hubble* Ultra Deep Field (ASPECS; Walter et al., 2016; Decarli et al., 2016b,a; Aravena et al., 2016b,a; Bouwens et al., 2016; Carilli et al., 2016), the ASPECS Large Program (ASPECS LP; Decarli et al., 2019; González-López et al., 2019; Boogaard et al., 2019; Popping et al., 2019; Decarli et al., 2020) and the CO Luminosity Density at High Redshift survey (COLDZ; Pavesi et al., 2018; Riechers et al., 2019). These blank-field surveys of CO line emission have provided valuable new constraints on the evolution of ρ_{H_2} over a redshift range $0 \lesssim z \lesssim 7$. However, due to low number statistics and the small survey areas (which are prone to strong clustering-enhanced sample variance) used to derive the CO luminosity functions, these measurements are hampered by large statistical uncertainties (see Figure 1.14).

To combat the shortfall in direct measurements of molecular gas Scoville (2013); Scoville et al. (2014, 2016, 2017) employ a complementary approach that uses submillimetre observations of the long wavelength dust continuum to measure the molecular gas mass of galaxies. Whilst ordinarily a conversion from dust to gas mass would require dust emissivity and dust-to-gas abundance to be constrained, Scoville et al. (2014, 2016, 2017) circumvent this by deriving an empirically calibrated *RJ luminosity-to-gas mass* ratio from measurements of CO ($J = 1 \rightarrow 0$) and submillimetre continuum for a sample of normal star-forming and starburst galaxies at low- z , and submillimetre galaxies (SMGs) at high- z . This approach makes assumptions about dust temperature and the evolution of the gas-to-dust mass ratio, but provides molecular gas mass (M_{mol}) estimates within factor of ≈ 2 accuracy (e.g., Scoville et al., 2016; Kaasinen et al., 2019). Since dust continuum measurements can be made in minutes (in contrast to CO line observations which can take multiple hours, e.g., Bothwell et al., 2013; Tacconi et al., 2013) this method can be used to derive molecular gas measurements for much larger samples of galaxies.

The Scoville et al. (2016) RJ luminosity-to-gas mass calibration has been used to estimate the molecular gas mass for ~ 700 ALMA-detected galaxies from the COSMOS field, with Scoville et al. (2017) deriving molecular gas masses for individual galaxies at redshifts $0.3 < z < 4.5$ and

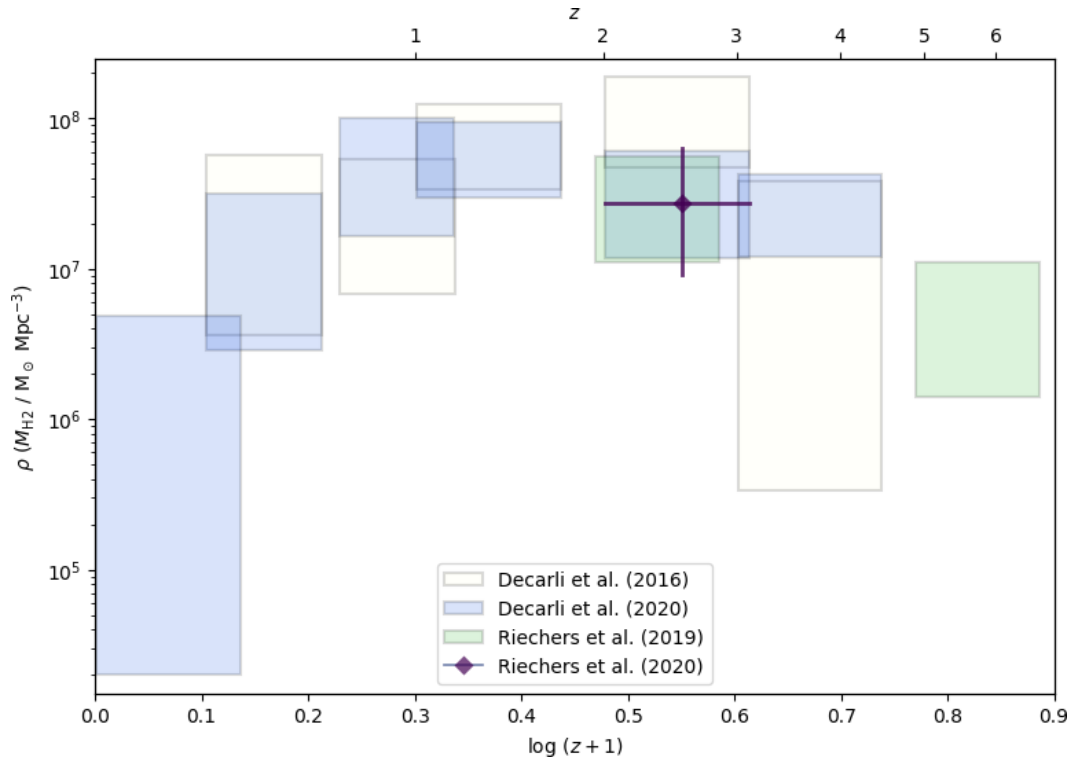


FIGURE 1.14: Estimates of the molecular gas mass density from direct measurements of CO line emission. We show the results from ASPECS (off white rectangles; Decarli et al., 2016a), ASPECS LP (blue rectangles; Decarli et al., 2020), COLDz (green rectangles; Riechers et al., 2019) and VLASPECS (purple diamond; Riechers et al., 2020), because of low number statistics these results are subject to large statistical uncertainties.

Liu et al. (2019a) extending this approach to redshifts of $z \approx 6$. This method has also been used in combination with stacking methodologies to estimate average molecular gas masses for large samples of galaxies. Millard et al. (2020) use the Scoville et al. (2016) calibration and apply this to a sample of 63,658 galaxies to measure the gas mass fraction out to $z \approx 5$. Magnelli et al. (2020) use a method similar to Scoville et al. (2016, and which is equivalent at solar metallicity) and apply this to a sample of 555 galaxies to estimate the molecular gas mass density to $z \approx 3$.

1.5 Overview

Observations at submillimetre wavelengths not only provide us with the opportunity to directly observe a previously hidden population of galaxies, but also the tools to investigate fundamental tracers of galaxy evolution. In this thesis we capitalise on this bi-modality to explore key outstanding questions in galaxy evolution.

We currently have a clear picture of the evolution of the star-formation rate density, which rises to a peak at $z \approx 2$ before declining to the present day. However, we do not yet understand what drives the evolution of the star-formation rate density - is a larger supply of molecular gas responsible for the peak epoch of star-formation at $z \approx 2$, or is this driven by individual galaxies forming stars more efficiently, or both?

In Chapter 2 we build on the work of Scoville et al. (2016), estimating the evolution of the cosmological molecular gas mass density as a function of redshift from the average submillimetre continuum emission of a sample of K -band selected galaxies. We find a cosmic evolution of molecular gas mass that mirrors the star-formation rate density, rising to a peak at $z \approx 2$ and the declining to the present day. Our results indicate that primary driver for the epoch of peak star formation is a larger supply of molecular gas in galaxies, rather than a significant evolution of the star-formation rate efficiency within individual galaxies.

Whilst we have a good understanding of the general $z \approx 2$ submillimetre population, our understanding of the bright, high-redshift tail of the submillimetre population is hampered by the small number of detections of bright $S_{850\mu\text{m}} > 15$ mJy galaxies. We expect (based on studies at infrared and millimetre wavelengths) that the over-abundance of bright single-dish submillimetre sources observed at $S_{850\mu\text{m}} > 15$ mJy is motivated by lensed galaxies, galaxies blended in the single-dish beam and intrinsically bright galaxies. However, the relative contribution of each of these sub-populations to the over-abundance of sources observed is unknown. Models often struggle to replicate both the observed abundance and the redshift distribution of bright submillimetre sources, hampered by a lack of robust observational data. To inform these models we need not only robust single-dish submillimetre numbers counts and accurate constraints on the redshift distribution at $S_{850\mu\text{m}} > 15$ mJy, but also measurements of the fraction of lensed, blended and intrinsically bright sources, at the bright-end tail of the submillimetre population.

In Chapter 3 we present the first results of the SCUBA-2 Large eXtragalactic Survey (S2LXS), a JCMT Large Program (PI: J. E. Geach and Y. Tamura) that covers an area of 10 deg^2 split over two fields - the X-Ray Multi-Mirror Large Scale Structure Survey field (XMM-LSS; Pierre et al., 2004) and the Extended Cosmic Evolution Survey field (E-COSMOS; Scoville et al., 2007). We robustly measure the $850\mu\text{m}$ number counts for the S2LXS XMM-LSS field, finding the characteristic over-abundance of sources at $S_{850\mu\text{m}} \gtrsim 15$ mJy. The S2LXS XMM-LSS number counts are best reproduced by model predictions that include either strong lensing or source

blending, indicating that both may make an important contribution to the over-abundance of bright sources observed in single-dish submillimetre surveys

In Chapter 4 we present the first results from our ALMA telescope proposal (PI: T. K. Garratt, Project ID: 2022.1.01030.S) targeting the 17 brightest sources in the S2LXS XMM-LSS catalogue. We find a multiplicity fraction of 54% at $S_{850\text{m}} > 12\text{mJy}$. Our initial results indicate that source blending does not significantly contribute to the abundance of sources observed at the bright-end tail of the $850\mu\text{m}$ single-dish number counts. This is unexpected given that the S2LXS XMM-LSS number counts are broadly reproduced by models that incorporate source blending, and further work is required to confirm this.

Chapter 2

Cosmic evolution of the H₂ mass density and the epoch of molecular gas

2.1 Introduction

Molecular gas is the fuel from which stars are made, thus the evolution of molecular gas plays a central role in the evolution of galaxies. The star formation history reaches a peak at $z \approx 2$, but it is uncertain whether this peak is driven by a larger supply of molecular gas onto galaxies or by improved star formation efficiency, or through a combination of both. Therefore, measuring the molecular gas content in galaxies across cosmic time is fundamental to inform our understanding of galaxy formation and evolution.

The most direct (and viable) route to estimate the molecular gas content of galaxies is through observations of CO line emission, with blank-field surveys of CO line emission providing valuable new constraints on the evolution of the molecular gas mass density to $z \approx 7$ (e.g., Decarli et al., 2016a; Riechers et al., 2019; Decarli et al., 2020; Riechers et al., 2020). However, direct CO line observations can take multiple hours (e.g., Bothwell et al., 2013; Tacconi et al., 2013) and so measurements of the molecular gas mass density via CO line emission are hampered by small number statistics. The Rayleigh-Jeans (RJ) tail is nearly always optically thin, therefore measurements of dust emission can be used as a direct probe of molecular gas mass (e.g., Eales et al., 2012; Magdis et al., 2012). Since dust continuum measurements can be made in minutes this approach can be used to derive molecular gas estimates for much larger samples of galaxies. Scoville et al. (2014, 2016, 2017) derive an empirically calibrated *RJ luminosity-to-gas*

mass ratio from measurements of CO ($J = 1 \rightarrow 0$) and submillimetre continuum for a sample of normal star-forming and starburst galaxies at low- z , and submillimetre galaxies (SMGs) at high- z . This approach provides molecular gas mass (M_{mol}) estimates within factor of ≈ 2 accuracy (e.g., Scoville et al., 2016; Kaasinen et al., 2019).

In this thesis we contribute to the picture of cosmic galaxy evolution by building on the approach of Scoville (2013); Scoville et al. (2014, 2016, 2017) to estimate the evolution of the cosmological mass density of molecular hydrogen to $z \approx 2.5$ via the average submillimetre continuum emission of a sample of 150,000 galaxies selected from a deep near-infrared survey in the well studied UKIDSS-UDS field. The Ultra-Deep Survey (UDS) is the deepest component of the UK InfraRed Telescope (UKIRT) Infrared Deep Sky Survey (UKIDSS; Lawrence et al., 2007). We limit our estimate of the molecular gas mass density to $z \approx 2.5$ as the Scoville et al. (2016) calibration has only been shown to be robust out to this redshift. Adopting a statistical approach allows us to take advantage of a near-infrared selected sample which is an order of magnitude larger than in surveys that measure dust emission (e.g., Scoville et al., 2017; Liu et al., 2019a; Magnelli et al., 2020) or CO spectral line emission (e.g., Walter et al., 2016; Riechers et al., 2019; Decarli et al., 2019; Kaasinen et al., 2019) for individual sources. Our method differs from previous stacking approaches (e.g., Millard et al., 2020; Magnelli et al., 2020) as we do not use a combination of spectroscopic and photometric redshifts for our binning. Instead, in the absence of a sample complete with spectroscopic redshifts, we utilise the full photometric redshift probability distribution functions for all our sources. Our method is complementary to previous works in this field (e.g., Decarli et al., 2020; Liu et al., 2019a; Magnelli et al., 2020; Riechers et al., 2019) and allows us to reduce the statistical uncertainties on the cosmological molecular gas mass density out to $z \approx 2.5$.

This chapter is organised as follows: in section 2.2, we define the maps and catalogues used; in section 2.3, we present a 3-dimensional stacking method which we employ to measure the average (stacked) observed $850 \mu\text{m}$ flux densities for near-infrared selected galaxies as a function of redshift; in section 2.4, we show that the approach of Scoville et al. (2016) can be applied to our stacked $850 \mu\text{m}$ flux densities to derive the cosmological molecular gas density to $z \approx 2.5$. We also demonstrate that the cosmic molecular gas density can be broadly modelled by 2 complementary approaches (i) from the halo mass function assuming a constant halo mass range, and employing stellar-halo mass and ISM-stellar mass ratios, and (ii) inverting the star-formation rate density assuming a “constant efficiency” model, and in section 2.5 we interpret the overall

evolution of the cosmic molecular gas mass density in the context of our results and in comparison to previous works. We present our conclusions in section 2.6. We assume a Planck 2015 cosmology, where $\Omega_m = 0.31$, $\Omega_\Lambda = 0.69$, $H_0 = 68 \text{ km s}^{-1} \text{ Mpc}^{-1}$ (Planck Collaboration et al., 2016), and a Chabrier (2003) Initial Mass Function. The AB magnitude system is used throughout.

2.2 Data

2.2.1 SCUBA-2 Cosmology Legacy Survey

The UKIDSS-UDS field was mapped at $850 \mu\text{m}$ as part of the Submillimetre Common-User Bolometer Array 2 (SCUBA-2) Cosmology Legacy Survey (Geach et al., 2017). The full details of the data collection, reduction and map properties are given in Geach et al. (2017). Briefly, the beam-convolved map spans approximately 1 deg^2 covering the bulk of the multi-wavelength coverage of this field, with a uniform (instrumental) noise of $\sigma_{850} = 0.9 \text{ mJy beam}^{-1}$. Geach et al. (2017) estimate the SCUBA-2 confusion limit to be $\sigma_{\text{conf}} = 0.8 \text{ mJy beam}^{-1}$. The beam full width half maximum (FWHM) is approximately $15''$, with a full analytic description of the point spread function (PSF) given by Geach et al. (2017).

2.2.2 UKIDSS-UDS ultraviolet–optical–mid-infrared imaging and catalogue

The UDS Data Release 11 (DR11) 12-band matched catalogue is K -band selected with the 95% completeness limit estimated to be $K_{\text{AB}} = 25 \text{ mag}$. The full details of this catalogue will be comprehensively provided in Almaini et al., (in prep.) and Hartley et al., (in prep.), and only a summary is given here. The catalogue provides photometry in 12 bands ($U, B, V, R, i', z', Y, J, H, K, 3.6 \mu\text{m}$ and $4.5 \mu\text{m}$), where available.

The $J, H,$ and K photometry is taken from the DR11 release of UKIDSS-UDS. The UKIDSS project, described in Lawrence et al. (2007) utilises the UKIRT Wide Field CAMera (WFCAM; Casali et al., 2007). The photometric system and calibration are outlined in Hewett et al. (2006) and Hodgkin et al. (2009), respectively, and the pipeline processing and science archive are described in Irwin et al., (in prep.) and Hambly et al. (2008). UKIDSS-UDS covers an area of 0.8 deg^2 , reaching median depths of $J= 25.6, H= 25.1,$ and $K= 25.3$ (5σ , AB, estimated from $2''$ apertures in source free areas; Almaini et al. in prep.).

The B , V , R , i' , and z' optical imaging is from the Subaru/*XMM-Newton* Deep Survey, which utilises Suprime-Cam on the Subaru Telescope (Furusawa et al., 2008). U -band data are from the Canada-France-Hawaii Telescope Megacam instrument (Almaini et al. in prep.) and Y -band imaging is obtained from the VISTA Deep Extragalactic Observations survey (VISTA-VIDEO: Jarvis et al., 2013). The InfraRed Array Camera (IRAC) imaging at $3.6\ \mu\text{m}$ and $4.5\ \mu\text{m}$ is from the Spitzer UKIDSS Ultra Deep Survey (SpUDS: PI Dunlop), combined with deeper data from the Spitzer Extended Deep Survey (SEDS: Ashby et al., 2013). To expand the coverage to outer regions of the field, shallower data are also used from the *Spitzer* Wide-area InfraRed Extragalactic survey (SWIRE: Lonsdale et al., 2003).

UDS DR11 provides image masks, with masked regions corresponding to image boundaries, artefacts, and bright stars. We employ the UDS binary mask for “good” regions which has an unmasked area of $0.64\ \text{deg}^2$. This binary mask combines the masked regions of the photometry images detailed above (not including the deeper SEDS or SpUDS IRAC images).

We also utilise the subsets feature of the UKIDSS-UDS catalogue and for our galaxy sample chose the catalogue-defined “good galaxy” subset, which comprises 217,429 sources. These sources have full 12-band photometry and lie within the corresponding “good” mask regions, are not cross-talk sources (for which JHK photometry is likely compromised), and are not classified as stars.

UDS DR11 also includes photometric redshifts derived using the code EAZY (Easy and Accurate Z_{phot} from Yale; Brammer et al., 2008). To estimate the photometric redshift for each source the 12-band broadband photometry was fit with a spectral energy distribution template producing a redshift probability distribution (Hartley et al. in prep.). We utilise both the maximum-likelihood photometric redshifts and redshift probability distributions provided with UDS DR11. EAZY performs well compared to other commonly used photometric redshift codes (e.g., ZPHOT, HYPERZ, RAINBOW; Dahlen et al., 2013), with the resulting normalised mean absolute deviation between EAZY derived photometric redshifts and spectroscopic redshifts found to be only $\sigma_{\text{nmad}} \approx 0.02$ (Hartley et al. in prep.).

2.3 Methods

We employ a 3-dimensional stacking approach based on the simultaneous stacking algorithm SIMSTACK (presented in detail in Viero et al., 2013). This method allows for the simultaneous

fitting of the average observed flux density for multiple populations that contribute to the flux density in the observed map (such as a population of galaxies split into bins of redshift). Importantly, this method takes into account the (usually) large beam in single-dish submillimetre maps with simulations demonstrating that this method returns an unbiased estimate of the average observed flux density for beam sizes ranging from $\text{FWHM} = 15\text{--}35''$ (Viero et al., 2013). This approach also mitigates against boosting of stacking signals from clustered galaxies (e.g., Chary and Pope, 2010; Alberts et al., 2014).

Our goal is to find the average observed submillimetre flux densities at given redshift intervals for a population of near-infrared selected galaxies that best fit the observed flux density in the SCUBA-2 map, taking into account the convolution of point sources with the large beam. In this work, rather than binning galaxies by discrete photometric redshift values, we split our sample across redshift intervals according to the redshift probability distribution of each source (see Figure 2.1 for a simplistic graphical representation of this binning).

First, we define our sample, performing a selection in observed K -band total magnitude, $K_{\text{AB}} \leq 25$ mag, with the faint-end corresponding to the 95% completeness limit of the UKIDSS-UDS catalogue, giving us a sample of 153,399 galaxies. At this limiting magnitude the 95% stellar mass completeness is $\approx 10^{9.5} M_{\odot}$ at $z = 2.5$ (Wilkinson et al. in prep.). The redshift probability distribution, $\mathcal{P}(z)$, for each source is discretized in bins of Δz (Hartley et al. in prep.). We make a completeness correction to the redshift probability distribution of each source, such that $\mathcal{P}(z)$ of a source of magnitude K integrates to $C(K)^{-1}$, where $C(K)$ is the catalogue completeness at K (Hartley et al. in prep.). We assume there is no systematic redshift bias in $C(K)$ for this correction.

With the sample defined we consider a sky model in which each galaxy contributes a flux density that can be described as

$$S_{\nu} = \int_0^{\infty} \mathcal{S}_{\nu}(z) \mathcal{P}(z) dz. \quad (2.1)$$

where $\mathcal{P}(z)$ is the normalised redshift probability distribution function and $\mathcal{S}_{\nu}(z)$ is the flux density “weighting” at redshift z . In practice we have discrete redshift probability distributions defined over R bins such that, for a population of N galaxies, the flux density in the i th pixel of

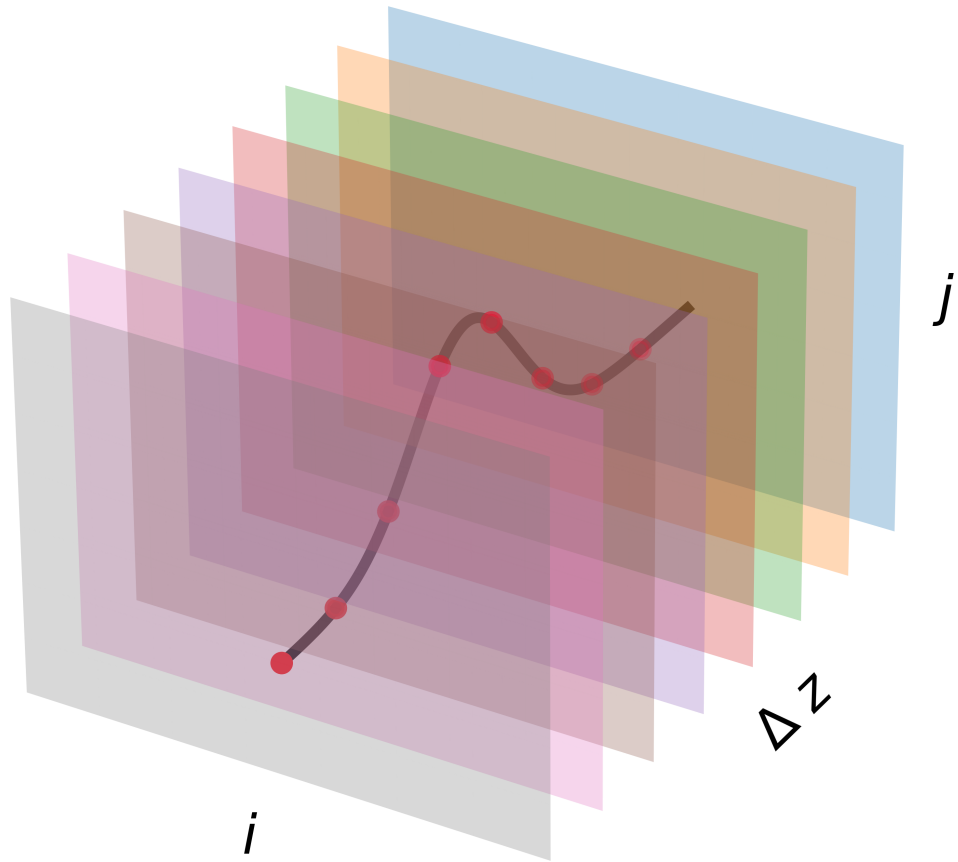


FIGURE 2.1: This is a simplistic graphic showing how we bin an individual galaxy according to its position in the observed map and its photometric redshift probability distribution. The position of the galaxy in our model (the ij th pixel) corresponds to the position of the galaxy in the observed map. The value of the ij th pixel in each redshift interval equals the value of the completeness corrected normalised redshift probability distribution for the galaxy at that redshift.

a map (M_{ij}) can be written

$$M_{ij} = \sum_p^{N_{ij}} \sum_q^R S_v(z_q)_{p,ij} \mathcal{P}(z_q)_{p,ij} \Delta z \quad (2.2)$$

Because of the PSF, the flux contribution of each galaxy is distributed over many pixels according to the convolution, where \mathcal{M} is the map once convolved with the SCUBA-2 PSF.

$$\mathcal{M} = M \otimes \text{PSF}. \quad (2.3)$$

In effect equation 2.1 uses $\mathcal{P}(z)$ to split each of the N galaxies in our K -selected sample into R redshift bins and assumes that the galaxies in each redshift bin can be represented by an average observed flux density, $\langle S_v(z) \rangle$. This is effectively the “stacked” flux density.

With the model sky defined we consider an optimization problem where the set of average

observed flux densities, $\langle S_\nu(z) \rangle$, per redshift interval in equation 2.1 are unknown coefficients. A key decision in defining our sky model is in the binning of $\mathcal{P}(z)$. The UKIDSS-UDS $\mathcal{P}(z)$ are binned in non-linear steps of $1 + z_{(n+1)} = 1.001(1 + z_n)$. This would result in hundreds of free parameters across the redshift range of interest, which is computationally impractical as well as unnecessary given the photometric redshift uncertainties. Instead we bin each $\mathcal{P}(z)$ to $\Delta z = 0.5$, giving 20 equally-sized bins across the redshift range $0 < z \lesssim 10$.

We aim to find the optimal set of average flux densities that minimises the square of the residual flux between the model in equation 2.3 and the observed beam-convolved map, weighted by the noise. We use the Markov chain Monte Carlo (MCMC) sampler emcee (Foreman-Mackey et al., 2013) to estimate the best fit flux densities and their uncertainties. We minimise a negative log likelihood $\ln(\mathcal{L}) = -0.5\chi^2$, with

$$\chi^2 = \sum_{ij} \left(\frac{\mathcal{O}_{ij} - \mathcal{M}_{ij}}{\sigma_{\text{rms},ij}} \right)^2 \quad (2.4)$$

where \mathcal{O} is the observed map and σ_{rms} is the instrumental noise map. We initialise 1000 “walkers” with an uninformative prior, such that each walker is set with a vector of flux densities (representing $S_\nu(z)$) with each flux density drawn from a Gaussian distribution of mean 0.5 mJy and width 0.05 mJy. The sampler runs for 1000 iterations with the first 500 iterations discarded as burn-in. The best fitting flux densities and the 1σ bounds are estimated from the 16th, 50th and 84th percentiles of accepted samples for 500 iterations. In Figures 2.2, 2.3 and 2.4 we show the emcee corner plot of the posterior distributions for all our free parameters.

To estimate the additional uncertainty on the stacked flux densities due to sampling variance we employ the “delete one” jackknife technique (Tukey, 1958), splitting the map into $A = 21$ approximately equal area sectors and running the MCMC fit for each jackknife. We find that the sampler chains converge quickly (within 200 steps), and tests indicate that the best fit parameters are insensitive to the initialisation parameters. The covariance matrix is given by

$$\mathcal{C}_{ij} = \frac{A-1}{A} \sum_{k=1}^A \left(S_i^k - \bar{S}_i \right) \left(S_j^k - \bar{S}_j \right) \quad (2.5)$$

where S_i^k is the average flux density in the i th redshift bin, eliminating the k th sample and \bar{S}_i is the average over all samples. The 1σ uncertainties on the stacked fluxes are estimated by the square root of the diagonal elements of \mathcal{C} .

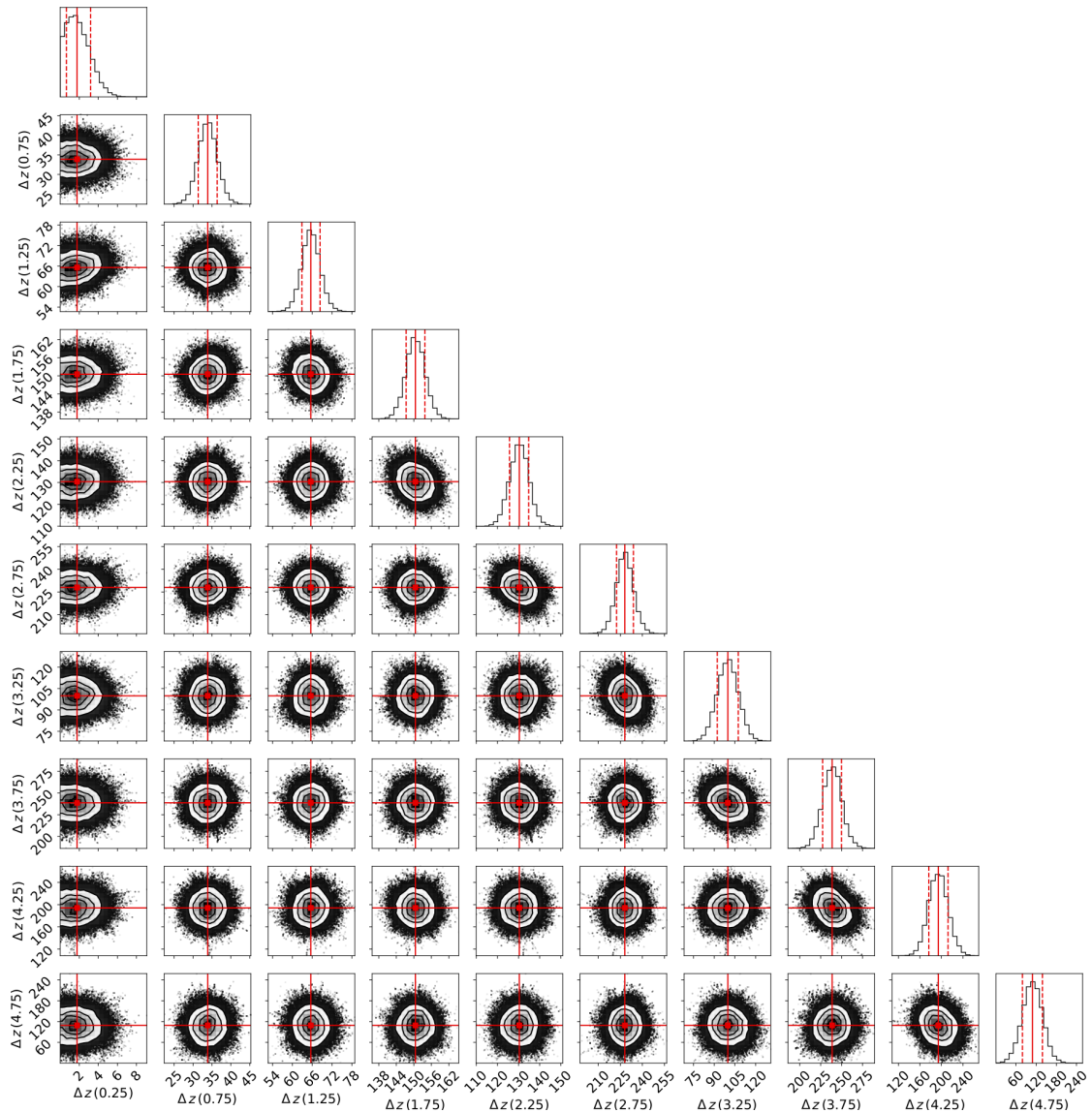


FIGURE 2.2: Standard emcee corner plot showing the one- and two-dimensional posterior distributions for our parameters (the average observed flux density in μJy of galaxies in each redshift bin) for the redshift intervals $\Delta z(0.25)$ – $\Delta z(4.75)$. The density of the points and the contours correlate with the posterior probability distributions from a 1000-step run (with 500 steps for burn-in discarded) based on our sky model and SCUBA-2 maps, and employing the “delete one” jackknife technique with the map segment area corresponding to $A = 1$ deleted to take into account sample variance (Tukey, 1958). The vertical red lines show the average $850\ \mu\text{m}$ flux density of galaxies for each redshift interval, with the dashed red lines showing the associated 1σ uncertainties (these values are not corrected for the influence of the CMB, see Table 2.1 for CMB corrected-estimates). As evidenced by this plot there are only very weak correlations between our parameters for the redshift intervals $\Delta z(0.25)$ – $\Delta z(4.75)$.

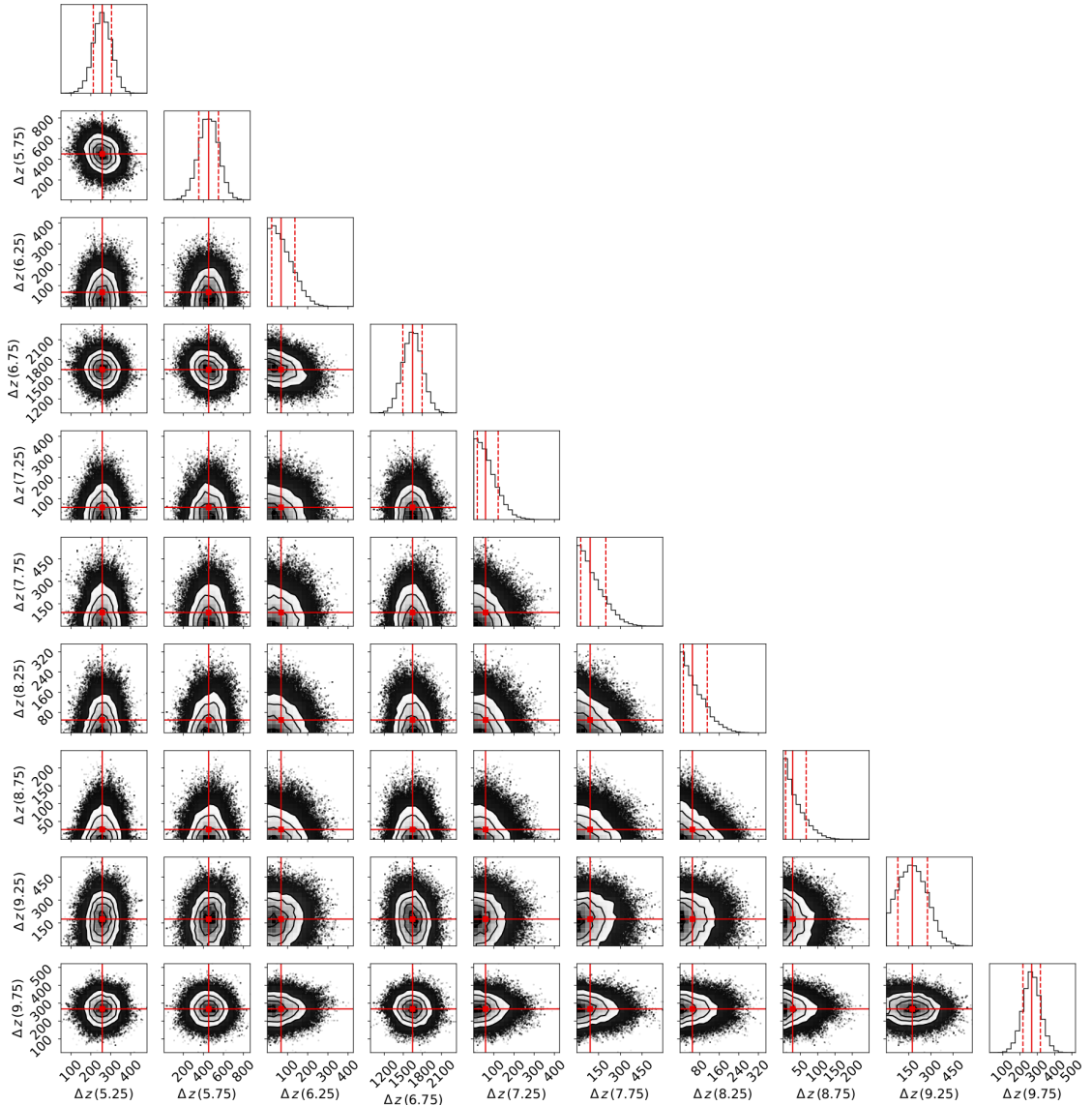


FIGURE 2.3: Standard emcee corner plot showing the one- and two-dimensional posterior distributions for our parameters (the average observed flux density in μJy of galaxies in each redshift bin) in the redshift intervals $\Delta z(5.25)$ – $\Delta z(9.75)$. Detailed description as in Figure 2.2. As evidenced by this plot there are only very weak correlations between our parameters for the redshift intervals $\Delta z(5.25)$ – $\Delta z(9.75)$.

At high- z the increase in the cosmic microwave background (CMB) temperature affects the measurement of submillimetre dust continuum in two ways (see da Cunha et al., 2013, for a detailed discussion). Firstly, the CMB provides an additional source of dust heating increasing the intrinsic dust temperature as shown in equation 2.6 (da Cunha et al., 2013):

$$T_{\text{dust}}(z) = \left((T_{\text{dust}}^{z=0})^{\beta+4} + (T_{\text{CMB}}^{z=0})^{\beta+4} [(1+z)^{\beta+4} - 1] \right)^{\frac{1}{\beta+4}} \quad (2.6)$$

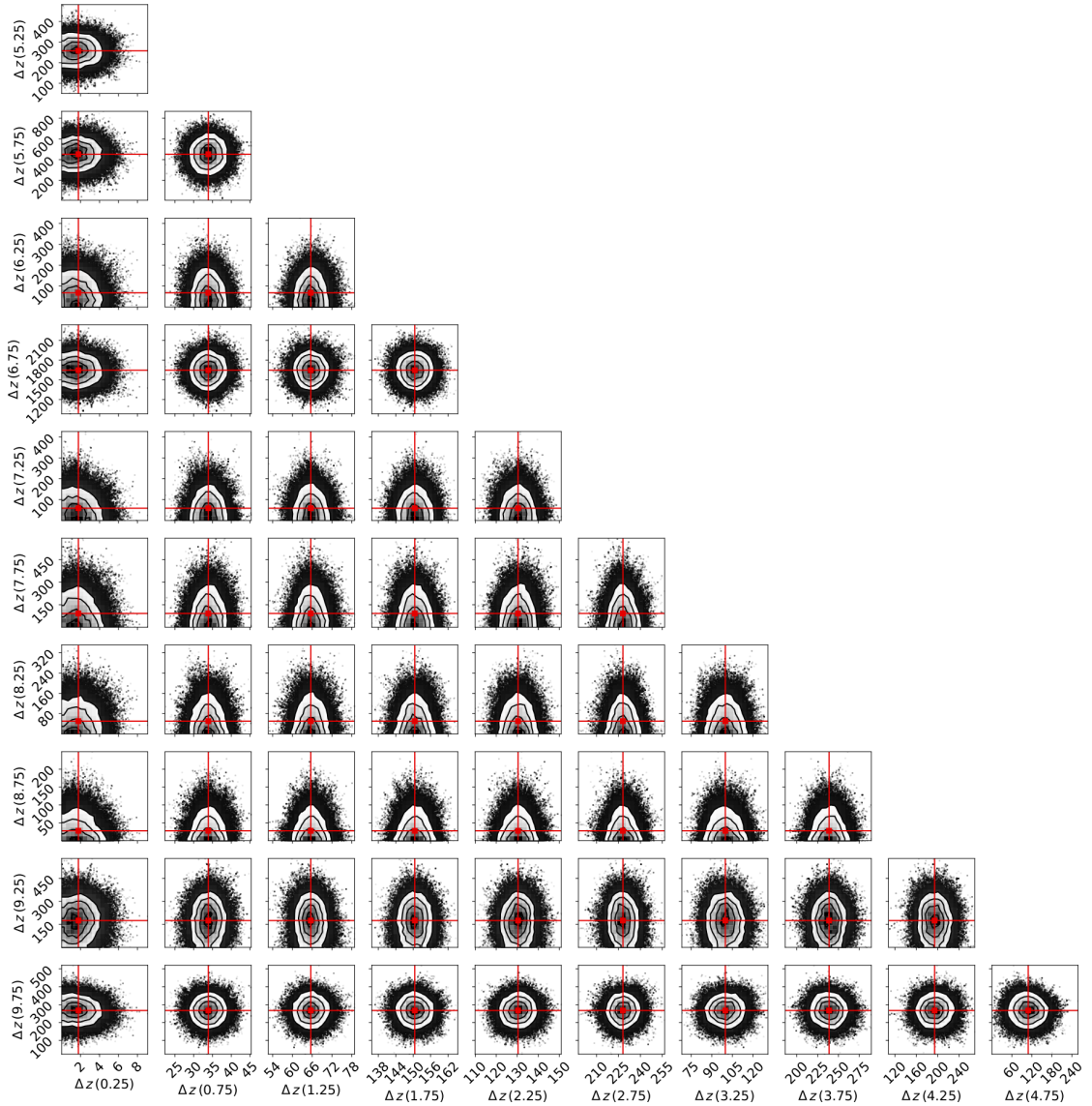


FIGURE 2.4: Standard emcee corner plot showing the two-dimensional posterior distributions for our parameters (the average observed flux density in μJy of galaxies in each redshift bin) for redshift intervals $\Delta z(0.25)$ – $\Delta z(4.75)$ and $\Delta z(5.25)$ – $\Delta z(9.75)$. Detailed description as in Figure 2.2. As evidenced by this plot there are only very weak correlations between our parameters for the redshift intervals $\Delta z(0.25)$ – $\Delta z(4.75)$ and $\Delta z(5.25)$ – $\Delta z(9.75)$.

Secondly, submillimetre observations of dust emission are always measured against the background of the CMB. At low- z $T_{\text{dust}}(z) \gg T_{\text{cmb}}(z)$, so essentially all the intrinsic flux is detected against the CMB. However, at high- z , as $T_{\text{cmb}}(z)$ approaches $T_{\text{dust}}(z)$, the fraction of submillimetre flux detected against the CMB decreases. Equation 2.7 (da Cunha et al., 2013) shows the fraction of the intrinsic dust emission from a galaxy measured at a given frequency, $\nu_{\text{obs}} = \nu_{\text{rest}}/(1+z)$ against the CMB background:

$$\frac{F_{\nu_{\text{obs}}}^{\text{obs against CMB}}}{F_{\nu_{\text{obs}}}^{\text{intrinsic}}} = 1 - \frac{B_{\nu}[T_{\text{CMB}}(z)]}{B_{\nu}[T_{\text{dust}}(z)]} \quad (2.7)$$

Assuming $T_{\text{CMB}}^{z=0} = 2.73 \text{ K}$, $T_{\text{dust}}^{z=0} = 25 \text{ K}$ (in line with the T_{dust} adopted in Scoville et al., 2016) and $\beta = 2$ we derive the fraction of submillimetre flux observed against the CMB for the redshift range $0 < z < 10$ at $\nu_{\text{obs}} = 353 \text{ GHz}$ ($\lambda_{\text{obs}} = 850 \mu\text{m}$), including the extra heating contributed by the CMB. We apply this correction to our average observed $850 \mu\text{m}$ flux densities in all redshift bins to account for the impact of the CMB on our estimates.

2.4 Results

2.4.1 Estimating molecular gas mass: Rayleigh-Jeans luminosity-to-gas mass relation

In Table 2.1 we present the average observed $850 \mu\text{m}$ flux densities for our galaxy sample as a function of redshift. We quote the uncertainties to 1σ and include the additional uncertainty due to sample variance. We note that at $z \gtrsim 6$ the UDS redshifts are untested. However, as our sample is binned according to the $\mathcal{P}(z)$ for each source, every galaxy effectively contributes to the flux in each redshift interval. Hence, we show the average $850 \mu\text{m}$ flux density estimates for our galaxy sample to $z = 10$.

We sum $\mathcal{P}(z)$ (which is completeness corrected) in each redshift bin, giving us the galaxy “weighting” for each redshift interval. The integral of the summed $\mathcal{P}(z)$ across all redshift intervals should be approximately equal to the total number of galaxies in our sample. We calculate this to be 154,839, which is consistent with our galaxy sample of 153,399 sources (taking into account the completeness corrections). With the summed $\mathcal{P}(z)$ and taking the area of our sample as the unmasked region of the SCUBA-2 $850 \mu\text{m}$ map (which corresponds to the UDS binary mask for “good galaxy” regions) we calculate the number density of galaxies as a function of redshift. By combining this with our average flux density (see Table 2.1 column 4 for CMB corrected values) we calculate the summed flux density for our galaxy sample in each redshift interval. In Figure 2.5 we present the number density and summed flux density for galaxies in our sample as a function of redshift. The distribution of the summed flux densities with redshift is broadly comparable to the redshift distribution found for SMGs, which peaks at $z \approx 2$ (e.g., Blain et al., 2002; Chapman et al., 2005; Simpson et al., 2014; Miettinen et al., 2017; Zavala et al., 2018), whilst the number density distribution generally declines with increasing redshift as expected. The difference in the evolution of these distributions demonstrates that our derived flux densities are not biased by the number density of galaxies in each redshift bin.

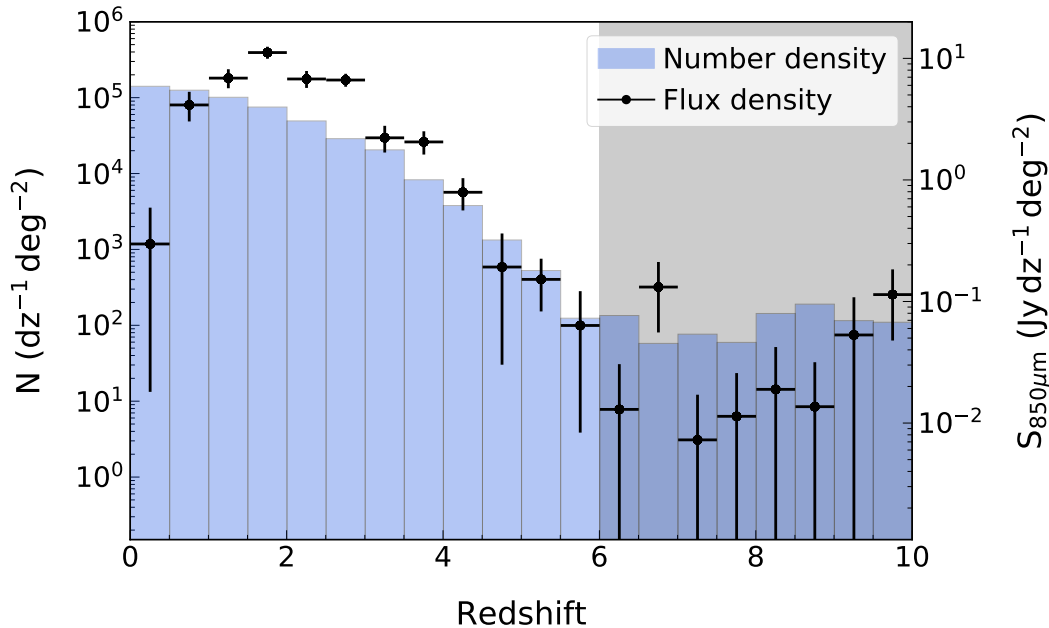


FIGURE 2.5: Number density of galaxies in each redshift bin (blue bars) calculated from the galaxy “weighting” (the sum of the completeness corrected $\mathcal{P}(z)$ in each redshift bin) and the area of the unmasked region of the SCUBA-2 image. The black points show the summed flux density of galaxies as a function of redshift derived by combining the number density and the average flux density of galaxies (see Table 2.1 column 4 for average flux density values) in each redshift bin. This figure shows the contrasting distributions, with the summed flux density mirroring the redshift distribution found for SMGs with a peak at $z \approx 2$, whereas the number density generally shows a steady decline. At $z \approx 7$ there is an unexpected upturn in the number density and the summed flux density of galaxies, this is likely due to a combination of uncertainties in the photometric redshift fitting at high- z (UDS photometric redshifts are untested at $z \gtrsim 6$) and the small number statistics in these bins with the galaxy weighting being $\lesssim 100$ per redshift interval.

We adopt the approach of Scoville et al. (2016, hereafter S16) and, utilising our flux density measurements, estimate the average molecular gas mass for our galaxy sample in each redshift interval. The full details of this approach are given in S16; however, we provide a brief description here.

The long wavelength RJ tail of dust emission is nearly always optically thin ($\tau \ll 1$) and consequently this provides a direct probe of the total dust mass and hence the molecular gas mass. S16 utilise this to obtain an empirically calibrated *RJ luminosity-to-gas mass* ratio

$$\left(\frac{M_{\text{mol}}}{M_{\odot}}\right) = \frac{1}{\alpha_{850}} \left(\frac{L_{850, \text{rest}}}{\text{erg s}^{-1} \text{Hz}^{-1}}\right) \text{ for } \lambda_{\text{rest}} \gtrsim 250 \mu\text{m} \quad (2.8)$$

with $\alpha_{850} = 6.7 \pm 1.7 \times 10^{19} \text{ erg s}^{-1} \text{Hz}^{-1} M_{\odot}^{-1}$. The restriction $\lambda_{\text{rest}} \gtrsim 250 \mu\text{m}$ is required to ensure that at an observed wavelength of $850 \mu\text{m}$ the rest-frame emission stays on the RJ tail. S16 demonstrate that this luminosity-to-mass ratio is relatively constant for high-stellar mass

TABLE 2.1: Redshift intervals, galaxy weighting in each redshift interval, average $850\ \mu\text{m}$ flux density, and average $850\ \mu\text{m}$ CMB corrected flux density.

Δz	Galaxy weighting	$\langle S_{850} \rangle$ [$\mu\text{Jy dz}^{-1}$]	CMB corr. $\langle S_{850} \rangle$ [$\mu\text{Jy dz}^{-1}$]
0.25	90003	2.1 ± 2.0	2.1 ± 2.0
0.75	79917	32.9 ± 8.2	33.0 ± 8.2
1.25	64475	67.5 ± 10.3	68.0 ± 10.3
1.75	47922	146.9 ± 12.8	148.5 ± 12.9
2.25	31448	135.0 ± 17.9	137.2 ± 18.2
2.75	18368	224.9 ± 21.5	230.3 ± 22.0
3.25	13071	104.6 ± 23.3	108.3 ± 24.1
3.75	5271	236.5 ± 45.1	248.4 ± 47.4
4.25	2413	195.0 ± 52.9	209.1 ± 56.7
4.75	848	130.8 ± 109.6	144.3 ± 120.9
5.25	336	251.2 ± 109.8	288.4 ± 126.1
5.75	79	422.9 ± 362.7	511.9 ± 439.0
6.25	86	74.2 ± 95.7	96.2 ± 124.1
6.75	37	1606.2 ± 868.8	2276.3 ± 1231.3
7.25	49	60.2 ± 77.3	95.2 ± 122.1
7.75	38	106.0 ± 127.0	190.8 ± 228.6
8.25	91	63.2 ± 73.7	132.2 ± 154.1
8.75	121	29.0 ± 36.5	71.8 ± 90.3
9.25	73	155.2 ± 152.5	460.6 ± 452.5
9.75	70	289.5 ± 161.3	1039.0 ± 578.9

Col. 1. Mid-point of each redshift interval (Δz); col. 2. the galaxy “weighting” which is the sum of the completeness corrected $\mathcal{P}(z)$ in each redshift bin. The summed $\mathcal{P}(z)$ across all redshift intervals integrates to 154,839, which is consistent with the number of galaxies in our sample (153,399) taking into account the completeness corrections; col. 3. average (stacked) $850\ \mu\text{m}$ flux density as a function of redshift with the uncertainty quoted to 1σ ; col. 4. average $850\ \mu\text{m}$ flux density corrected for the impact of the CMB as a function of redshift with the uncertainty quoted to 1σ .

($M_{\text{stellar}} = (2 - 40) \times 10^{10} M_{\odot}$) normal star-forming and star-bursting galaxies, both locally and at high- z .

TABLE 2.2: Redshift intervals, average rest-frame $850\mu\text{m}$ luminosity, average molecular gas mass, co-moving molecular gas mass density as a function of z .

Δz	$\langle L_{850,\text{rest}} \rangle$ [$10^{27} \text{ erg s}^{-1} \text{ Hz}^{-1} \text{ dz}^{-1}$]	$\langle M_{H_2} \rangle$ [$10^7 M_\odot \text{ dz}^{-1}$]	ρ_{H_2} [$10^6 M_\odot \text{ Mpc}^{-3}$]	Ω_{H_2} [10^{-7}]
0.25	1.64 ± 0.02	1.80 ± 0.03	1.92 ± 1.80	115.66 ± 108.42
0.75	81.97 ± 3.89	89.95 ± 4.26	17.12 ± 4.39	569.51 ± 146.13
1.25	217.79 ± 18.32	239.01 ± 20.10	23.22 ± 4.09	430.70 ± 75.93
1.75	514.61 ± 64.72	564.77 ± 71.02	34.67 ± 5.32	380.54 ± 58.41
2.25	492.12 ± 85.19	540.08 ± 93.49	20.74 ± 4.60	143.48 ± 31.84

Col. 1. Mid-point of each redshift interval (Δz); cols. 2 and 3. the average rest-frame $850\mu\text{m}$ luminosity and average molecular gas mass for galaxies in each redshift interval; col. 4. molecular gas mass density as a function of redshift and col. 5. molecular gas mass density in terms of the critical mass density. We restrict our results to $z \lesssim 2.5$ to ensure that the observed $850\mu\text{m}$ dust emission is tracing the RJ tail.

We estimate the average rest-frame $850\mu\text{m}$ luminosity density of galaxies as a function of redshift using the average flux densities detailed in Table 2.1, assuming a mass-weighted dust temperature of 25 K ¹ and employing the relation from S16:

$$L_{\nu 850} = S_\nu [\text{Jy}] \times 1.19 \times 10^{27} \times \left(\frac{\nu(850\mu\text{m})}{\nu_{\text{obs}}(1+z)} \right)^{3.8} \times \frac{(d_L [\text{Mpc}])^2}{1+z} \times \frac{\Gamma_{\text{RJ}}(25, \nu_{850\mu\text{m}}, 0)}{\Gamma_{\text{RJ}}(25, \nu_{\text{obs}}, z)} [\text{erg s}^{-1} \text{ Hz}^{-1}] \quad (2.9)$$

The Γ_{RJ} term in equation 2.10 corrects for departures from the RJ ν^2 dependence as the observed emission approaches the spectral energy distribution (SED) peak in the rest frame and where T_{dust} is the mass-weighted temperature characterizing the RJ dust emission

$$\Gamma_{\text{RJ}}(T_{\text{dust}}, \nu_{\text{obs}}, z) = \frac{h\nu_{\text{obs}}(1+z)/kT_{\text{dust}}}{e^{h\nu_{\text{obs}}(1+z)/kT_{\text{dust}}} - 1} \quad (2.10)$$

We restrict our estimates of the average rest-frame $850\mu\text{m}$ luminosity to $z \lesssim 2.5$ to ensure that rest-frame emission stays on the RJ tail. With the average rest-frame $850\mu\text{m}$ luminosity density derived (detailed in Table 2.2) we use the *RJ luminosity-to-gas mass* ratio from equation 2.8 to estimate the average molecular gas mass as a function of redshift to $z \approx 2.5$. This calibration includes a factor of 1.36 to account for the associated mass of heavy elements (mostly Helium at 8% by number), so we correct our results by a factor $1/1.36$ (M_{mol}) to obtain M_{H_2} .

¹The S16 calibration uses a mass-weighted temperature of 25 K , rather than a luminosity-weighted dust temperature (see Appendix A.2 of S16)

Since the summed photometric redshift probability distributions inform us about the galaxy “weighting” in each redshift interval and the UDS binary mask for “good” regions gives us the unmasked area of the SCUBA-2 850 μm map, we combine this information with the average molecular gas mass and differential co-moving volume element to estimate the co-moving volume density of molecular gas

$$\rho_{\text{H}_2} = \Omega \int_{z-\Delta z/2}^{z+\Delta z/2} N(z) \langle M_{\text{H}_2}(z) \rangle \frac{dV}{dz d\Omega} dz. \quad (2.11)$$

We present our values for $\rho_{\text{H}_2}(z)$ in Table 2.2 as a function of redshift, also giving this in terms of the critical mass density $\Omega_{\text{H}_2} = \rho_{\text{H}_2}(z)/\rho_{\text{crit}}(z)$. We use a Monte Carlo analysis to calculate the uncertainties for our values of $L_{850, \text{rest}}$, M_{H_2} and $\rho_{\text{H}_2}(z)$, first drawing random values for S_{ν} from a Gaussian distribution where the mean is the average flux density and width the uncertainty on the average flux density, and then drawing values for a mass-weighted T_{dust} from a Gaussian distribution with a mean of 25 K (corresponding to the constant T_{dust} assumed by S16), and width 3 K. Observations (e.g., Planck Collaboration 2011; S16) and simulations (e.g., Liang et al., 2018, 2019) find that a mass-weighted T_{dust} shows little variation with galaxy L_{850} or redshift (cf. Behrens et al., 2018), and by utilising a temperature distribution with $\sigma = \pm 3$ K we recognise this minimal variance in our uncertainty calculations. We use these values to estimate $L_{850, \text{rest}}$, M_{H_2} and $\rho_{\text{H}_2}(z)$ from equations 2.9, 2.8, and 2.11 respectively for 1000 runs, with the uncertainty being taken as the standard deviation across these trials.

We note that the galaxy sample we use to derive the results in Tables 2.1 and 2.2 includes all galaxies in the “good galaxy” subset of the UDS DR11 catalogue, regardless of the reliability of photometric redshifts for individual sources. If we apply a χ^2 cut to exclude galaxies with the least reliable redshifts (omitting galaxies with a reduced χ^2 value for the photometric redshift of > 10) and repeat the process outlined in Sections 2.3 and 2.4 above we find a less than 2% variation in our results with estimates consistent with those in Table 2.2 within the uncertainties.

We plot $\rho_{\text{H}_2}(z)$ in Figure 2.6, compared to direct CO line estimates from ASPECS (Decarli et al., 2016a; Decarli et al., 2020), COLDZ (Riechers et al., 2019) and VLASPECS (Riechers et al., 2020), as well as values derived using far-infrared and UV photometry (Berta et al., 2013). We fit a function of the same form as the star-formation rate density function presented in Madau and Dickinson (2014) to the log of our results, and derive the best fit parameters for our data

using emcee. This yields:

$$\log_{10} \left(\frac{\rho_{H_2}}{M_{\odot} \text{Mpc}^{-3}} \right) = (6.59 \pm 0.30) \times \frac{(1+z)^{0.38 \pm 0.16}}{1 + [(1+z)/5.57 \pm 1.69]^{1.78 \pm 0.61}} \quad (2.12)$$

which we plot in Figure 2.6. Our results show a peak $\rho_{H_2}(z)$ at $z \approx 2$ mirroring existing constraints.

2.4.2 Deriving molecular gas mass density from the halo mass function.

Using an alternative approach we derive $\rho_{H_2}(z)$ from first principles using the halo mass function from Murray et al. (2013) and assuming a constant halo mass range of $10^{11.5} - 10^{15} M_{\odot}$. We estimate the molecular gas mass density as a function of halo mass (for redshifts $0 \leq z \leq 7$) using the stellar-halo mass ratio from Moster et al. (2013) and the ISM-stellar mass relation from Scoville et al. (2017). The ISM-stellar mass relation is calibrated using a sample of high mass galaxies ($M_{\text{stellar}} \gtrsim 10^{10} M_{\odot}$), therefore we adopt a halo mass range for which the corresponding stellar masses are comparable with the Scoville et al. (2017) calibration sample. Integrating these estimates with respect to halo mass gives the total molecular gas density as a function of redshift, which we present in Figure 2.6.

2.4.3 Estimating molecular gas mass density using a “constant efficiency” model

We also estimate $\rho_{H_2}(z)$ from the star-formation rate density, $\rho_{M_*}(z)$, assuming a corresponding volume averaged star-formation “efficiency”, $\eta(z) = \rho_{H_2}(z)/\psi_*(z)$. We use the functional fit of Wilkins et al. (2019), a recalibration of the well-known Madau and Dickinson (2014) cosmic star formation history. We make the assumption that $\eta(z)$ is constant and that the *total* molecular gas mass per galaxy can be related to on-going star formation as $\xi M_{H_2} = \text{SFR}/\varepsilon$ (Geach and Papadopoulos, 2012). Here ξ is the ratio of dense, actively star-forming molecular gas to the total molecular reservoir with $\xi \approx 0.04$ for quiescent disks and $\xi > 0.5$ for starbursts (e.g., Papadopoulos and Geach, 2012), while the factor ε describes the rate at which the dense molecular gas forms stars. Figure 2.6 shows the predicted $\rho_{H_2}(z)$ inferred from the Wilkins et al. (2019) fit, assuming a constant “average” $\eta(z) = 0.3 \text{ Gyr}$ corresponding to $\xi = 0.1$ and $\varepsilon = 37 \text{ Gyr}^{-1}$ (e.g., Geach and Papadopoulos, 2012).

This value for $\eta(z)$ is similar to the typical values of $t_{\text{dep}} (M_{H_2}/\text{SFR}) \approx 1$ Gyr (e.g., Tacconi et al., 2018) for main-sequence galaxies. Tacconi et al. (2018) find a relatively weak dependence of t_{dep} with redshift, $t_{\text{dep}} \propto (1+z)^{-0.57}$ to $z < 2.5$, consistent with our picture of a common mode of star formation in normal galaxies, at least out to the peak epoch. We use this relation from Tacconi et al. (2018) and the Wilkins et al. (2019) fit to derive an estimate of $\rho_{H_2}(z)$ which incorporates a weakly evolving star-formation efficiency. We present our predicted $\rho_{H_2}(z)$ in Figure 2.6.

2.5 Discussion

Our results appear to be in reasonable agreement with existing empirical constraints, indicating that the epoch of molecular gas coincided with the epoch of peak star formation at $z \approx 2$. So what does this mean in terms of the evolving molecular gas budget? We might ask what is the *complete* picture of $\rho_{H_2}(z)$, or rather, what galaxies host the majority of the cosmic molecular gas budget across cosmic time? In the following discussion we interpret the overall evolution of the cosmic molecular gas density, in the context of our results, within the established framework of star formation in galaxies from the cosmic dawn to the present day.

2.5.1 Evolution of cosmic molecular gas mass density at $0 \leq z \leq 2.5$

2.5.1.1 The impact of the mass-metallicity relation

The S16 *RJ luminosity-to-gas mass* ratio has been shown to provide molecular gas mass estimates accurate to within a factor of around 2 when compared with measurements made via direct CO ($J = 1 \rightarrow 0$) line observations (e.g., Scoville et al., 2017; Kaasinen et al., 2019), with variations in the dust emissivity index, temperature, and gas-to-dust ratios being accountable for the deviations. This factor of 2 accuracy is based on samples of galaxies with high stellar masses $M_{\text{stellar}} = (2 - 40) \times 10^{10} M_{\odot}$ as the gas-to-dust mass ratio is typically constant in high stellar mass galaxies (Tremonti et al., 2004). This avoids probing low metallicity sources for which the dust-to-gas abundance ratio is likely to drop or the CO gas fraction is low (Bolatto et al., 2013). However, we note that the mass-metallicity relation (MZR) evolves with redshift, so that for a fixed stellar mass the metallicity decreases towards higher redshifts. Therefore, whilst a $10^{10} M_{\odot}$ galaxy in the local Universe is likely to have near-solar metallicity (e.g., Tremonti et al., 2004),

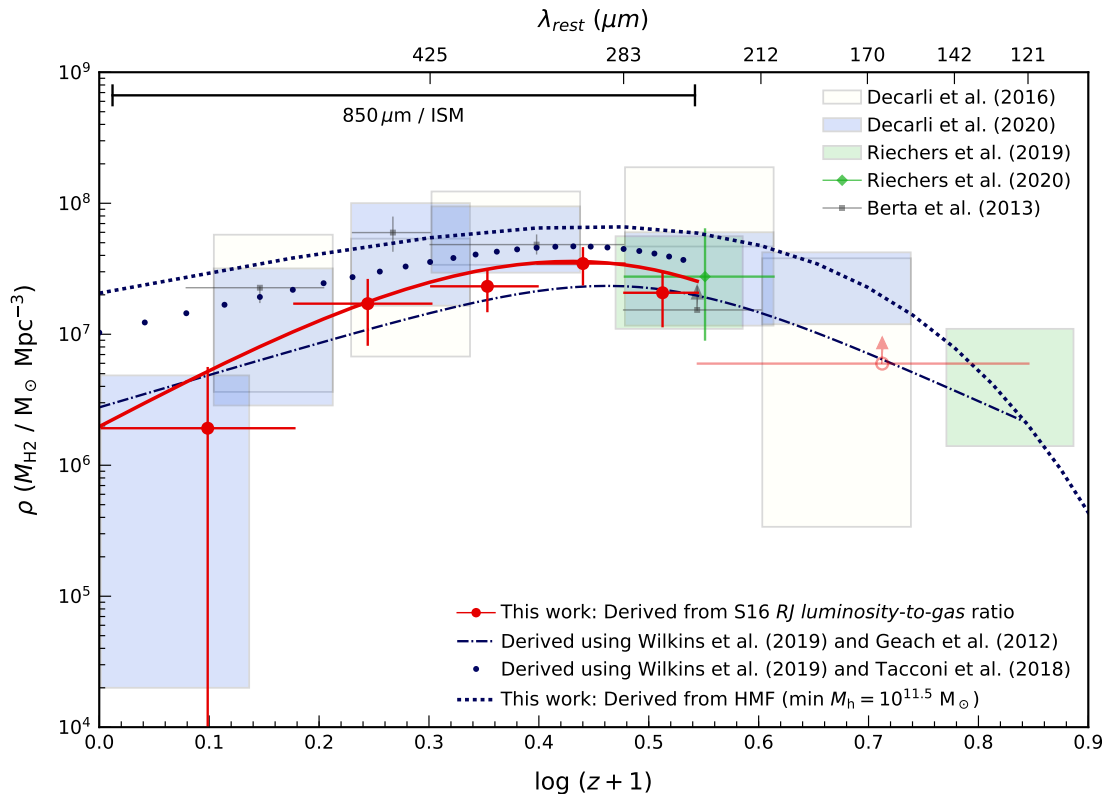


FIGURE 2.6: Values for $\rho_{H_2}(z)$ (CMB corrected) derived using a 3D stacking method and the RJ luminosity-to-gas mass ratio of S16. The upper x-axis shows the rest-frame wavelength of observed $850\mu\text{m}$ emission for the redshift range shown, illustrating the range at which rest-frame emission traces the long-wavelength RJ tail (i.e. $\lambda_{\text{rest}} \gtrsim 250\mu\text{m}$) and the S16 calibration can be reliably applied. Our estimates are represented by the red points (uncertainties shown to 2σ) with the solid red line showing the best-fit function derived using `emcee` and a function of the same form as the star-formation rate density function from Madau and Dickinson (2014). We note that at $z \gtrsim 2.5$ our results should be considered speculative as the observed $850\mu\text{m}$ emission no longer traces the rest-frame RJ tail. Hence we only show an average of our estimates after this point. We do not include any estimates for $z \gtrsim 6$ as the UDS photometric redshifts beyond this are untested and as such highly uncertain. Alongside our values we show results from ASPECS (off white rectangles; Decarli et al., 2016a), ASPECS LP (blue rectangles; Decarli et al., 2020), COLDz (green rectangles; Riechers et al., 2019) and VLASPECS (green diamond; Riechers et al., 2020) which are derived from direct measurements of CO line emission. The grey points show values from Berta et al. (2013), estimated using deep far-infrared and UV data, and assuming either typical gas depletion times (Tacconi et al., 2013) or from IR luminosity and obscuration properties (Nordon et al., 2013). We plot our “constant efficiency” models derived using the re-calibrated star formation history from Wilkins et al. (2019) and assuming either a corresponding constant (e.g., Geach and Papadopoulos, 2012) or weakly evolving (e.g., Tacconi et al., 2018) volume averaged star-formation “efficiency” to infer $\rho_{H_2}(z)$. The former is shown as the dark blue dot dash line and the latter illustrated by the dark blue circles. We also plot $\rho_{H_2}(z)$ to $z \approx 7$ derived from the halo mass function (Murray et al., 2013), assuming the stellar-halo mass ratio from Moster et al. (2013) and ISM-stellar-mass relation from Scoville et al. (2017). The dotted dark blue line corresponds to a halo mass range $10^{11.5} - 10^{15} M_{\odot}$, with the minimum stellar masses derived for this range ($\approx 10^{9.5} M_{\odot}$) being consistent with the lowest stellar masses probed in ASPECS LP (Boogaard et al., 2019).

at the redshifts probed by SMGs ($z \approx 2$) the metallicity of a $10^{10} M_\odot$ galaxy is likely to be less (e.g., Sanders et al., 2021; Zahid et al., 2013). Given that the S16 approach has been calibrated using samples of galaxies up to $z \approx 2$, we make the assumption that the estimated factor of 2 accuracy of this approach incorporates any deviation due to the evolution of the MZR relation.

In Figure 2.7 we show the marginalised stellar mass estimates for UDS galaxies (Almaini et al. in prep.) and the corresponding 95% stellar mass completeness (derived using the method of Pozzetti et al., 2010, Wilkinson et al. in prep.) for the UDS catalogue. As can be seen in Figure 2.7 our galaxy sample includes a proportion of galaxies with stellar masses lower than those used to derive the S16 *RJ luminosity-to-gas mass* ratio, with these sources being more abundant in lower redshift bins.

The dust-to-gas relation has been found to be relatively consistent for nearby galaxies with $M_{\text{stellar}} > 10^9 M_\odot$ (e.g., Groves et al., 2015), but drops for galaxies with lower stellar masses (hence lower metallicities). Cosmological galaxy formation simulations have shown that deviations from this relation become significant ($\gtrsim 0.5$ dex) at $L_{850} \lesssim 10^{28} \text{ erg s}^{-1} \text{ Hz}^{-1}$ in the redshift range $0 < z < 9.5$ (e.g., Privon et al., 2018). As shown in Figure 2.7 at $z \gtrsim 1$ the majority of our sample are likely to have $M_{\text{stellar}} > 10^9 M_\odot$ and Table 2.2 shows that the mean rest-frame $850 \mu\text{m}$ luminosity for our sample in all but the lowest redshift interval ($\Delta z = 0.25$) is $L_{850\mu\text{m}} \gtrsim 10^{28} \text{ erg s}^{-1} \text{ Hz}^{-1}$. Therefore, whilst the *RJ luminosity-to-gas mass* ratio has been calibrated on high stellar mass galaxies ($M_{\text{stellar}} = (2 - 40) \times 10^{10} M_\odot$), we make the assumption that applying this calibration to our sample at redshifts $z \gtrsim 0.5$ is likely to result in comparable uncertainties (i.e. a factor of 2). However, in the redshift bin $\Delta z = 0.25$ the mean rest-frame luminosity is $\langle L_{850\mu\text{m}} \rangle = 1.6 \times 10^{27} \text{ erg s}^{-1} \text{ Hz}^{-1}$, and as such our results are likely to be under-predicted by $\gtrsim 0.5$ dex (e.g., Privon et al., 2018) due to the abundance of lower mass (low metallicity) galaxies in this redshift interval.

2.5.1.2 Bright SMGs undetected in the *K*-band

We expect that approximately 20% of SMGs will be undetected in the *K*-band catalogue used to define our sample (e.g., Dudzevičiūtė et al., 2019). We can crudely infer which of the S2CLS-UDS SMGs are not included in our sky model (see section 2.3) by matching the UKIDSS-UDS *K*-band catalogue to the S2CLS-UDS SMG catalogue, to find those SMGs with no *K*-band counterparts. We can also infer the molecular gas mass of these SMGs from the $850 \mu\text{m}$ flux densities using the S16 approach. However, in the absence of photometric redshift distributions

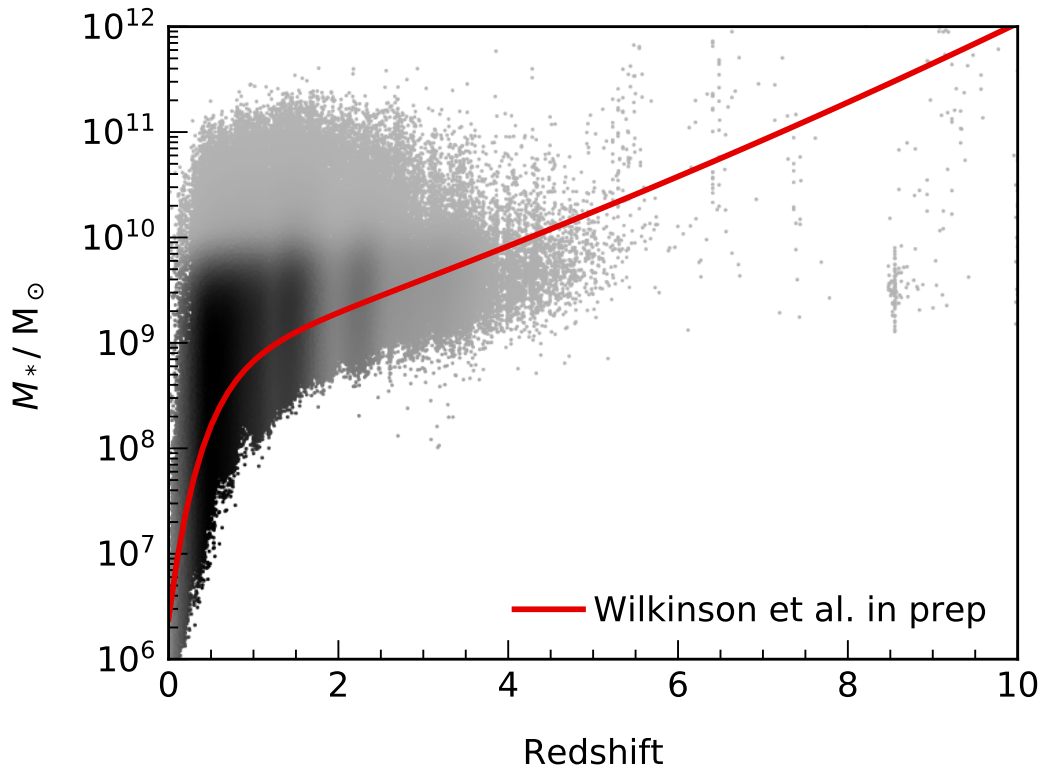


FIGURE 2.7: Marginalised stellar mass estimates (Almaini et al. in prep.) for UDS galaxies in our sample as a density plot, with darker colours corresponding to higher number densities of galaxies. The red line corresponds to the UDS catalogue 95% stellar mass completeness (derived using the method of Pozzetti et al., 2010, see Wilkinson et al. in prep.). This figure demonstrates that at high redshifts we are only sensitive to the most massive galaxies.

for these sources, we cannot map this additional molecular gas mass back to the molecular gas mass density in the different redshift bins. We note that these sources are in our observed map, which we use to estimate a best fit flux density for each redshift interval. Therefore, these sources will act as noise in the MCMC sampling, and will likely boost the average flux density across all redshift intervals. This means that whilst we are not directly including these undetected SMGs, the flux from these sources is included in some way (although not fully) in our results.

2.5.2 Comparison of the evolution of molecular gas mass density to other studies in the literature

In Figure 2.6 we compare our results, which are revised to account for the influence of the CMB, to those from direct CO line surveys (e.g., Decarli et al., 2016a; Decarli et al., 2020; Riechers et al., 2019; Riechers et al., 2020). We limit our discussion to the results from these surveys at $z \lesssim 2.5$ as we are restricted to this redshift range due to the wavelength of our observations ($\lambda_{\text{obs}} = 850 \mu\text{m}$). Whilst the results from ASPECS/ASPECS LP (Decarli et al., 2016a; Decarli

et al., 2020) and COLDz (Riechers et al., 2019; Riechers et al., 2020) were not corrected for the influence of the CMB, we note that this is not necessary at $z \lesssim 4.5$ as the effect of the CMB on measurements of molecular gas mass density from direct CO line observations is minimal ($\lesssim 15\%$, e.g., Decarli et al., 2019) and as such this does not impact on our analysis here.

We find that our results are broadly consistent with the estimates from direct CO line surveys within uncertainties and show notably good agreement with results obtained through observations of the ground state CO line (ASPECS LP at $\Delta z \simeq 0.25$ and COLDZ at $\Delta z \simeq 2.25$). Albeit, we caution that our results at $\Delta z \simeq 0.25$ are likely under estimated due to the abundance of low stellar mass galaxies in this redshift bin.

When compared with the ASPECS LP survey (Decarli et al., 2020) our results generally trace the lower boundaries of their estimates between $0.75 \lesssim z \lesssim 1.75$. The S16 RJ luminosity-to-gas mass ratio is calibrated using the ground state CO ($J = 1 \rightarrow 0$) line, whereas at $z > 0.75$ the ASPECS LP results are derived from observations of higher state excitation CO lines. Therefore, this offset could be explained by the uncertainties associated with translating higher excitation CO lines observations to ground state CO ($J = 1 \rightarrow 0$) luminosities. However, in the redshift interval $\Delta z = 1.25$, even if the extreme case of thermalised gas is assumed, our upper estimate (taking into account 1σ uncertainties) falls a factor of 1.42 below the lower boundary of the ASPECS LP survey (e.g., $38.90 \times 10^6 M_\odot \text{Mpc}^{-3}$, Table A3. Decarli et al., 2019). As such the uncertainties in CO line ratios do not fully account for the offset we see.

Building on previous studies Liu et al. (2019a) derive the molecular gas mass density using a dataset comprised of ≈ 700 ALMA continuum detected galaxies and ≈ 1000 galaxies with CO observations (taken from the literature). To derive molecular gas masses for the continuum detected galaxies Liu et al. (2019a) employ the Hughes et al. (2017) luminosity-to-gas mass calibration. Liu et al. (2019a) estimate a SMF (stellar mass function) integrated molecular gas mass density based on the SMF integrated to $M_{\text{stellar}} = 10^9 M_\odot$ and using a gas fraction function derived from their composite sample of ≈ 1700 galaxies. Their results trace the upper boundaries of the molecular gas mass density derived from the most recent blank field CO line surveys (e.g., Decarli et al., 2019; Riechers et al., 2019) and are ≈ 1 dex higher than our estimates. This offset with our estimates of molecular gas mass density could be in part due to assumptions made in Liu et al. (2019a) to derive an SMF integrated molecular gas mass density (i.e. that all star-forming galaxies are on the main-sequence) or potentially differences in sample selection. The majority (≈ 800) of the CO detected sources in the Liu et al. (2019a) composite sample are in

the Local Universe (i.e $z < 0.3$), so at $z > 0.3$ their dataset is dominated by ALMA continuum detected galaxies which are preferentially massive and dust-rich (and hence, using a dust-to-gas mass conversion, gas-rich). In contrast our galaxy sample is near-infrared selected and as such our selection is less likely to sample these luminous dust-rich SMGs, with previous studies finding that $\approx 20\%$ of SMGs are missed in optical/new-infrared surveys (e.g. Dudzevičiūtė et al., 2019).

Magnelli et al. (2020) use a stacking approach to measure the comoving gas mass density of a sample of 555 near-infrared selected galaxies, with galaxies split into bins of z and M_{stellar} . Their stacking method accounts for the metallicity of galaxies in these bins (inferred using the stellar mass-metallicity from Tacconi et al., 2018) and is equivalent to the S16 calibration at solar metallicity. Our results trace the lower boundaries of their estimates, but are inconsistent (within 1σ uncertainties) at $z > 1$. This discrepancy may be in part due to our method not accounting for the metallicity of low mass galaxies, resulting in an under-estimation of the molecular gas mass for galaxies with $M_{\text{stellar}} < 10^9 M_{\odot}$. However, if this was the sole reason for the difference in our results we would expect this to have more of an impact at $z < 1$ where this effect will be more prominent.

We caution that our results also rely solely on photometric redshifts, which despite the high quality 12 band photometry of the UDS catalogue, cannot compete with the accuracy of redshifts derived via spectroscopic surveys. By utilising the redshift probability distributions in our 3D stacking approach we aim to provide mitigation against these uncertainties. However, whilst our estimates rely exclusively on the use of photometric redshifts, the results obtained in both ASPECS LP (Decarli et al., 2020; Magnelli et al., 2020) and Liu et al. (2019a) benefit from the inclusion of sources with more reliable spectroscopic redshifts. This may also play a part in deviations seen when we compare our estimates with these previous surveys.

2.5.3 Contribution of the brightest submillimetre sources to the cosmic evolution of the molecular gas mass density

In order to present the most complete view of the evolution of the molecular gas mass density we stack all sources in our near-infrared selected sample, including counterparts to the bright submillimetre sources in the SCUBA-2 UDS map. To test the contribution of these galaxies to our results we repeat our stacking analysis with the SCUBA2 UDS source subtracted map. As expected excluding the ~ 1000 UDS submillimetre sources reduces the average observed $850\mu\text{m}$

flux in our redshift intervals, which propagates to our estimate of the comoving molecular gas mass density. At $z < 1.5$ the exclusion of the UDS submillimetre sources has a minimal impact on our estimates of $\rho_{H_2}(z)$ and these remain consistent within the 1σ uncertainties. However, at $z > 1.5$ our estimates of $\rho_{H_2}(z)$ drop by a factor of 2.05 and 2.33 in the redshift intervals $\Delta z = 1.75$ and $\Delta z = 2.25$ respectively. This coincides with the peak number density of SMGs at $z \approx 2$. This indicates that approximately 50% of the molecular gas mass density at the peak of the star formation rate density is locked in dust-rich SMGs. We note that our inferred contribution of SMGs is also likely under-estimated as we expect that approximately 20% of SMGs are undetected in our near-infrared selected sample (e.g., Dudzevičiūtė et al., 2019). Our finding is in keeping with Zavala et al. (2021) who find that bright SMGS ($L_{IR} > 10^{12}L_{\odot}$) dominate the obscured star formation rate density at $z \approx 2$ and also Magnelli et al. (2020) who find that the bulk of dust and gas in galaxies is locked in massive star-forming galaxies.

2.5.4 Additional constraints on the evolution of molecular gas mass density

We have added further valuable constraints to this picture of cosmic molecular gas evolution using two alternative approaches.

We estimate $\rho_{H_2}(z)$ from the halo mass function (Murray et al., 2013) assuming a constant halo mass range of $10^{11.5}-10^{15}M_{\odot}$, and using the stellar-halo mass ratio from Moster et al. (2013) and the ISM-stellar mass relation from Scoville et al. (2017). For the latter relation we make the assumption that all galaxies are on the star-forming main sequence (e.g., $sSFR/sSFR_{MS} = 1$). The evolution of our halo mass derived $\rho_{H_2}(z)$ (shown in Figure 2.6) follows a similar shape to the star-formation rate density, rising to a peak at $1 \lesssim z \lesssim 3$ and decreasing to the present day. The minimum halo mass we assume corresponds to stellar masses of $\approx 10^{9.5}M_{\odot}$ (e.g., Moster et al., 2013), equivalent to the lowest stellar masses probed in the ASPECS LP survey (Decarli et al., 2020). Our $\rho_{H_2}(z)$ estimates show good agreement with the ASPECS/ASPECS LP surveys (Decarli et al., 2016a; Decarli et al., 2020) at $z \gtrsim 0.6$. However, as shown in Figure 2.6 at $z \lesssim 0.6$ our estimate of $\rho_{H_2}(z)$ lies above the lowest redshift bins from the ASPECS LP survey (Decarli et al., 2020) and is ≈ 1 dex higher than our estimate of $\rho_{H_2}(z)$ derived from measurements of observed $850\mu\text{m}$ flux. To obtain an estimate of $\rho_{H_2}(z)$ from the halo mass function we make the assumption that all galaxies are star-forming. As such our estimate of $\rho_{H_2}(z)$ derived from the halo mass function can be seen as an upper limit $\rho_{H_2}(z)$ for the stellar mass range sampled.

It follows that we see a more significant deviation between our estimate and observationally derived results at lower redshifts as the fraction of passive galaxies is higher at later epochs.

We also estimate $\rho_{H_2}(z)$ from the star-formation rate density (Wilkins et al., 2019), assuming a constant (Geach and Papadopoulos, 2012) and weakly evolving (Tacconi et al., 2018) star-formation efficiency. These “constant efficiency” models predict a co-moving molecular gas mass density in good agreement with both measurements of molecular gas mass via observations of direct CO line emission (Decarli et al., 2016a; Decarli et al., 2020; Riechers et al., 2019; Riechers et al., 2020) and our results derived from measurements of the long-wavelength dust emission, out to a peak at $z \approx 2$. A simple conclusion is that the epoch of peak star formation at $z \approx 2$ is not driven by significantly more efficient (or starburst-like) star formation in galaxies, but by a higher abundance of molecular fuel in galaxies. We note that the estimate derived from weakly evolving star-formation is ≈ 1 dex higher than our results at $\Delta z \simeq 0.25$. This is likely a consequence of the latter being under estimated due to the abundance of low stellar mass galaxies in this redshift bin.

We recognise that our assumption of a “constant efficiency” model is at odds with Scoville et al. (2017), who argue that whilst cold molecular gas reservoirs increase with z (as $(1+z)^{1.84}$), the star-formation rate increases more rapidly (as $(1+z)^{2.9}$), indicating that the peak of star formation is a consequence of both increased molecular gas content in galaxies and higher star-formation efficiency. We also note that at $z \gtrsim 1$ early-type galaxies have been shown to be more compact for a given stellar mass than their local counterparts (e.g., Daddi et al., 2005; Cappellari et al., 2009), which taken in combination with the “Kennicutt-Schmidt” relation (a power-law relation between star-formation rate and gas surface densities, Kennicutt, 1998; Schmidt, 1959) implies that star formation may be more efficient at $z \gtrsim 1$.

The 3D stacking approach we use derives the *average* properties for galaxies in our sample as a function of redshift, and thus we do not measure the molecular gas mass and star-formation rates for individual sources. Whilst the UDS DR11 catalogue does include M_{stellar} estimates (which are evaluated at the peak maximum likelihood redshift) for individual galaxies, our 3D stacking method bins galaxies according to the discretized redshift probability distribution ($\mathcal{P}(z)$), and as such each galaxy in our sample effectively contributes to the flux in all redshift intervals. Hence, using this 3D stacking method precludes a M_{stellar} selection relative to our redshift bins. Therefore, we are not able to repeat the analysis from Scoville et al. (2017) to test their assertion of an evolving star-formation efficiency.

2.5.5 The epoch of molecular gas

Although we cannot quantify the contribution of higher star-formation efficiencies to the peak of star-formation rate density at $z \approx 2$, the symmetry between our “constant efficiency” models with our statistically derived $\rho_{\text{H}_2}(z)$ indicates a star formation history which is predominantly driven by an increased supply of molecular gas in galaxies, rather than a significant evolution in star-formation efficiency (consistent with the findings of Decarli et al., 2020; Magnelli et al., 2020). With this in mind we now turn to the formation of H₂ itself.

Cazaux and Spaans (2004) combine a microscopic model for the relative rates of gas-phase and dust H₂ production with a cosmological model to show the more efficient dust-phase production becomes the dominant route to H₂ formation at $z \approx 3\text{--}6$ for reasonable assumptions about the conditions of the interstellar medium of early galaxies. Therefore, there is a perfect storm for massive galaxy growth at $z \approx 2$: not only is the cosmic accretion rate at its peak, massive halos have had time to grow, galaxies have increased gas densities, and previous generations of stars in the progenitors of these systems have provided the metal enrichment that accelerates the formation of H₂, which, as the fuel for star formation, drives galaxy growth; this could be described as the epoch of molecular gas.

2.5.6 Estimating the evolution of cosmic molecular gas mass density at $z \gtrsim 2.5$

S16 intentionally restrict their calibration sample to galaxies at $z \leq 3$ to ensure observed 850 μm emission is from the rest-frame long wavelength RJ tail, where dust is optically thin and emission is dominated by the contribution of cold dust (which is well represented by a mass-weighted $T_{\text{dust}} = 25$ K). In Figure 2.6 we have shown an average of our $\rho_{\text{H}_2}(z)$ estimates at $2.5 \lesssim z \lesssim 6$ (the UDS redshifts are untested at earlier epochs as there are no UDS galaxies with spectroscopic redshifts at $z \gtrsim 6.5$), but note that at these redshifts estimates are less reliable due to large uncertainties in the RJ correction (see equation 2.10) as rest-frame emission approaches the peak of the SED.

In the optically thick regime (as rest-frame dust emission moves off the long-wavelength RJ tail) the rest-frame emission no longer correlates with the total dust mass of a galaxy and probes only the surface dust, which using the approach of S16 would result in under-estimation of L_{850} and hence the molecular gas mass. However, as the rest-frame emission approaches the peak of the SED we are increasingly sensitive to the dense, warm dust component, which significantly

boosts the luminosity (with only a small mass fraction) and dominates the emission close to the SED peak. Consequently rest-frame dust emission at high- z is not well represented by a mass-weighted $T_{\text{dust}} = 25$ K, which would result in a over-estimate of the dust and gas mass.

In addition to these competing effects, we are also likely to be missing a significant population of lower mass galaxies at $z > 2.5$. As shown in Figure 2.7 the 95% stellar mass completeness at $z \approx 2.5$ is predicted to be $\simeq 10^{9.5} M_{\odot}$, so we are simply not sensitive to the majority of low mass galaxies at the highest redshifts. In addition, although relatively rare (with number counts $N(> 3.5 \text{ mJy}) \simeq 3000 \text{ deg}^{-2}$; Geach et al., 2017) SMGs are dust-rich ($M_{\text{dust}} \sim 10^9 M_{\odot}$; e.g., Da Cunha et al., 2015; Magnelli et al., 2019) and about 20% are undetected in optical/near-infrared surveys (e.g., Dudzevičiūtė et al., 2019). This non-detection of SMGs is unlikely to have a significant impact on our estimates at low z . However, at $z \gtrsim 2.5$ since we are significantly under-sampling the galaxy population and as the number of galaxies in our redshift bins fall the non-detection of dust-rich SMGs becomes more statistically significant, further contributing to an under-estimation of the molecular gas mass density at $z \gtrsim 2.5$.

The overall impact of the above is difficult to quantify. However, as shown by Figure 2.6 our results at $z \gtrsim 2.5$ are systematically lower than the estimates obtained via direct CO line emission, which suggests that the use of this method past $z \approx 2.5$ (when $\lambda_{\text{obs}} = 850 \mu\text{m}$ no longer probes the rest-frame RJ tail) results in an under-estimation of the molecular gas mass density. In consequence, whilst our results are highly uncertain at $z > 2.5$ we suggest that to $z \lesssim 6$ these can be seen as providing a lower-limit to the molecular gas mass density.

2.6 Conclusions

We employ a 3-dimensional stacking method (Viero et al., 2013) and an empirically calibrated *RJ luminosity-to-gas mass* ratio (S16) to derive the average molecular gas mass as a function of redshift utilising a sample of $\approx 150,000$ galaxies in the UKIDSS-UDS field. By combining these techniques we are able to reduce the statistical uncertainties on the evolution of the molecular gas mass density, $\rho_{\text{H}_2}(z)$, within the redshift range $0.5 \lesssim z \lesssim 2.5$. We find that:

- $\rho_{\text{H}_2}(z)$ shows a clear evolution over cosmic time which traces that of the star-formation rate density with a peak $\approx 2 \times 10^7 M_{\odot} \text{ Mpc}^{-3}$ at $z \approx 2$.

- Our results are consistent with those of blank field CO line surveys, albeit our estimates are systematically lower than those derived using observations of higher excitation CO lines. This may in part be a consequence of the line ratios used to translate higher excitation CO line luminosity to ground state CO line luminosity.
- Our results are an order of magnitude lower than those derived by Liu et al. (2019a) who use the Hughes et al. (2017) *luminosity-to-gas mass* calibration to estimate molecular gas masses for the ALMA continuum detected galaxies in their sample. This difference in these results is likely due to the different sample selections. The ALMA-selected sample of Liu et al. (2019a) selects dust-rich (and consequently gas-rich), sources, whereas by using a NIR selection we are sampling a more general population of galaxies and are likely to miss $\approx 20\%$ of these dust-rich SMGs. Therefore, the Liu et al. (2019a) results may be biased towards higher values, whilst our results are more conservative.
- $\rho_{H_2}(z)$ can be broadly modelled by inverting the star-formation rate density (Wilkins et al., 2019) with a constant (Geach and Papadopoulos, 2012) or weakly evolving (Tacconi et al., 2018) volume averaged star-formation efficiency. Our “constant efficiency” models closely align to our statistically derived $\rho_{H_2}(z)$.
- $\rho_{H_2}(z)$ can be derived from first principles from the halo mass function (Murray et al., 2013) in conjunction with stellar-halo mass (Moster et al., 2013) and ISM-stellar mass ratios (Scoville et al., 2017). To obtain this estimate we make the assumption that all galaxies are star-forming and hence this can be seen as an upper limit for $\rho_{H_2}(z)$ with respect to the stellar mass range sampled.

We have demonstrated that by applying a statistical method and the approach of Scoville et al. (2016) we can provide robust, statistically significant constraints to the cosmological gas mass density to $z \lesssim 2.5$. Our results show an evolution that mirrors that of the star-formation rate density indicating that the peak of the star formation history is primarily driven by an increased supply of molecular gas rather than a significantly increased star-formation efficiency. We have shown that at $z \gtrsim 2.5$ we detect dust emission from high mass galaxies, even with our near-infrared selected sample. Hence, in the future there is potential for this approach to be extended to provide improved constraints at higher- z through 1 mm/3 mm wide-field surveys with facilities such as the Large Millimeter Telescope.

Chapter 3

The SCUBA-2 Large eXtragalactic Survey: 850 μm map, catalogue and the bright-end number counts of the XMM-LSS field

3.1 Introduction

The SCUBA-2 Large eXtragalactic Survey (S2LXS) is a JCMT Large Program (PI: J. E. Geach and Y. Tamura, Program ID M17BL001) and covers an area of 10deg^2 split over two fields - the X-ray Multi-Mirror Large Scale Structure Survey field (XMM-LSS; Pierre et al., 2004) and the Extended Cosmic Evolution Survey field (E-COSMOS; Scoville et al., 2007). In the context of other JCMT Large Programs S2LXS can be seen as a wide, moderately deep tier, complementing the SCUBA-2 Cosmology Legacy Survey (S2CLS; Geach et al., 2017), the SCUBA-2 COSMOS survey (S2COSMOS; Simpson et al., 2019) and the SCUBA-2 Ultra Deep Imaging East Asian Observatory Survey (STUDIES; Wang et al., 2017), which map smaller areas to higher sensitivity. S2LXS covers an area $2\times$ larger than S2CLS, is effectively $2\times$ deeper than SPT-SZ (Vieira et al., 2010; Mocanu et al., 2013) and at a wavelength of $850\mu\text{m}$ is more sensitive to dust emission from high redshift ($z \gtrsim 4$) SMGs than far-infrared surveys (i.e., H-ATLAS, HerMES; Eales et al., 2010; Oliver et al., 2012). The primary aim of S2LXS is to detect the most luminous and highest redshift submillimetre sources, thus providing robust

constraints on the bright-end of the single-dish $850\mu\text{m}$ number counts and unveiling a new distant population of SMGs.

In this thesis we present the results of the S2LXS XMM-LSS field and provide the map and source catalogue for public use¹. This chapter is organised as follows: in section 3.2 we define the survey and describe the data reduction; in section 3.3 we present the maps and describe the cataloguing procedure; in section 3.4 we use these data to measure the bright-end of the $850\mu\text{m}$ number counts and compare to recent results from model predictions; and in section 3.5 we summarise the chapter.

3.2 The SCUBA-2 Large eXtragalactic Survey

The SCUBA-2 Large eXtragalactic Survey (S2LXS) is a wide area ($>10\text{deg}^2$) survey at $850\mu\text{m}$ split over two fields: XMM-LSS (9deg^2); and E-COSMOS (3deg^2). These fields were selected to take advantage of the wealth of legacy multi-wavelength data available (this data is essential for identifying SMG counterparts) and for the accessibility to key submillimetre/millimetre interferometers for follow-up observations. The S2LXS observations of the E-COSMOS field are currently less than 50 per cent complete and continue under programme ID M20AL026 (PI: J. E. Geach and Y. Tamura). The S2LXS map, catalogue and results for the E-COSMOS field will be the subject of a future paper. Therefore the focus of this chapter is the S2LXS XMM-LSS field, which is mapped at $850\mu\text{m}$ to a median depth of $1\sigma \simeq 4\text{mJybeam}^{-1}$. Although SCUBA-2 simultaneously collects data at both $850\mu\text{m}$ and $450\mu\text{m}$ we do not process the complementary $450\mu\text{m}$ data. At $450\mu\text{m}$ the estimated sensitivity is $1\sigma \simeq 50\text{mJybeam}^{-1}$ and so these data are not expected to have sufficient depth to reliably detect (at $>3.5\sigma$) even the most luminous submillimetre sources in the S2LXS XMM-LSS field.

XMM-LSS benefits from being a well-studied deep field in the Hyper Suprime-Cam (HSC) Subaru Strategic Program (HSC-SSP). The HSC-SSP is multi-band (*grizy*+narrow-band) imaging survey (Aihara et al., 2018) conducted using the HSC digital imaging camera on the 8.2m Subaru Telescope. This survey comprises three tiers; a Wide tier (1400deg^2 , $r_{\text{AB}} \simeq 26$), a Deep tier (28deg^2 , $r_{\text{AB}} \simeq 27$) and an Ultra-Deep tier (13.5deg^2 , $r_{\text{AB}} \simeq 28$). The XMM-LSS field is also covered by legacy datasets at X-ray, ultra-violet, infrared and radio wavelengths (see Table

¹The data are available at the DOI <https://doi.org/10.5281/zenodo.7371860>

3.1 for a summary of the multi-wavelength imaging available). Multi-wavelength data is essential for identifying counterparts and companions (e.g., satellite galaxies that are not dusty) to sources detected at $850\mu\text{m}$.

3.2.1 Observations

The S2LXS XMM-LSS observations were conducted with SCUBA-2 (Holland et al., 2013) on the James Clerk Maxwell telescope (JCMT) over 3 years from July 2017 to January 2020, totalling 170 hours. The XMM-LSS field was mapped using the SCUBA-2 PONG mapping strategy (Holland et al., 2013) for large fields in which the telescope array tracks across a target multiple times bouncing off the edges of a defined rectangular map area. Once the PONG pattern fills the map area the map is rotated and the pattern is repeated at the new angle. In Figure 3.1 we show an example of the telescope track to illustrate the rotating PONG pattern. Observations were conducted for S2LXS XMM-LSS using the SCUBA-2 PONG 1800 arcsec diameter map pattern, which has a telescope scanning speed of 400arcsec s^{-1} with 8 rotations of the map during each observation to ensure a uniform coverage of the field. The final S2LXS XMM-LSS field map is a mosaic of 42 hexagonally arranged 1800 arcsec diameter PONG tiles with each tile overlapping with its neighbours. We show the layout of the PONG tiles in Figure 3.1. There is a gap in the observations centred on $\alpha = 34^\circ.4542$, $\delta = -5^\circ.0986$. This absence of data reflects the area of the deeper ($1\sigma = 1\text{mJy beam}^{-1}$) S2CLS observations of the UKIRT Infrared Deep Sky Survey-Ultra Deep Survey field (S2CLS UKIDSS-UDS; Geach et al., 2017). This region was not observed again in S2LXS XMM-LSS.

The original objective of S2LXS was to map the XMM-LSS field to a depth of $1\sigma \simeq 2\text{mJy beam}^{-1}$ at $850\mu\text{m}$. Progress of the survey was slow due to ongoing bad weather conditions on Mauna Kea and S2LXS XMM-LSS was consequently scaled back with the revised aim to map the S2LXS XMM-LSS field to a target sensitivity of $1\sigma \simeq 4\text{mJy beam}^{-1}$. At this depth the primary objective of S2LXS, to uncover the intrinsically rare, bright-end of the SMG population, is still realised. The individual PONG observations were limited to an integration time of 40 minutes to allow for accurate monitoring of variations in the observing conditions with regular pointing observations being made throughout the night. Each of the 42 PONG tiles were observed over a minimum of 5 scans (a minimum combined observing time of 3 hours) to achieve the target sensitivity of $1\sigma \simeq 4\text{mJy beam}^{-1}$. The majority of observations (97 per cent) were conducted in band 1, 2 or 3 weather conditions (i.e., $\tau_{225\text{GHz}} \leq 0.12$). The remaining 3 per cent of

TABLE 3.1: Summary of ancillary multi-wavelength data for the S2LXS XMM-LSS field. Note that a region of this field (central coordinates $\alpha = 34^{\circ}.4542$, $\delta = -5^{\circ}.0986$) was observed at $850\ \mu\text{m}$ in S2CLS (Geach et al., 2017). Observations of this region are not repeated in S2LXS.

Survey/Instrument	Abbreviation	Band	Reference
X-ray Multi-Mirror Large Scale Structure survey	XMM-LSS	[0.5-2] keV	Pierre et al. (2004)
X-ray Multi-Mirror <i>Spitzer</i> Extragalactic Representative Volume Survey	XMM-SERVS	[0.5-10] keV	Chen et al. (2018)
Canada-France-Hawaii Telescope Large Area <i>U</i> -band Deep Survey	CFHT CLAUDS	<i>u</i> *	Sawicki et al. (2019)
Hyper Suprime-Cam Subaru Strategic Program	HSC-SSP	<i>grizy</i>	Aihara et al. (2018)
Visible and Infrared Survey Telescope for Astronomy Deep Extragalactic Observations survey	VISTA VIDEO	<i>YJHK</i>	Jarvis et al. (2013)
United Kingdom infrared telescope Infrared Deep Sky Survey Deep eXtragalactic Survey	UKIDSS DXS	<i>YJHK</i>	Lawrence et al. (2007)
<i>Spitzer</i> Extragalactic Representative Volume Survey	SERVS	$3.6\ \mu\text{m}$, $4.5\ \mu\text{m}$	Mauduit et al. (2012)
<i>Spitzer</i> survey of the Deep Drilling Fields	Deep Drill	$3.6\ \mu\text{m}$, $4.5\ \mu\text{m}$	Lacy et al. (2021)
<i>Spitzer</i> Wide-area InfraRed Extragalactic survey	SWIRE	$3.6\ \mu\text{m}$, $4.5\ \mu\text{m}$, $5.8\ \mu\text{m}$, $8.0\ \mu\text{m}$, $24\ \mu\text{m}$, $70\ \mu\text{m}$, $160\ \mu\text{m}$	Lonsdale et al. (2003)
<i>Herschel</i> Multi-tiered Extragalactic Survey	HerMES	$250\ \mu\text{m}$, $350\ \mu\text{m}$, $500\ \mu\text{m}$	Oliver et al. (2012)
Low Frequency Array	LOFAR	120-168 MHz	Hale et al. (2019)
MeerKAT International GigaHertz Tiered Extragalactic Explorations	MIGHTEE	856-1712 MHz	Heywood et al. (2022); Jarvis et al. (2016)
Very Large Array 1-2 GHz survey	–	1–2 GHz	Heywood et al. (2020)
SCUBA-2 Cosmology Legacy Survey	S2CLS	$450\ \mu\text{m}$, $850\ \mu\text{m}$	Geach et al. (2017)

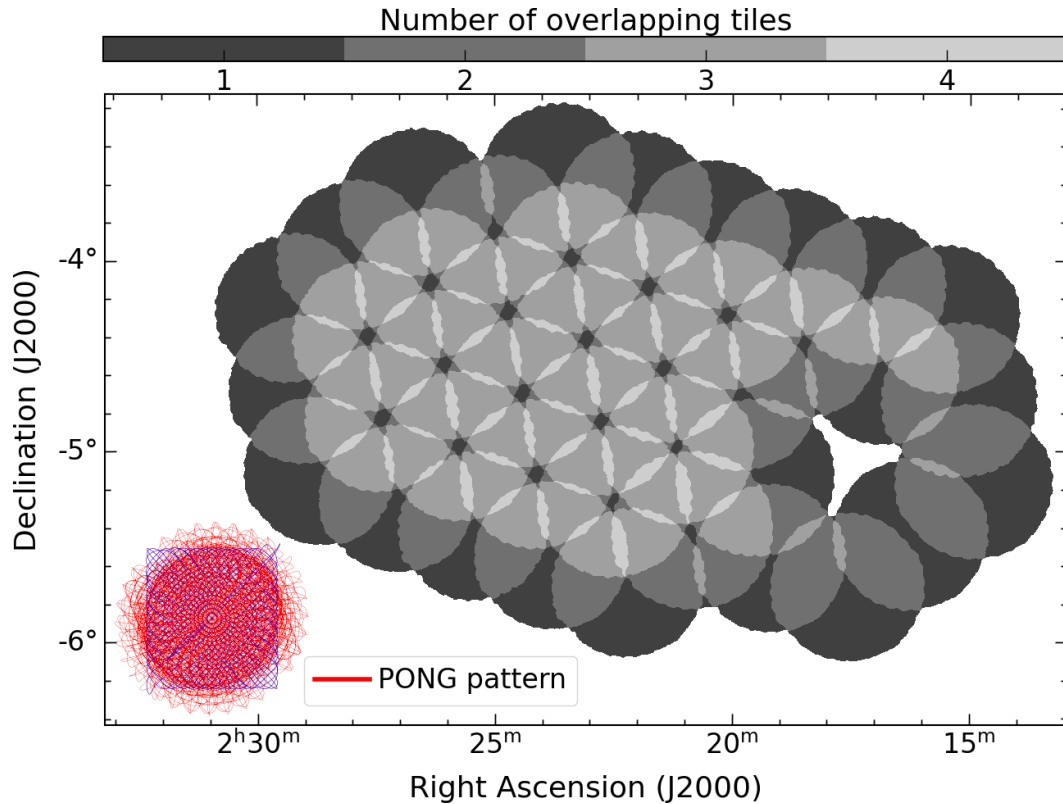


FIGURE 3.1: Layout of the S2LXS map showing the 42 hexagonally arranged PONG tiles. An exposure time crop is applied to each individual PONG tile (see section 3.2.2 for details) before these are mosaicked. The colour map shows the number of PONG tiles that overlap across the map. The absence of data around $\alpha = 34^{\circ}.4542$, $\delta = -5^{\circ}.0986$ corresponds to the area of the deeper $1\sigma = 1 \text{ mJy beam}^{-1}$ S2CLS UKIDSS-UDS field observations (Geach et al., 2017). This region was not observed again in S2LXS. In the lower left of the figure we also show an example of the telescope track for a PONG observation to illustrate the rotating PONG pattern (Holland et al., 2013). The blue line shows the telescope track for a single rotation of the map, and the red line shows the complete PONG pattern (i.e., 8 rotations of the map).

observations were taken in band 4 conditions in which the opacity at 225 GHz is in the range $0.12 < \tau_{225\text{GHz}} < 0.16$ (see Figure 3.2). In the following section we describe the process used to produce the S2LXS XMM-LSS maps.

3.2.2 Data reduction

The SCUBA-2 bolometers each record a time-varying signal containing contributions from astronomical signal, atmospheric extinction and noise. We reduce the S2LXS time-series data using the Dynamical Iterative Map-Maker (DIMM) tool, part of the Submillimetre Common User Reduction Facility software package (SMURF; Chapin et al., 2013). The primary purpose of this data reduction is to extract the astronomical signal from the SCUBA-2 bolometer time streams and to bin the resulting data into a two-dimensional celestial projection. DIMM includes

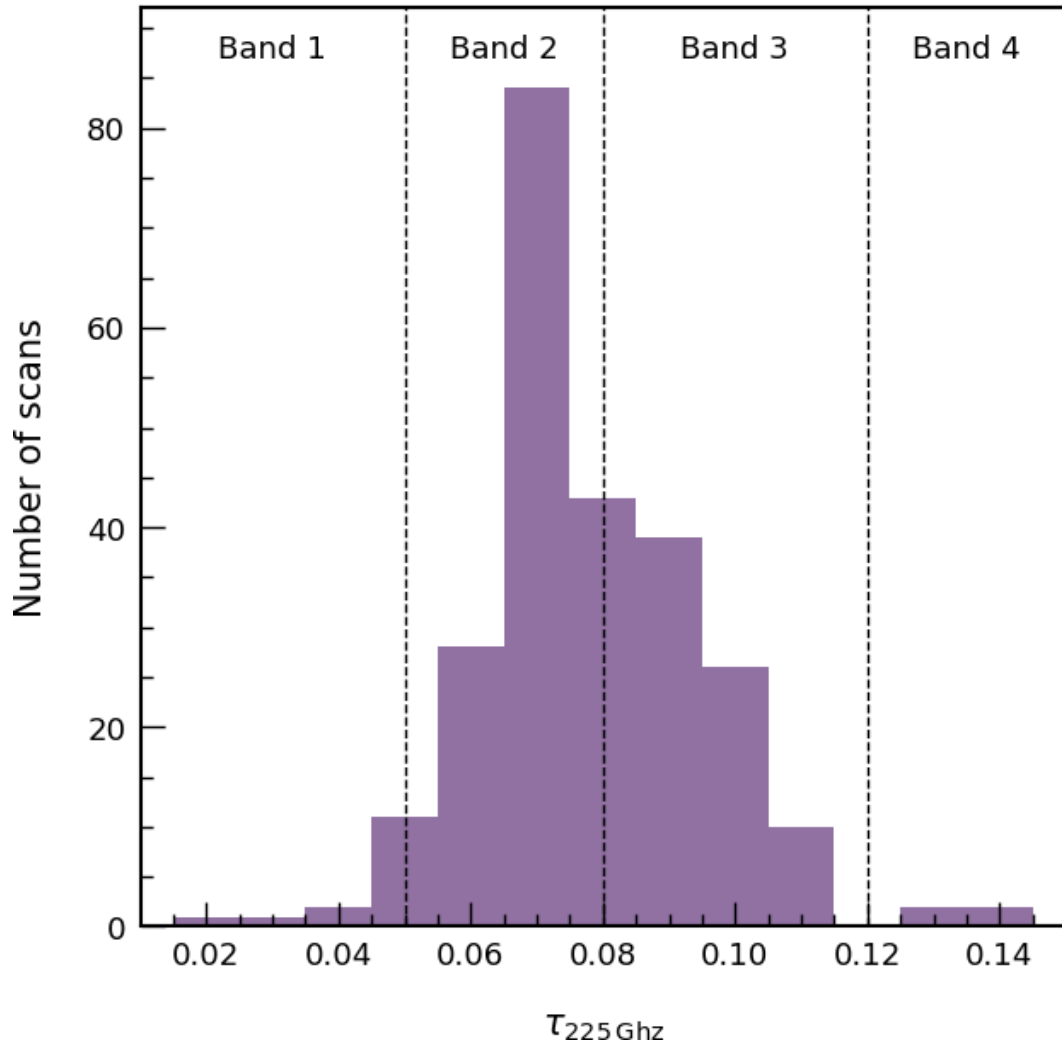


FIGURE 3.2: Zenith opacity at 225 GHz. The opacity is recorded at the beginning and end of each PONG scan. We show the distribution of the average of these measurements (i.e., $\tau_{225} = (\tau_{\text{start}} + \tau_{\text{end}})/2$). For clarity we also show the boundaries of the JCMT weather bands.

a specialised ‘blank-field’ configuration with parameters tuned for data reduction in extragalactic surveys. These parameters were optimised in the SCUBA-2 Cosmology Legacy Survey (S2CLS; Geach et al., 2017). Taking this optimised configuration as the starting point we run several test data reductions using the S2LXS XMM-LSS raw data, varying the DIMM parameters and analysing the output (the reduced data). Our aim is to find the combination of parameters that best reduce residual noise in the S2LXS XMM-LSS map without overly compromising the astronomical signal. For full details of DIMM see Chapin et al. (2013). Here we provide a short description of the main stages of DIMM data reduction (illustrated in the flow chart in Figure 3.3) and describe the specific parameters we use to reduce the S2LXS XMM-LSS data.

The first step in DIMM data reduction is the pre-processing stage in which the time-stream data

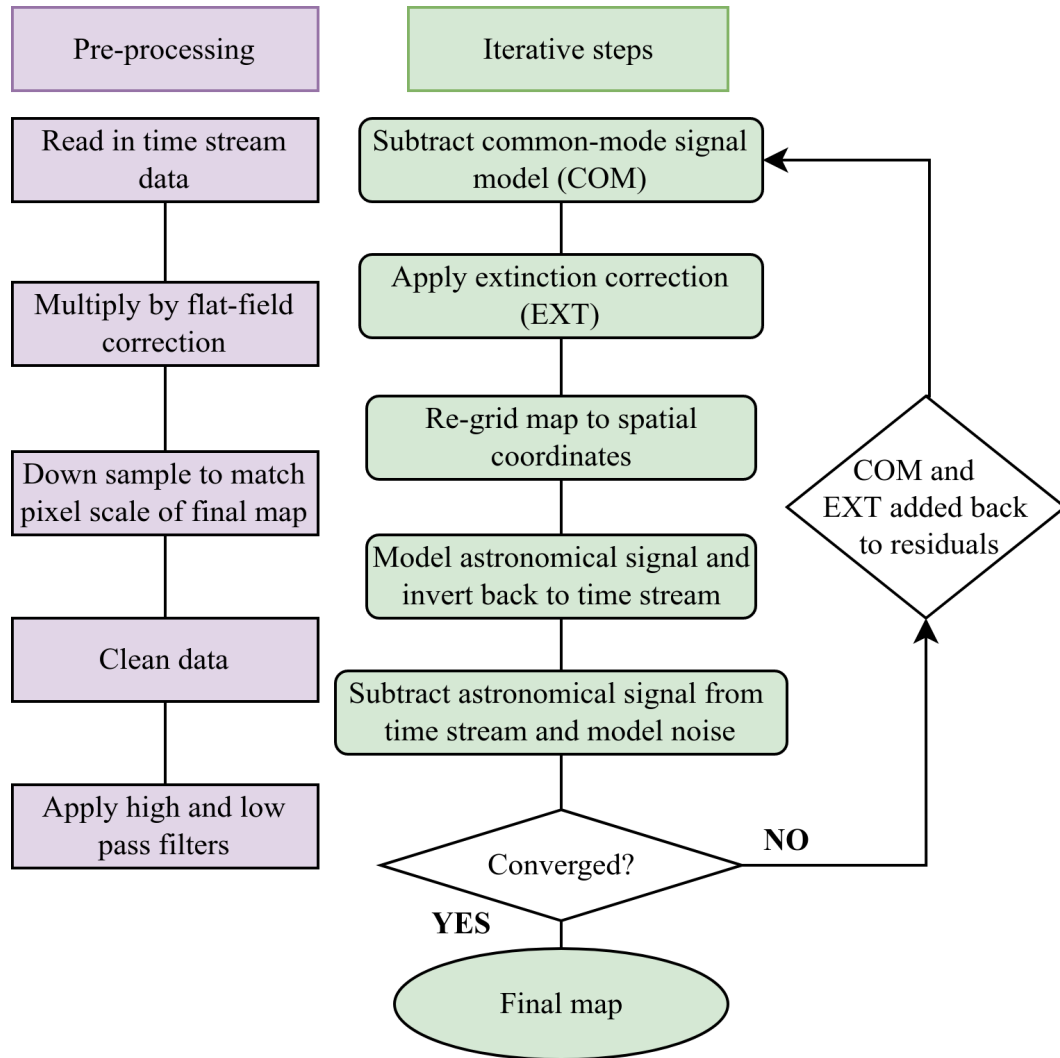


FIGURE 3.3: Flowchart illustrating the main stages of DIMM data reduction

are down-sampled and cleaned. The response of each bolometer to changing sky power is measured at the beginning and end of each observation (flat-field scans). In the pre-processing stage the raw data are first multiplied by a flat-field correction (estimated using the flat-field scans) to calibrate the bolometers. The time-streams are then down-sampled to a rate that matches the pixel scale of the final map (2 arcsec). Next the time-stream data are cleaned for short-duration and high-amplitude spikes. In this step the signal from bright point sources can be mistaken for high-amplitude noise spikes and erroneously excluded. To avoid this we adopt a conservative threshold of 5σ and a box width of 50 time slices. At each time slice the median value of samples within a box centred on the time slice is measured. A time slice is flagged as a spike if the residual between the time slice value and this median value is greater than $5 \times$ the local noise (the standard deviation of values in the neighbouring ‘down-stream’ box). Next any sudden steps in the time series are identified and removed. Gaps are filled using a linear interpolation of

the 50 time slices preceding and the 50 time slices following the excluded data. An order 1 polynomial (i.e., linear) estimate of the base-line is then removed from each bolometer. In the final step of the DIMM pre-processing stage each bolometer time stream is independently filtered. A high pass filter is used to remove frequencies that correspond to spatial scales of $\theta > 150$ arcsec (to suppress large scale structures) and a low pass filter used to exclude data corresponding to angular scales of $\theta < 2$ arcsec (so that the beam is fully sampled).

Next DIMM begins an iterative process. First the common-mode signal (the average signal seen by all bolometers) is independently modelled for each SCUBA-2 sub-array and subtracted from the cleaned time-stream data. A multiplicative extinction correction (derived from atmospheric opacity measurements from the JCMT water vapour monitor) is then applied. In the second and any subsequent iterations the model of the astronomical signal estimated in the previous iteration is added back into the time series data at this stage. The next step is to model the astronomical signal. To do this the time series data are first binned onto a two-dimensional celestial projection. Each pixel in this two-dimensional grid is sampled many times by independent bolometers owing to the PONG scanning pattern and so, assuming that previous steps have removed all other sources of emission, the astronomical signal can be accurately estimated for a given pixel by taking the weighted average of the bolometer values that contribute to that pixel. The astronomical signal model is inverted back to the time stream and subtracted from the data, leaving just residual noise (made up of instrumental noise and atmospheric effects). This step in the iterative process can also be used to perform map-based despiking in which the scatter in the samples of a given map pixel is used to exclude outliers in the time-stream data. Since real astronomical sources have a fixed spatial location, bright point sources are unlikely to be falsely identified as spikes in this approach and so we can use a more stringent threshold here. Time-series residuals that differ by more than 3σ from the mean value in a map pixel are flagged and these are not used in following iterations. Finally a noise model is estimated for each bolometer by measuring the residual. This noise model is only estimated on the first iteration and is used to weight the data during the mapping process in subsequent iterations. This iterative process continues until either 20 iterations have completed or the normalised mean change between consecutive maps is less than 0.05. If further iterations are needed then all models (except the astronomical signal which is added back in later) are added back into the time-stream residuals.

To convert the map from units of pW to Jy beam^{-1} we apply a flux conversion factor (FCF) to the reduced map. We use the recently revised values for the standard FCF from Mairs et al. (2021), and for observations taken before 30 June 2018 we adopt the standard FCF value of

$516 \text{ Jy beam}^{-1} \text{ pW}^{-1}$ and for observations taken after this date we use the standard FCF value of $495 \text{ Jy beam}^{-1} \text{ pW}^{-1}$. We also apply an upwards correction of 10 per cent (estimated in S2CLS, see Geach et al., 2017) to account for the loss of flux density due to the filtering steps of the data reduction. The absolute flux calibration is estimated to be accurate to within 15 per cent (e.g., Geach et al., 2017).

Each of the approximately 40 minute PONG observations (PONG scans) are reduced independently to produce a set of individual maps for each of the 42 PONG regions. We combine all scans for each PONG region using the PICARD package within SMURF and the recipe MO-SAIC_JCMT_IMAGES. This recipe combines the maps using inverse-variance weighting with the variance of the final map calculated from the input variances. This gives us the 42 PONG tiles which will make up the final S2LXS XMM-LSS map.

The PONG mapping strategy provides uniform coverage within the PONG diameter (i.e., within a 1800 arcsec diameter). However, outside the PONG diameter (the over-scan region) each map pixel in the PONG scan is sampled less frequently. As the map pixels are sparsely sampled at the edges of the over-scan region the steps taken in the DIMM reduction to remove high amplitude spikes perform poorly. Consequently, at the edges of this over-scan region we see a multitude of very high (low) value pixels. The paucity of the sampling also results in variance estimates which are not robust. This is problematic as a very high pixel value combined with an inaccurate variance estimate can masquerade as a bright point source in the outskirts of a PONG tile (see Figure 3.4). To mitigate this we apply an exposure time crop to the PONG tiles with the aim of eliminating these (obviously) spurious sources, whilst preserving as much of the data as possible. We iterate through increasingly stringent exposure time cuts until we find the minimum exposure time limit that effectively excludes these high (low) value pixels in the over-scan regions. In Figure 3.4 we highlight the optimum exposure time limit of 1.7s.

We use the software package SWARP (Bertin et al., 2002) to individually resample the PONG tiles (using nearest neighbour interpolation) to match the astrometric projection and pixel grid of the final science map. The resampled PONG tiles are then combined using inverse variance weighting to produce a map of the S2LXS XMM-LSS field (see Figure 3.1 for the layout of the PONG tiles).

To optimise the detection of point sources we apply a matched filter to the final mosaic using the PICARD recipe SCUBA2_MATCHED_FILTER. Matched filtering consists of two stages. First the S2LXS map is smoothed with a Gaussian of full-width-half-maximum (FWHM) 30 arcsec and

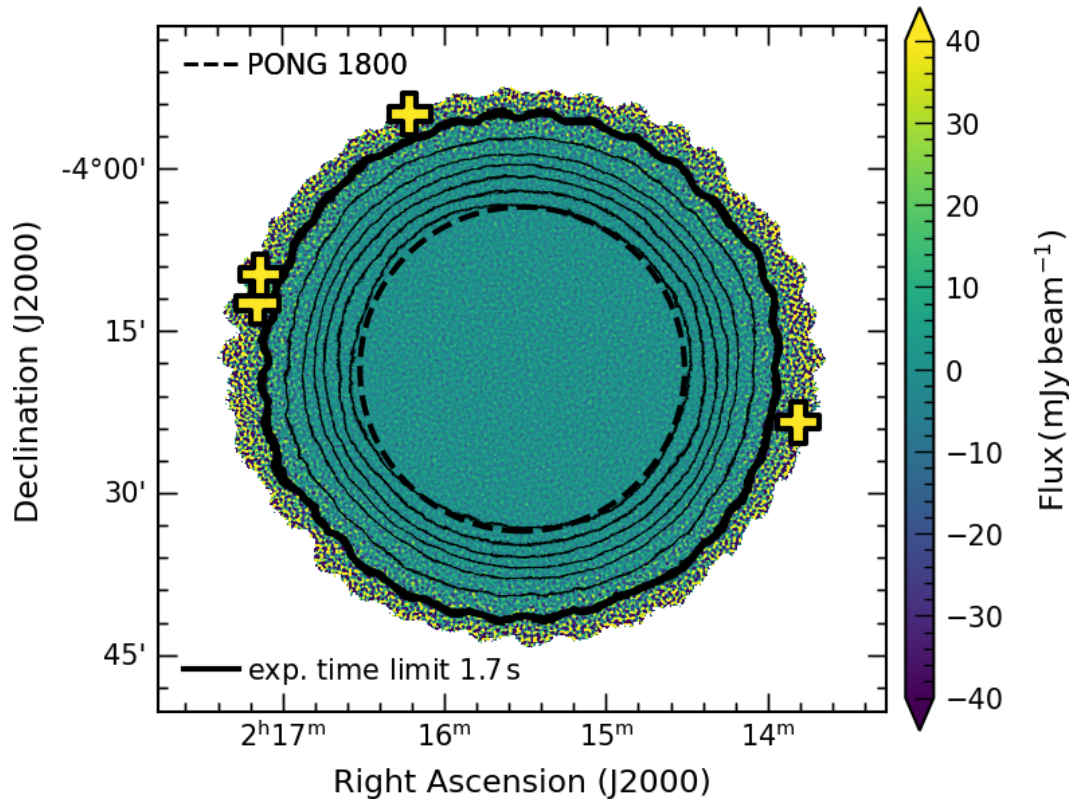


FIGURE 3.4: An example PONG tile (matched-filtered flux density map). The colour bar shows the flux density in mJy and the dashed circle shows the PONG map diameter of 1800 arcsec. Contours plotted in a thin black line are at 5-25 s in steps of 5 s, and illustrate how the exposure time decreases in the over-scan region (outside the diameter of the PONG). The optimum exposure time cut of 1.7 s is shown in the thick black line (see text for details of how this limit is derived and used). We also plot all $> 5\sigma$ detections in this tile (crosses coloured with respect to the colour bar). All these (confirmed as spurious) detections lie in the over-scan region of the PONG tile with flux densities > 200 mJy. These erroneous detections highlight the need to apply a crop to the over-scan region of the PONG tiles.

the result is subtracted from the original map. This step removes large-scale residual noise not eliminated by the filtering applied during DIMM data reduction. The same smoothing operation and subtraction are applied to a Gaussian kernel of FWHM 14 arcsec (equal to the Airy disk radius at $850 \mu\text{m}$), and in the final step of matched filtering the background-subtracted map is convolved with this kernel.

In Figure 3.5 we show a $0.5 \text{ deg} \times 0.5 \text{ deg}$ section of the S2LXS XMM-LSS field matched filtered signal-to-noise ratio map, highlighting the position of 4 of the sources in the S2LXS XMM-LSS $> 5\sigma$ catalogue. We also show the S2LXS XMM-LSS field matched filtered instrumental noise mosaic in Figure 3.6. S2LXS did not re-observe areas covered in S2CLS, hence the absence of data in the region corresponding to the S2CLS UKIDSS-UDS field ($\alpha = 34^\circ.4542$, $\delta = -5^\circ.0986$). We overplot the footprints of CFHT CLAUDS (u^*), SWIRE mid-infrared ($24 \mu\text{m}$) and near-infrared ($4.5 \mu\text{m}$) imaging (Lonsdale et al., 2003), the HSC survey (Deep

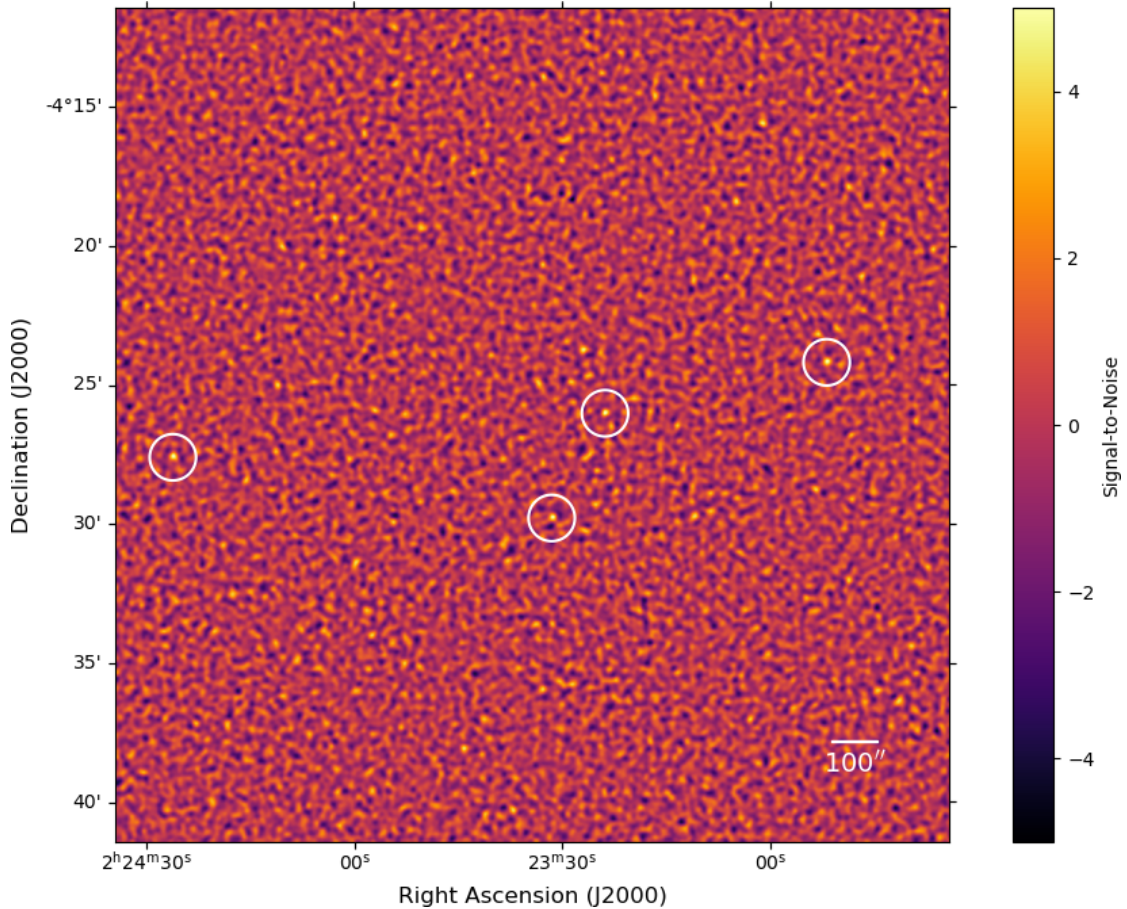


FIGURE 3.5: S2LXS XMM-LSS matched filtered signal-to-noise ratio map. The white circles in this figure indicate the positions of 4 of the $>5\sigma$ sources detected in the S2LXS XMM-LSS field.

tier; Aihara et al., 2018) and the VISTA-VIDEO survey (Jarvis et al., 2013), highlighting the extent of multi-wavelength coverage for the S2LXS XMM-LSS field. We note that the area of the S2LXS XMM-LSS field is fully encompassed by HerMES (Oliver et al., 2012), the HSC-Wide survey (Aihara et al., 2018) and XMM-LSS (Pierre et al., 2004), and so the footprints of these surveys are not plotted. The position of the 40 $>5\sigma$ sources that make up the S2LXS XMM-LSS catalogue are also shown (see section 3.3.2 for details of the catalogue).

3.2.3 Astrometric refinement and registration

During JCMT observations standard calibrators are regularly observed to identify and correct for drifts in the telescope pointing. Typical corrections are of the order of 1-2 arcsec. To refine the astrometry of the S2LXS XMM-LSS map we require archival data from a survey which offers full coverage of the S2LXS XMM-LSS field. The HerMES and HSC-Wide survey both fully encompass the area of the S2LXS XMM-LSS science map. However, HSC-Wide is an optical

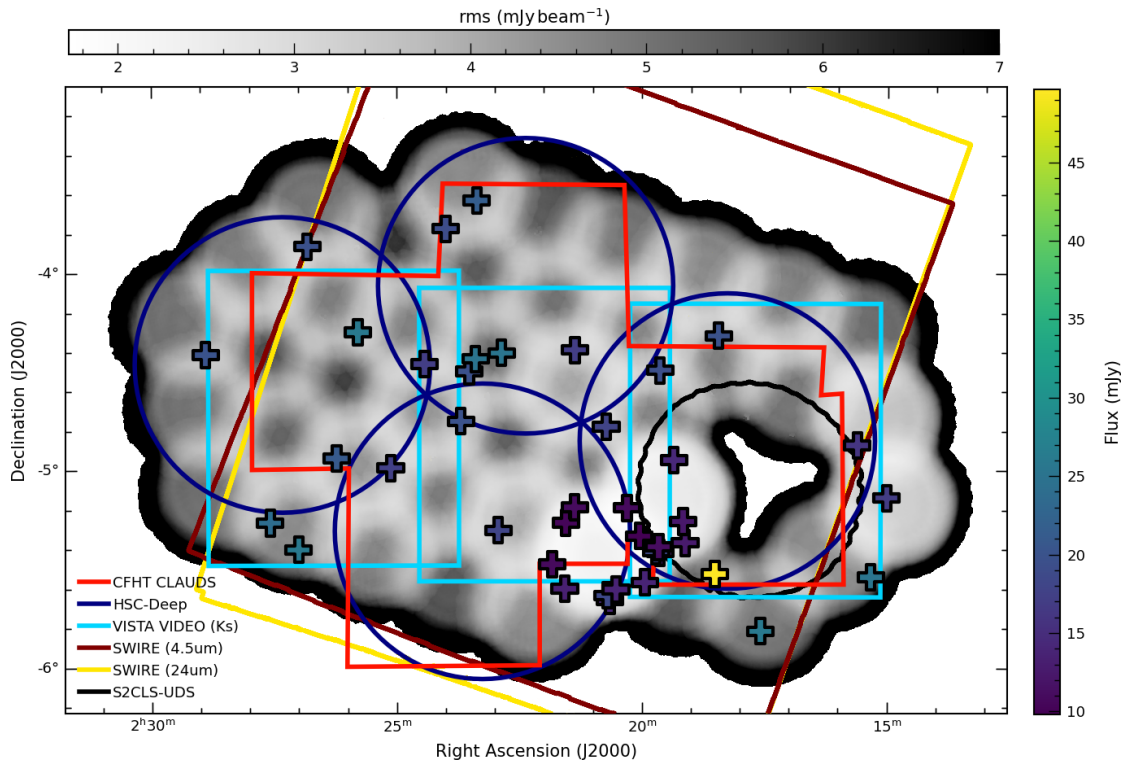


FIGURE 3.6: S2LXS XMM-LSS matched filtered instrumental noise map. The mosaic is made up of 42 hexagonally arranged PONG tiles which are cropped to an exposure time of 1.7 s. The colour map shows the 1σ depth in mJy beam^{-1} (horizontal colour bar). The S2LXS XMM-LSS map median rms is $1\sigma \simeq 4 \text{ mJy beam}^{-1}$. The absence of data corresponds to the previously observed S2CLS UKIDSS-UDS field ($\alpha = 34^\circ.4542$, $\delta = -5^\circ.0986$ – black outline; Geach et al., 2017), which was not observed in S2LXS. We overplot the footprints of CFHT CLAUDS (u^*), the HSC-Deep survey (Aihara et al., 2018), the VISTA-VIDEO survey (Jarvis et al., 2013), and SWIRE $4.5 \mu\text{m}$ and $24 \mu\text{m}$ imaging (Lonsdale et al., 2003) to demonstrate the coverage of the multi-wavelength data. The area of the S2LXS XMM-LSS field is fully encompassed by HerMES (Oliver et al., 2012), the HSC-Wide survey (Aihara et al., 2018) and XMM-LSS (Pierre et al., 2004), so the footprints of those surveys are not shown. The crosses in this figure indicate the positions of the 40 $>5\sigma$ sources detected in the S2LXS XMM-LSS field, coloured with respect to the observed flux (vertical colour bar). We note that whilst some of the S2LXS XMM-LSS sources appear to cluster (potentially tracing large scale structure), the location of these sources is more likely a consequence of the variation in instrumental noise across the map, in part due to the overlap of the PONG tiles, with the majority of sources (67.5 per cent) detected in regions where at least 3 tiles overlap. This is not unexpected given that map is more sensitive ($1\sigma \simeq 3.6 \text{ mJy beam}^{-1}$) in these overlap regions.

survey and so samples a different population of galaxies compared to the population of dusty star-forming galaxies targeted in S2LXS XMM-LSS. In our tests (using the stacking method detailed below) with the HSC-Wide y -band data ($\lambda_{\text{eff}} = 0.9762 \mu\text{m}$) we do not get an adequate signal-to-noise in the final stack for a robust measurement of the offset in α and δ . Therefore, to refine the astrometry of our final science map we make use of the HerMES data, specifically the release 4 (DR4) xID250 catalogue, which comprises about 70,000 sources. Sources in the HerMES catalogue are blind detections at $250 \mu\text{m}$ with fluxes extracted in all *Herschel* Spectral and Photometric Imaging Receiver (SPIRE) bands (Roseboom et al., 2010, 2012; Oliver et al.,

2012). We exclude sources that are detected at the edge of the *Herschel* SPIRE map, sources with $S_{250\mu\text{m}} = 0$ and sources that fall outside the footprint of the S2LXS XMM-LSS mosaic, leaving us with a sample of approximately 30,000 sources. The individual PONG observations were taken over a prolonged period of 3 years and so we would expect the drift in the telescope pointing to be different for individual PONG scans. However, there are not a sufficient number of HerMES sources within the footprint of each PONG tile to robustly measure the astrometry offset for each observation, noting that when we tested this using the individual PONG scans the uncertainties in the offsets derived were bigger than the offset values themselves. Therefore, our aim here is to identify and correct for any large-scale offset in the S2LXS XMM-LSS map. To do this we centre $100\text{ arcsec} \times 100\text{ arcsec}$ cutouts of the S2LXS matched-filtered flux map at the positions of the HerMES sources and calculate the median value at each pixel position to create a median stack. We then use `ASTROPY FIND_PEAKE`s (see section 3.3.2 for details of this function) to measure the centroid position of the peak signal in the stack. The offset in α and δ is taken as the difference between the coordinates of the peak signal and the coordinates of the centre of the stack. We repeat this process several times, each time updating the world coordinate system reference pixel coordinates with the small changes in α and δ . The goal is to find the $\Delta\alpha$ and $\Delta\delta$ that maximise the signal-to-noise of the stack in the central pixel and so this process is repeated until both $\Delta\alpha$ and $\Delta\delta$ converge. We measure offsets of $\Delta\alpha \simeq +0.84'' \pm 0.17''$ and $\Delta\delta \simeq -2.30'' \pm 0.17''$ which are comparable to the expected magnitude of the pointing drift. We apply these small systematic corrections to the S2LXS science maps.

3.3 Analysis

3.3.1 Area Coverage

In Figure 3.6 we show the S2LXS XMM-LSS instrumental noise map which has a median 1σ depth of $1\sigma \simeq 4\text{ mJy beam}^{-1}$. The instrumental noise map is inhomogeneous, primarily due to (i) the variation in the median 1σ depth between the 42 PONG tiles that make up the S2LXS XMM-LSS map (see section 3.2.2 for details of how the map was made), which ranges from 3.2 to 7.7 mJy beam^{-1} and (ii) the arrangement of the PONG tiles in an overlapping hexagonal pattern. The difference in the median 1σ depth of individual PONG tiles is largely driven by the number of PONG scans that are stacked to produce each PONG tile. The majority of the PONG tiles were observed over 5 PONG scans, however, due to the scheduling of observations

6 PONG tiles were observed more than 5 times, and so we have a larger number of PONG scans for these tiles (i.e., 6, 7, 10, 10, 18, 21 scans). The PONG tiles with additional scans are deeper (i.e., with 21 scans we reach a median 1σ depth of $1\sigma = 3.2 \text{ mJy beam}^{-1}$) than the majority of PONG tiles that make up the map. The depth of the individual PONG tiles is also influenced by the weather conditions at the time of the observations and, in the case of one PONG tile (centred on $\alpha = 36.2566^\circ$, $\delta = -3.8432^\circ$) is due to one scan with only half the typical observation time (20 minutes). The instrumental noise across the S2LXS XMM-LSS map also varies depending on the number of overlapping PONG tiles. The median 1σ depth in the regions of the S2LXS XMM-LSS map with no overlapping PONG tiles is $1\sigma \simeq 5.9 \text{ mJy beam}^{-1}$, compared to $1\sigma \simeq 4.3 \text{ mJy beam}^{-1}$ for regions with 2 overlapping tiles and $1\sigma \simeq 3.6 \text{ mJy beam}^{-1}$ for regions with ≥ 3 overlapping tiles. The instrumental noise also increases rapidly (to a maximum noise of $1\sigma_{\text{max}} = 27.0 \text{ mJy beam}^{-1}$) in the outer edges of the S2LXS XMM-LSS mosaic, where the over-scan regions of individual PONG tiles do not overlap with neighbouring tiles. In Figure 3.7 we show the cumulative area of the map as a function of depth highlighting the contribution due to the number of overlapping PONG tiles. The S2LXS XMM-LSS science map has an approximate area coverage of 9 deg^2 .

The confusion limit (σ_c ; Scheuer 1957) is the flux level at which pixel-to-pixel variance (σ^2) ceases to reduce even with increased exposure time, due to the crowding of faint sources within the telescope beam. The confusion limit of an image is typically reached when the surface density of sources exceeds 0.03 per beam (e.g., Condon, 1974; Hogg, 2001). The confusion limit is measured in previous SCUBA-2 surveys and estimated to be $\sigma_c \simeq 1 \text{ mJy beam}^{-1}$ at $850 \mu\text{m}$ (e.g., Geach et al., 2017; Simpson et al., 2019). With a median 1σ depth of $1\sigma \simeq 4 \text{ mJy beam}^{-1}$ the variance in our maps is dominated by instrumental noise (even in deeper overlap areas) and so we do not consider the sub-dominant effect of confusion noise on the S2LXS XMM-LSS survey any further.

3.3.2 Source extraction

The S2LXS XMM-LSS field has extensive multi-wavelength coverage that might ordinarily encourage a prior-based source extraction approach. However, about 20 per cent of SMGs that are detected at $850 \mu\text{m}$ are undetected in sensitive near-infrared imaging at $K \gtrsim 25.7 \text{ mag}_{\text{AB}}$ (e.g., Dudzevičiūtė et al., 2019). To avoid overlooking this otherwise obscure minority of the SMG population we opt for a blind source extraction approach, in keeping with S2CLS (Geach

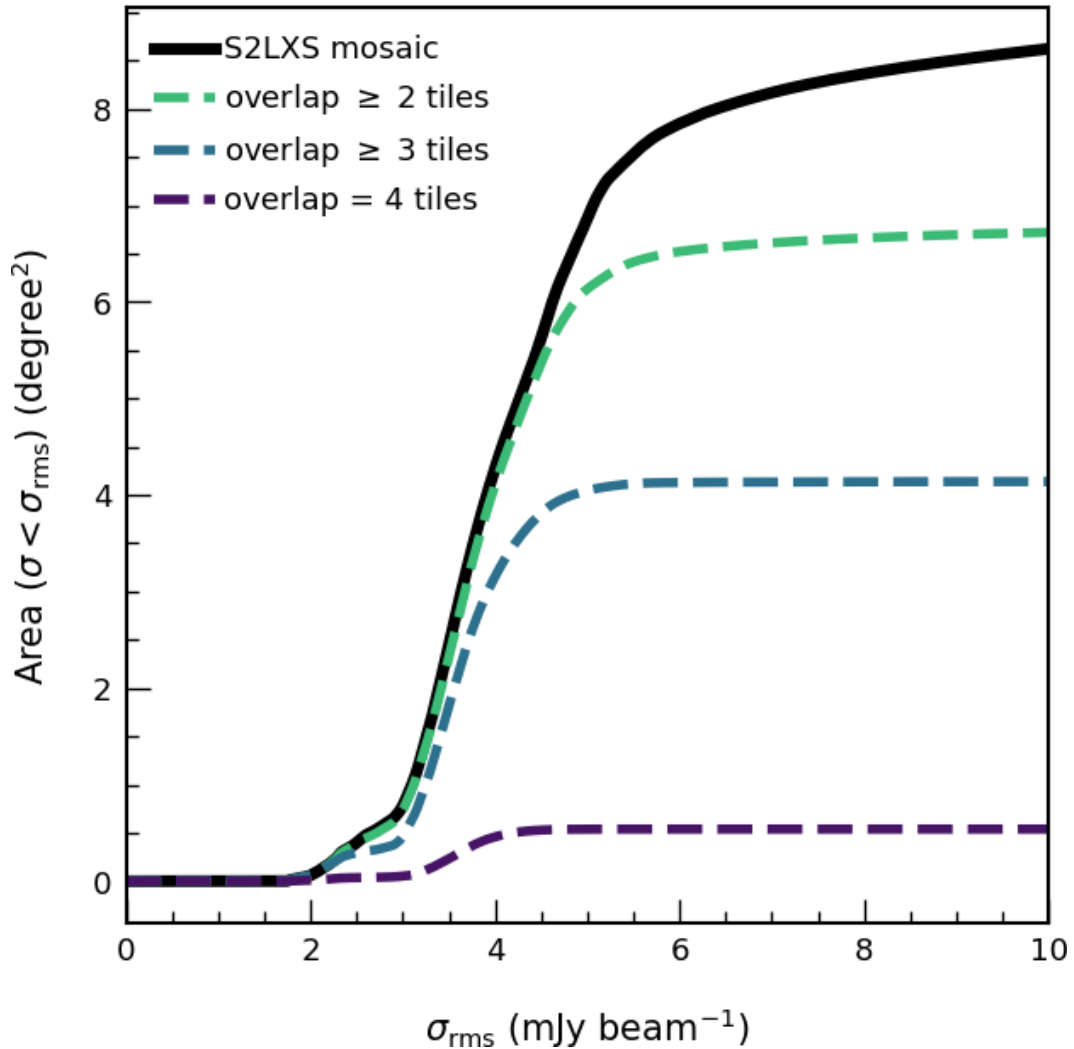


FIGURE 3.7: Cumulative area of the S2LXS XMM-LSS field mosaic as a function of instrumental noise (black solid line). We also show the cumulative area for regions of the map with ≥ 2 , ≥ 3 and 4 overlapping PONG tiles, to highlight how the arrangement of the PONG tiles influences the depth of the S2LXS XMM-LSS map.

et al., 2017) and S2COSMOS (Simpson et al., 2019). We caveat that a limitation of using a blind source extraction approach is that we will not separate out multiple discrete sources blended in the coarse 15 arcsec resolution of the SCUBA-2 beam (e.g., Simpson et al., 2015; Stach et al., 2018).

The S2LXS XMM-LSS maps have already been optimised for the detection of point source emission with the application of a matched-filter (see section 3.2.2 for details). We use PHOTUTILS², an ASTROPY affiliated python package to detect sources in the S2LXS XMM-LSS signal-to-noise ratio matched-filtered map. This package includes a function FIND_PEAKS to locate local maxima in an astronomical image that are above a specified threshold value. We

²In this work we use ASTROPY version 4.2.1 and PHOTUTILS version 1.0.1

set a detection value of 3.5σ . Setting a low detection threshold allows us to explore the statistical properties of sources detected at the lowest significance in the S2LXS map, noting that it is simple to execute further cuts directly on the source catalogue. We also impose a separation limit, requiring sources to be separated by >15 arcsec (equivalent to the FWHM of the SCUBA-2 beam). If more than one source is detected above the detection threshold in a box size of 15 arcsec only the coordinates of the source with the highest signal-to-noise ratio are returned. This prevents double counting of bright sources if more than one pixel associated with a source exceeds the detection threshold. Whilst the bright-end of the $850\mu\text{m}$ number counts is poorly constrained, these sources are expected to be rare (e.g., Béthermin et al., 2017; Cowley et al., 2015), with approximately 10 sources with flux densities above 10 mJy per square degree (e.g., Geach et al., 2017). Assuming sources are randomly distributed the probability of finding two 10 mJy sources separated by <15 arcsec is less than 0.1 per cent, so we are unlikely to overlook any bright sources by imposing this separation limit. However, we note that if bright sources are clustered (as seen at fainter fluxes e.g., Cairns et al., 2022; Greenslade et al., 2020) or are part of merging systems, imposing this separation limit may potentially exclude some sources. To mitigate this we can check for additional bright sources by visually inspecting the S2LXS XMM-LSS science map at the position of the sources in the survey catalogue, searching for elongated sources or clearly separated $>5\sigma$ signal-to-noise ratio peaks within the SCUBA-2 beam (noting that confirmation of multiple galaxies within the SCUBA-2 beam requires follow up by high resolution interferometers). The `FIND_PEAKE`s function allows the user to input a user-defined centroid function to calculate the coordinates of a source to sub-pixel accuracy. We create a function that calculates the centroid by fitting a model of the SCUBA-2 instrumental point spread function³ (Dempsey et al., 2013) to the 2-dimensional distribution of the data. Using `FIND_PEAKE`s and the parameters above we detect 1966 sources at $>3.5\sigma$ and 40 at $>5\sigma$. We inspect the S2LXS XMM-LSS images at the positions of sources in the $>5\sigma$ catalogue to check for multiple bright sources clustered within the SCUBA-2 beam, but find no evidence for this. The formal detection limit set for S2LXS XMM-LSS is 5σ and this is the threshold limit at which we define the survey catalogue. At this threshold we estimate that the false detection rate is 10 per cent (see section 3.3.7 for details). We note that whilst some of the S2LXS XMM-LSS sources appear to cluster (potentially tracing large scale structure), the location of these sources in the S2LXS XMM-LSS map is more likely a consequence of the variation in instrumental

³The SCUBA-2 point spread function (PSF) is well described by the superposition of two Gaussian functions: the primary component has a FWHM 13 arcsec and contains 98 per cent of the total flux; and the secondary component has a FWHM 48 arcsec and contains 2 per cent of the total flux (Dempsey et al., 2013).

noise across the map, in part due to the overlap of the PONG tiles, with the majority of sources (95 per cent) in the survey catalogue detected in deeper regions where ≥ 2 PONG tiles overlap.

3.3.3 Simulated SCUBA-2 maps

To test the reliability of our source extraction we create simulated SCUBA-2 maps projected onto the same pixel grid as the observed S2LXS XMM-LSS mosaic. To create our fake maps we must first produce a realistic instrumental noise map. We do this by creating a jackknife map, which are typically produced by randomly inverting the flux densities for 50 per cent of the observed data before combining. This removes the astronomical signal from the stack and creates a realistic realisation of the instrumental noise. The S2LXS XMM-LSS mosaic is made up of 42 PONG tiles that are produced by stacking the ~ 40 minute PONG observations (i.e., the PONG scans, see section 3.3 for details). For each PONG tile the simplest way to invert 50 per cent of the observed data is to invert the flux densities of half the PONG scans before combining. We do this for all PONG tiles composed of an even number of observations. However, the majority of the PONG tiles are observed over 5 scans and so for these tiles we cannot simply invert the flux densities of half the PONG scans. Therefore, for these PONG tiles, we randomly select one PONG scan and reduce the data (using the `dim` reduction process and parameters described in section 3.3) in two consecutive halves, producing two reduced maps each composed of 50 per cent of the data for the observation. For a PONG tile composed of 5 scans (for example) we can then invert 50 per cent of the observed data by inverting the flux densities of 2 randomly selected scans and of one of these ‘split’ scans (i.e., inverting the observed data for 2.5 scans).

To create a corresponding jackknife tile for each PONG tile we invert the flux densities for 50 per cent of the observed data (as described above) and then combine with the remaining observations using the PICARD recipe `MOSAIC_JCMT_IMAGES`. To produce the jackknife mosaic we then combine the 42 jackknife tiles following the same method we used to create the S2LXS XMM-LSS mosaic (see section 3.2.2). In brief, we first apply a 1.7 s exposure time crop to each of the jackknife tiles and then resample these individually to match the astrometric projection of the final science map. We then use inverse-variance weighting to combine the 42 re-sampled jackknife tiles to produce the jackknife mosaic. In Figure 3.8 we compare the distribution of pixel values for the jackknife signal-to-noise ratio matched-filtered mosaic to the distribution of pixel values in the S2LXS XMM-LSS signal-to-noise ratio map. We also show the S2LXS

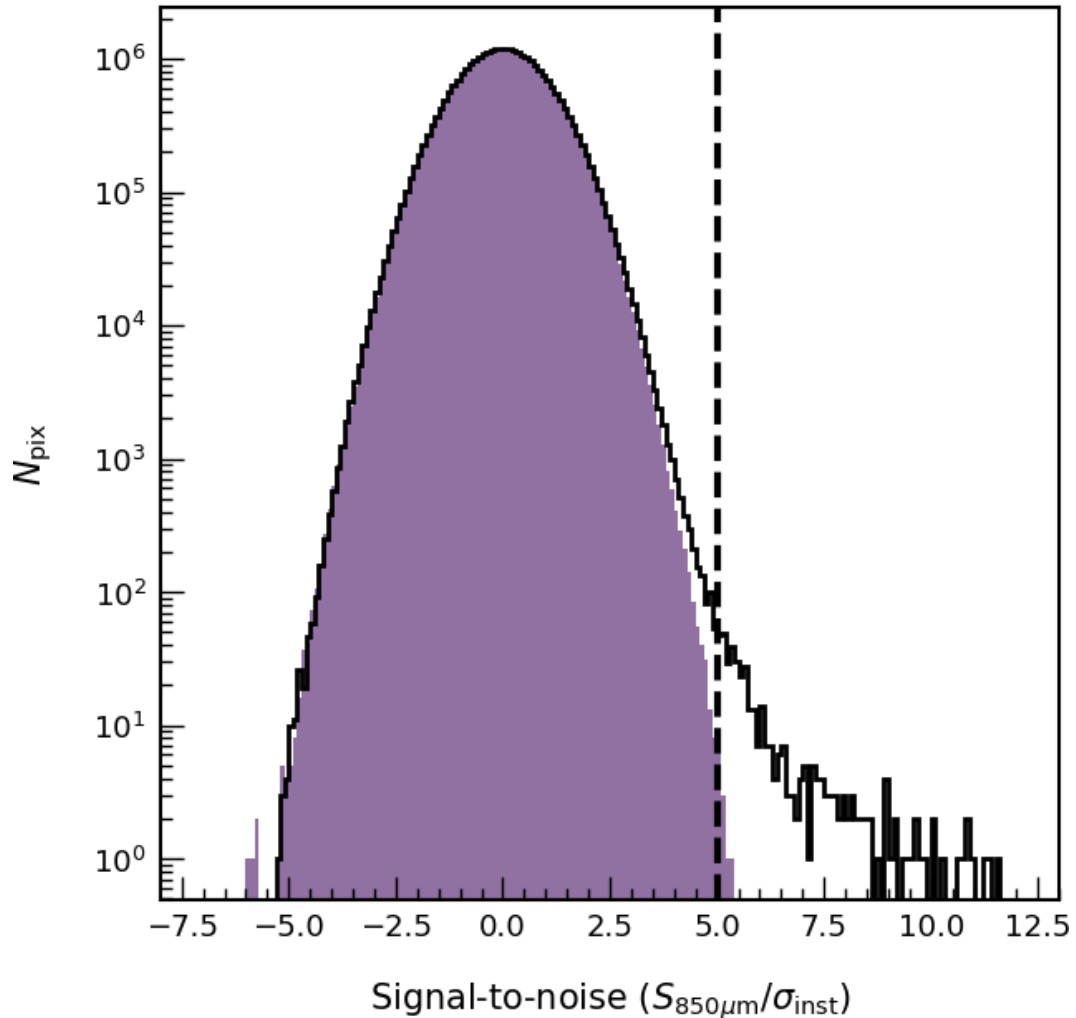


FIGURE 3.8: Distribution of pixel values in the matched-filtered signal-to-noise ratio jackknife map (filled histogram). We also show the distribution of pixel values from the S2LXS XMM-LSS matched-filtered signal-to-noise ratio map (black stepped histogram) and the S2XLS XMM-LSS formal detection threshold of 5σ (black dashed line). This figure illustrates the characteristic tail of astronomical signal at positive fluxes. We also see a small number of pixel values with a signal-to-noise of < -5 in the jackknife map. This is likely caused by isolated pixels with very low flux values in the sparsely sampled over-scan regions of the PONG maps.

XMM-LSS $> 5\sigma$ detection limit. This figure highlights the characteristic tail of astronomical signal, which is pronounced at $> 5\sigma$.

The next step to create our simulated maps is to insert fake sources matching a realistic source count model into the jackknife noise map. The faint end of the $850\mu\text{m}$ number counts is well constrained and so we use the Schechter (1976) fit from Geach et al. (2017) to model the source counts below 15 mJy. However, the bright-end of the $850\mu\text{m}$ number counts is not well constrained, with only 5 extragalactic sources in S2CLS with $S_{850\mu\text{m}} > 15\text{mJy}$. Therefore, to model the source counts above 15 mJy we fit a simple powerlaw to the S2LXS XMM-LSS observed number counts.

We simulate an observed SCUBA-2 source by convolving a point source of a given flux with the SCUBA-2 instrumental PSF (Dempsey et al., 2013), noting we impose a minimum flux limit of 1 mJy (in keeping with Geach et al., 2017). The simulated SCUBA-2 sources are then injected at random positions in the jackknife noise map (we do not apply any conditions on the positioning of sources, these are inserted purely at random) to generate a simulated map. We then use the PICARD recipe SCUBA2_MATCHED_FILTER to apply a matched-filter to the simulated map and ASTROPY FIND_PEAKS to detect sources in the map above the floor detection threshold value ($>3.5\sigma$), mimicking the source extraction method used on the S2LXS XMM-LSS mosaic (see section 3.3.2). A fake source is recovered if it is found above the detection threshold and at a maximum separation of 11 arcsec ($0.75\times$ the FWHM of the SCUBA-2 beam) from the input coordinates. We note that this matching threshold is somewhat arbitrary, but is intentionally generous (and in keeping with the matching threshold used in Geach et al., 2017; Simpson et al., 2019). If there are multiple detections within this radius then the closest match is taken as the recovered source. If a source is recovered then the fake source catalogue will include the recovered flux density, rms and coordinates of the source, as well as the signal-to-noise ratio of the detection. To allow us to fully sample the flux regime we are interested in (i.e., $S_{850\mu\text{m}} > 15\text{mJy}$) we repeat this process 100,000 times, creating 100,000 simulated maps and corresponding fake source catalogues. For the source extraction on our simulated maps we use a floor detection limit of $>3.5\sigma$ to investigate the statistical properties of the simulated sources detected at low significance, and to compare to sources detected at the same threshold in the S2LXS XMM-LSS mosaic. However, for the remainder of this chapter we assume the formal detection limit of S2LXS XMM-LSS which is 5σ .

3.3.4 Flux boosting

The flux density of galaxies detected at a relatively low signal-to-noise ratio is likely to be boosted upwards due to fluctuations in the noise (e.g., Hogg and Turner, 1998). Flux boosting occurs in 2 ways, and is related to the Eddington bias and confusion noise. Due to the steep slope of the number counts faint sources are more numerous than bright sources, and so in a flux-limited survey there will be more faint galaxies detected with fluxes scattered upwards by fluctuations in the noise, than bright galaxies with fluxes scattered downwards (i.e., the Eddington bias). The flux of sources is also boosted due to source blending within the SCUBA-2 beam (i.e., confusion noise). This means that the flux of faint sources that fall below the detection limit, contributes to the observed flux of brighter sources detected above the detection limit.

We can estimate the effect of flux boosting on the S2LXS XMM-LSS survey by comparing the recovered flux density to the intrinsic flux density for each source detected at $>5\sigma$ in the fake source catalogue. In Figure 3.9 we show average flux boosting as a function of observed flux density and local instrumental noise, and as a function of signal-to-noise ratio. As expected the effect of flux boosting is most significant at a relatively low signal-to-noise ratio. At 5σ the observed flux density is approximately 66 per cent higher on average than the intrinsic flux density. We find that the relation between boosting ($\mathcal{B} = S_{\text{obs}}/S_{\text{true}}$) and signal-to-noise ratio is well described by a power law (equation 3.1). In keeping with Geach et al. (2017) we use a power law of the form $y = 1 + ax^k$, where a and k are constants, $y = \mathcal{B}$ and $x = (\text{SNR}/5)$:

$$\mathcal{B} = 1 + 0.66 \left(\frac{\text{SNR}}{5} \right)^{-3.83} \quad (3.1)$$

In Figure 3.9 we compare the average effect of flux boosting in S2LXS XMM-LSS to S2CLS (Geach et al., 2017), and find that the average effect of flux boosting is stronger in S2LXS XMM-LSS. We attribute this difference to the higher instrumental noise of the S2LXS XMM-LSS map.

Due to the statistical nature of flux boosting the intrinsic (true) flux density of a source with an observed flux density S_{obs} is drawn from a distribution $p(S_{\text{true}})$. We can empirically estimate the effect of flux boosting by measuring the histogram of injected flux densities of fake sources in bins of observed flux density and instrumental noise (see Figure 3.10 for example). This empirical approach has been shown to be comparable (e.g., Geach et al., 2017) to traditional Bayesian techniques (e.g., Jauncey, 1968; Coppin et al., 2005). To estimate the deboosted (true) flux density for each source in our $>5\sigma$ catalogue we draw 1000 samples from the $p(S_{\text{true}})$ distribution measured from our simulations for an observed flux density and local instrumental noise corresponding to that of the real source. We take the mean of the samples as the deboosted flux density of the real source and the standard deviation of the sample as the error on the deboosted flux density.

3.3.5 Completeness

We investigate the completeness of the S2LXS XMM-LSS survey by comparing the number of sources injected into the simulated SCUBA-2 maps to the number of sources recovered at $>5\sigma$, evaluated in bins of input flux density and local instrumental noise. In Figure 3.11 we show the

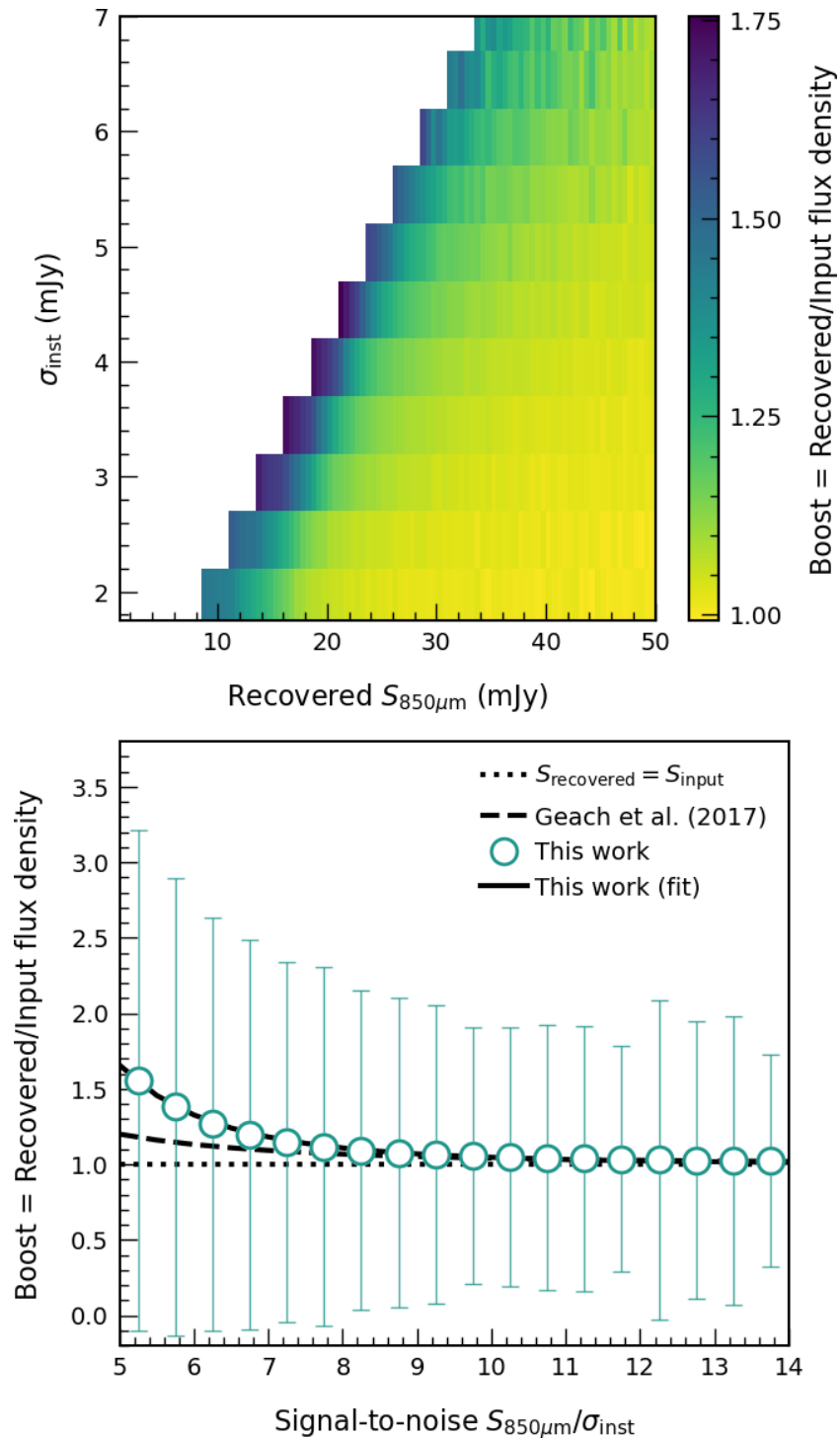


FIGURE 3.9: Flux boosting is measured by comparing the recovered flux density to the injected flux density for each source in the fake source catalogue. The top panel shows average flux boosting as a function of recovered (i.e., observed) flux density and local instrumental noise. In the bottom panel we show average flux boosting (uncertainties shown as $\pm 1\sigma$) as a function of recovered signal-to-noise ratio (teal circles). We also plot the power law relation from S2CLS (Geach et al., 2017, dashed curve) and the power law fit from this work (solid curve, see equation 3.1). The dotted line shows $S_{\text{recovered}} = S_{\text{output}}$. The average effect of flux boosting is stronger in S2LXS XMM-LSS compared to S2CLS, which is likely motivated by the higher instrumental noise of the S2LXS XMM-LSS survey. As expected the effect of flux boosting is most significant for sources detected at relatively low signal-to-noise ratio.

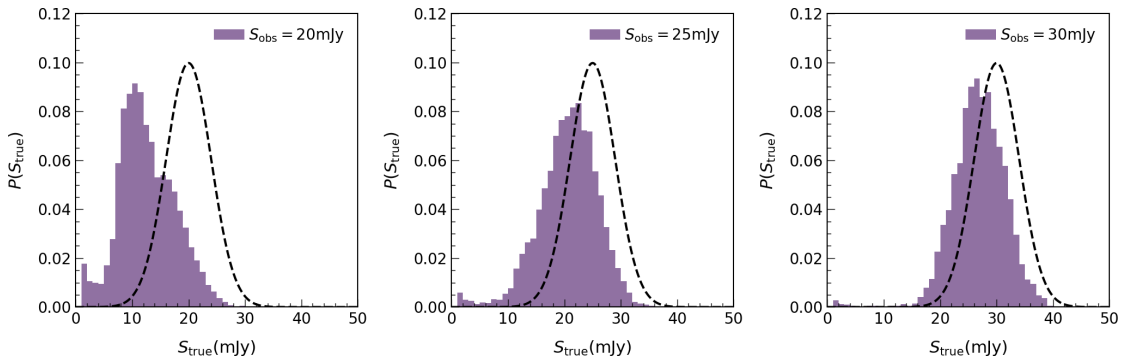


FIGURE 3.10: Distribution of injected (true) flux densities of sources in the fake source catalogue in bins of S_{obs} (shown in legend) and $\sigma_{\text{inst}} = 4 \text{ mJy}$ (approximately the 1σ median map depth). We also show a normal distribution centred on S_{obs} with a standard deviation of 4 mJy (dashed line). As expected for sources that are observationally bright (i.e., observed at higher signal-to-noise ratio with σ_{inst} fixed) the effect of flux boosting is diminished.

injected source counts and the estimated S2LXS XMM-LSS survey completeness as a function of input (true) flux density and local instrumental noise. The survey 50 per cent (90 per cent) completeness at the median map depth ($1\sigma \simeq 4 \text{ mJy beam}^{-1}$) is 19.8 mJy (26.0 mJy). In Figure 3.11 we plot the survey completeness across a range of map depths (2.0 to 6.5 mJy) to demonstrate the variation in survey completeness over the full survey area. Our binned completeness values act as a lookup table and we use 2-dimensional spline interpolation to estimate the completeness rate at the de-boosted flux density and local instrumental noise for each source in the S2LXS XMM-LSS $>5\sigma$ catalogue.

3.3.6 Positional uncertainty

Positional uncertainties are expected to scale with signal-to-noise ratio for a given Gaussian-like beam (Condon, 1997; Ivison et al., 2007). We measure the positional offset ($\Delta\theta$) for each source in our fake catalogue by calculating the difference between the injected and recovered coordinates. In Figure 3.12 we show the average positional offset as a function of signal-to-noise ratio for sources in the fake catalogue recovered at $>5\sigma$. We find that the relation is well described by a simple power law of the form

$$\Delta\theta = 2.17 \text{ arcsec} \times \left(\frac{\text{SNR}}{5} \right)^{-1.19}. \quad (3.2)$$

The average positional offset for sources detected at 5σ in S2LXS XMM-LSS is approximately 2 arcsec . This offset is consistent with theoretical predictions (e.g., equation B8 of Ivison et al., 2007), and the results of some SCUBA-2 wide-field surveys (e.g., Shim et al., 2020; Simpson

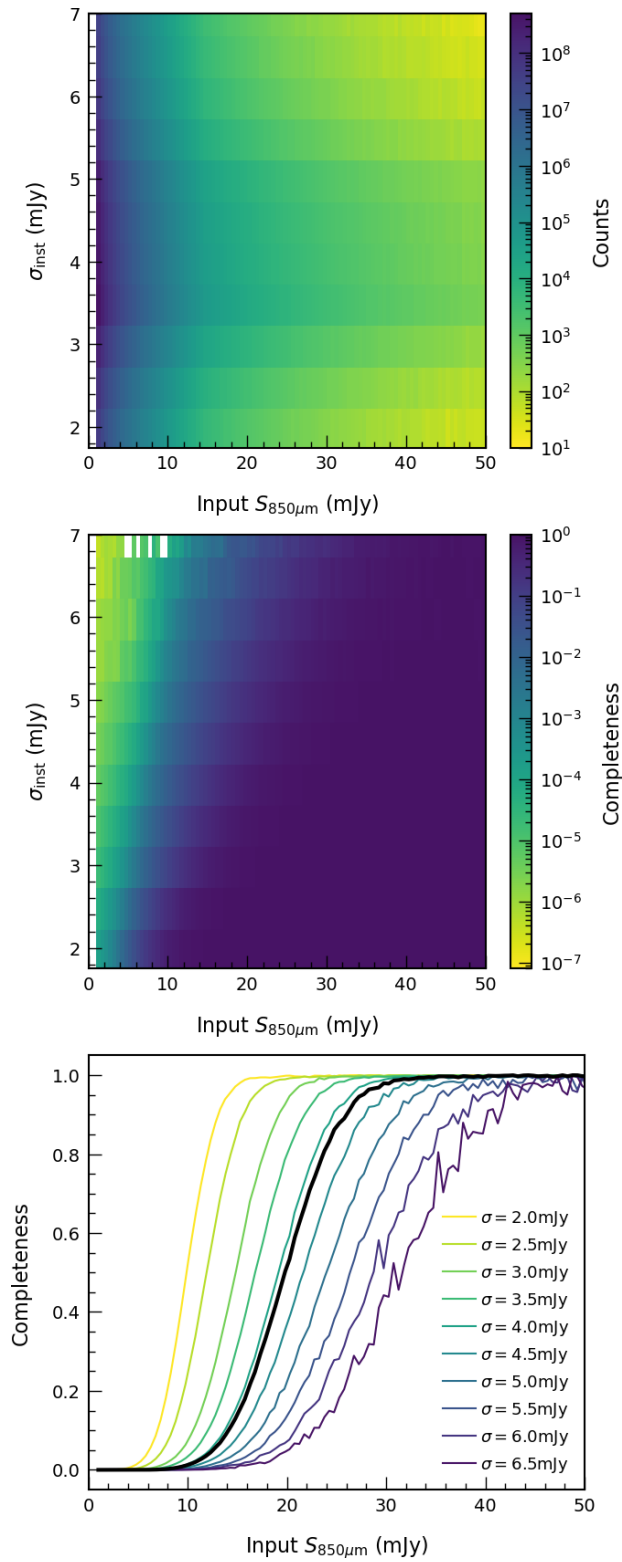


FIGURE 3.11: S2LXS XMM-LSS survey completeness estimated by comparing the number of sources injected into our fake maps to the number recovered at a detection threshold of 5σ . In the top panel we show the injected fake source counts and in the centre panel the completeness ratio, both as a function of input flux density and local instrumental noise. In the bottom panel we plot the survey completeness at the median map depth ($\sigma_{\text{inst}} \simeq 4 \text{ mJy beam}^{-1}$, black solid line) and at a range of map depths (see legend) to show the variation in completeness across the full S2LXS XMM-LSS survey area.

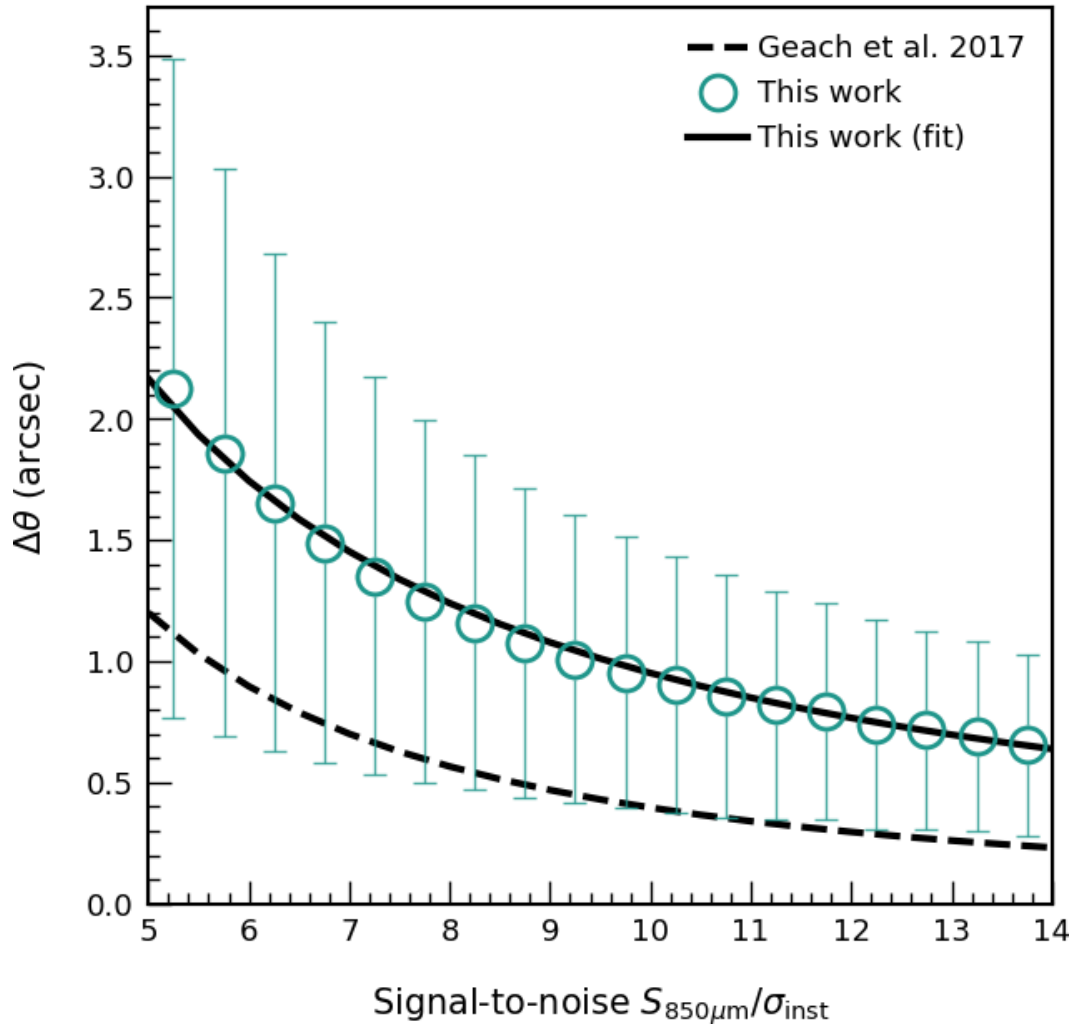


FIGURE 3.12: Positional offset ($\Delta\theta$) estimated by calculating the difference between the injected and recovered coordinates for each source in the fake catalogue. The average positional offset is shown (with $\pm 1\sigma$ uncertainties) as a function of signal-to-noise ratio (teal circles). We plot the power law relation from Geach et al. (2017) (dashed line) and the power law fit from this work (solid line, see equation 3.2). The positional offset is almost double the average positional uncertainty found in S2CLS, possibly due to S2CLS being a much deeper survey ($1\sigma \simeq 1$ mJy).

et al., 2019). However, this is almost double the average positional uncertainty found in S2CLS (see Figure 3.12), possibly due to S2CLS being a much deeper survey ($1\sigma \simeq 1$ mJy). The positional offset (equation 3.2) should be taken into account when identifying multi-wavelength counterparts to sources in the S2LXS XMM-LSS $>5\sigma$ catalogue.

3.3.7 False detection rate

To estimate the false detection rate for the S2LXS XMM-LSS survey we compare the number of sources detected above a given threshold in the S2LXS XMM-LSS match-filtered signal-to-noise ratio map to the number of ‘sources’ (i.e., spurious detections) detected above the same threshold in the matched-filtered jackknife map (see section 3.3.3 for details of how the jackknife map is created). In Figure 3.13 we show the number of sources detected in the S2LXS XMM-LSS science map compared to the number of sources detected in the jackknife map as a function of signal-to-noise ratio. We plot the purity rate (P) calculated as $P = (N_p - N_n)/N_p$, where N_p is the number of real+spurious sources detected above a given threshold in the S2LXS XMM-LSS mosaic and N_n is the number of jackknife ‘source’ detections above the same limit. We find a false detection rate (purity rate) of 10.0 per cent (90.0 per cent) at $>5\sigma$ and 41.23 per cent (58.77 per cent) at $>4.5\sigma$.

As a check we repeat our analysis but instead of using the jackknife map to estimate the number of spurious detections, we use the inverse of the S2LXS XMM-LSS match-filtered signal-to-noise map. The match-filtering process creates negative bowling around bright sources, and so we mask areas of negative bowling in the inverse map to avoid this contaminating our results. The estimated purity rate using this inverse method is comparable to that obtained using the jackknife approach. We show the results from both methods in Figure 3.13. In keeping with recent SCUBA-2 wide-field surveys (e.g., Geach et al., 2017; Simpson et al., 2019) we use the false detection rate estimates from the jackknife approach for the remainder of this work. The S2LXS XMM-LSS survey formal detection threshold of $> 5\sigma$ is chosen to give a 90 per cent purity rate. At this purity rate we expect ~ 4 of the 40 sources in the $>5\sigma$ catalogue to be spurious. We note that the false detection rate in S2XLS XMM-LSS is higher than expected at a detection threshold of 5σ (comparing to previous SCUBA-2 surveys, e.g., Geach et al., 2017; Simpson et al., 2019). This is possibly motivated by the steep slope of the $850\mu\text{m}$ number counts; at $> 15\text{mJy}$ there are very few real sources and so even a small number of spurious detections dramatically increases the false detection rate.

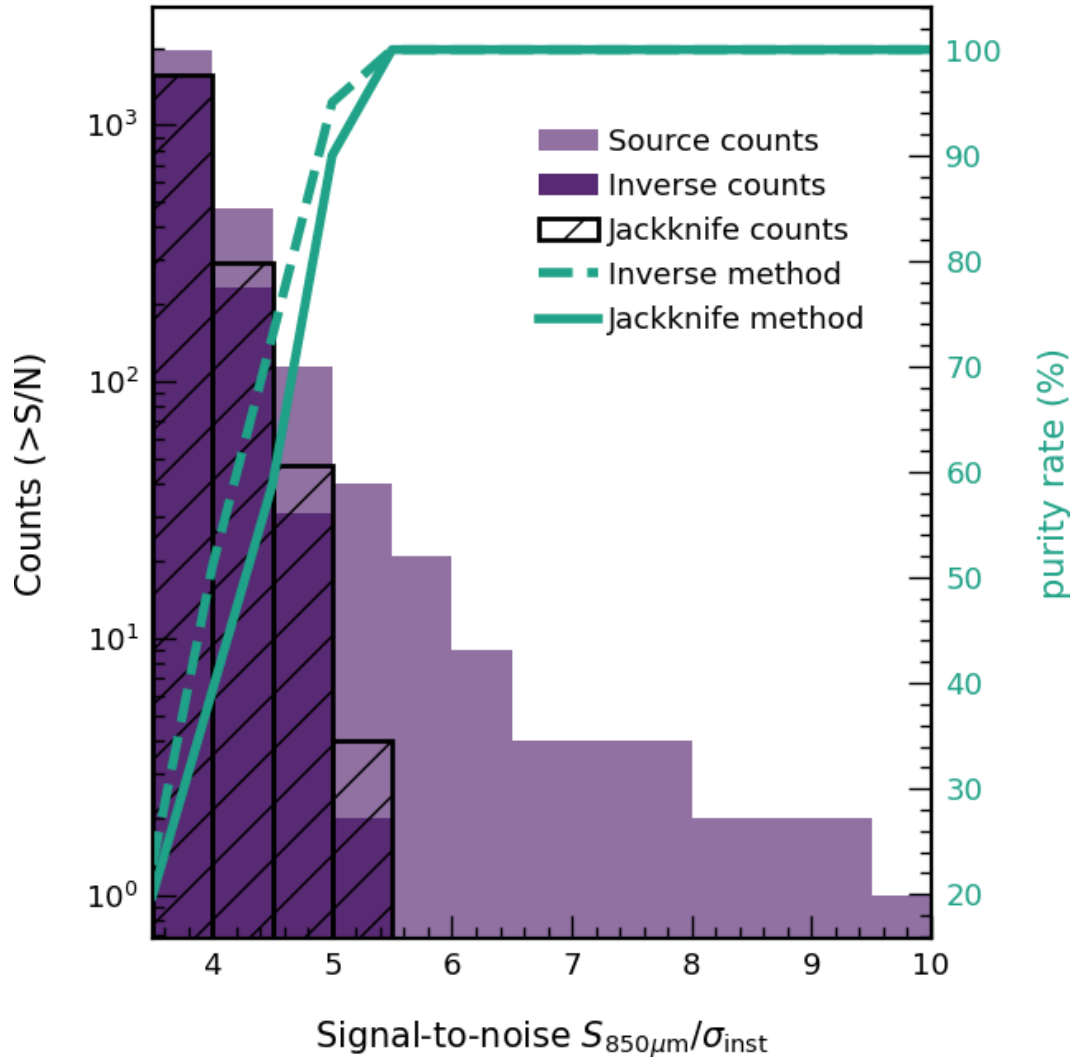


FIGURE 3.13: Purity rate estimated by comparing the number of sources in the S2XLS XMM-LSS science map to the number of spurious detections in the jackknife map (solid line) above a signal-to-noise threshold. The purity rate is also estimated by comparing to the ‘source’ counts in the inverted S2XLS XMM-LSS science map (dashed line). We show the counts obtained from the S2XLS XMM-LSS science map (light purple), the inverse map (dark purple) and the jackknife map (hatched histogram).

3.4 Discussion

3.4.1 Bright-end number counts of the $850\mu m$ population

In Table 3.2 we present the S2LXS XMM-LSS catalogue, which contains 40 sources with intrinsic flux densities in the range 7 to 48 mJy detected at a significance of $>5\sigma$. This catalogue includes observed and deboosted flux densities, completeness levels, positional uncertainties and purity rates.

TABLE 3.2: S2LXS XMM-LSS catalogue. This catalogue contains 40 sources detected at a significance of $>5\sigma$. Coordinates are J2000. The $S_{850\mu\text{m}}^{\text{obs}} \pm \sigma_{\text{inst}}$ column gives the observed flux density and instrumental noise, the S/N column gives the signal-to-noise ratio of the detection, and the $S_{850\mu\text{m}}^{\text{deb}} \pm \sigma_{\text{tot}}$ column gives the estimated deboosted (true) flux density and combined total (instrumental and deboosting) uncertainty. Column C gives the completeness level, $\Delta\theta$ the positional uncertainty (calculated from equation 3.2) and the final column P gives the purity rate.

S2LXS ID	RA	Dec	$S_{850\mu\text{m}}^{\text{obs}} \pm \sigma_{\text{inst}}$ [mJy]	S/N	$S_{850\mu\text{m}}^{\text{deb}} \pm \sigma_{\text{tot}}$ [mJy]	C	$\Delta\theta$ arcsec	P
S2LXSJ021831-053131 ^{ad}	02 18 30.7	-05 31 31.3	49.7 ± 4.3	11.5	48.1 ± 6.3	1.00	0.80	1.00
S2LXSJ022700-052405	02 27 00.3	-05 24 05.2	26.0 ± 4.5	5.7	20.3 ± 7.4	0.37	1.85	1.00
S2LXSJ021735-054854	02 17 34.9	-05 48 53.6	25.9 ± 4.8	5.4	18.5 ± 7.9	0.19	1.99	0.97
S2LXSJ022548-041751 ^b	02 25 47.7	-04 17 51.5	25.9 ± 3.3	7.7	23.1 ± 5.4	0.97	1.29	1.00
S2LXSJ021520-053222	02 15 19.9	-05 32 21.8	25.4 ± 4.6	5.5	18.4 ± 7.7	0.22	1.95	0.99
S2LXSJ022252-042412	02 22 51.8	-04 24 12.0	25.3 ± 4.9	5.2	16.8 ± 8.0	0.10	2.09	0.93
S2LXSJ022324-042602	02 23 23.8	-04 26 01.7	25.1 ± 4.7	5.4	17.9 ± 7.7	0.19	1.99	0.98
S2LXSJ022735-051558	02 27 35.2	-05 15 58.0	23.8 ± 4.1	5.9	18.6 ± 6.5	0.43	1.79	1.00
S2LXSJ022322-033747	02 23 22.1	-03 37 47.5	21.5 ± 4.1	5.3	14.1 ± 6.8	0.10	2.04	0.95
S2LXSJ022614-045616	02 26 13.7	-04 56 15.5	21.0 ± 3.7	5.6	15.2 ± 6.2	0.25	1.89	1.00
S2LXSJ022854-042445	02 28 54.0	-04 24 45.2	20.0 ± 3.6	5.6	13.8 ± 5.9	0.19	1.90	1.00
S2LXSJ021826-041900	02 18 26.4	-04 18 59.1	19.9 ± 3.8	5.2	13.1 ± 6.2	0.10	2.07	0.94

^a Ultra-bright lensed submillimetre galaxy known as ‘Orochi’ (Ikarashi et al., 2011).

^b Lensed hyper-luminous infrared galaxy (HXMM05; Oliver et al., 2012; Bussmann et al., 2015).

^c The SCUBA-2 source has five ALMA counterparts (Oliver et al., 2012; Bussmann et al., 2015).

^d S2CLS UKIDSS-UDS source (Geach et al., 2017) with ALMA follow up observations (Stach et al., 2019).

TABLE 3.2: S2LXS XMM-LSS catalogue (Continued)

S2LXS ID	RA	Dec	$S_{850\mu\text{m}}^{\text{obs}} \pm \sigma_{\text{inst}}$ [mJy]	S/N	$S_{850\mu\text{m}}^{\text{leb}} \pm \sigma_{\text{tot}}$ [mJy]	C	$\Delta\theta$ arcsec	P
S2LXSJ022342-044501	02 23 41.8	-04 45 01.0	19.8 ± 3.5	5.7	14.0 ± 5.9	0.23	1.85	1.00
S2LXSJ022332-042948	02 23 31.5	-04 29 47.6	19.8 ± 3.9	5.1	12.7 ± 6.3	0.08	2.11	0.92
S2LXSJ022649-035146	02 26 49.3	-03 51 46.0	19.7 ± 3.4	5.8	14.1 ± 5.8	0.26	1.83	1.00
S2LXSJ021938-042930	02 19 37.9	-04 29 30.4	19.4 ± 3.1	6.3	14.9 ± 5.3	0.47	1.65	1.00
S2LXSJ022400-034623	02 24 00.3	-03 46 22.6	19.1 ± 3.4	5.6	13.4 ± 5.8	0.21	1.89	1.00
S2LXSJ022042-053806	02 20 42.0	-05 38 05.7	18.6 ± 2.4	7.9	16.4 ± 4.1	0.96	1.26	1.00
S2LXSJ021943-052436 ^c	02 19 42.8	-05 24 35.8	18.4 ± 2.0	9.3	16.7 ± 3.7	0.99	1.03	1.00
S2LXSJ022256-051816	02 22 56.1	-05 18 15.6	17.9 ± 3.6	5.0	11.5 ± 5.5	0.07	2.16	0.90
S2LXSJ022044-044641	02 20 43.8	-04 46 40.8	17.8 ± 3.0	6.0	12.8 ± 5.2	0.28	1.74	1.00
S2LXSJ022508-045914	02 25 07.5	-04 59 13.7	17.4 ± 3.5	5.0	10.6 ± 5.3	0.05	2.16	0.91
S2LXSJ022122-042315	02 21 21.9	-04 23 15.1	17.0 ± 3.2	5.4	11.0 ± 5.1	0.11	1.98	0.98
S2LXSJ022426-042736	02 24 26.2	-04 27 36.1	17.0 ± 3.3	5.2	10.8 ± 5.1	0.08	2.07	0.94
S2LXSJ021501-050817	02 15 00.6	-05 08 16.6	16.8 ± 3.2	5.3	10.6 ± 5.1	0.08	2.04	0.95
S2LXSJ021536-045218	02 15 36.4	-04 52 17.9	15.9 ± 3.1	5.2	10.0 ± 4.8	0.07	2.08	0.94

^a Ultra-bright lensed submillimetre galaxy known as ‘Orochi’ (Ikarashi et al., 2011).

^b Lensed hyper-luminous infrared galaxy (HXMM05; Oliver et al., 2012; Bussmann et al., 2015).

^c The SCUBA-2 source has five ALMA counterparts (Oliver et al., 2012; Bussmann et al., 2015).

^d S2CLS UKIDSS-UDS source (Geach et al., 2017) with ALMA follow up observations (Stach et al., 2019).

TABLE 3.2: S2LXS XMM-LSS catalogue (Continued)

S2LXS ID	RA	Dec	$S_{850\mu\text{m}}^{\text{obs}} \pm \sigma_{\text{inst}}$ [mJy]	S/N	$S_{850\mu\text{m}}^{\text{leb}} \pm \sigma_{\text{tot}}$ [mJy]	C	$\Delta\theta$ arcsec	P
S2LXSJ021921-045651 ^d	02 19 20.9	-04 56 51.1	14.2 ± 2.3	6.1	10.3 ± 3.9	0.36	1.73	1.00
S2LXSJ022039-053937	02 20 39.3	-05 39 37.3	14.2 ± 2.6	5.5	9.5 ± 4.1	0.16	1.94	1.00
S2LXSJ021957-053406	02 19 56.5	-05 34 06.4	13.7 ± 2.5	5.6	9.4 ± 4.0	0.19	1.91	1.00
S2LXSJ022032-053615	02 20 31.7	-05 36 15.3	13.6 ± 2.3	5.8	9.6 ± 3.7	0.28	1.80	1.00
S2LXSJ021938-052502	02 19 37.9	-05 25 02.1	13.4 ± 2.1	6.5	9.9 ± 3.5	0.46	1.60	1.00
S2LXSJ022134-053558	02 21 34.5	-05 35 58.2	13.3 ± 2.3	5.7	9.3 ± 3.7	0.26	1.84	1.00
S2LXSJ021907-052202 ^d	02 19 07.1	-05 22 01.6	12.7 ± 2.5	5.1	8.5 ± 3.9	0.10	2.14	0.91
S2LXSJ021910-051532 ^d	02 19 09.8	-05 15 32.0	12.4 ± 2.4	5.1	8.4 ± 3.7	0.11	2.12	0.92
S2LXSJ021939-052315 ^d	02 19 39.3	-05 23 15.0	11.1 ± 2.0	5.6	7.5 ± 3.1	0.15	1.89	1.00
S2LXSJ022122-051113	02 21 22.4	-05 11 13.0	11.0 ± 2.2	5.1	7.6 ± 3.3	0.12	2.14	0.91
S2LXSJ022018-051124	02 20 18.4	-05 11 23.9	10.9 ± 1.8	6.1	7.7 ± 3.0	0.18	1.72	1.00
S2LXSJ022150-052835	02 21 49.8	-05 28 34.6	10.8 ± 2.1	5.3	7.4 ± 3.1	0.13	2.03	0.96
S2LXSJ022133-051558	02 21 33.2	-05 15 57.5	10.4 ± 2.0	5.2	7.2 ± 3.1	0.12	2.09	0.93
S2LXSJ022003-052000	02 20 03.1	-05 19 59.5	9.8 ± 1.8	5.6	6.8 ± 2.9	0.09	1.91	1.00

^a Ultra-bright lensed submillimetre galaxy known as ‘Orochi’ (Ikarashi et al., 2011).

^b Lensed hyper-luminous infrared galaxy (HXMM05; Oliver et al., 2012; Bussmann et al., 2015).

^c The SCUBA-2 source has five ALMA counterparts (Oliver et al., 2012; Bussmann et al., 2015).

^d S2CLS UKIDSS-UDS source (Geach et al., 2017) with ALMA follow up observations (Stach et al., 2019).

Number counts describe the surface density of sources per observed flux density interval (dN/dS), providing a simple measure of source abundance and a valuable tool to compare with model predictions. We estimate the $850\mu\text{m}$ number counts for S2LXS XMM-LSS from the survey catalogue, correcting for the effects of flux boosting, incompleteness and the probability that an individual source is a false detection. We provide a brief description of this process here. For each of the 40 sources in the $>5\sigma$ catalogue (Table 3.2) we first estimate the deboosted (true) flux density by drawing a random sample from a $p(S_{\text{true}})$ distribution (estimated from our simulated maps, see Section 3.3.4 for details) consistent with the observed flux density and local instrumental noise of the source. We then apply a completeness correction, retrieving the completeness rate (which is estimated in bins of deboosted flux density and local instrumental noise) via 2-dimensional spline interpolation from the look up table generated in section 3.3.5. Next we correct for the probability that a source is spurious based on the signal-to-noise ratio of the source detection (see Section 3.3.7). Once we have applied these corrections we evaluate the corrected counts for the S2LXS XMM-LSS catalogue in flux intervals of $\Delta\log_{10}(S) = 0.1$, and then divide by the area of the S2LXS XMM-LSS science map⁴ to measure the number counts (dN/dS) per flux interval per square degree. Since the observed flux density of a source maps onto a range of intrinsic flux densities, we evaluate dN/dS 1000 times (following the process above), each time randomly drawing the deboosted flux density for a source from the full intrinsic flux distribution ($p(S_{\text{true}})$). We take the final number counts as the mean of dN/dS across the 1000 realisations and the standard deviation of dN/dS in each flux bin as an additional uncertainty (to the Poisson error; Gehrels, 1986). We note that the corrections for flux boosting and completeness are estimated in bins of flux density and instrumental noise to account for the variation in the instrumental noise in the S2LXS XMM-LSS mosaic.

The purpose of the various corrections we make is to recover the ‘true’ underlying source distribution. However, the simulations we use to derive the corrections are imperfect; i.e., the source count model we use at $S_{850\mu\text{m}} > 15\text{ mJy}$ is based on the observed source counts of the S2LXS XMM-LSS survey. Therefore, it is important to test if any systematic biases remain. We also note that owing to the variation in instrumental noise across the S2LXS XMM-LSS mosaic we detect 95% of sources in deeper regions of the map where at least 2 PONG tiles overlap, and so it is also crucial to test whether the location of sources detected in our map will influence our results.

⁴To calculate the number counts per square degree we divide by the full area of the S2LXS XMM-LSS mosaic, as given the statistical nature of flux boosting a source in even the lowest flux bin could be found at any position in the S2LXS XMM-LSS mosaic.

To do this we inject a realistic source count model into our jackknife map (see section 3.3.3 for details of how the jackknife map is created). The faint-end of the number counts is well constrained and so we use the Schechter (1976) fit from Geach et al. (2017) to model the source counts below 15 mJy. To produce a realistic number counts model above 15 mJy (noting that the bright-end of the $850\ \mu\text{m}$ number counts is not well constrained in previous work) we fit a simple power law of the form $y = ax^k$ to the S2LXS XMM-LSS corrected number counts (see equation 3.3). We make an arbitrary distinction between the ‘faint’ and ‘bright’ source count models at 15 mJy as this is consistent with the S2CLS results, which show an upturn in the $850\ \mu\text{m}$ number counts above this flux density (Geach et al., 2017). We recover sources in an identical manner to the real data, adopting the formal detection threshold of the S2LXS XMM-LSS survey ($>5\sigma$). We then apply the various corrections (Sections 3.3.4, 3.3.5 and 3.3.7) to estimate the number counts. By comparing the recovered counts (before and after corrections) to the exact model counts injected into the maps we can test the effectiveness of our corrections. To check that our number counts corrections are not overly biased by the input source count model, we repeat the process above for two more extreme source count models (at the bright-end) by varying the slope k of the power law fit (in equation 3.3), using a model with a steeper slope $k = -6.60$ and a model with a shallower slope $k = -4.60$. We produce 100 simulated maps for each source count model, and take an average of the counts before and after the corrections.

In Figure 3.14 we show the average $((dN/dS)_{\text{rec}} - (dN/dS)_{\text{true}})/(dN/dS)_{\text{true}}$ before and after corrections have been applied for all three source count models. In the absence of corrections the number counts are under-estimated by up to 99 per cent in the faintest flux bins ($S_{850\ \mu\text{m}} \leq 18\ \text{mJy}$), largely influenced by the incompleteness of the S2LXS XMM-LSS survey at these flux densities. For brighter flux bins we generally see an over-estimation of the number counts due to flux boosting. Once we apply corrections the right-hand panel of Figure 3.14 shows that we can reliably recover the true source counts for all three source count models, noting that for the brightest flux bins $S_{850\ \mu\text{m}} > 30\ \text{mJy}$ the corrections appear less effective, likely due to low number statistics (evidenced by the large Poisson errors).

The S2LXS XMM-LSS $850\ \mu\text{m}$ differential and cumulative number counts are presented in Table 3.3 and Figure 3.15. We show our results for intrinsic flux densities $>7\ \text{mJy}$, with the minimum flux consistent with the deboosted flux density of the faintest source in the S2LXS XMM-LSS catalogue. Since the bright-end ($>15\ \text{mJy}$) of the $850\ \mu\text{m}$ differential number counts are no longer well represented by a Schechter (1976) function we fit the S2LXS XMM-LSS

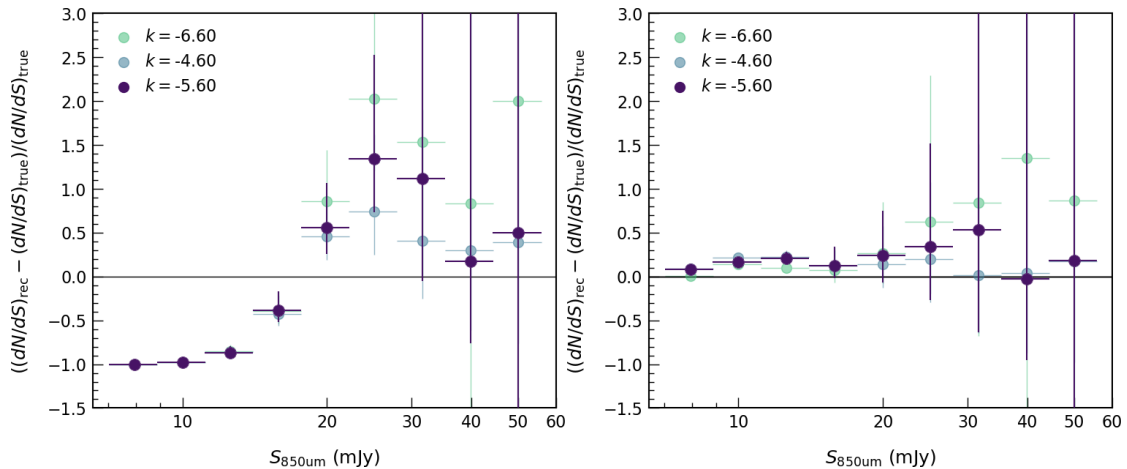


FIGURE 3.14: Comparison of recovered number counts to the ‘true’ number counts in simulated maps. We inject a realistic source count model into a jackknife realisation of the S2LXS XMM-LSS mosaic and then recover sources detected at $> 5\sigma$ (the formal detection threshold of S2LXS XMM-LSS). To check that our number counts corrections are not overly biased by the input source count model we repeat this for two more extreme models by varying the slope k of the power law that we use to model the bright-end source count. In the left panel the recovered counts are not corrected for the effects of flux boosting, incompleteness or the probability that a source is a false detection. We show that in the absence of corrections the number counts are under-estimated by up to 99 per cent in the faintest flux density bins ($S_{850\mu\text{m}} \leq 18\text{mJy}$) in which incompleteness dominates. At brighter flux densities the number counts are generally over-estimated due to flux boosting. In the right panel we show these counts with the various corrections applied, illustrating that the ‘true’ number counts can be robustly recovered. We note that in the brightest flux density bins ($S_{850\mu\text{m}} > 30\text{mJy}$) the corrections are less effective, likely due to the low number statistics in these bins (evidenced by the large Poisson errors).

The error bars in both panels show Poisson uncertainties (Gehrels, 1986) only.

850 μm differential number counts (see Table 3.3 for values) with a power law (Figure 3.15, solid black line):

$$\frac{dN}{dS} = (2.8 \pm 0.3) \times 10^6 \times \left(\frac{S_{850\mu\text{m}}}{\text{mJy}} \right)^{-5.6 \pm 0.5}. \quad (3.3)$$

In Figure 3.15 we also plot the observational constraints from S2CLS (Geach et al., 2017), S2COSMOS (Simpson et al., 2019) and the other main 850 μm wide-area surveys (e.g., Casey et al., 2013; Chen et al., 2013; Coppin et al., 2006; Shim et al., 2020; Weiß et al., 2009) for comparison. The results from S2XLS XMM-LSS are in good agreement with these previous surveys for the flux range probed. We note that since the S2LXS XMM-LSS survey has a contiguous survey area of 9deg^2 cosmic variance will have a smaller affect on our number count estimates compared to previous work, with Simpson et al. (2019) finding no significant variation in the 850 μm number counts on scales of $0.5\text{--}3\text{deg}^2$.

Owing to a slight overlap in the S2LXS XMM-LSS and S2CLS UKIDSS-UDS maps these surveys have 5 sources in common. One of these sources is an ultra-bright lensed galaxy (‘Orochi’; Ikarashi et al., 2011); with a flux density of $S_{850\mu\text{m}} \simeq 50\text{mJy}$ this is the brightest extra-galactic source detected in either survey. Geach et al. (2017) find an excess in the S2CLS differential number counts (i.e., above the Schechter (1976) function fit) at $S_{850\mu\text{m}} > 15\text{mJy}$ (see Figure 3.15). We find a similar upturn in the S2LXS XMM-LSS differential number counts, but with a survey area of 9deg^2 we detect double the number of $S_{850\mu\text{m}} > 15\text{mJy}$ extragalactic sources (with 11 sources detected at $>5\sigma$), and so we are able to reduce the Poisson errors on these measurements. The S2LXS XMM-LSS catalogue only includes one source with an observed flux density $S_{850\mu\text{m}} > 30\text{mJy}$, and so our survey is hampered by low number statistics in this flux regime. This, coupled with our correction for the effects of flux boosting⁵, means we see large Poisson uncertainties on our number counts estimates at flux densities above 30mJy. At flux densities $S_{850\mu\text{m}} > 30\text{mJy}$ our number counts show a more conservative excess when compared with S2CLS (Geach et al., 2017). With only one (and the same) $S_{850\mu\text{m}} > 30\text{mJy}$ source detected in both the S2LXS XMM-LSS field and S2CLS, the higher excess seen in S2CLS is likely due to the smaller survey area and the effect of cosmic variance.

An excess at the bright-end of the number counts is also observed in studies at shorter (e.g., *Herschel* 500 μm ; Negrello et al., 2010; Wardlow et al., 2013) and longer (e.g., South Pole Telescope 1.4mm; Vieira et al., 2010; Mocanu et al., 2013) wavelengths, and is attributed to the presence of local objects and high-redshift gravitationally lensed sources (e.g., Negrello et al., 2010; Vieira et al., 2010). S2CLS provides tentative evidence that the over-abundance of sources at the bright-end of the $S_{850\mu\text{m}}$ number counts is similarly influenced (Geach et al., 2017); of the three sources detected above 20mJy in S2CLS the brightest ($S_{850\mu\text{m}} \simeq 200\text{mJy}$) is a well-known Galactic object in the *Akari*-North Ecliptic Pole (the Cat’s Eye Nebula) and another is a known ultra-bright lensed submillimetre galaxy (‘Orochi’ Ikarashi et al., 2011) which lies at $z_{\text{phot}} \simeq 3.5$, (Dudzevičiūtė et al., 2019). The S2XLS XMM-LSS $>5\sigma$ catalogue includes at least two gravitationally lensed sources; ‘Orochi’ (Ikarashi et al., 2011) and a high-redshift ($z_{\text{spec}} \sim 3$) hyperluminous infrared galaxy from HerMES (Oliver et al., 2012; Busmann et al., 2015; Leung et al., 2019). We visually inspect the available multi-wavelength imaging (see Table 3.1) centred on the

⁵We evaluate dN/dS 1000 times each time randomly drawing the deboosted flux density for a source from a $p(S_{\text{true}})$ distribution (estimated from our simulated maps, see Section 3.3.4 for details) consistent with the observed flux density and local instrumental noise of the source. As we are sampling the full intrinsic flux distribution for a source, over the course of 1000 iterations, the estimated deboosted flux densities may map to more than one flux density bin. This is the reason we recover a number counts estimate for intrinsic flux densities $30\text{mJy} < S_{850\mu\text{m}} < 48\text{mJy}$ despite no sources with observed flux densities in this range.

position of each S2LXS XMM-LSS source and query the NASA/IPAC Extragalactic Database (NED) for nearby $z < 0.1$ sources, allowing us to confirm that there are no Galactic objects in the S2LXS XMM-LSS catalogue. We also search the multi-wavelength imaging and NED around the position of each S2LXS XMM-LSS source to identify bright, massive foreground galaxies, which are indicative of strong lensing. We find that for 16 (40 per cent) sources in the S2LXS XMM-LSS catalogue there is a bright, massive foreground galaxy within the SCUBA-2 beam. Whilst it is reasonable to expect (based on previous work) that the over-abundance of sources observed at high flux densities in the S2LXS XMM-LSS survey is, at least in part, motivated by the presence high-redshift lensed galaxies, we cannot rule out a contribution from intrinsically bright sources (i.e., similar to GN20 a $S_{850\mu\text{m}} > 20\text{mJy}$ galaxy detected in the SCUBA survey of the GOODS-North field; Pope et al., 2005; Daddi et al., 2009) or proto-cluster core type objects such as the Distant Red Core (DRC; Ivison et al., 2016; Oteo et al., 2018). It is also well known that a fraction of single-dish $850\mu\text{m}$ selected sources are the product of multiple fainter submillimetre galaxies that are blended in the coarse 15 arcsec resolution of the SCUBA-2 beam (e.g., Simpson et al., 2015; Stach et al., 2018). The multiplicity fraction increases with the brightness of the single-dish source, with an estimated multiplicity fraction of 44 per cent for single-dish $850\mu\text{m}$ selected sources with flux densities $S_{850\mu\text{m}} > 9\text{mJy}$ (e.g., Stach et al., 2018). Surveys following up observations of single-dish selected $S_{850\mu\text{m}}$ sources with sub-arcsecond resolution interferometers find a systematic reduction in the estimated number counts by a factor of approximately 41 per cent at $S_{870\mu\text{m}} \geq 7\text{mJy}$ and 24–30 per cent at $S_{870\mu\text{m}} \geq 12\text{mJy}$, though due to small number statistics the latter is not well constrained (e.g., Hill et al., 2018; Stach et al., 2018). We will explore the nature of the S2LXS XMM-LSS sources via follow up ALMA observations (Project ID: 2022.1.01030.S, PI: T. K. Garratt) of the brightest sources in the S2LXS XMM-LSS catalogue. With the exquisite resolution of ALMA we expect to pinpoint the position of multi-wavelength counterparts to the brightest S2LXS XMM-LSS sources, allowing us to constrain the relative contributions of source blending, lensing and intrinsically bright sources to the bright-end of the $850\mu\text{m}$ number counts.

3.4.2 Comparison to models

In Figure 3.15 we compare our results to: semi-analytic models GALFORM (Cowley et al., 2015; Lacey et al., 2016) and SHARK (Lagos et al., 2019); empirical models SIDES (B  thermin et al., 2017) and the Cai-Negrello model (Cai et al., 2013; Negrello et al., 2017); and the cosmological hydrodynamical simulation SIMBA (Lovell et al., 2021). These models are all able to broadly

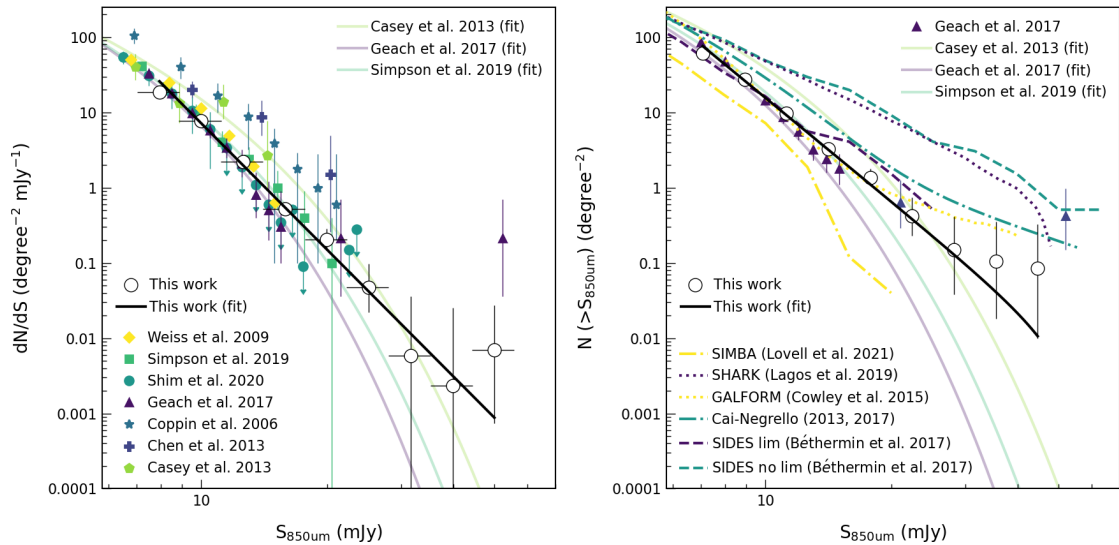


FIGURE 3.15: Number counts of $850\mu\text{m}$ sources measured from the S2LXS XMM-LSS survey 5σ catalogue (white circles with black outline). In the left panel we present the differential number counts from this work along with observational constraints from S2CLS (Geach et al., 2017), S2COSMOS (Simpson et al., 2019) and the other main blank-field surveys (Casey et al., 2013; Coppin et al., 2006; Shim et al., 2020; Weiß et al., 2009), as well as from Chen et al. (2013) who combine data from two cluster lensing fields and three blank fields. The S2LXS XMM-LSS differential number counts are consistent with these previous studies within the uncertainties for the flux range probed. We find an excess in the number counts (above the Schechter (1976) function fit of Geach et al. (2017)) at $\gtrsim 15$ mJy, similar to that found in S2CLS (Geach et al., 2017). In the right panel we present the S2LXS XMM-LSS cumulative number counts, comparing both to observations and several simulated galaxy models. For clarity we only plot the observational constraints from S2LXS XMM-LSS and S2CLS, and the model fits from S2COSMOS and Casey et al. (2013). We show the $850\mu\text{m}$ number counts from semi-analytic models (Cowley et al., 2015; Lagos et al., 2019), empirical models (Béthermin et al., 2017; Cai et al., 2013; Negrello et al., 2017) and the cosmological hydrodynamical simulation SIMBA (Lovell et al., 2021). The results from Lovell et al. (2021) and Cowley et al. (2015) both take into account blending from a 15 arcsec beam. The Béthermin et al. (2017) standard model has a star-formation rate limit of $1000 M_{\odot} \text{yr}^{-1}$. We show the results both with and without this limit. The Béthermin et al. (2017) models shown do not take account of blending, but do include a prescription for lensing. The Cai-Negrello model combines the counts of unlensed and strongly-lensed galaxies. The excess in the S2LXS XMM-LSS number counts at $\gtrsim 15$ mJy is most consistent with the results from the Cai-Negrello empirical model (Cai et al., 2013; Negrello et al., 2017), the semi-analytic model of Cowley et al. (2015), and the standard empirical model of Béthermin et al. (2017). The error bars in both panels show Poisson uncertainties (Gehrels, 1986).

reproduce the faint-end of the $850\mu\text{m}$ number counts (e.g., Geach et al., 2017; Simpson et al., 2019).

The blending of multiple faint submillimetre galaxies in the coarse 15 arcsec resolution of the SCUBA-2 beam is known to boost estimates of the $850\mu\text{m}$ number counts, with follow up surveys (using sub-arcsecond resolution interferometers) finding a systematic reduction in the estimated number counts by a factor of approximately 41 per cent at $S_{870\mu\text{m}} \geq 7$ mJy. Of the models discussed here the semi-analytic model GALFORM, the empirical model SIDES and the

TABLE 3.3: Differential (dN/dS) and cumulative ($N > S'$) $850\mu\text{m}$ number counts measured from the S2LXS XMM-LSS survey. We evaluate dN/dS 1000 times taking the mean as the final number counts estimate. The flux density bin widths are $\Delta\log_{10}(S) = 0.1$, with S and S' the flux bin centres and edges respectively. The first set of errors shown are the Poisson uncertainties (Gehrels, 1986) and the second set are the standard deviation on the number counts estimates over the 1000 realisations (see text for details).

$\log_{10}(S/\text{mJy})$	S [mJy]	S' [mJy]	dN/dS [$10^{-3} \text{ deg}^{-2} \text{ mJy}^{-1}$]	$N > S'$ [10^{-3} deg^{-2}]
0.9	7.9	7.1	$18,637^{+203}_{-131} \pm 28,569$	$61,807^{+735}_{-618} \pm 53,964$
1.0	10.0	8.9	$7,762^{+179}_{-123} \pm 6,564$	$27,644^{+684}_{-566} \pm 14,965$
1.1	12.6	11.2	$2,221^{+138}_{-93} \pm 1,460$	$9,733^{+605}_{-485} \pm 4,056$
1.2	15.8	14.1	$525^{+103}_{-67} \pm 291$	$3,281^{+520}_{-398} \pm 981$
1.3	20.0	17.8	$204^{+79}_{-50} \pm 91$	$1,361^{+433}_{-306} \pm 403$
1.4	25.1	22.4	$47^{+50}_{-25} \pm 28$	$421^{+329}_{-191} \pm 165$
1.5	31.6	28.2	$6^{+30}_{-6} \pm 9$	$149^{+264}_{-111} \pm 64$
1.6	39.8	35.5	$2^{+23}_{-2} \pm 5$	$106^{+248}_{-88} \pm 13$
1.7	50.1	44.7	$7^{+21}_{-6} \pm 4$	$85^{+240}_{-75} \pm 44$

hydrodynamical simulation SIMBA all simulate the effects of source blending in a 15 arcsec beam, which allows us to make a more ‘like-for-like’ comparison with the observed S2LXS XMM-LSS number counts. Lovell et al. (2021) use a 3D dust continuum radiative transfer code to estimate the submillimetre fluxes of galaxies in the cosmological hydrodynamic simulation SIMBA. To model the effects of source blending a projected SIMBA $850\mu\text{m}$ lightcone is convolved with the SCUBA-2 point spread function (Dempsey et al., 2013) to produce an ‘observed’ SCUBA-2 map. The SIMBA predicted $850\mu\text{m}$ number counts are more than a factor of 2 below the observed S2LXS XMM-LSS counts. The semi-analytic model GALFORM (Lacey et al., 2016) invokes a mildly top-heavy initial mass function in starbursts to reproduce the observed number counts and redshift distribution (e.g., Simpson et al., 2014; Wardlow et al., 2011) of $850\mu\text{m}$ selected sources (although we note this model is unable to reproduce the redshift distribution of bright SMGs with flux densities $S_{850\mu\text{m}} > 9 \text{ mJy}$; Chen et al., 2022). Sources are extracted from the simulated maps using a top-down peak-finding approach and the number counts derived from the source-extracted catalogue. The GALFORM model is in good agreement with the observed S2LXS XMM-LSS counts within the uncertainties.

The upturn in the $850\mu\text{m}$ number counts is motivated, at least in part, by the presence of high-redshift gravitationally lensed sources. A prescription for lensing is included in the empirical model of Béthermin et al. (2017), which uses an updated version of the two star-formation modes

(B  thermin et al., 2012; Sargent et al., 2012) galaxy evolution model to derive global galaxy properties using empirical relations from observations. Taking the galaxy properties generated from this model, B  thermin et al. (2017) use an abundance matching technique to populate dark-matter halos with galaxies to produce a 2deg^2 simulation of the extragalactic sky. The simulation includes a simple estimate of lensing that depends on redshift but does not account for the mass distributions in the foreground. Intrinsic number counts are estimated from the simulated catalogue. The standard model includes a sharp star-formation limit of $1000M_{\odot}\text{yr}^{-1}$. In Figure 3.15 we plot the predicted intrinsic counts from B  thermin et al. (2017) for the standard model and the model with no star-formation limit. We note that B  thermin et al. (2017) also estimate the number counts from a source-extracted catalogue to take into account source blending. The source-extracted counts mirror the intrinsic counts at bright flux densities and so for clarity we do not plot the source extracted counts in Figure 3.15. The standard model is broadly in agreement with the S2LXS observed number counts below 30mJy, but fails to reproduce the observed counts at higher flux densities. The model without a star-formation limit significantly over-predicts the counts by up to a factor 20 across the flux density range probed, which indicates that including a star-formation limit in some form is necessary for this model to reproduce the observed counts. The Cai-Negrello empirical model (Cai et al., 2013; Negrello et al., 2017) also takes into account the influence of strongly lensed galaxies, by combining theoretical counts for late-type, unlensed and strongly lensed galaxies. The maximum magnification assumed for calculating the strongly lensed number counts is $\mu_{\text{max}} = 15$. We note that the Cai model (Cai et al., 2013) presented here has been re-calibrated in line with recent number counts measurements from Geach et al. (2017) and Simpson et al. (2019). The Cai-Negrello model over-predicts the S2LXS XMM-LSS observed number counts by a factor of approximately 2, apart from in the brightest flux bins where the counts are consistent within the uncertainties.

The semi-analytic model SHARK does not include a prescription for lensing or model the effects of source blending, and so, given these are known to be important influences, boosting the bright-end of the single-dish $850\mu\text{m}$, we might expect this model to under-predict the number counts compared to the observed S2LXS XMM-LSS counts. Lagos et al. (2019) combine the SHARK semi-analytical model (Lagos et al., 2018) with attenuation curves derived from EAGLE using the 3D dust radiative transfer code SKIRT (Trayford et al., 2017) to model the emission of galaxies from far-ultraviolet to far-infrared wavelengths. In Figure 3.15 we show that the SHARK semi-analytical model over-predicts the bright-end of the number counts compared to the S2LXS XMM-LSS observed counts by up to a factor of 20.

The S2LXS XMM-LSS number counts are in broad agreement with the Cai-Negrello empirical model, the empirical model SIDES (at flux densities below 30 mJy) and the semi-analytic model GALFORM, which include gravitational lensing and/or the effects of source blending in a low-resolution single-dish telescope beam, indicating that both may be important motivators for the observed over-abundance of bright single-dish selected 850 μm sources. With follow up ALMA observations (Project ID: 2022.1.01030.S) of the brightest sources in the S2LXS XMM-LSS catalogue we aim to place strong constraints on the contribution of intrinsically bright, lensed and blended sources to the bright-end of the 850 μm counts, vital to inform future models.

3.5 Summary

We have presented the 850 μm maps and catalogue for the James Clerk Maxwell Telescope SCUBA-2 Large Extragalactic Survey of the XMM-LSS field. The S2LXS XMM-LSS survey maps a contiguous area of 9 deg^2 to a moderate depth of about 4 mJy beam^{-1} . This is the largest extragalactic area at 850 μm mapped with the JCMT to date. The wide area of the S2LXS XMM-LSS survey allows us to detect ultra-bright ($S_{850\mu\text{m}} > 15 \text{ mJy}$), but intrinsically rare sources, with approximately three sources expected per square degree with deboosted flux densities $> 15 \text{ mJy}$. The S2LXS XMM-LSS $> 5\sigma$ catalogue comprises 40 sources, of which 11 have deboosted fluxes above 15 mJy. This is twice the number of bright ($S_{850\mu\text{m}} > 15 \text{ mJy}$) extragalactic sources detected in S2CLS. We use the S2LXS XMM-LSS $> 5\sigma$ catalogue to estimate the number counts at intrinsic flux densities above 7 mJy, significantly reducing the Poisson errors on existing measurements (e.g., Chen et al., 2013; Coppin et al., 2006; Geach et al., 2017; Simpson et al., 2019; Shim et al., 2020). We observe the distinctive upturn in the number counts that is expected to be caused by submillimetre emission from Galactic objects and gravitationally lensed high-redshift galaxies. We note that at least two sources in the S2LXS XMM-LSS 5σ catalogue are already known, lensed, high-redshift ($z \gtrsim 3$) galaxies (Busmann et al., 2015; Geach et al., 2017). With the benefit of a wider survey area S2LXS XMM-LSS provides a more conservative estimate of the number counts at $S_{850\mu\text{m}} > 30 \text{ mJy}$ (comparing to S2CLS), which is more in keeping with current models that are often unable to reproduce the very bright-end of the S2CLS 850 μm number counts (e.g., Béthermin et al., 2017; Cai et al., 2013; Negrello et al., 2017; Cowley et al., 2015).

Follow up ALMA observations (Project ID: 2022.1.01030.S, PI: T. K. Garratt) of the brightest sources in the S2LXS XMM-LSS catalogue will be a key step in unravelling the nature of

the sources that contribute to the over-abundance observed at the bright-end of the single-dish $850\ \mu\text{m}$ number counts. With the exquisite resolution of ALMA we aim to constrain the relative contributions of source blending, lensing and intrinsically bright sources to the bright-end of the $850\ \mu\text{m}$ number counts; measure the redshift distribution for these rare, highly luminous galaxies; and explore whether a simple flux cut at $850\ \mu\text{m}$ is an effective selection method to identify high-redshift, gravitationally lensed galaxies (Garratt et al. in prep).

Chapter 4

ALMA follow-up of the SCUBA-2 Large eXtragalactic Survey XMM-LSS field: Source catalogue and first results

4.1 Introduction

The galaxies that inhabit the bright-end of the submillimetre population are intrinsically rare with source densities at $S_{850\mu\text{m}} > 15$ mJy currently estimated to be $\approx 1\text{--}3$ galaxies per square degree (e.g., Geach et al., 2017, Chapter 3). It is likely that bright (i.e., $S_{850\mu\text{m}} > 15$ mJy) sources detected in single-dish submillimetre surveys are a mix of strongly gravitationally lensed galaxies, intrinsically bright galaxies, blends of multiple submillimetre galaxies or local sources of submillimetre emission. However, the relative contribution of each of these sub-populations to the bright-end of the single-dish submillimetre number counts is currently unknown, because of the small number of ultra-bright submillimetre sources detected in blank-field single-dish $850\mu\text{m}$ surveys (e.g., Coppin et al., 2006; Geach et al., 2017; Simpson et al., 2019; Shim et al., 2020). The brightest SMGs detected at $850\mu\text{m}$ have also been shown to be the most distant (e.g., Stach et al., 2019; Simpson et al., 2020; Chen et al., 2022), but with only a small number of $S_{850\mu\text{m}} > 15$ mJy sources detected in single-dish surveys (e.g., Geach et al., 2017; Simpson et al., 2019; Shim et al., 2020) the redshift distribution of SMGs in the ultra-bright regime and the trend of increasing redshift with submillimetre flux has barely been explored.

S2LXS is the largest contiguous extragalactic survey at $850\mu\text{m}$ with the JCMT to date, and with an area $>10\text{deg}^2$ it offers an opportunity to explore this intrinsically rare, highly infrared luminous and potentially high-redshift population of galaxies in a uniform and systematic way. The S2LXS XMM-LSS main catalogue includes 40 sources detected at a significance of $>5\sigma$ with deboosted $850\mu\text{m}$ flux densities in the range 7 mJy to 48 mJy. To uncover the true nature of these sources we must first pinpoint the position of the individual submillimetre galaxies contributing to the single-dish submillimetre emission. However, identifying unambiguous multi-wavelength counterparts to single-dish selected submillimetre sources is hindered by the resolution of single-dish surveys (i.e., the SCUBA-2 beam-size is $15''$). In Figure 4.1 we show multi-wavelength cutouts for three sources in the S2LXS XMM-LSS catalogue, all of which have ALMA observations, to illustrate the difficulty in identifying the true multi-wavelength counterparts to single-dish selected submillimetre sources.

In this chapter we present the first results from an ALMA survey (PI: T. K. Garratt, Project ID: 2022.1.01030.S) targeting the 17 brightest sources in the S2LXS XMM-LSS main catalogue. The primary aims of our ALMA proposal are to: (1) determine the relative contributions of intrinsically bright galaxies, strongly-gravitationally lensed galaxies, and sources blended in the single-dish beam to the bright-end of the $850\mu\text{m}$ source counts¹, (2) robustly measure the redshift distribution for this highly-luminous population.

4.2 Pinpointing the position of $850\mu\text{m}$ selected sources from S2LXS XMM-LSS with ALMA

Submillimeter interferometry is the most straight-forward route to accurately pinpoint the position of single-dish selected submillimetre sources. We successfully applied to ALMA Cycle 9 to observe the brightest 17 sources² in the S2LXS XMM-LSS $>5\sigma$ catalogue (excluding those sources with prior ALMA observations). Our observations use the default set up for ALMA band 7 continuum observations centred on a frequency of 343.50 GHz ($\lambda = 870\mu\text{m}$), similar to the wavelength of the single-dish detection (and in keeping with the approach of previous

¹We have already ruled out local sources of submillimetre emission in the S2LXS XMM-LSS catalogue by visually inspecting the multi-wavelength imaging and querying the NASA/IPAC Extragalactic Database to confirm that there are no $z < 0.1$ sources of emission within an $8''$ radius of the position of each S2LXS source, i.e., within the FWHM of the SCUBA-2 beam.

²At the time we submitted our ALMA proposal the S2LXS $>5\sigma$ catalogue included 19 sources, 2 that had prior ALMA observations, and so our proposal was for follow up of 17 sources. We have since added data to the map, which has expanded the catalogue to 40 sources.

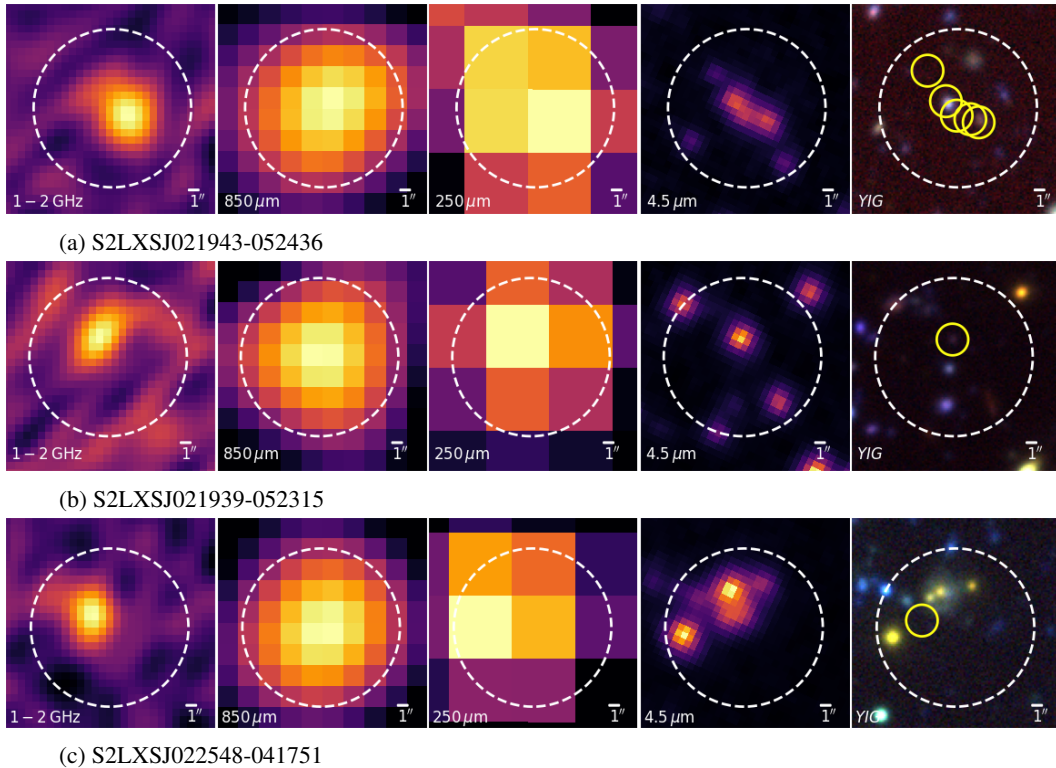


FIGURE 4.1: Multi-wavelength $20'' \times 20''$ cutouts for three sources in the S2LXS XMM-LSS $>5\sigma$ catalogue. We show images (left to right) from the VLA 1-2 GHz survey of the XMM-LSS field (Heywood et al., 2020), the S2LXS XMM-LSS survey at $850\mu\text{m}$ (Chapter 3), the *Herschel* Multi-tiered Extragalactic Survey at a wavelength of $250\mu\text{m}$ (HerMES; Oliver et al., 2012), the *Spitzer* Survey of the Deep Drilling Fields centred on a wavelength of $4.5\mu\text{m}$ (Deep Drill; Lacy et al., 2021) and a colour image made using y -, i - and g -band data from the Hyper Suprime-Cam Subaru Strategic Program (HSC-SSP; Aihara et al., 2018). In subplot (a) and (c) we show the ALMA counterparts (yellow circles) to a sample of galaxies detected in HerMES (Bussmann et al., 2015), and in subplot (b) we show the ALMA counterparts to a single-dish $850\mu\text{m}$ selected source from the S2CLS UDS field (Stach et al., 2019), illustrating the difficulty in identifying the true multi-wavelength counterparts within the SCUBA-2 beam (white dashed circle) without the finer resolution of a submillimetre interferometer.

ALMA follow up observations, e.g., Stach et al., 2018; Simpson et al., 2020). A single-dish selected $850\mu\text{m}$ source is typically defined as a multiple if two or more submillimetre galaxies with $S_{870\mu\text{m}} \geq 1\text{ mJy}$ are detected within the primary beam of the corresponding ALMA map (e.g., Stach et al., 2018; Simpson et al., 2020). Following this convention we request a sensitivity of $1\sigma \sim 0.2\text{ mJy}$ so we can detect ALMA $S_{870\mu\text{m}} \geq 1\text{ mJy}$ counterparts to the S2LXS XMM-LSS single-dish sources at a significance of $\geq 5\sigma$. Our primary goal is to pinpoint the position of the ALMA counterparts and as we do not want to resolve out flux (which may become a risk at finer resolutions) risking non-detection of fainter counterparts, we request a minimum angular resolution of $0.5''$. To allow us to robustly identify optical/near infrared counterparts to the S2LXS XMM-LSS sources we request a maximum resolution of $1''$, consistent with the resolution of the *Spitzer* Extragalactic Representative Volume Survey (SERVS) $3.6\mu\text{m}$ and $4.5\mu\text{m}$

images (Mauduit et al., 2012). As multiple systems are typically separated by $2''$ – $6''$ (e.g., Ivison et al., 2007), at this resolution we will also mitigate against source blending in the ALMA beam. Our proposed continuum observations require a total observing time of ~ 35 minutes (including overheads).

4.2.1 ALMA observations and data reduction

The 17 brightest sources in the S2LXS XMM-LSS $> 5\sigma$ catalogue were observed with ALMA in Band 7 (Project ID: 2022.1.01030.S, PI: T. K. Garratt) on 8th October 2022. Our ALMA observations use the standard correlator set-up for continuum observations, with four basebands covering a total bandwidth of 7.5 GHz centred on a frequency of 344 GHz (equivalent to $\lambda \approx 870 \mu\text{m}$). At our observing frequency the ALMA primary beam (FWHM = $17.3''$) fully encompasses the FWHM of the SCUBA-2 beam at $850 \mu\text{m}$ ($\sim 15''$). Our observations are conducted with 45 12 m antennae on baselines ranging from 15 m to 500 m, yielding a synthesised beam size of $0.55'' \times 0.43''$.

We calibrate the ALMA data using the COMMON ASTRONOMY SOFTWARE APPLICATION (CASA; McMullin et al., 2007) v6.4.1.12 and the default ALMA Science pipeline. The calibration uses J0238 + 1636 for the bandpass and flux calibrator, and J0239 – 0234 for the phase calibrator. We visually inspect the data finding this to be of high quality, and so do not apply any additional flags.

We use the CASA TCLEAN task to image the ALMA data. The first step is to create a dirty map for each of our ALMA observations. We use the default parameters of the ALMA Science pipeline and the multi-frequency synthesis algorithm, which combines data from all selected spectral channels into a single continuum image. We apply a Briggs weighting with $\text{robust} = +1.0$ to generate dirty maps with a median synthesised beam size of $0.59'' \times 0.50''$, which is in keeping with the angular resolution requested in our proposal. At this resolution we expect that the majority of our sources will be unresolved, with previous studies finding submillimetre intrinsic sizes of $\sim 0.3''$ (e.g., Simpson et al., 2015; Hodge et al., 2016). With this resolution we will also mitigate against source blending in the ALMA beam (noting that galaxies in multiple systems are typically separated by 2 – $6''$; Ivison et al., 2007).

The next step is to estimate the sensitivity of our dirty maps. To do this we use an iterative sigma-clipping routine (with $\pm 4\sigma$) to remove pixels associated with potential sources. We then

measure the root mean square (rms) value of the unclipped values (σ). Next we clean the dirty maps using the CASA TCLEAN task and the default parameters of the ALMA Science pipeline. With the TCLEAN automasking routine we mask emission detected at $>4.5\sigma$ and clean the maps to 2σ , where σ is the rms calculated using the sigma clipping routine discussed above. The resulting maps are 300×300 pixels in size and have a pixel scale of $0.099''$.

4.2.2 Source extraction

We generate a noise map for each ALMA continuum map following the strategy of Franco et al. (2018). In steps of 1 pixel we estimate the standard deviation and median in a box size of 51 pixels centred on each pixel. All pixels inside this box that have a value 3 times the standard deviation from the median are then masked. We repeat this process 3 times. We select this box size to balance the need to take into account the variation in the local noise, whilst also assuring that the median pixel value of the resulting noise map is consistent with the typical value of noise in the ALMA continuum map. Finally the value of the standard deviation of the non-masked pixels is assigned to the central pixel. The median 1σ sensitivity of these ALMA noise maps is 0.11 mJy

For each ALMA observation we combine the non-primary beam corrected continuum image with the noise map, to create a signal-to-noise ratio map. We use PHOTUTILS³, an ASTROPY affiliated python package to detect sources in the ALMA signal-to-noise ratio maps. This package includes a function FIND_PEAKS to locate local maxima in an astronomical image that are above a specified threshold value. We set a detection value of 3σ . We also impose a separation limit, requiring sources to be separated by $0.5''$ (approximately the size of the synthesised beam). This prevents double counting of bright sources if more than one pixel associated with a source exceeds the detection threshold. If more than one source is detected above the detection threshold in a box size of $0.5''$ only the coordinates of the source with the highest signal-to-noise ratio are returned. We note that we would not typically expect to find two sources separated by $<0.5''$ (and galaxies would be blended within the ALMA beam if so) as multiple sources are usually separated by $2''$ – $6''$ (e.g., Ivison et al., 2007). We produce two catalogues; a main catalogue comprising of sources that are detected within the ALMA primary beam (FWHM $\sim 17''$) and a supplementary catalogue comprising of sources detected outside the area of the ALMA primary beam.

³In this work we use ASTROPY version 4.2.1 and PHOTUTILS version 1.0.1

To estimate the false detection rate for the survey we invert the non-primary beam corrected continuum maps and repeat the source extraction process, using PHOTUTILS to search for 3σ peaks in a box size of $0.5''$. We then estimate the false detection rate in intervals of signal to noise ratio. Within the ALMA primary beam (i.e. the main catalogue) the false detection rate is 100% at $<4.5\sigma$, there are no sources detected in any of the ALMA continuum maps at 4.5σ – 5σ , and the false detection rate is 0% at $>5\sigma$. Therefore we use a formal detection limit of 5σ to define the AS2LXS main catalogue. We note that the $>3\sigma$ supplementary catalogue contains no sources with a signal-to-noise ratio above 4.5σ and so we do not consider the sources in this catalogue in any further analysis.

For each source in the AS2LXS main catalogue we measure a $1''$ diameter aperture flux density from the primary beam corrected maps. We estimate the $1''$ diameter aperture noise level for each ALMA map by randomly placing 100 apertures on the primary beam corrected map and measuring the flux. The noise level for a map is calculated as the standard deviation of the resulting aperture fluxes. The estimated aperture noise level for all the ALMA maps ($1\sigma \sim 0.2$ mJy) is consistent with the sensitivity requested in our proposal. In Figure 4.2 we show the 13 ALMA signal-to-noise ratio maps that include sources detected at $>5\sigma$.

In Table 4.1 we present the AS2LXS catalogue, which comprises 22 sources from 13 ALMA maps with peak flux densities in the range 0.5 mJy to 11 mJy. This catalogue contains both the peak and aperture fluxes for each source, with associated errors. We note that these flux densities have not yet been corrected for the effects of flux boosting, and we have not yet applied an aperture correction to the aperture fluxes. When we compare the peak flux to the aperture flux (in the primary beam corrected map) for individual sources we find that for some sources the aperture flux density is much higher (i.e., for AS2LXS04.0 the aperture flux is 50% higher than the peak flux in the primary beam corrected map). This may be because these sources are larger than the synthesised beam and so are marginally resolved. We do not detect any ALMA sources at $>5\sigma$ in four of the ALMA maps. This is a higher number of blank maps than expected given the 10% false detection rate of the S2LXS XMM-LSS survey. It is possible that all these S2LXS XMM-LSS sources are spurious. However, it is also possible that multiple faint submillimetre galaxies, which are too faint to be detected at the detection threshold ($>5\sigma$) of the ALMA survey, are responsible for the single-dish submillimetre emission.

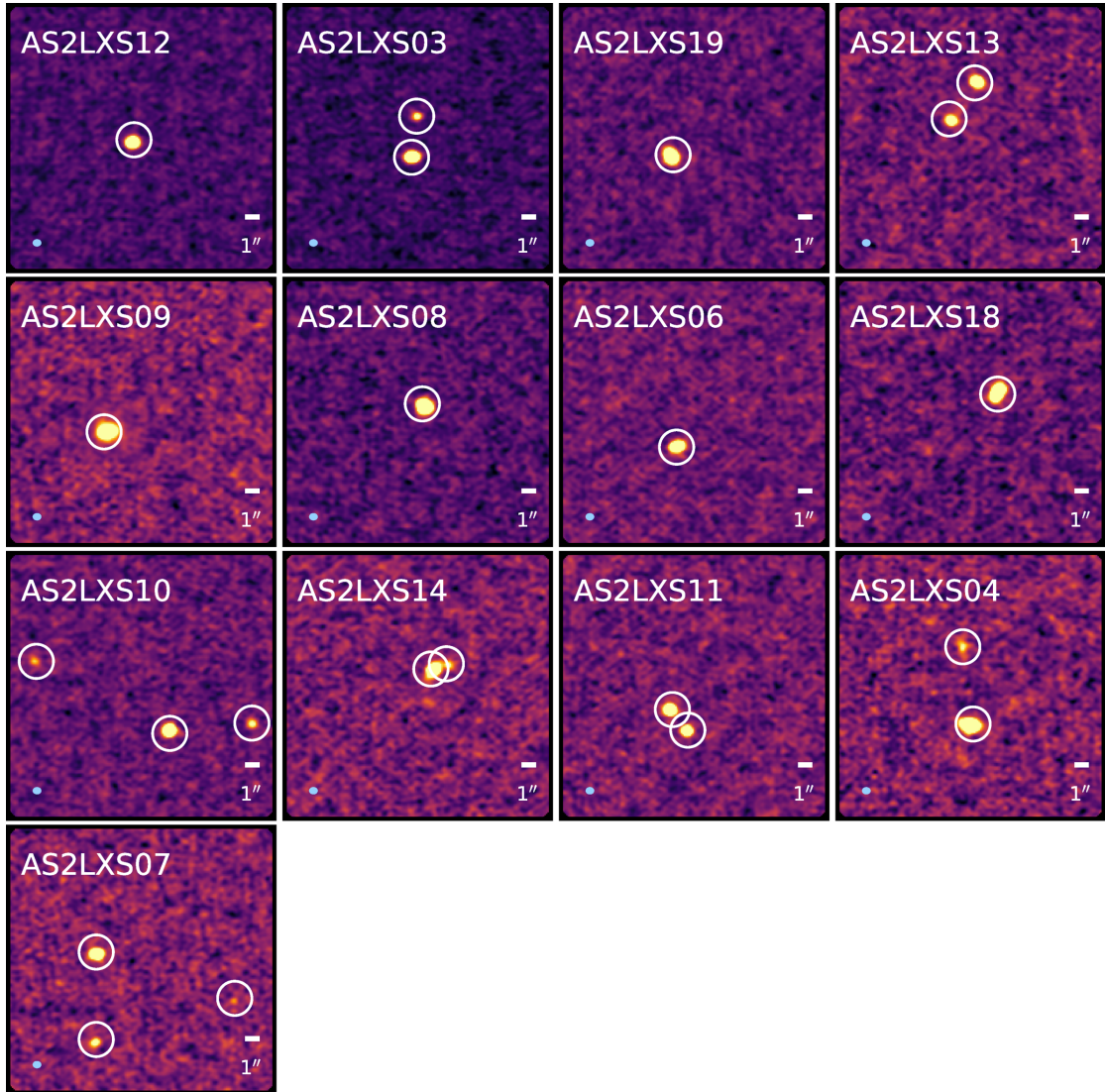


FIGURE 4.2: ALMA signal-to-noise ratio maps showing the 22 sources detected at $>5\sigma$ in the AS2LXS catalogue. We show the ALMA beam (blue ellipse) in the bottom left of the cutouts, and the scale of the images in the bottom right. The $>5\sigma$ sources are indicated by the white circles.

4.2.3 Multiplicity Fraction

In keeping with previous surveys (e.g, Simpson et al., 2015; Stach et al., 2018; Simpson et al., 2020) we define a multiple map as an ALMA map with more than one $S_{870\mu\text{m}} \gtrsim 1$ mJy galaxy detected within the ALMA Band 7 primary beam. At our observing frequency the ALMA primary beam (FWHM= $17.3''$) is well matched in size to the SCUBA-2 $850\mu\text{m}$ PSF ($\sim 15''$). Our ALMA observations target 17 sources in the S2LXS XMM-LSS $>5\sigma$ catalogue; seven of the ALMA maps contain multiple sources with flux densities $S_{870\mu\text{m}} \gtrsim 1$ mJy (detected at a significance $>5\sigma$), six of the ALMA maps contain just one $S_{870\mu\text{m}} \gtrsim 1$ mJy source and 4 of the maps are blank, giving a multiplicity fraction (excluding the blank maps) of 54% for single-dish

TABLE 4.1: AS2LXS catalogue. This catalogue contains 22 sources detected at a significance of $>5\sigma$. Coordinates are J2000. The $S_{870\mu\text{m}}^{\text{peak}} \pm \sigma$ column gives the peak flux density and error measured from the non-primary beam corrected map, and the S/N^{peak} column gives the signal-to-noise ratio of the detection. The $S_{870\mu\text{m}}^{\text{aperture}} \pm \sigma$ column gives the $1''$ diameter aperture flux density and error measured from the primary beam corrected map, and the S/N^{aperture} column gives the signal-to-noise ratio of the aperture detection.

ALMA ID	RA	Dec	$S_{870\mu\text{m}}^{\text{peak}} \pm \sigma$ [mJy beam $^{-1}$]	S/N^{peak}	$S_{870\mu\text{m}}^{\text{aperture}} \pm \sigma$ [mJy]	S/N^{aperture}
AS2LXS12.0	37.2251	-4.4126	10.9 ± 0.1	75.9	11.6 ± 0.2	55.4
AS2LXS03.0	35.1751	-5.6353	9.3 ± 0.1	82.0	10.3 ± 0.2	51.6
AS2LXS19.0	35.8422	-3.6305	7.8 ± 0.1	59.0	10.3 ± 0.2	47.9
AS2LXS13.0	34.9080	-4.4909	6.9 ± 0.2	43.8	7.9 ± 0.2	37.8
AS2LXS09.0	35.8499	-4.4342	6.6 ± 0.2	37.6	9.3 ± 0.2	46.7
AS2LXS08.0	35.8812	-4.4964	6.5 ± 0.1	56.6	8.8 ± 0.2	44.5
AS2LXS06.0	36.8975	-5.2670	6.2 ± 0.1	52.4	7.0 ± 0.2	41.0
AS2LXS18.0	36.0006	-3.7726	6.1 ± 0.1	43.3	8.3 ± 0.2	39.0
AS2LXS10.0	35.1822	-4.7785	6.0 ± 0.1	53.7	7.3 ± 0.2	36.9
AS2LXS14.0	35.7156	-4.4030	5.9 ± 0.2	39.3	6.8 ± 0.2	33.9
AS2LXS11.0	35.9246	-4.7505	5.7 ± 0.1	44.9	6.1 ± 0.2	30.3
AS2LXS04.0	36.7513	-5.4019	5.2 ± 0.1	35.0	8.2 ± 0.2	40.1
AS2LXS11.1	35.9243	-4.7509	4.8 ± 0.1	34.0	5.0 ± 0.2	24.8
AS2LXS07.0	36.5581	-4.9375	4.6 ± 0.1	38.4	5.3 ± 0.2	31.1
AS2LXS13.1	34.9085	-4.4916	4.1 ± 0.2	26.2	4.2 ± 0.2	20.1
AS2LXS03.1	35.1750	-5.6345	2.4 ± 0.1	21.7	2.3 ± 0.2	11.7
AS2LXS10.1	35.1806	-4.7783	1.7 ± 0.1	13.4	3.0 ± 0.2	15.3
AS2LXS07.1	36.5581	-4.9392	1.4 ± 0.1	11.0	2.0 ± 0.2	12.0
AS2LXS14.1	35.7153	-4.4029	1.2 ± 0.1	8.8	1.6 ± 0.2	7.8
AS2LXS10.2	35.1848	-4.7771	1.2 ± 0.1	8.6	2.3 ± 0.2	11.5
AS2LXS04.1	36.7515	-5.4004	0.9 ± 0.1	7.7	1.2 ± 0.2	5.9
AS2LXS07.2	36.5554	-4.9384	0.5 ± 0.1	5.1	0.6 ± 0.2	3.3

sources with deboosted flux densities $S_{850\mu\text{m}} > 12\text{mJy}$. There are three additional sources in the S2LXS XMM-LSS $>5\sigma$ catalogue with deboosted flux densities above 12mJy for which archival ALMA data exists (S2LXSJ021831-053131, S2LXSJ022548-041751, S2LXSJ021943-052436). If we include these sources in our analysis the multiplicity fraction increases to 56%. The level of multiplicity in AS2LXS is in keeping with the multiplicity fraction of 53% (for single-dish sources with flux densities $S_{850\mu\text{m}} > 12\text{mJy}$) measured in the ALMA follow up survey of the brightest submillimetre galaxies in the SCUBA-2 COSMOS field (AS2COSMOS; Simpson et al., 2020).

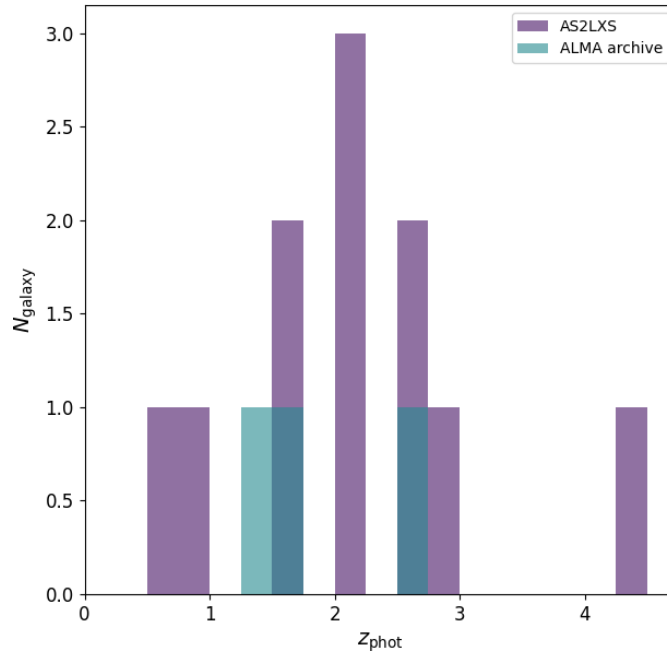


FIGURE 4.3: Redshift distribution for ALMA counterparts to the brightest submillimetre sources in the S2LXS XMM-LSS $>5\sigma$ catalogue (Chapter 3). The photometric redshifts are taken from the K_s -band selected catalogue of Adams et al. (2020); Hatfield et al. (2022). We note that this catalogue does not include the photometric redshift probability distribution function so we are not able to show these here. The median redshift for this sample of 14 submillimetre galaxies is $z = 2.1$. We note that this photometric redshift estimate is possibly biased low as the Hierarchical Bayesian model used to derive these redshifts may favour low redshift solutions (Hatfield et al., 2022). We may also see a lower median redshift because some or all of the 7 galaxies that do not have K_s -band counterparts lie at higher redshifts.

4.2.4 Redshift distribution

In Figure 4.3 we show a tentative photometric redshift distribution for the galaxies in the AS2LXS $>5\sigma$ catalogue. The photometric redshifts are taken from the K_s -band selected (down to a limiting magnitude of $K_s = 23.9$) catalogue of Adams et al. (2020); Hatfield et al. (2022). The K_s -band data is from the VISTA-VIDEO survey (Jarvis et al., 2013) and so this catalogue offers good, but not complete coverage of the S2LXS XMM-LSS survey field (see Figure 3.6). This catalogue includes photometric redshifts estimated via template fitting and machine learning, and consensus photometric redshifts, which are derived by combining the results from template fitting and machine learning in a Hierarchical Bayesian model. We use the consensus photometric redshifts, which have an outlier fraction of $\sim 3 - 4\%$, in our analysis.

Of the 22 sources in the AS2LXS $>5\sigma$ catalogue; 5 galaxies lie outside the footprint of the VISTA VIDEO survey (Jarvis et al., 2013), 11 galaxies have a K_s -band selected counterpart within a $1''$ radius and 6 galaxies do not have counterpart in the K_s -band selected catalogue.

It is expected that about 20% of SMGs that are detected at $850\mu\text{m}$ will be undetected in sensitive near-infrared imaging at $K \gtrsim 25.7\text{ mag}_{\text{AB}}$ (e.g., Dudzevičiūtė et al., 2019). We find that approximately 35% of sources in the AS2LXS catalogue (that lie within the footprint of the VISTA VIDEO survey) do not have counterparts in the K_s -band catalogue. This is a higher fraction than expected, but may be because the galaxies in the near-infrared catalogue we use are selected to a brighter limiting magnitude ($K_s = 23.9$). We also match the archival ALMA data (discussed above) to this catalogue finding counterparts for 3 additional galaxies. The median redshift for our sample of 14 submillimetre galaxies with counterpart matches in the K_s -band selected catalogue is $z = 2.1$. The median redshift derived is much lower than estimates from the ALMA follow up survey of the S2CLS UDS field ($z \approx 2.6$; Stach et al., 2019) and AS2COSMOS ($z \approx 2.9$ Simpson et al., 2020), and is unexpected given that the brightest SMGs selected at $850\mu\text{m}$ are also observed to be the most distant (e.g., Stach et al., 2019; Simpson et al., 2020; Chen et al., 2022). We note that our photometric redshift estimate is possibly biased low as the Hierarchical Bayesian model may favour low redshift solutions (Hatfield et al., 2022). We see some possible evidence for this bias when we match the ALMA archival data to the K_s -band selected catalogue; using the K_s -band selected catalogue we retrieve a photometric redshift of $z \approx 1.1$ for the ultra-bright lensed galaxy ‘Orochi’, however, previous studies (e.g., Dudzevičiūtė et al., 2019) derive a significantly higher photometric redshift ($z \approx 3.5$) for the same galaxy (note that we are not making a judgement here on which photometric redshift is more accurate). We may also see a lower median redshift because some or all of the 6 galaxies that do not have K_s -band counterparts lie at higher redshifts. In future work we will explore whether expanding the wavelength coverage to longer wavelengths (mid-infrared to radio) and using different template fitting codes affects the photometric redshift estimates for the AS2LXS galaxies.

4.2.5 Summary

In this chapter we have presented the first results from an ALMA survey of the SCUBA-2 Large eXtragalactic Survey XMM-LSS field. The exquisite resolution of our ALMA observations allows us to pinpoint (to sub-arcsecond accuracy) the position of the submillimetre galaxies that contribute to the single-dish $850\mu\text{m}$ emission of the brightest sources in the S2LXS XMM-LSS $>5\sigma$ catalogue. The AS2LXS catalogue comprises 22 galaxies with flux densities of 0.6 mJy to 12 mJy.

We show the position(s) of the ALMA counterpart(s) for each of the S2LXS XMM-LSS sources on the multi-wavelength imaging in Appendix A. The importance of obtaining ALMA follow up for these sources is highlighted by this multi-wavelength imaging. For 8 of the ALMA maps with $>5\sigma$ detections there are no radio sources in the corresponding VLA maps, meaning that multi-wavelength counterparts can not be identified via the position of a radio source. The multi-wavelength imaging also highlights that the position of galaxies detected by ALMA does not always align with the position of galaxies in the K -band or $4.5\mu\text{m}$ data. Both these bands are commonly used in optical-near-infrared colour selections, and so using a colour selection approach to identify counterparts for sources in the S2LXS XMM-LSS catalogue would likely result in a number of inaccurate counterpart matches. Notably there are 6 ALMA sources that do not have K -band counterparts and 5 ALMA sources that do not have Deep Drill counterparts within the $< 1''$ matching radius. However, for all these ALMA sources there are galaxies in the K -band and Deep Drills maps that lie outside the matching radius that could potentially be (incorrectly) identified as counterparts via a colour selection approach.

We derive a multiplicity fraction of 56% for single-dish detected sources with flux densities $S_{850\mu\text{m}} > 12\text{mJy}$, which is consistent with the multiplicity levels found in previous ALMA follow up surveys of bright single-dish detected submillimetre sources (e.g., Simpson et al., 2020). Whilst both the AS2LXS and AS2COSMOS (Simpson et al., 2020) catalogues include single-dish sources with $850\mu\text{m}$ fluxes ranging from 12 mJy to 20 mJy, the distribution of fluxes is different with only 26% of sources in AS2COSMOS with $S_{850\mu\text{m}} > 15\text{mJy}$, compared to 46% of sources in S2LXS. Previous surveys (e.g., Simpson et al., 2020; Stach et al., 2019) have found that the multiplicity fraction increases with the single-dish $850\mu\text{m}$ flux, however, the results from AS2LXS indicate that there is a (high) flux limit at which this positive relationship ceases. This indicates that multiplicity does not significantly contribute to the excess in the single-dish number counts at $S_{850\mu\text{m}} \gtrsim 15\text{mJy}$. This is unexpected given that the S2LXS XMM-LSS number counts are broadly reproduced by models that incorporate source blending, and further work is required to confirm this.

For a sample of 14 AS2LXS galaxies (which lie in the footprint of the VISTA VIDEO survey) we use photometric redshifts from the K_s -band selected catalogue of Adams et al. (2020); Hatfield et al. (2022) to derive a tentative redshift distribution, measuring a median redshift for our sample of $z \approx 2.1$. This estimate is likely biased low, but further work is required to make any firmer conclusions.

Going forward, our goal is measure the lensing magnifications for galaxies in the AS2LXS catalogue (i.e., via LENSTOOL following a similar process to Chen et al., 2022) to estimate the fraction of our sample that is strongly lensed, ultimately with a view to determining the contribution of intrinsically bright, lensed and blended sources to the bright-end of the $850\ \mu\text{m}$ counts, vital to inform galaxy formation models.

Chapter 5

Conclusions

In this thesis we demonstrate that observations in the submillimetre part of the electromagnetic spectrum are a valuable tool for understanding the evolution of galaxies over cosmic time, and can provide valuable constraints for galaxy models. We use data from the two largest extragalactic submillimetre surveys at $850\mu\text{m}$ with the JCMT to date; the SCUBA-2 Cosmology Legacy Survey and the SCUBA-2 Large eXtragalactic Survey, and recent data from an ALMA survey of the S2LXS XMM-LSS field.

5.1 Evolution of the molecular gas mass density

Since molecular gas is the fuel from which stars are made, understanding how the molecular gas mass density evolves over cosmic time is key to understanding galaxy evolution. It is accepted that the star-formation rate density rises to a peak at $z \approx 2$ before declining to the present day. However, a fundamental question remains; what drives the peak epoch of star-formation, is it a larger supply of gas in galaxies, or are individual galaxies forming stars more efficiently, or both?

Making direct measurements of molecular gas via observations of CO line emission is time expensive and reliant on facilities that are over-subscribed, and so current estimates of the molecular gas mass density are hampered by large statistical uncertainties due to low number statistics. An alternative route to measuring molecular gas mass comes via measurements of dust emission at submillimetre wavelengths. This is possible because the dust-to-gas mass ratio is relatively

constant for massive galaxies ($M_{\text{stellar}} > 10^{10} M_{\odot}$). The Rayleigh-Jeans tail (the cold dust continuum) is nearly always optically thin, therefore measurements of dust emission can be used as a direct probe of molecular gas mass.

In Chapter 2 we use a 3-dimensional stacking method and the empirically calibrated RJ *luminosity-to-gass mass* ratio from Scoville et al. (2016) to estimate the molecular gas mass density to $z \approx 2.5$ via the average submillimetre continuum emission of a sample of 150,000 *K*-band selected galaxies from the well-studied UKIDSS-UDS field. Our estimates of the molecular gas mass density broadly align with the results from surveys of CO line emission, but with a sample over an order of magnitude larger, we are able to reduce the statistical uncertainties on these measurements. We show that the evolution of molecular gas mass density mirrors the star-formation rate density, indicating that the peak of the star-formation history is primarily motivated by an increased supply of gas, rather than galaxies forming stars more efficiently (e.g., driven by galaxy mergers/instabilities etc).

5.2 The bright-end of the single-dish $850\mu\text{m}$ selected submillimetre population

Highly luminous Submillimetre Galaxies are intrinsically rare with source densities at flux densities of $S_{850\mu\text{m}} > 15 \text{ mJy}$ currently estimated to be $\approx 1\text{--}3$ galaxies per square degree (e.g., Geach et al., 2017, Chapter 3). With very few observations of galaxies with flux densities $S_{850\mu\text{m}} > 15 \text{ mJy}$ the bright-end of the single-dish $850\mu\text{m}$ number counts and the redshift distribution for these ultra-bright submillimetre sources are poorly constrained. Previous single-dish submillimetre surveys have observed an over-abundance of bright sources at $850\mu\text{m}$, and it is expected that this over-abundance is motivated by lensed galaxies, galaxies blended in the single-dish beam and intrinsically bright galaxies. However, the relative contributions of each these sub-populations to the over-abundance of sources observed is unknown. Models currently struggle to replicate both the abundance and the redshift distribution of bright sources observed in single-dish submillimetre surveys. To inform further models we not only require robust constraints on the abundance and redshift distribution of bright $850\mu\text{m}$ sources, but also a clear understanding of the contribution of lensed, blended and intrinsically bright galaxies to the excess of bright single-dish sources observed.

In Chapter 3 we present the $850\mu\text{m}$ maps for the SCUBA-2 Large eXtragalactic Survey of the XMM-LSS field. This is the largest extragalactic survey at $850\mu\text{m}$ with JCMT to date, allowing us to probe the bright-end of the submillimetre population. We detect 40 sources at a significance of $>5\sigma$ in the S2XLS XMM-LSS map, with 11 sources having deboosted flux densities of $S_{850\mu\text{m}} > 15\text{ mJy}$, twice the number detected in S2CLS. We use the S2LXS XMM-LSS $>5\sigma$ catalogue to place strong constraints on the bright-end of the single-dish $850\mu\text{m}$ number counts, reducing the Poisson errors by a factor of 2 compared to previous work. We observe an over-abundance of bright sources with flux densities above 15 mJy , in keeping with the findings of S2CLS, but note that in light of the wider survey area of S2LXS XMM-LSS our estimate at $S_{850\mu\text{m}} \gtrsim 30\text{ mJy}$ is more conservative. This over-abundance of sources at the bright-end of the number counts is expected to be motivated by submillimetre emission from Galactic objects and gravitationally lensed high-redshift galaxies. We show that the S2LXS XMM-LSS number counts are best reproduced by model predictions that include either strong lensing or source blending from a $15''$ beam, which may indicate that both make an important contribution to the over-abundance of sources we observe at the bright-end of the single-dish $850\mu\text{m}$ number counts. We note that the S2LXS XMM-LSS number counts at $S_{850\mu\text{m}} \gtrsim 30\text{ mJy}$ are broadly consistent with these models, which are typically unable to reproduce the very bright-end of the S2CLS $850\mu\text{m}$ number counts.

In Chapter 4 we present the first results for an ALMA follow-up survey of the 17 brightest sources in the S2LXS XMM-LSS main catalogue. With the exquisite resolution of these ALMA observations (median synthesised beam size of $0.59'' \times 0.50''$) we pinpoint the position of the $S_{850\mu\text{m}} > 1\text{ mJy}$ submillimetre galaxies contributing to the single-dish submillimetre emission, finding a multiplicity fraction (excluding blank maps) of 54% at $S_{850\mu\text{m}} > 12\text{ mJy}$. Our initial results indicate that source blending does not significantly contribute to the abundance of sources observed at the bright-end tail of the $850\mu\text{m}$ single-dish number counts. This is unexpected given that the S2LXS XMM-LSS number counts are broadly reproduced by models that incorporate source blending, and further work is required to confirm this.

Chapter 6

The future of submillimetre astronomy

6.1 Future Infrared/Submillimetre Instruments

Since the first infrared observations in the 1970s (e.g., Low and Kleinmann, 1968; Kleinmann and Low, 1970) the boom in far-infrared and submillimetre facilities has revolutionised our understanding of the Universe, uncovering a cosmologically important population of dust-enshrouded galaxies, some of which are too faint to be detected in the optical surveys of today (e.g., Shu et al., 2022; Wang et al., 2019). Far-infrared/submillimetre facilities largely fall into two distinct categories: those that offer the opportunity for surveys of large areas of the sky to moderate depth and resolution, and those that provide deep observations at sub-arcsecond resolution. Wide area far-infrared/submillimetre surveys can be conducted with facilities in space such as the *Herschel Space Observatory* and *Planck* (noting that the lifespan of space missions is usually only a few years), or using single-dish instruments such as the Atacama Pathfinder Experiment, (APEX, 12m diameter), JCMT (15 m diameter), IRAM (30m diameter) and the Large Millimeter Telescope (LMT, 50m diameter), with the largest surveys ranging from a few degrees (e.g., S2CLS; Geach et al., 2017), through a few hundred degrees (e.g., H-ATLAS; Eales et al., 2010) to all sky surveys (e.g., Planck Collaboration et al., 2020). Whereas surveys requiring sub-arcsecond spatial resolution make use of (sub-)millimetre interferometers such as the Northern Extended Millimeter Array, the Submillimetre Array and ALMA. These facilities complement one another, and it is common in extragalactic astronomy to make use of space observatories or single-dish telescopes for wide-area surveys to first identify far-infrared luminous galaxies or galaxy clusters, and to then follow up on these detections with interferometers for sub-arcsecond imaging

and spectroscopy. Going forward future facilities aim to close the gap between these methods of observation; offering large area surveys with improved spatial resolution and sensitivity.

6.1.1 Atacama Large Aperture Submillimetre Telescope

The Atacama Large Aperture Submillimetre Telescope (AtLAST) is a concept for a 50m diameter (sub)millimetre single dish telescope¹ that will deliver efficient continuum and spectroscopic observations (Klaassen et al., 2020). The planned telescope will have a large field of view (≈ 2 deg diameter) and mapping speeds hundreds of times greater than any current (or proposed) >12 m aperture facilities. The telescope will be fully powered by renewable energy and will be located at a high, dry site in the Atacama desert, with the goal to start construction in the 2030s. At the planned elevation ($\approx 5100 - 5500$ m above sea level) there will be good atmospheric transmission up to $\nu \sim 1$ THz (Klaassen et al., 2020). Confusion noise currently limits existing single-dish facilities to detecting only the most extreme star-burst galaxies. However, with a larger aperture (and so finer angular resolution, $\approx 1.8''$ at $450 \mu\text{m}$) than existing far-infrared/submillimetre facilities AtLAST will push down the confusion limit, allowing for more sensitive observations, making it possible to detect “normal” star-forming galaxies at high redshift (Ramasawmy et al., 2022). The science goals of AtLAST cross all scales; from investigating how the Sun’s thermal and magnetic properties evolve over time, to measuring the cold diffuse gas in the circumgalactic medium of nearby and distant galaxies, to detecting and spatially resolving the kinetic and thermal Sunyaev-Zel’dovich effect on the scale of galaxy clusters (Ramasawmy et al., 2022).

6.1.2 James Webb Space Telescope

The James Webb Space Telescope (JWST) launched on 25th December 2021. This infrared telescope has an innovative design featuring an approximately 6.5m diameter primary mirror made up of 18 separate segments that unfold and adjust to shape once in space. Onboard are four scientific instruments for imaging and spectroscopy; the Near Infrared Camera (NIRCam), the Near Infrared Spectrograph (NIRSpec), the Mid Infrared Instrument (MIRI) and the Fine Guidance Sensor/Near Infrared Imager and Slitless Spectrograph (FGS-NIRISS), which combined are sensitive over a wavelength range $0.6 \mu\text{m} - 28.3 \mu\text{m}$. JWST has an angular resolution

¹The AtLAST design study project is funded by the European Union’s Horizon 2020 research and innovation programme.

of $0.07''$ at $\lambda = 2\mu\text{m}$ and $0.8''$ at $\lambda = 25.5\mu\text{m}$, vastly improving on existing facilities (for comparison, the VISTA VIDEO K_s -band has a FWHM of $\lambda = 0.8''$ and the SWIRE Multiband Imaging Photometer a FWHM of $\sim 6''$ at $24\mu\text{m}$; Jarvis et al., 2013; Lonsdale et al., 2003). The primary science goals of the JWST mission are to search for the first galaxies after the Big Bang, to study the formation of galaxies, stars and planets, and to measure the physical and chemical properties of planetary systems to investigate the potential for life in these systems. The primary aims of JWST are already beginning to be realised, with four galaxies already detected with spectroscopically confirmed redshifts $10.3 \leq z \leq 13.2$, less than 450 million years after the Big Bang (Curtis-Lake et al., 2022).

6.1.3 Third generation $850\mu\text{m}$ camera on the JCMT

The proposed third generation wide-field camera for the JCMT will have a detector array of 3,636 pixels, each comprising two Microwave Kinetic Induction Detectors (MKID). The new $850\mu\text{m}$ camera will have a field of view of $12'$, almost double that of SCUBA-2, and will provide a mapping speed 10 times greater than its predecessor (Liu et al., 2019b). The largest extragalactic surveys with JCMT at $850\mu\text{m}$ to date map areas of $\lesssim 10\text{deg}^2$, falling significantly short compared to far-infrared surveys which cover 100s of square degrees (e.g., HerMES; Oliver et al., 2012). Surveys at $850\mu\text{m}$ are more sensitive to $z > 4$ dust emission than observations in the far-infrared, but with areas of only $\lesssim 10\text{deg}^2$, surveys such as S2LXS (see Chapter 3) only probe the tip of the high redshift, dust obscured galaxy population. This third generation camera for the JCMT has the ability to perform larger area and deeper surveys making it possible to survey $\sim 300\text{deg}^2$ to a depth of 2mJy beam^{-1} in 2500 hours, matching the coverage at shorter wavelengths (Wang et al., 2020).

6.1.4 Origins

Origins is a concept study for a NASA near-to-far infrared space telescope. This is currently being evaluated by NASA, along with three other studies, for selection as the next NASA large strategic science mission. Origins will have a broad wavelength coverage ($2.8\mu\text{m}$ – $588\mu\text{m}$) and is 1000 times more sensitive (Meixner et al., 2019) than previous far-infrared space missions (i.e., *Herschel Space Observatory*). The preliminary science goals for this mission are wide ranging from using high resolution mid-to-far infrared spectroscopy to assess the availability of water for habitable planets and searching for signs of life, to measuring spectra and photometry

for millions of galaxies with a view to estimating redshifts, star formation rates and black hole accretion rates back to the epoch of reionization (Meixner et al., 2019).

6.1.5 TolTEC camera for the Large Millimeter-wave Telescope

TolTEC is the new camera for the Large Millimeter-wave Telescope (LMT) and will operate at wavelengths of 1.1 mm, 1.4 mm and 2 mm. The TolTEC public legacy surveys include an ultra-deep survey ($\sim 1 \text{ deg}^2$) with a spatial resolution of $5''$ (at 1.1 mm) that targets the Luminous Infrared Galaxy population ($L_{\text{IR}} > 10^{11} L_{\odot}$). Millimeter wavelengths are sensitive to dust emission out to the highest redshifts, and so this survey is expected to detect star-forming galaxies out to $z \sim 10$. By linking these star-forming galaxies to their optical counterparts, this survey aims to trace the build up of stellar mass and metals through cosmic time (Pope et al., 2019).

6.1.6 Large Latin American Millimeter Array

The Large Latin American Millimeter Array (LLAMA) is a 12 m single dish telescope currently under construction in the Puna de Atacama desert in Argentina. LLAMA is a multipurpose facility designed to function as both a stand-alone telescope or as part of a larger interferometer, and operates over a wavelength range of $320 \mu\text{m}$ to 10 mm (Romero, 2020). With such a broad wavelength coverage LLAMA has many possible science applications including observing the lower solar chromosphere, investigating the chemical enrichment of the interstellar medium around galaxies, detecting Ultra-Luminous Infrared Galaxies and studying fluctuations in the CMB (Romero, 2020).

6.1.7 Cerro Chajnantor Atacama Telescope - prime

The Cerro Chajnantor Atacama Telescope - prime (CCAT-prime)² is a 6 m diameter submillimeter/millimeter telescope that will be located at an elevation of 5600 m on Cerro Chajnantor in the Atacama Desert (Parshley et al., 2018). CCAT-prime is designed to operate over a wavelength range of $200 \mu\text{m}$ to 3 mm, albeit observations at $200 \mu\text{m}$ will only be possible in the best weather conditions. CCAT-prime has a finer spatial resolution at $350 \mu\text{m}$ ($\sim 15''$) than the *Herschel Space Observatory* and a field of view of 0.78 deg^2 (200,000 times larger than ALMA at

²CCAT-Prime was renamed as the Fred Young Submillimeter Telescope in 2020

this wavelength), and so is ideally placed for conducting wide area, confusion-limited surveys ($\sim 3\times$ deeper than *Herschel*) of star-forming galaxies out to $z < 4$ (CCAT-Prime collaboration et al., 2021).

6.2 Summary

The launch of JWST and the (potential) construction of these upcoming facilities, along with existing state of the art facilities (i.e., ALMA, SMA, NOEMA), will help to answer fundamental outstanding questions in the field of submillimetre astronomy such as; *when and how did the earliest dust enrichment happen, how do SMGs form (i.e., via galaxy mergers or disk instabilities), and what is the nature of the earliest SMGs?* With AtLAST, Origins, CCAT-prime and the third generation camera on the JCMT we can look forward to wide area imaging and spectroscopy surveys of the extragalactic sky at infrared and submillimetre wavelengths, with surveys detecting not only the most extreme star-forming galaxies, but extending to “normal” star-forming galaxies (even at high redshifts) allowing us to study if/how the formation mechanism for these “normal” star-forming galaxies differs from the most extreme, star-burst galaxies. Ultra-deep extragalactic surveys with the TolTEC camera on the LMT are expected to detect star-forming galaxies to even higher redshifts ($z \lesssim 10$), allowing us to probe the build up of stellar mass and metals during the first 3 Gyr of cosmic time. JWST will enable us, for the first time, to resolve the rest-frame near-infrared emission of the host galaxies of SMGs (e.g., Cheng et al., 2022), revealing the stellar morphology of these galaxies and allowing us to explore the trigger for the extreme star formation activity of SMGs. With the unrivaled depth of JWST we also expect to observe SMG host galaxies back to the first few hundred million years after the Big Bang, allowing us to investigate the formation of the earliest SMGs right back to the epoch of reionization. With this continuing investment in infrared/submillimetre facilities, the next few decades in the field of submillimetre astronomy will no doubt bring with it many exciting discoveries.

Appendix A

Multi-wavelength imaging for sources in the SCUBA-2 Large eXtragalactic Survey main catalogue

For each source in the S2LXS XMM-LSS $>5\sigma$ catalogue we show (where available) image cutouts from the VLA 1-2GHz survey of the XMM-LSS field (Heywood et al., 2020), the S2LXS XMM-LSS survey at $850\mu\text{m}$ (Chapter 3), the *Herschel* Multi-tiered Extragalactic Survey at a wavelength of $250\mu\text{m}$ (HerMES; Oliver et al., 2012), the *Spitzer* Survey of the Deep Drilling Fields centred on a wavelength of $4.5\mu\text{m}$ (Deep Drill; Lacy et al., 2021), and the Visible and Infrared Survey Telescope for Astronomy Deep Extragalactic Observations survey in the K_s -band (VISTA VIDEO; Jarvis et al., 2013). We also show a colour image made using y -, i - and g -band data from the Hyper Suprime-Cam Subaru Strategic Program (HSC-SSP; Aihara et al., 2018).

S2LXSJ021831-053131

S2LXSJ021831-053131 (Figure A.1) is the brightest source in S2LXS XMM-LSS with a deboosted flux density of $S_{850\mu\text{m}} = 48.1 \pm 6.3\text{mJy}$. This source, which was also detected in S2CLS UDS (Geach et al., 2017), is a strongly-lensed galaxy commonly known as ‘Orochi’ (Ikarashi et al., 2011). ALMA follow up has identified 2 counterparts to the single-dish source; AS2UDS0001.0 with a flux density of $S_{870\mu\text{m}} = 30.3\text{mJy}$ and AS2UDS0001.1 with a flux density of $S_{870\mu\text{m}} = 5.2\text{mJy}$ (e.g., Stach et al., 2019).

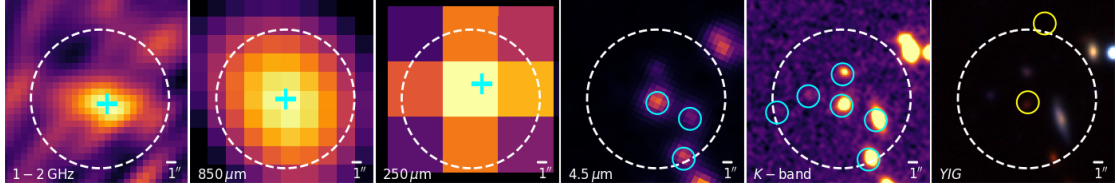


FIGURE A.1: We show multi-wavelength image cutouts ($20'' \times 20''$) centred on the position of source S2LXSJ021831-053131 from the $>5\sigma$ catalogue of the S2LXS-XMM-LSS survey (Chapter 3). Image data is from (left to right) the VLA 1-2GHz survey of the XMM-LSS field (Heywood et al., 2020), the S2LXS XMM-LSS survey at $850\mu\text{m}$ (Chapter 3), HerMES at a wavelength of $250\mu\text{m}$ (Oliver et al., 2012), Deep Drill centred on a wavelength of $4.5\mu\text{m}$ (Lacy et al., 2021) and VISTA VIDEO in the K_s -band (Jarvis et al., 2013). The colour image (far right) is made using y -, i - and g -band data from HSC-SSP (Aihara et al., 2018). In the $850\mu\text{m}$ image we show the position of the S2LXS XMM-LSS source marked with a cyan cross. We overplot the position (cyan cross) of potential multi-wavelength counterparts from the VLA 1-2GHz survey of the XMM-LSS field (Heywood et al., 2020) and the HerMES data release 4 (DR4) xID250 catalogue (Roseboom et al., 2010, 2012; Oliver et al., 2012) in the corresponding images. In the Deep Drill $4.5\mu\text{m}$ image we overplot the position of potential counterparts (cyan circles) from the Deep Drill dual band catalogue, which includes sources detected at both $3.6\mu\text{m}$ and $4.5\mu\text{m}$ (Lacy et al., 2021). In the VISTA VIDEO K_s -band image we overplot the position of potential counterparts (cyan circles) from the K_s -band selected catalogue of Adams et al. (2020); Hatfield et al. (2022). The position of ALMA counterparts from the AS2UDS catalogue (Stach et al., 2019) are shown in the colour image (yellow circles).

S2LXSJ022700-052405

S2LXSJ022700-052405 (Figure A.2) has a deboosted flux density of $S_{850\mu\text{m}} = 20.3 \pm 7.4$ mJy and is one of the sources observed with ALMA in Cycle 9. This source has two ALMA counterparts; AS2LXS04.0 with a flux density of 8.2 ± 0.2 mJy and AS2LXS04.1 with a flux density of 1.2 ± 0.2 mJy (Chapter 4). Both of the ALMA galaxies have a near-infrared counterpart (within a $<1''$ matching radius) in the K_s -band selected catalogue of Adams et al. (2020); Hatfield et al. (2022). These galaxies are not detected in the VLA 1-2GHz survey of the XMM-LSS field (Heywood et al., 2020), which may indicate that one or more of the ALMA counterparts lies at a redshift $z > 3.5$ (see subsection 1.3.1 for discussion of the positive K correction at radio wavelengths).

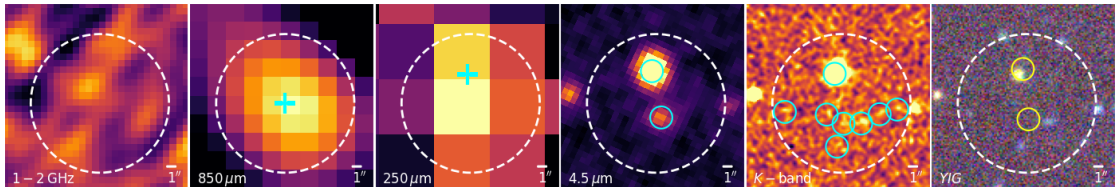


FIGURE A.2: We show multi-wavelength image cutouts ($20'' \times 20''$) centred on the position of source S2LXSJ022700-052405 from the $>5\sigma$ catalogue of the S2LXS-XMM-LSS survey (Chapter 3). The figure description is the same as for Figure A.1 (where image and catalogue data are available). The ALMA counterparts were identified in an ALMA follow up survey of the brightest S2LXS galaxies (Chapter 4).

S2LXSJ021735-054854

S2LXSJ021735-054854 (Figure A.3) has a deboosted flux density of $S_{850\mu\text{m}} = 18.5 \pm 7.9$ mJy and is one of the sources observed with ALMA in Cycle 9. This source is not detected at the detection threshold ($>5\sigma$) of the ALMA survey (Chapter 4). There are no potential *Herschel* 250 μm counterparts within the SCUBA-2 beam, but this source has one potential counterpart in Deep Drill (Lacy et al., 2021), albeit this lies $\approx 7''$ from the position of the S2LXS XMM-LSS source. The lack of a detection in the *Herschel* 250 μm and ALMA maps, and the lack of a possible near-infrared counterpart nearby points to this being a spurious detection in the S2LXS XMM-LSS mosaic (noting that the false detection rate in S2LXS XMM-LSS is 10% at $>5\sigma$, so statistically we expect around 4 sources in the $>5\sigma$ catalogue to be spurious, see Chapter 3 for details). Whilst this source seems likely to be a spurious detection, it is also possible that multiple faint submillimetre galaxies, which are too faint to be detected at the detection threshold ($>5\sigma$) of the ALMA survey, are responsible for the single-dish submillimetre emission.

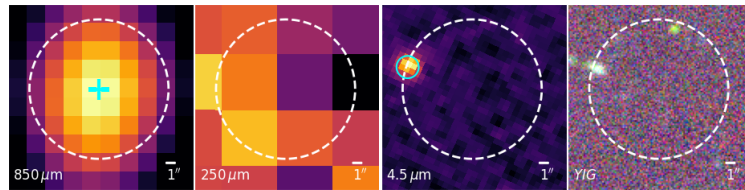


FIGURE A.3: We show multi-wavelength image cutouts ($20'' \times 20''$) centred on the position of source S2LXSJ021735-054854 from the $>5\sigma$ catalogue of the S2LXS-XMM-LSS survey (Chapter 3). The figure description is the same as for Figure A.1 (where image and catalogue data are available).

S2LXSJ022548-041751

S2LXSJ022548-041751 (Figure A.4) has a deboosted flux density of $S_{850\mu\text{m}} = 23.1 \pm 5.4$ mJy. This source was observed in an ALMA survey of a sample of galaxies from HerMES (Bussmann et al., 2015) and has one counterpart with a flux of $S_{870\mu\text{m}} = 17.96$ mJy. This galaxy is weakly lensed (Bussmann et al., 2015) and has a spectroscopic redshift of $z \sim 3$ (Leung et al., 2019). This galaxy has multiple potential counterparts within the SCUBA-2 beam in the Deep Drill (Lacy et al., 2021) and VISTA VIDEO (Jarvis et al., 2013) maps, and so identifying the true counterpart would be difficult in the absence of the ALMA observations.

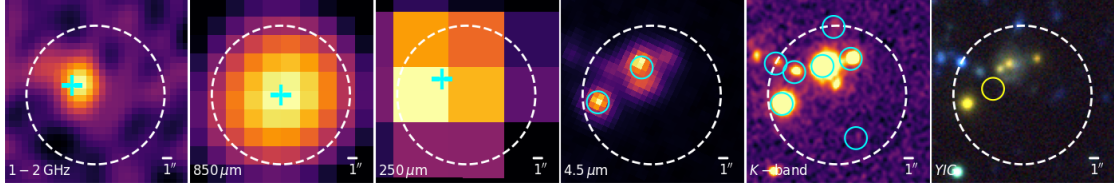


FIGURE A.4: We show multi-wavelength image cutouts ($20'' \times 20''$) centred on the position of source S2LXSJ022548-041751 from the $>5\sigma$ catalogue of the S2LXS-XMM-LSS survey (Chapter 3). The figure description is the same as for Figure A.1 (where image and catalogue data are available). The ALMA counterpart was identified in an ALMA survey of a sample of HerMES galaxies (Bussmann et al., 2015).

S2LXSJ021520-053222

S2LXSJ021520-053222 (Figure A.5) has a deboosted flux density of $S_{850\mu\text{m}} = 18.4 \pm 7.7$ mJy and is one of the sources observed with ALMA in Cycle 9. This source is not detected at the detection threshold ($>5\sigma$) of the ALMA survey (Chapter 4), and there are no potential *Herschel* 250 μm or VLA 1-2 GHz counterparts within the SCUBA-2 beam. The lack of a detection in the *Herschel* 250 μm , VLA 1-2 GHz and ALMA maps points to this being a spurious detection in the S2LXS XMM-LSS mosaic. Whilst this source seems likely to be a spurious detection, it is also possible that multiple faint submillimetre galaxies, which are too faint to be detected at the detection threshold ($>5\sigma$) of the ALMA survey, are responsible for the single-dish submillimetre emission.

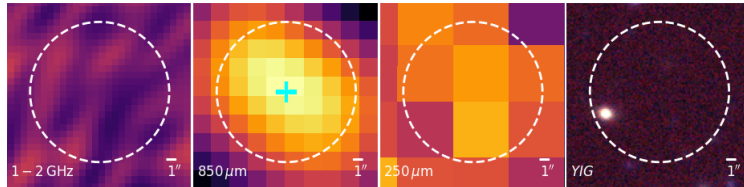


FIGURE A.5: We show multi-wavelength image cutouts ($20'' \times 20''$) centred on the position of source S2LXSJ021520-053222 from the $>5\sigma$ catalogue of the S2LXS-XMM-LSS survey (Chapter 3). The figure description is the same as for Figure A.1 (where image and catalogue data are available).

S2LXSJ022252-042412

S2LXSJ022252-042412 (Figure A.6) has a deboosted flux density of $S_{850\mu\text{m}} = 16.8 \pm 8.0$ mJy and is one of the sources observed with ALMA in Cycle 9. This source has two ALMA counterparts; AS2LXS14.0 with a flux density of 6.8 ± 0.2 mJy and AS2LXS14.1 with a flux density of 1.6 ± 0.2 mJy (Chapter 4). Only one of the ALMA galaxies (AS2LXS14.0) has a near-infrared counterpart (within a $<1''$ matching radius) in the K_s -band selected catalogue of Adams et al. (2020); Hatfield et al. (2022). The ALMA galaxies are separated by $\sim 1''$ so it may be that the

near-infrared emission from these sources is blended in the VISTA VIDEO K_s -band map (Jarvis et al., 2013), which has a resolution of $0.8''$. Alternatively AS2LXS14.1 may just be too faint at near-infrared wavelengths to be detected in the VISTA VIDEO survey.

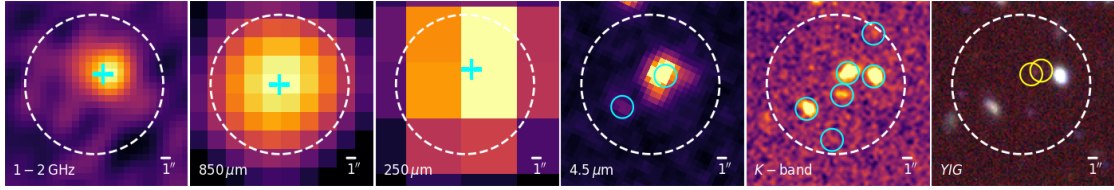


FIGURE A.6: We show multi-wavelength image cutouts ($20'' \times 20''$) centred on the position of source S2LXSJ022252-042412 from the $>5\sigma$ catalogue of the S2LXS-XMM-LSS survey (Chapter 3). The figure description is the same as for Figure A.1 (where image and catalogue data are available). The ALMA counterparts were identified in an ALMA follow up survey of the brightest S2LXS galaxies (Chapter 4).

S2LXSJ022324-042602

S2LXSJ022324-042602 (Figure A.7) has a deboosted flux density of $S_{850\mu\text{m}} = 17.9 \pm 7.7$ mJy and is one of the sources observed with ALMA in Cycle 9. This source has one ALMA counterpart; AS2LXS09.0 with a flux density of 9.3 ± 0.2 mJy (Chapter 4). The ALMA galaxy has a near-infrared counterpart (with a $<1''$ matching radius) in the K_s -band selected catalogue of Adams et al. (2020); Hatfield et al. (2022).

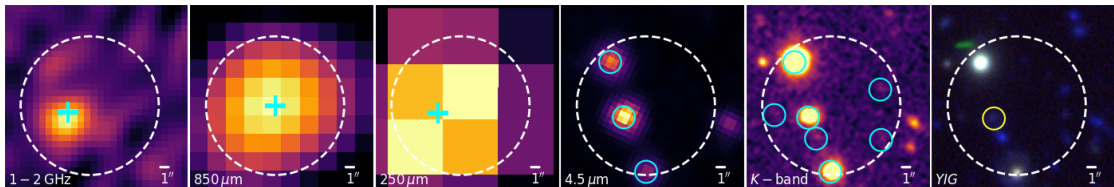


FIGURE A.7: We show multi-wavelength image cutouts ($20'' \times 20''$) centred on the position of source S2LXSJ022324-042602 from the $>5\sigma$ catalogue of the S2LXS-XMM-LSS survey (Chapter 3). The figure description is the same as for Figure A.1 (where image and catalogue data are available). The ALMA counterpart was identified in an ALMA follow up survey of the brightest S2LXS galaxies (Chapter 4).

S2LXSJ022735-051558

S2LXSJ022735-051558 (Figure A.8) has a deboosted flux density of $S_{850\mu\text{m}} = 18.6 \pm 6.5$ mJy and is one of the sources observed with ALMA in Cycle 9. This source has one ALMA counterpart; AS2LXS06.0 with a flux density of 7.0 ± 0.2 mJy (Chapter 4). The ALMA galaxy has a near-infrared counterpart (with a matching radius $<1''$) in the K_s -band selected catalogue of Adams et al. (2020); Hatfield et al. (2022).

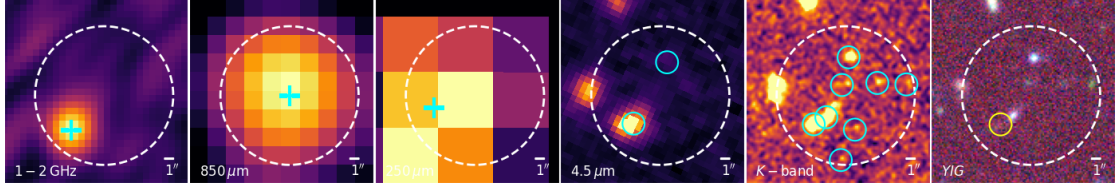


FIGURE A.8: We show multi-wavelength image cutouts ($20'' \times 20''$) centred on the position of source S2LXSJ022735-051558 from the $>5\sigma$ catalogue of the S2LXS-XMM-LSS survey (Chapter 3). The figure description is the same as for Figure A.1 (where image and catalogue data are available). The ALMA counterpart was identified in an ALMA follow up survey of the brightest S2LXS galaxies (Chapter 4).

S2LXSJ022322-033747

S2LXSJ022322-033747 (Figure A.9) has a deboosted flux density of $S_{850\mu\text{m}} = 14.1 \pm 6.8$ mJy and is one of the sources observed with ALMA in Cycle 9. This source has one ALMA counterpart; AS2LXS19.0 with a flux density of 10.3 ± 0.2 mJy (Chapter 4). This source lies outside the footprints of the VLA 1-2 GHz map of the XMM-LSS field (Heywood et al., 2020) and the VISTA VIDEO survey (Jarvis et al., 2013). The ALMA galaxy has a near-infrared counterpart (with a $<1''$ matching radius) in Deep Drill (Lacy et al., 2021).

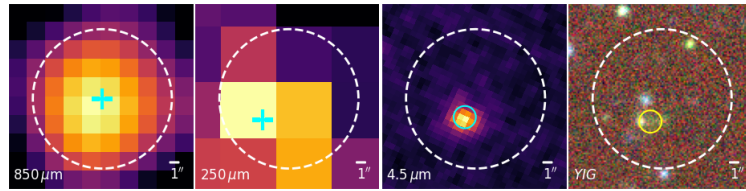


FIGURE A.9: We show multi-wavelength image cutouts ($20'' \times 20''$) centred on the position of source S2LXSJ022322-033747 from the $>5\sigma$ catalogue of the S2LXS-XMM-LSS survey (Chapter 3). The figure description is the same as for Figure A.1 (where image and catalogue data are available). The ALMA counterpart was identified in an ALMA follow up survey of the brightest S2LXS galaxies (Chapter 4).

S2LXSJ022614-045616

S2LXSJ022614-045616 (Figure A.10) has a deboosted flux density of $S_{850\mu\text{m}} = 15.2 \pm 6.2$ mJy and is one of the sources observed with ALMA in Cycle 9. This source has three ALMA counterparts; AS2LXS07.0 with a flux density of 5.3 ± 0.2 mJy, AS2LXS07.1 with a flux density of 2.0 ± 0.2 mJy and AS2LXS07.3 with a flux density of 0.6 ± 0.2 mJy (Chapter 4). Two of the ALMA galaxies (AS2LXS07.0 and AS2LXS07.1) have near-infrared counterparts (within a $<1''$ matching radius) in the K_s -band selected catalogue of Adams et al. (2020); Hatfield et al. (2022). The remaining galaxy (AS2LXS07.2) is too faint at near-infrared wavelengths to be detected in the VISTA VIDEO survey. The ALMA galaxies are not detected in the VLA 1-2 GHz survey

of the XMM-LSS field (Heywood et al., 2020), which may indicate that one or more of these ALMA counterparts lies at a redshift $z > 3.5$.

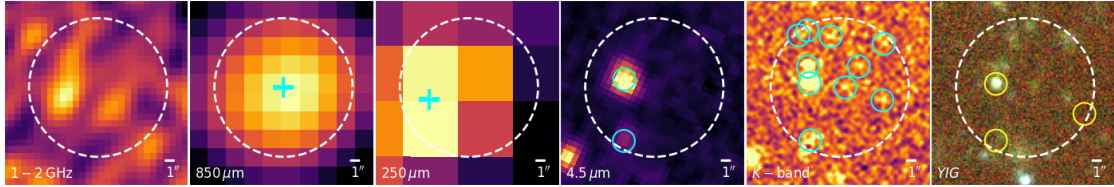


FIGURE A.10: We show multi-wavelength image cutouts ($20'' \times 20''$) centred on the position of source S2LXSJ022614-045616 from the $>5\sigma$ catalogue of the S2LXS-XMM-LSS survey (Chapter 3). The figure description is the same as for Figure A.1 (where image and catalogue data are available). The ALMA counterparts were identified in an ALMA follow up survey of the brightest S2LXS galaxies (Chapter 4).

S2LXSJ022854-042445

S2LXSJ022854-042445 (Figure A.11) has a deboosted flux density of $S_{850\mu\text{m}} = 13.8 \pm 5.9$ mJy and is one of the sources observed with ALMA in Cycle 9. The source has one ALMA counterpart; AS2LXS12.0 with a flux density of 11.6 ± 0.2 mJy (Chapter 4). The ALMA galaxy lies outside the footprint of VISTA VIDEO (Jarvis et al., 2013), but has a near-infrared counterpart (with a $<1''$ matching radius) in Deep Drill (Lacy et al., 2021). This source is not detected in the VLA 1-2GHz survey of the XMM-LSS field (Heywood et al., 2020), which may indicate this lies at a redshift $z > 3.5$.

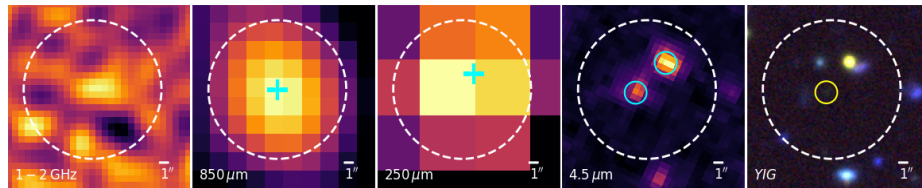


FIGURE A.11: We show multi-wavelength image cutouts ($20'' \times 20''$) centred on the position of source S2LXSJ022854-042445 from the $>5\sigma$ catalogue of the S2LXS-XMM-LSS survey (Chapter 3). The figure description is the same as for Figure A.1 (where image and catalogue data are available). The ALMA counterpart was identified in an ALMA follow up survey of the brightest S2LXS galaxies (Chapter 4).

S2LXSJ021826-041900

S2LXSJ021826-041900 (Figure A.12) has a deboosted flux density of $S_{850\mu\text{m}} = 13.1 \pm 6.2$ mJy and is one of the sources observed with ALMA in Cycle 9. This source is not detected at the detection threshold ($>5\sigma$) of the ALMA survey (Chapter 4), which is points to this being a spurious detection in the S2LXS XMM-LSS mosaic. However, there is a potential *Herschel* 250 μm counterpart from the HerMES DR4 xID250 catalogue (Roseboom et al., 2010, 2012;

Oliver et al., 2012) within the SCUBA-2 beam, which supports this source being a real detection in the S2LXS XMM-LSS mosaic. If this is not a spurious detection in the S2LXS XMM-LSS map, it may be that the galaxy responsible for the submillimetre emission is larger than the ALMA beam, meaning that the flux is spread out over multiple ALMA beams, and so the source falls below the detection threshold of the ALMA survey.

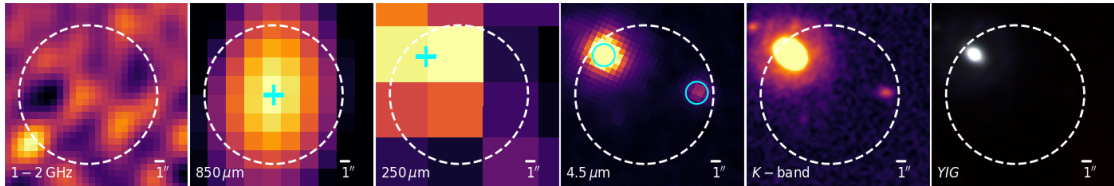


FIGURE A.12: We show multi-wavelength image cutouts ($20'' \times 20''$) centred on the position of source S2LXSJ021826-041900 from the $>5\sigma$ catalogue of the S2LXS-XMM-LSS survey (Chapter 3). The figure description is the same as for Figure A.1 (where image and catalogue data are available).

S2LXSJ022342-044501

S2LXSJ022342-044501 (Figure A.13) has a deboosted flux density of $S_{850\mu\text{m}} = 14.0 \pm 5.9$ mJy and is one of the sources observed with ALMA in Cycle 9. This source has two ALMA counterparts; AS2LXS11.0 with a flux density of 6.1 ± 0.2 mJy and AS2LXS11.1 with a flux density of 5.0 ± 0.2 mJy (Chapter 4). Both of the ALMA galaxies have near-infrared counterparts (within a $<1''$ matching radius) in the K_s -band selected catalogue of Adams et al. (2020); Hatfield et al. (2022). Neither ALMA galaxy is detected in the VLA 1-2GHz survey of the XMM-LSS field (Heywood et al., 2020), which may indicate that one or both of these galaxies lies at a redshift $z > 3.5$.

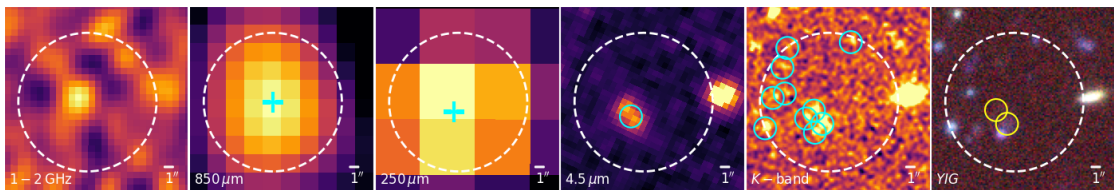


FIGURE A.13: We show multi-wavelength image cutouts ($20'' \times 20''$) centred on the position of source S2LXSJ022342-044501 from the $>5\sigma$ catalogue of the S2LXS-XMM-LSS survey (Chapter 3). The figure description is the same as for Figure A.1 (where image and catalogue data are available). The ALMA counterparts were identified in an ALMA follow up survey of the brightest S2LXS galaxies (Chapter 4).

S2LXSJ022332-042948

S2LXSJ022332-042948 (Figure A.14) has a deboosted flux density of $S_{850\mu\text{m}} = 12.7 \pm 6.3$ mJy and is one of the sources observed with ALMA in Cycle 9. This source has one ALMA counterpart; A2SLXS08.0 with a flux density of 8.8 ± 0.2 mJy (Chapter 4). This source does not have a near-infrared counterpart in either Deep Drill (Lacy et al., 2021) or the K_s -band selected catalogue of Adams et al. (2020); Hatfield et al. (2022). This source is not detected in the VLA 1-2 GHz survey of the XMM-LSS field (Heywood et al., 2020), which may indicate this lies at a redshift $z > 3.5$.

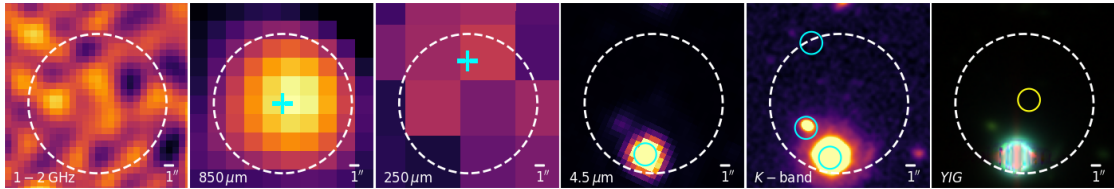


FIGURE A.14: We show multi-wavelength image cutouts ($20'' \times 20''$) centred on the position of source S2LXSJ022332-042948 from the $>5\sigma$ catalogue of the S2LXS-XMM-LSS survey (Chapter 3). The figure description is the same as for Figure A.1 (where image and catalogue data are available). The ALMA counterpart was identified in an ALMA follow up survey of the brightest S2LXS galaxies (Chapter 4).

S2LXSJ022649-035146

S2LXSJ022649-035146 (Figure A.15) has a deboosted flux density of $S_{850\mu\text{m}} = 14.1 \pm 5.8$ mJy and is one of the sources observed with ALMA in Cycle 9. This source is not detected at the detection threshold ($>5\sigma$) of the ALMA survey (Chapter 4), and there are no potential VLA 1-2 GHz, *Herschel* 250 μm or Deep Drill counterparts within the SCUBA-2 beam. The lack of a detection in the VLA 1-2 GHz, *Herschel* 250 μm and ALMA maps points to this being a spurious detection in the S2LXS XMM-LSS mosaic. Whilst this source seems likely to be a spurious detection, it is also possible that multiple faint submillimetre galaxies, which are too faint to be detected at the detection threshold ($>5\sigma$) of the ALMA survey, are responsible for the single-dish submillimetre emission.

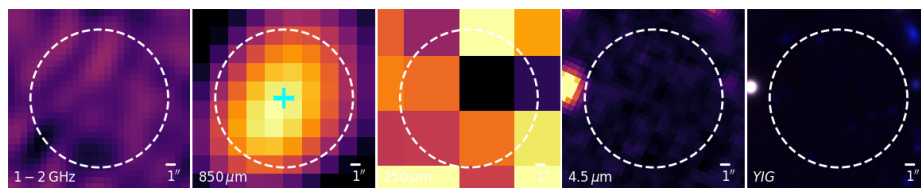


FIGURE A.15: We show multi-wavelength image cutouts ($20'' \times 20''$) centred on the position of source S2LXSJ022649-035146 from the $>5\sigma$ catalogue of the S2LXS-XMM-LSS survey (Chapter 3). The figure description is the same as for Figure A.1 (where image and catalogue data are available).

S2LXSJ021938-042930

S2LXSJ021938-042930 (Figure A.16) has a deboosted flux density of $S_{850\mu\text{m}} = 14.9 \pm 5.3$ mJy and is one of the sources observed with ALMA in Cycle 9. This source has two ALMA counterparts; AS2LXS13.0 with a flux density of 7.9 ± 0.2 mJy and AS2LXS13.1 with a flux density of 4.2 ± 0.2 mJy (Chapter 4). Neither ALMA galaxy has a near-infrared counterpart (within a matching radius of $<1''$) in Deep Drill (Lacy et al., 2021) or the K_s -band selected catalogue of Adams et al. (2020); Hatfield et al. (2022). However, if we extend the matching radius to $<1.5''$, AS2LXS13.1 matches to a source in both near-infrared catalogues. This non-detection in the near-infrared maps may be due to the ALMA counterparts being too faint at near-infrared wavelengths to be detected or due to a positional offset between the ALMA and near-infrared maps. Neither ALMA galaxy is detected in the VLA 1-2 GHz survey of the XMM-LSS field (Heywood et al., 2020), which may indicate that one or both of these galaxies lie at a redshift $z > 3.5$.

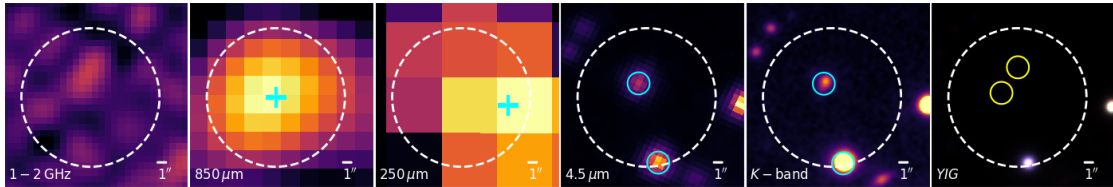


FIGURE A.16: We show multi-wavelength image cutouts ($20'' \times 20''$) centred on the position of source S2LXSJ021938-042930 from the $>5\sigma$ catalogue of the S2LXS-XMM-LSS survey (Chapter 3). The figure description is the same as for Figure A.1 (where image and catalogue data are available). The ALMA counterparts were identified in an ALMA follow up survey of the brightest S2LXS galaxies (Chapter 4).

S2LXSJ022400-034623

S2LXSJ022400-034623 (Figure A.17) has a deboosted flux density of $S_{850\mu\text{m}} = 13.4 \pm 5.8$ mJy and is one of the sources observed with ALMA in Cycle 9. This source has one ALMA counterpart; AS2LXS18.0 with a flux density of 8.3 ± 0.2 mJy (Chapter 4). This source lies outside the footprints of the VLA 1-2 GHz map of the XMM-LSS field (Heywood et al., 2020) and the VISTA VIDEO survey (Jarvis et al., 2013). The ALMA galaxy does not have a near-infrared counterpart in Deep Drill (Lacy et al., 2021).

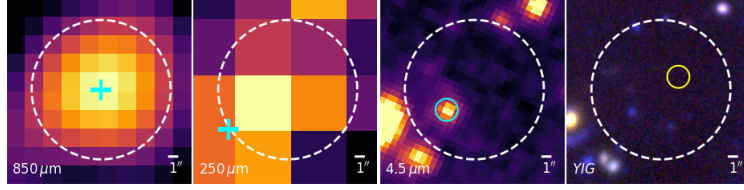


FIGURE A.17: We show multi-wavelength image cutouts ($20'' \times 20''$) centred on the position of source S2LXSJ022400-034623 from the $>5\sigma$ catalogue of the S2LXS-XMM-LSS survey (Chapter 3). The figure description is the same as for Figure A.1 (where image and catalogue data are available). The ALMA counterpart was identified in an ALMA follow up survey of the brightest S2LXS galaxies (Chapter 4).

S2LXSJ022042-053806

S2LXSJ022042-053806 (Figure A.18) has a deboosted flux density of $S_{850\mu\text{m}} = 16.4 \pm 4.1$ mJy and is one of the sources observed with ALMA in Cycle 9. This source has two ALMA counterparts; AS2LXS03.0 with a flux density of 11.6 ± 0.2 mJy and AS2LXS03.1 with a flux density of 2.3 ± 0.2 mJy (Chapter 4). These ALMA galaxies lie outside the footprint of the VISTA VIDEO survey (Jarvis et al., 2013), but one of these galaxies, AS2LXS03.0, has a counterpart in Deep Drill (Lacy et al., 2021). Neither ALMA galaxy is detected in the VLA 1-2 GHz survey of the XMM-LSS field (Heywood et al., 2020), which may indicate that one or both of these galaxies lies at a redshift $z > 3.5$.

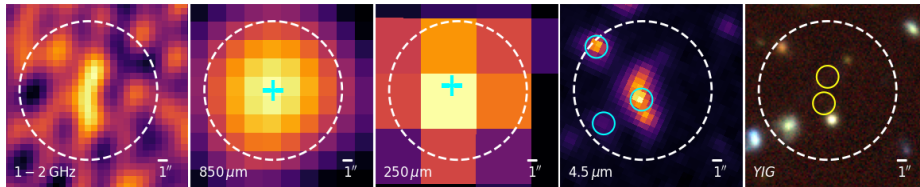


FIGURE A.18: We show multi-wavelength image cutouts ($20'' \times 20''$) centred on the position of source S2LXSJ022042-053806 from the $>5\sigma$ catalogue of the S2LXS-XMM-LSS survey (Chapter 3). The figure description is the same as for Figure A.1 (where image and catalogue data are available). The ALMA counterparts were identified in an ALMA follow up survey of the brightest S2LXS galaxies (Chapter 4).

S2LXSJ021943-052436

S2LXSJ021943-052436 (Figure A.19) has a deboosted flux density of $S_{850\mu\text{m}} = 16.7 \pm 3.7$ mJy. This source was observed in an ALMA survey of a sample of galaxies from HerMES (Bussmann et al., 2015) and has five counterparts with fluxes in the range $S_{870\mu\text{m}} = 0.94\text{--}7.15$ mJy. These galaxies do not appear to be lensed (Bussmann et al., 2015) and lie in an arc-like shape, indicating that these galaxies may reside in a larger filamentary over density. This galaxy has

two potential counterparts within the SCUBA-2 beam in Deep Drill (Lacy et al., 2021). However, there appears to be possible counterparts at the centre of the $4.5\ \mu\text{m}$ image which are not included in the $4.5\ \mu\text{m}$ Deep Drill catalogue. The single-dish source also has multiple potential counterparts in the VISTA VIDEO (Jarvis et al., 2013) maps, although 3 of the ALMA counterparts are not detected in this image and so identifying the true multi-wavelength counterparts would be difficult in the absence of the ALMA observations.

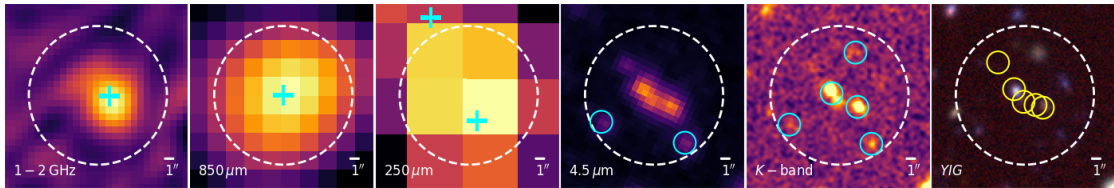


FIGURE A.19: We show multi-wavelength image cutouts ($20'' \times 20''$) centred on the position of source S2LXSJ021943-052436 from the $>5\sigma$ catalogue of the S2LXS-XMM-LSS survey (Chapter 3). The figure description is the same as for Figure A.1 (where image and catalogue data are available). The ALMA counterpart was identified in an ALMA survey of a sample of HerMES galaxies (Bussmann et al., 2015).

S2LXSJ022256-051816

S2LXSJ022256-051816 (Figure A.20) has a deboosted flux density of $S_{850\ \mu\text{m}} = 11.5 \pm 5.5\ \text{mJy}$ and is not one of the sources observed with ALMA in Cycle 9. The S2LXS XMM-LSS source has one potential counterpart from the VLA 1-2GHz survey of the XMM-LSS field (Heywood et al., 2020), one potential *Herschel* $250\ \mu\text{m}$ counterpart from the HerMES DR4 xID250 catalogue (Roseboom et al., 2010, 2012; Oliver et al., 2012), five potential counterparts from Deep Drill (Lacy et al., 2021), and multiple possible near-infrared counterparts from the K_s -band selected catalogue of Adams et al. (2020); Hatfield et al. (2022). The bright source in the colour image (also seen in the VLA, VISTA-VIDEO and Deep Drill images) has been classified as a quasar (Healey et al., 2007).

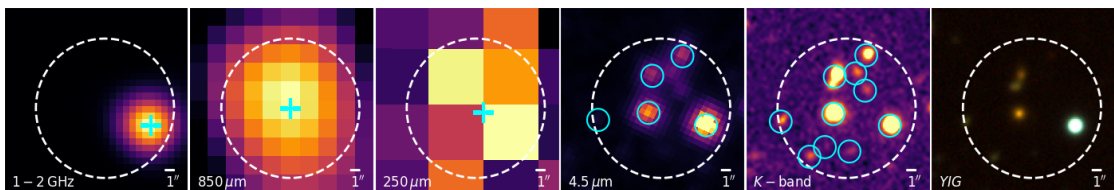


FIGURE A.20: We show multi-wavelength image cutouts ($20'' \times 20''$) centred on the position of source S2LXSJ022256-051816 from the $>5\sigma$ catalogue of the S2LXS-XMM-LSS survey (Chapter 3). The figure description is the same as for Figure A.1 (where image and catalogue data are available).

S2LXSJ022044-044641

S2LXSJ022044-044641 (Figure A.21) has a deboosted flux density of $S_{850\mu\text{m}} = 12.8 \pm 5.2$ mJy and is one of the sources observed with ALMA in Cycle 9. This source has three ALMA counterparts; AS2LXS10.0 with a flux density of 7.3 ± 0.2 mJy, AS2LXS10.1 with a flux density of 3.0 ± 0.2 mJy and AS2LXS10.2 with a flux density of 2.3 ± 0.2 mJy (Chapter 4). Two of the ALMA galaxies (AS2LXS10.1 and AS2LXS10.2) have near-infrared counterparts (within a $<1''$ matching radius) in the K_s -band selected catalogue of Adams et al. (2020); Hatfield et al. (2022). The remaining galaxy (AS2LXS10.0) is too faint at near-infrared wavelengths to be detected in the VISTA VIDEO survey. The ALMA galaxies are not detected in the VLA 1-2GHz survey of the XMM-LSS field (Heywood et al., 2020), which may indicate that one or more of these galaxies lies at a redshift $z > 3.5$.

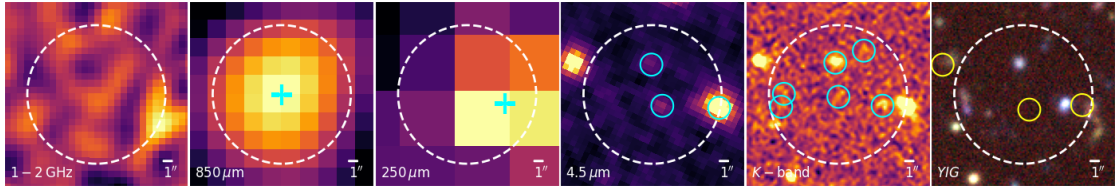


FIGURE A.21: We show multi-wavelength image cutouts ($20'' \times 20''$) centred on the position of source S2LXSJ022044-044641 from the $>5\sigma$ catalogue of the S2LXS-XMM-LSS survey (Chapter 3). The figure description is the same as for Figure A.1 (where image and catalogue data are available). The ALMA counterparts were identified in an ALMA follow up survey of the brightest S2LXS galaxies (Chapter 4).

S2LXSJ022508-045914

S2LXSJ022508-045914 (Figure A.22) has a deboosted flux density of $S_{850\mu\text{m}} = 10.6 \pm 5.3$ mJy and is not one of the sources observed with ALMA in Cycle 9. The S2LXS XMM-LSS source has four potential counterparts from Deep Drill (Lacy et al., 2021), and multiple near-infrared counterparts from the K_s -band selected catalogue of Adams et al. (2020); Hatfield et al. (2022). There are no potential VLA 1-2GHz or *Herschel* 250 μm counterparts within the SCUBA-2 beam. The lack of a detection in these images suggests that this is either a high-redshift source or this may be a spurious detection in the S2XLS XMM-LSS map.

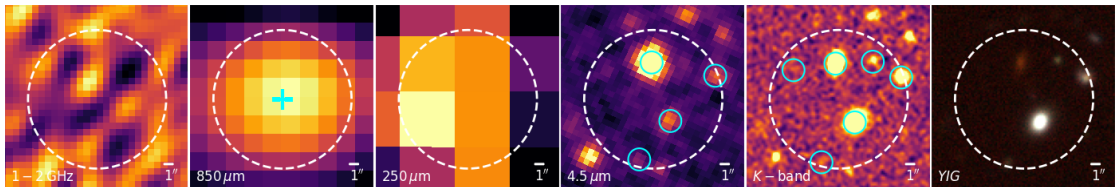


FIGURE A.22: We show multi-wavelength image cutouts ($20'' \times 20''$) centred on the position of source S2LXSJ022508-045914 from the $>5\sigma$ catalogue of the S2LXS-XMM-LSS survey (Chapter 3). The figure description is the same as for Figure A.1 (where image and catalogue data are available).

S2LXSJ022122-042315

S2LXSJ022122-042315 (Figure A.23) has a deboosted flux density of $S_{850\mu\text{m}} = 11.0 \pm 5.1$ mJy and is not one of the sources observed with ALMA in Cycle 9. The S2LXS XMM-LSS source has one potential *Herschel* 250 μm counterpart from the HerMES DR4 xID250 catalogue (Roseboom et al., 2010, 2012; Oliver et al., 2012), one potential counterpart from Deep Drill (Lacy et al., 2021), and four near-infrared counterparts from the K_s -band selected catalogue of Adams et al. (2020); Hatfield et al. (2022), noting that the Deep Drill detection appears to be a blend of 2 sources in the finer resolution of the VISTA VIDEO K_s -band image (Jarvis et al., 2013). This source is not detected in the VLA 1-2GHz survey of the XMM-LSS field (Heywood et al., 2020), which may indicate this lies at a redshift $z > 3.5$.

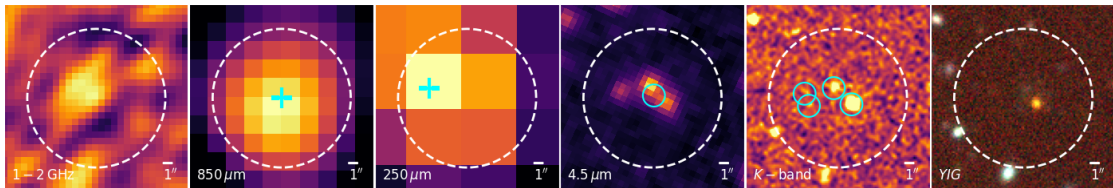


FIGURE A.23: We show multi-wavelength image cutouts ($20'' \times 20''$) centred on the position of source S2LXSJ022122-042315 from the $>5\sigma$ catalogue of the S2LXS-XMM-LSS survey (Chapter 3). The figure description is the same as for Figure A.1 (where image and catalogue data are available).

S2LXSJ022426-042736

S2LXSJ022426-042736 (Figure A.24) has a deboosted flux density of $S_{850\mu\text{m}} = 10.8 \pm 5.1$ mJy and is not one of the sources observed with ALMA in Cycle 9. The S2LXS XMM-LSS source has one potential counterpart from the VLA 1-2GHz survey of the XMM-LSS field (Heywood et al., 2020), two potential *Herschel* 250 μm counterparts from the HerMES DR4 xID250 catalogue (Roseboom et al., 2010, 2012; Oliver et al., 2012), five potential counterparts from Deep Drill (Lacy et al., 2021), and multiple possible near-infrared counterparts from the K_s -band selected catalogue of Adams et al. (2020); Hatfield et al. (2022). Whilst the VLA 1-2GHz survey catalogue includes only one source within the SCUBA-2 beam there appear to be 2 distinct sources of emission in the 1–2 GHz image; these seem to align with the 2 potential counterparts in the HerMES image.

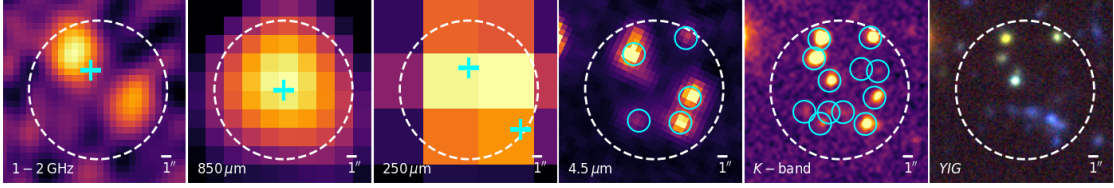


FIGURE A.24: We show multi-wavelength image cutouts ($20'' \times 20''$) centred on the position of source S2LXSJ022426-042736 from the $>5\sigma$ catalogue of the S2LXS-XMM-LSS survey (Chapter 3). The figure description is the same as for Figure A.1 (where image and catalogue data are available).

S2LXSJ021501-050817

S2LXSJ021501-050817 (Figure A.25) has a deboosted flux density of $S_{850\mu\text{m}} = 10.6 \pm 5.1$ mJy and is not one of the sources observed with ALMA in Cycle 9. There are no potential *Herschel* 250 μm or VLA 1-2 GHz counterparts within the SCUBA-2 beam. This source lies outside the footprint of VISTA VIDEO (Jarvis et al., 2013) and Deep Drill (Lacy et al., 2021). The lack of a detection in the *Herschel* 250 μm map suggests that this is either a high-redshift source or this may be a spurious detection in the S2XLS XMM-LSS map.

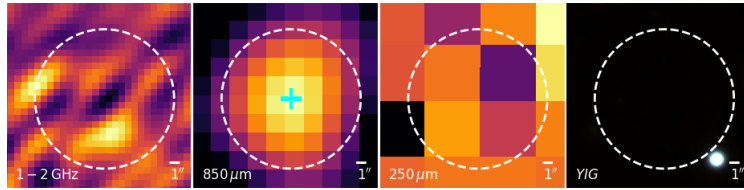


FIGURE A.25: We show multi-wavelength image cutouts ($20'' \times 20''$) centred on the position of source S2LXSJ021501-050817 from the $>5\sigma$ catalogue of the S2LXS-XMM-LSS survey (Chapter 3). The figure description is the same as for Figure A.1 (where image and catalogue data are available).

S2LXSJ021536-045218

S2LXSJ021536-045218 (Figure A.26) has a deboosted flux density of $S_{850\mu\text{m}} = 10.0 \pm 4.8$ mJy and is not one of the sources observed with ALMA in Cycle 9. The S2LXS XMM-LSS source has one potential counterpart from the VLA 1-2 GHz survey of the XMM-LSS field (Heywood et al., 2020), one potential *Herschel* 250 μm counterpart from the HerMES DR4 xID250 catalogue (Roseboom et al., 2010, 2012; Oliver et al., 2012), one potential counterpart from Deep Drill (Lacy et al., 2021), and three possible near-infrared counterparts from the K_s -band selected catalogue of Adams et al. (2020); Hatfield et al. (2022).

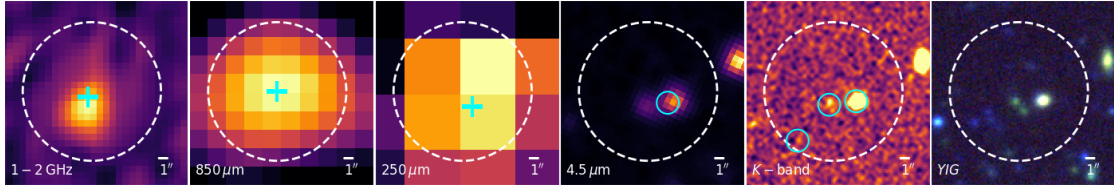


FIGURE A.26: We show multi-wavelength image cutouts ($20'' \times 20''$) centred on the position of source S2LXSJ021536-045218 from the $>5\sigma$ catalogue of the S2LXS-XMM-LSS survey (Chapter 3). The figure description is the same as for Figure A.1 (where image and catalogue data are available).

S2LXSJ021921-045651

S2LXSJ021921-045651 (Figure A.27) has a deboosted flux density of $S_{850\mu\text{m}} = 10.3 \pm 3.9$ mJy. This source was observed in an ALMA survey of a sample of galaxies from the S2CLS UDS field (AS2UDS; Stach et al., 2019) and has three counterparts; AS2UDS0003.0 with a flux density of $S_{870\mu\text{m}} = 7.9$ mJy and $z_{\text{phot}} \approx 3.93$, AS2UDS0003.1 with a flux density of $S_{870\mu\text{m}} = 4.4$ mJy and $z_{\text{phot}} \approx 3.35$, and AS2UDS0003.2 with a flux density of $S_{870\mu\text{m}} = 1.1$ mJy and $z_{\text{phot}} \approx 2.72$ (Dudzevičiūtė et al., 2019).

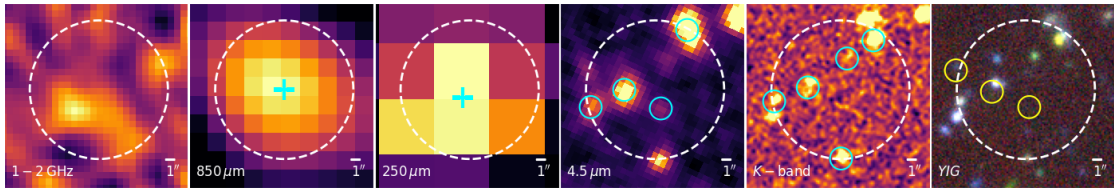


FIGURE A.27: We show multi-wavelength image cutouts ($20'' \times 20''$) centred on the position of source S2LXSJ021921-045651 from the $>5\sigma$ catalogue of the S2LXS-XMM-LSS survey (Chapter 3). The figure description is the same as for Figure A.1 (where image and catalogue data are available). The position of ALMA counterparts from the AS2UDS catalogue (Stach et al., 2019) are shown in the colour image (yellow circles).

S2LXSJ022039-053937

S2LXSJ022039-053937 (Figure A.28) has a deboosted flux density of $S_{850\mu\text{m}} = 9.5 \pm 4.1$ mJy and is not one of the sources observed with ALMA in Cycle 9. There are no potential *Herschel* 250 μm or VLA 1-2 GHz counterparts within the SCUBA-2 beam, and this source lies outside the footprint of the VISTA VIDEO survey (Jarvis et al., 2013). There are four potential counterparts from Deep Drill (Lacy et al., 2021). The lack of a detection in the *Herschel* 250 μm map suggests that this is either a high-redshift source or this may be a spurious detection in the S2XLS XMM-LSS map.

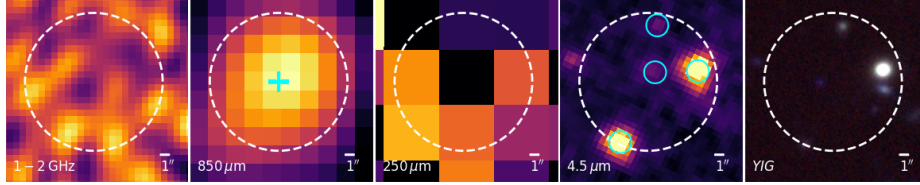


FIGURE A.28: We show multi-wavelength image cutouts ($20'' \times 20''$) centred on the position of source S2LXSJ022039-053937 from the $>5\sigma$ catalogue of the S2LXS-XMM-LSS survey (Chapter 3). The figure description is the same as for Figure A.1 (where image and catalogue data are available).

S2LXSJ021957-053406

S2LXSJ021957-053406 (Figure A.29) has a deboosted flux density of $S_{850\mu\text{m}} = 9.4 \pm 4.0$ mJy and is not one of the sources observed with ALMA in Cycle 9. The S2LXS XMM-LSS source has one potential *Herschel* 250 μm counterpart from the HerMES DR4 xID250 catalogue (Roseboom et al., 2010, 2012; Oliver et al., 2012), two potential counterparts from Deep Drill (Lacy et al., 2021), and four possible near-infrared counterparts from the K_s -band selected catalogue of Adams et al. (2020); Hatfield et al. (2022). This source is not detected in the VLA 1-2 GHz survey of the XMM-LSS field (Heywood et al., 2020), which may indicate this lies at a redshift $z > 3.5$.

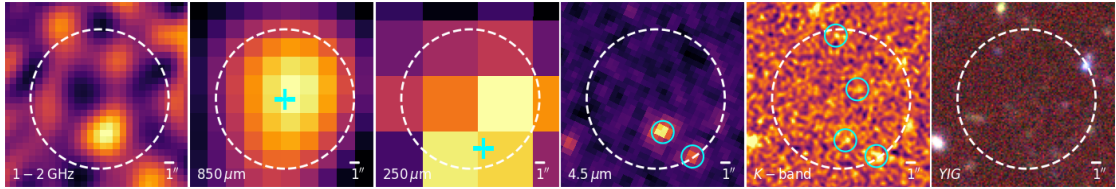


FIGURE A.29: We show multi-wavelength image cutouts ($20'' \times 20''$) centred on the position of source S2LXSJ021957-053406 from the $>5\sigma$ catalogue of the S2LXS-XMM-LSS survey (Chapter 3). The figure description is the same as for Figure A.1 (where image and catalogue data are available).

S2LXSJ022032-053615

S2LXSJ022032-053615 (Figure A.30) has a deboosted flux density of $S_{850\mu\text{m}} = 9.6 \pm 3.7$ mJy and is not one of the sources observed with ALMA in Cycle 9. The S2LXS XMM-LSS source has one potential *Herschel* 250 μm counterpart from the HerMES DR4 xID250 catalogue (Roseboom et al., 2010, 2012; Oliver et al., 2012) and one potential counterpart from Deep Drill (Lacy et al., 2021). This source lies outside the footprint of the VISTA VIDEO survey (Jarvis et al., 2013). This source is not detected in the VLA 1-2 GHz survey of the XMM-LSS field (Heywood et al., 2020), which may indicate this lies at a redshift $z > 3.5$.

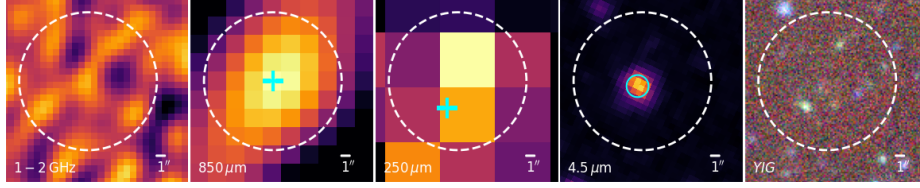


FIGURE A.30: We show multi-wavelength image cutouts ($20'' \times 20''$) centred on the position of source S2LXSJ022032-053615 from the $>5\sigma$ catalogue of the S2LXS-XMM-LSS survey (Chapter 3). The figure description is the same as for Figure A.1 (where image and catalogue data are available).

S2LXSJ021938-052502

S2LXSJ021938-052502 (Figure A.31) has a deboosted flux density of $S_{850\mu\text{m}} = 9.9 \pm 3.5$ mJy and is not one of the sources observed with ALMA in Cycle 9. The S2LXS XMM-LSS source has one potential *Herschel* 250 μm counterpart from the HerMES DR4 xID250 catalogue (Roseboom et al., 2010, 2012; Oliver et al., 2012), one potential counterpart from Deep Drill (Lacy et al., 2021), and multiple possible near-infrared counterparts from the K_s -band selected catalogue of Adams et al. (2020); Hatfield et al. (2022). This source is not detected in the VLA 1-2 GHz survey of the XMM-LSS field (Heywood et al., 2020), which may indicate this lies at a redshift $z > 3.5$.

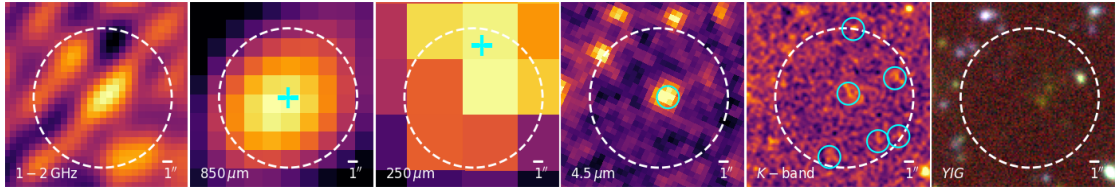


FIGURE A.31: We show multi-wavelength image cutouts ($20'' \times 20''$) centred on the position of source S2LXSJ021938-052502 from the $>5\sigma$ catalogue of the S2LXS-XMM-LSS survey (Chapter 3). The figure description is the same as for Figure A.1 (where image and catalogue data are available).

S2LXSJ022134-053558

S2LXSJ022134-053558 (Figure A.32) has a deboosted flux density of $S_{850\mu\text{m}} = 9.3 \pm 3.7$ mJy and is not one of the sources observed with ALMA in Cycle 9. The S2LXS XMM-LSS source has one potential *Herschel* 250 μm counterpart from the HerMES DR4 xID250 catalogue (Roseboom et al., 2010, 2012; Oliver et al., 2012) and one potential counterpart from Deep Drill (Lacy et al., 2021). This source lies outside the footprint of the VISTA VIDEO survey (Jarvis et al., 2013). This source is not detected in the VLA 1-2 GHz survey of the XMM-LSS field (Heywood et al., 2020), which may indicate this lies at a redshift $z > 3.5$.

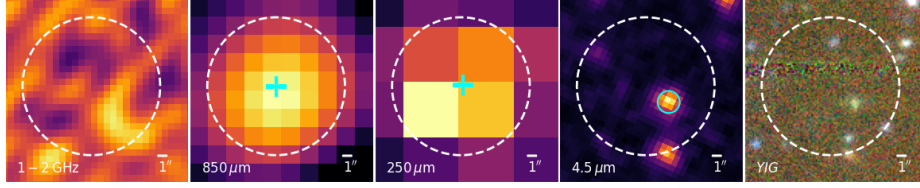


FIGURE A.32: We show multi-wavelength image cutouts ($20'' \times 20''$) centred on the position of source S2LXSJ022134-053558 from the $>5\sigma$ catalogue of the S2LXS-XMM-LSS survey (Chapter 3). The figure description is the same as for Figure A.1 (where image and catalogue data are available).

S2LXSJ021907-052202

S2LXSJ021907-052202 (Figure A.33) has a deboosted flux density of $S_{850\mu\text{m}} = 8.5 \pm 3.9\text{mJy}$. This source was observed in an ALMA survey of a sample of galaxies from the S2CLS UDS field (AS2UDS; Stach et al., 2019) and has two counterparts; AS2UDS0038.0 with a flux density of $S_{870\mu\text{m}} = 7.7\text{mJy}$ and $z_{\text{phot}} \approx 2.6$, and AS2UDS0038.1 with a flux density of $S_{870\mu\text{m}} = 1.2\text{mJy}$ and $z_{\text{phot}} \approx 2.7$ (Dudzevičiūtė et al., 2019). AS2UDS0038.1 does not have a counterpart in the VLA 1-2GHz image or in Deep Drill (Lacy et al., 2021), and so without ALMA observations it would be very difficult to identify both the multi-wavelength counterparts to this single-dish submillimetre source.

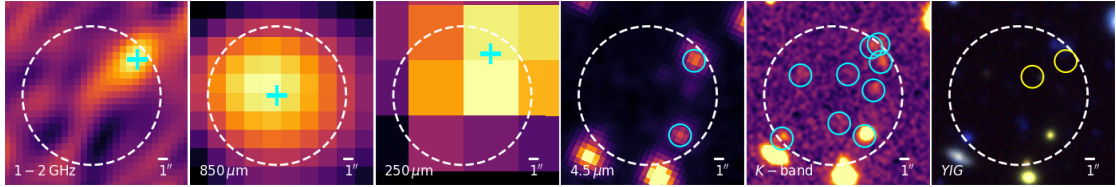


FIGURE A.33: We show multi-wavelength image cutouts ($20'' \times 20''$) centred on the position of source S2LXSJ021907-052202 from the $>5\sigma$ catalogue of the S2LXS-XMM-LSS survey (Chapter 3). The figure description is the same as for Figure A.1 (where image and catalogue data are available). The position of ALMA counterparts from the AS2UDS catalogue (Stach et al., 2019) are shown in the colour image (yellow circles).

S2LXSJ021910-051532

S2LXSJ021910-051532 (Figure A.34) has a deboosted flux density of $S_{850\mu\text{m}} = 8.4 \pm 3.7\text{mJy}$. This source was observed in an ALMA survey of a sample of galaxies from the S2CLS UDS field (AS2UDS; Stach et al., 2019) and has one counterpart; AS2UDS0039.0 with a flux density of $S_{870\mu\text{m}} = 5.8\text{mJy}$ and $z_{\text{phot}} \approx 2.9$. Since this source is not detected in the VLA 1-2GHz survey and has three potential counterparts in Deep Drill (Lacy et al., 2021), without ALMA observations it would be very difficult to identify the true multi-wavelength counterpart to this single-dish submillimetre source.

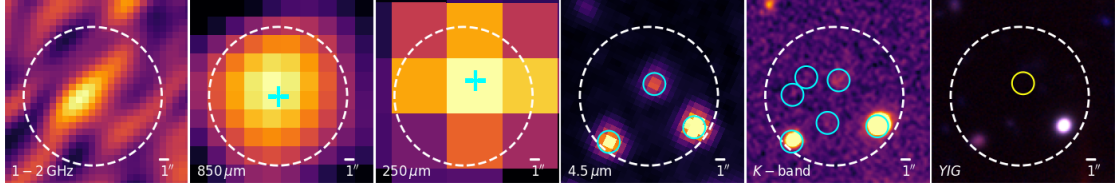


FIGURE A.34: We show multi-wavelength image cutouts ($20'' \times 20''$) centred on the position of source S2LXSJ021910-051532 from the $>5\sigma$ catalogue of the S2LXS-XMM-LSS survey (Chapter 3). The figure description is the same as for Figure A.1 (where image and catalogue data are available). The position of ALMA counterparts from the AS2UDS catalogue (Stach et al., 2019) are shown in the colour image (yellow circles).

S2LXSJ021939-052315

S2LXSJ021939-052315 (Figure A.35) has a deboosted flux density of $S_{850\mu\text{m}} = 7.5 \pm 3.1$ mJy. This source was observed in an ALMA survey of a sample of galaxies from the S2CLS UDS field (AS2UDS; Stach et al., 2019) and has one counterpart; AS2UDS0296.0 with a flux density of $S_{870\mu\text{m}} = 6.8$ mJy and $z_{\text{phot}} \approx 1.8$.

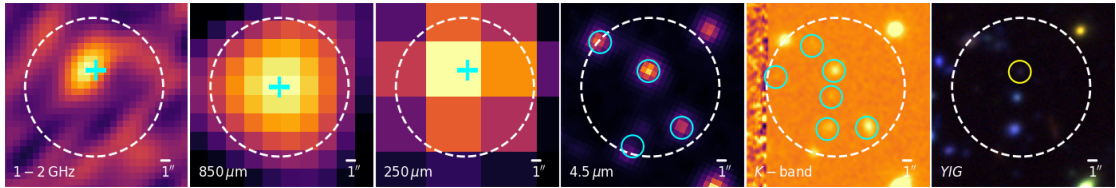


FIGURE A.35: We show multi-wavelength image cutouts ($20'' \times 20''$) centred on the position of source S2LXSJ021939-052315 from the $>5\sigma$ catalogue of the S2LXS-XMM-LSS survey (Chapter 3). The figure description is the same as for Figure A.1 (where image and catalogue data are available). The position of ALMA counterparts from the AS2UDS catalogue (Stach et al., 2019) are shown in the colour image (yellow circles).

S2LXSJ022122-051113

S2LXSJ022122-051113 (Figure A.36) has a deboosted flux density of $S_{850\mu\text{m}} = 7.6 \pm 3.3$ mJy and is not one of the sources observed with ALMA in Cycle 9. The S2LXS XMM-LSS source has one potential *Herschel* 250 μm counterpart from the HerMES DR4 xID250 catalogue (Roseboom et al., 2010, 2012; Oliver et al., 2012), two potential counterparts from Deep Drill (Lacy et al., 2021), and multiple possible near-infrared counterparts from the K_s -band selected catalogue of Adams et al. (2020); Hatfield et al. (2022). This source is not detected in the VLA 1-2 GHz survey of the XMM-LSS field (Heywood et al., 2020), which may indicate this lies at a redshift $z > 3.5$.

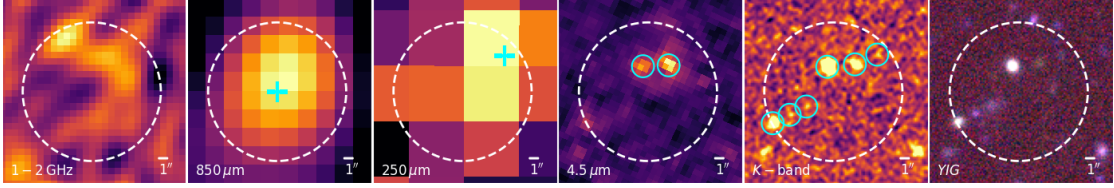


FIGURE A.36: We show multi-wavelength image cutouts ($20'' \times 20''$) centred on the position of source S2LXSJ022122-051113 from the $>5\sigma$ catalogue of the S2LXS-XMM-LSS survey (Chapter 3). The figure description is the same as for Figure A.1 (where image and catalogue data are available).

S2LXSJ022018-051124

S2LXSJ022018-051124 (Figure A.37) has a deboosted flux density of $S_{850\mu\text{m}} = 7.7 \pm 3.0$ mJy and is not one of the sources observed with ALMA in Cycle 9. The S2LXS XMM-LSS source has one potential counterpart from the VLA 1-2 GHz survey of the XMM-LSS field (Heywood et al., 2020), one potential *Herschel* 250 μm counterpart from the HerMES DR4 xID250 catalogue (Roseboom et al., 2010, 2012; Oliver et al., 2012), two potential counterparts from Deep Drill (Lacy et al., 2021), and multiple possible near-infrared counterparts from the K_s -band selected catalogue of Adams et al. (2020); Hatfield et al. (2022).

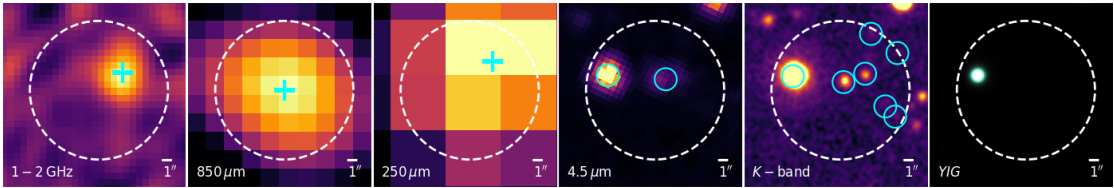


FIGURE A.37: We show multi-wavelength image cutouts ($20'' \times 20''$) centred on the position of source S2LXSJ022018-051124 from the $>5\sigma$ catalogue of the S2LXS-XMM-LSS survey (Chapter 3). The figure description is the same as for Figure A.1 (where image and catalogue data are available).

S2LXSJ022150-052835

S2LXSJ022150-052835 (Figure A.38) has a deboosted flux density of $S_{850\mu\text{m}} = 7.4 \pm 3.1$ mJy and is not one of the sources observed with ALMA in Cycle 9. The S2LXS XMM-LSS source has one potential *Herschel* 250 μm counterpart from the HerMES DR4 xID250 catalogue (Roseboom et al., 2010, 2012; Oliver et al., 2012), and multiple possible near-infrared counterparts from the K_s -band selected catalogue of Adams et al. (2020); Hatfield et al. (2022). There is one potential counterpart from Deep Drill (Lacy et al., 2021), however, there appears to be another possible counterpart at the centre of the 4.5 μm image which is not included in the 4.5 μm Deep

Drill catalogue. This source is not detected in the VLA 1-2 GHz survey of the XMM-LSS field (Heywood et al., 2020), which may indicate this lies at a redshift $z > 3.5$.

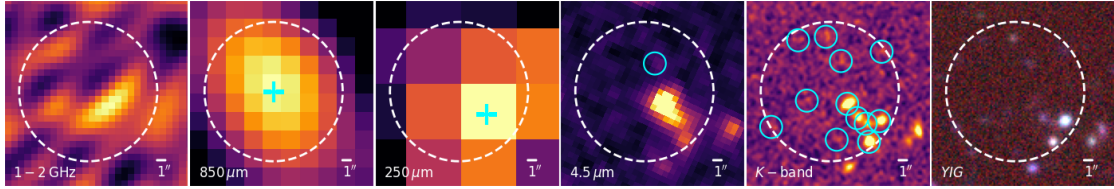


FIGURE A.38: We show multi-wavelength image cutouts ($20'' \times 20''$) centred on the position of source S2LXSJ022150-052835 from the $>5\sigma$ catalogue of the S2LXS-XMM-LSS survey (Chapter 3). The figure description is the same as for Figure A.1 (where image and catalogue data are available).

S2LXSJ022133-051558

S2LXSJ022133-051558 (Figure A.39) has a deboosted flux density of $S_{850\mu\text{m}} = 7.2 \pm 3.1$ mJy and is not one of the sources observed with ALMA in Cycle 9. The S2LXS XMM-LSS source has one potential *Herschel* 250 μm counterpart from the HerMES DR4 xID250 catalogue (Roseboom et al., 2010, 2012; Oliver et al., 2012), four potential counterparts from Deep Drill (Lacy et al., 2021), and multiple possible near-infrared counterparts from the K_s -band selected catalogue of Adams et al. (2020); Hatfield et al. (2022). This source is not detected in the VLA 1-2 GHz survey of the XMM-LSS field (Heywood et al., 2020), which may indicate this lies at a redshift $z > 3.5$.

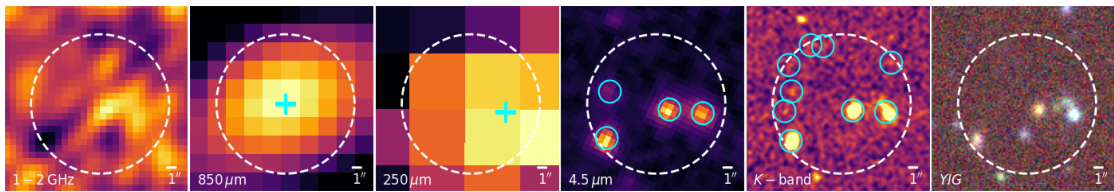


FIGURE A.39: We show multi-wavelength image cutouts ($20'' \times 20''$) centred on the position of source S2LXSJ022133-051558 from the $>5\sigma$ catalogue of the S2LXS-XMM-LSS survey (Chapter 3). The figure description is the same as for Figure A.1 (where image and catalogue data are available).

S2LXSJ022003-052000

S2LXSJ022003-052000 (Figure A.40) has a deboosted flux density of $S_{850\mu\text{m}} = 6.8 \pm 2.9$ mJy and is not one of the sources observed with ALMA in Cycle 9. The S2LXS XMM-LSS source has three potential counterparts from Deep Drill (Lacy et al., 2021), and multiple near-infrared counterparts from the K_s -band selected catalogue of Adams et al. (2020); Hatfield et al. (2022). There are no potential VLA 1-2 GHz or *Herschel* 250 μm counterparts within the SCUBA-2

beam. The lack of a detection in these images suggests that this is either a high-redshift source or this may be a spurious detection in the S2XLS XMM-LSS map.

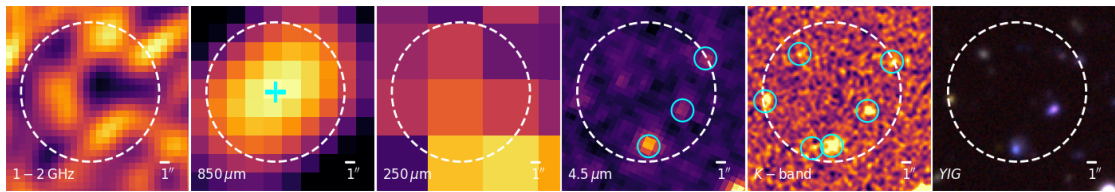


FIGURE A.40: We show multi-wavelength image cutouts ($20'' \times 20''$) centred on the position of source S2LXSJ022003-052000 from the $>5\sigma$ catalogue of the S2LXS-XMM-LSS survey (Chapter 3). The figure description is the same as for Figure A.1 (where image and catalogue data are available).

Bibliography

- Adams, N.J., Bowler, R.A.A., Jarvis, M.J., et al., 2020. The rest-frame UV luminosity function at $z \simeq 4$: a significant contribution of AGNs to the bright end of the galaxy population. *MNRAS*, (2):1771.
- Aihara, H., Arimoto, N., Armstrong, R., et al., 2018. The Hyper Suprime-Cam SSP Survey: Overview and survey design. *Publications of the Astronomical Society of Japan*, 70:S4.
- Alberts, S., Pope, A., Brodwin, M., et al., 2014. The evolution of dust-obscured star formation activity in galaxy clusters relative to the field over the last 9 billion years. *MNRAS*, 437(1):437.
- Alberts, S., Wilson, G.W., Lu, Y., et al., 2013. Submm/mm galaxy counterpart identification using a characteristic density distribution. *MNRAS*, 431(1):194.
- Alexander, D.M., Bauer, F.E., Chapman, S.C., et al., 2005. The X-Ray Spectral Properties of SCUBA Galaxies. *ApJ*, 632(2):736.
- Algera, H.S.B., Smail, I., Dudzevičiūtė, U., et al., 2020. An ALMA Survey of the SCUBA-2 Cosmology Legacy Survey UKIDSS/UDS Field: The Far-infrared/Radio Correlation for High-redshift Dusty Star-forming Galaxies. *ApJ*, 903(2):138.
- An, F.X., Simpson, J.M., Smail, I., et al., 2019. Multi-wavelength Properties of Radio- and Machine-learning-identified Counterparts to Submillimeter Sources in S2COSMOS. *ApJ*, 886(1):48.
- Aravena, M., Decarli, R., Walter, F., et al., 2016a. The ALMA Spectroscopic Survey in the Hubble Ultra Deep Field: Continuum Number Counts, Resolved 1.2 mm Extragalactic Background, and Properties of the Faintest Dusty Star-forming Galaxies. *ApJ*, 833(1):68.
- Aravena, M., Decarli, R., Walter, F., et al., 2016b. The ALMA Spectroscopic Survey in the Hubble Ultra Deep Field: Search for [CII] Line and Dust Emission in 6. *ApJ*, 833(1):71.

- Ashby, M.L.N., Willner, S.P., Fazio, G.G., et al., 2013. SEDS: The Spitzer Extended Deep Survey. Survey Design, Photometry, and Deep IRAC Source Counts. *ApJ*, 769:80.
- Barger, A.J., Cowie, L.L., Sanders, D.B., et al., 1998. Submillimetre-wavelength detection of dusty star-forming galaxies at high redshift. *Nature*, 394:248.
- Baugh, C.M., Lacey, C.G., Frenk, C.S., et al., 2005. Can the faint submillimetre galaxies be explained in the Λ cold dark matter model? *MNRAS*, 356(3):1191.
- Baumann, D., 2012. Tasi lectures on inflation.
- Behrens, C., Pallottini, A., Ferrara, A., et al., 2018. Dusty galaxies in the Epoch of Reionization: simulations. *MNRAS*, 477:552.
- Beichman, C.A., Neugebauer, G., Habing, H.J., et al., 1988. Infrared Astronomical Satellite (IRAS) Catalogs and Atlases. Volume 1: Explanatory Supplement. In *Infrared astronomical satellite (IRAS) catalogs and atlases. Volume 1: Explanatory supplement*, volume 1.
- Benson, A.J., 2010. Galaxy formation theory. *Physics Reports*, 495:33.
- Berta, S., Lutz, D., Nordon, R., et al., 2013. Molecular gas mass functions of normal star-forming galaxies since $z \sim 3$. *A&A*, 555:L8.
- Bertin, E., Mellier, Y., Radovich, M., et al., 2002. The TERAPIX Pipeline. In D.A. Bohlender, D. Durand, and T.H. Handley, editors, *Astronomical Data Analysis Software and Systems XI*, volume 281 of *Astronomical Society of the Pacific Conference Series*, page 228.
- B  thermin, M., Daddi, E., Magdis, G., et al., 2012. A Unified Empirical Model for Infrared Galaxy Counts Based on the Observed Physical Evolution of Distant Galaxies. *ApJ*, 757(2):L23.
- B  thermin, M., Wu, H.Y., Lagache, G., et al., 2017. The impact of clustering and angular resolution on far-infrared and millimeter continuum observations. *A&A*, 607:A89.
- Biggs, A.D., Ivison, R.J., Ibar, E., et al., 2011. The LABOCA survey of the Extended Chandra Deep Field-South - radio and mid-infrared counterparts to submillimetre galaxies. *MNRAS*, 413(4):2314.
- Birnboim, Y. and Dekel, A., 2003. Virial shocks in galactic haloes? *MNRAS*, 345(1):349.
- Blain, A.W., Smail, I., Ivison, R.J., et al., 2002. Submillimeter galaxies. *Physics Reports*, 369:111.

- Bogges, N.W., Mather, J.C., Weiss, R., et al., 1992. The COBE Mission: Its Design and Performance Two Years after Launch. *ApJ*, 397:420.
- Bolato, A.D., Wolfire, M., and Leroy, A.K., 2013. The CO-to-H₂ Conversion Factor. *Annual Review of Astronomy and Astrophysics*, 51(1):207.
- Boogaard, L.A., Decarli, R., González-López, J., et al., 2019. The ALMA Spectroscopic Survey in the HUDF: Nature and Physical Properties of Gas-mass Selected Galaxies Using MUSE Spectroscopy. *ApJ*, 882(2):140.
- Bothwell, M.S., Smail, I., Chapman, S.C., et al., 2013. A survey of molecular gas in luminous sub-millimetre galaxies. *MNRAS*, 429:3047.
- Bouwens, R.J., Aravena, M., Decarli, R., et al., 2016. ALMA Spectroscopic Survey in the Hubble Ultra Deep Field: The Infrared Excess of UV-Selected $z = 2-10$ Galaxies as a Function of UV-Continuum Slope and Stellar Mass. *ApJ*, 833(1):72.
- Brammer, G.B., van Dokkum, P.G., and Coppi, P., 2008. EAZY: A Fast, Public Photometric Redshift Code. *The Astrophysical Journal*, 686(2):1503.
- Brisbin, D., Miettinen, O., Aravena, M., et al., 2017. An ALMA survey of submillimeter galaxies in the COSMOS field: Multiwavelength counterparts and redshift distribution. *A&A*, 608:A15.
- Bull, P., Akrami, Y., Adamek, J., et al., 2016. Beyond Λ CDM: Problems, solutions, and the road ahead. *Physics of the Dark Universe*, 12:56.
- Bussmann, R.S., Riechers, D., Fialkov, A., et al., 2015. HerMES: ALMA Imaging of Herschel-selected Dusty Star-forming Galaxies. *ApJ*, 812(1):43.
- Cai, Z.Y., Lapi, A., Xia, J.Q., et al., 2013. A Hybrid Model for the Evolution of Galaxies and Active Galactic Nuclei in the Infrared. *ApJ*, 768(1):21.
- Cairns, J., Clements, D.L., Greenslade, J., et al., 2022. The Nature of 500 Micron Risers II: Sub-mm Faint Dusty Star Forming Galaxies. *arXiv e-prints*, arXiv:2203.01049.
- Cappellari, M., di Serego Alighieri, S., Cimatti, A., et al., 2009. Dynamical Masses of Early-Type Galaxies at $z \sim 2$: Are they Truly Superdense? *ApJ*, 704(1):L34.

- Carilli, C.L., Chluba, J., Decarli, R., et al., 2016. The ALMA Spectroscopic Survey in the Hubble Ultra Deep Field: Implications for Spectral Line Intensity Mapping at Millimeter Wavelengths and CMB Spectral Distortions. *ApJ*, 833:73.
- Carilli, C.L. and Walter, F., 2013. Cool Gas in High-Redshift Galaxies. *Annual Review of Astronomy and Astrophysics*, 51(1):105.
- Casali, M., Adamson, A., Alves de Oliveira, C., et al., 2007. The UKIRT wide-field camera. *A&A*, 467:777.
- Casey, C.M., Chen, C.C., Cowie, L.L., et al., 2013. Characterization of Scuba-2 450 μ m and 850 μ m selected galaxies in the COSMOS field. *Monthly Notices of the Royal Astronomical Society*, 436(3):1919.
- Casey, C.M., Narayanan, D., and Cooray, A., 2014. Dusty star-forming galaxies at high redshift. *Physics Reports*, 541:45.
- Cazaux, S. and Spaans, M., 2004. Molecular Hydrogen Formation on Dust Grains in the High-Redshift Universe. *ApJ*, 611(1):40.
- CCAT-Prime collaboration, Aravena, M., Austermann, J.E., et al., 2021. CCAT-prime Collaboration: Science Goals and Forecasts with Prime-Cam on the Fred Young Submillimeter Telescope. *arXiv e-prints*, arXiv:2107.10364.
- Chabrier, G., 2003. Galactic stellar and substellar initial mass function. *Publications of the Astronomical Society of the Pacific*, 115(809):763.
- Chapin, E.L., Berry, D.S., Gibb, A.G., et al., 2013. SCUBA-2: iterative map-making with the Sub-Millimetre User Reduction Facility. *MNRAS*, 430(4):2545.
- Chapin, E.L., Pope, A., Scott, D., et al., 2009. An AzTEC 1.1mm survey of the GOODS-N field - II. Multiwavelength identifications and redshift distribution. *MNRAS*, 398(4):1793.
- Chapman, S.C., Blain, A.W., Smail, I., et al., 2005. A Redshift Survey of the Submillimeter Galaxy Population. *ApJ*, 622(2):772.
- Chapman, S.C., Windhorst, R., Odewahn, S., et al., 2003. Hubble Space Telescope Images of Submillimeter Sources: Large Irregular Galaxies at High Redshift. *ApJ*, 599(1):92.

- Chary, R.R. and Pope, A., 2010. New Observational Constraints and Modeling of the Infrared Background: Dust Obscured Star-Formation at $z > 1$ and Dust in the Outer Solar System. *arXiv e-prints*, arXiv:1003.1731.
- Chen, C.C., Cowie, L.L., Barger, A.J., et al., 2013. Resolving the Cosmic Far-infrared Background at 450 and 850 μm with SCUBA-2. *ApJ*, 776(2):131.
- Chen, C.C., Liao, C.L., Smail, I., et al., 2022. An ALMA Spectroscopic Survey of the Brightest Submillimeter Galaxies in the SCUBA-2-COSMOS Field (AS2COSPEC): Survey Description and First Results. *ApJ*, 929(2):159.
- Chen, C.C., Smail, I., Ivison, R.J., et al., 2016. The SCUBA-2 Cosmology Legacy Survey: Multiwavelength Counterparts to 10^3 Submillimeter Galaxies in the UKIDSS-UDS Field. *ApJ*, 820:82.
- Chen, C.C., Smail, I., Swinbank, A.M., et al., 2015. An ALMA Survey of Submillimeter Galaxies in the Extended Chandra Deep Field South: Near-infrared Morphologies and Stellar Sizes. *ApJ*, 799(2):194.
- Chen, C.T.J., Brandt, W.N., Luo, B., et al., 2018. The XMM-SERVS survey: new XMM-Newton point-source catalogue for the XMM-LSS field. *MNRAS*, 478(2):2132.
- Cheng, C., Yan, H., Huang, J.S., et al., 2022. Properties of Host Galaxies of Submillimeter Sources as Revealed by JWST Early Release Observations in SMACS J0723.3-7327. *ApJ*, 936(2):L19.
- Cole, S., Lacey, C.G., Baugh, C.M., et al., 2000. Hierarchical galaxy formation. *MNRAS*, 319(1):168.
- Condon, J.J., 1974. Confusion and Flux-Density Error Distributions. *ApJ*, 188:279.
- Condon, J.J., 1992. Radio emission from normal galaxies. *Annual Review of Astronomy and Astrophysics*, 30:575.
- Condon, J.J., 1997. Errors in Elliptical Gaussian Fits. *PASP*, 109:166.
- Conselice, C.J., Blackburne, J.A., and Papovich, C., 2005. The Luminosity, Stellar Mass, and Number Density Evolution of Field Galaxies of Known Morphology from $z = 0.5$ to 3. *ApJ*, 620(2):564.

- Coppin, K., Chapin, E.L., Mortier, A.M.J., et al., 2006. The SCUBA Half-Degree Extragalactic Survey - II. Submillimetre maps, catalogue and number counts. *MNRAS*, 372(4):1621.
- Coppin, K., Halpern, M., Scott, D., et al., 2005. An 850- μm SCUBA map of the Groth Strip and reliable source extraction. *MNRAS*, 357(3):1022.
- Coppin, K.E.K., Swinbank, A.M., Neri, R., et al., 2007. A Detailed Study of Gas and Star Formation in a Highly Magnified Lyman Break Galaxy at $z = 3.07$. *ApJ*, 665(2):936.
- Cowie, L.L., Barger, A.J., Hsu, L.Y., et al., 2017. A Submillimeter Perspective on the GOODS Fields (SUPER GOODS). I. An Ultradeep SCUBA-2 Survey of the GOODS-N. *ApJ*, 837(2):139.
- Cowley, W.I., Lacey, C.G., Baugh, C.M., et al., 2015. Simulated observations of sub-millimetre galaxies: the impact of single-dish resolution and field variance. *Monthly Notices of the Royal Astronomical Society*, 446(2):1784.
- Cowley, W.I., Lacey, C.G., Baugh, C.M., et al., 2019. The evolution of the UV-to-mm extragalactic background light: evidence for a top-heavy initial mass function? *MNRAS*, 487(3):3082.
- Curtis-Lake, E., Carniani, S., Cameron, A., et al., 2022. Spectroscopy of four metal-poor galaxies beyond redshift ten. *arXiv e-prints*, arXiv:2212.04568.
- da Cunha, E., Groves, B., Walter, F., et al., 2013. On the Effect of the Cosmic Microwave Background in High-redshift (Sub-)millimeter Observations. *ApJ*, 766(1):13.
- Da Cunha, E., Walter, F., Smail, I.R., et al., 2015. An ALMA Survey of Sub-millimeter Galaxies in the Extended Chandra Deep Field South: Physical Properties Derived from Ultraviolet-to-radio Modeling. *ApJ*, 806:110.
- Daddi, E., Dannerbauer, H., Stern, D., et al., 2009. Two Bright Submillimeter Galaxies in a $z = 4.05$ Protocluster in Goods-North, and Accurate Radio-Infrared Photometric Redshifts. *ApJ*, 694(2):1517.
- Daddi, E., Dickinson, M., Morrison, G., et al., 2007. Multiwavelength Study of Massive Galaxies at $z \sim 2$. I. Star Formation and Galaxy Growth. *ApJ*, 670(1):156.
- Daddi, E., Renzini, A., Pirzkal, N., et al., 2005. Passively Evolving Early-Type Galaxies at $1.4 < z < 2.5$ in the Hubble Ultra Deep Field. *ApJ*, 626(2):680.

- Dahlen, T., Mobasher, B., Faber, S.M., et al., 2013. A Critical Assessment of Photometric Redshift Methods: A CANDELS Investigation. *ApJ*, 775(2):93.
- Davé, R., Finlator, K., Oppenheimer, B.D., et al., 2010. The nature of submillimetre galaxies in cosmological hydrodynamic simulations. *MNRAS*, 404(3):1355.
- de Vaucouleurs, G., 1959. Classification and Morphology of External Galaxies. *Handbuch der Physik*, 53:275.
- Decarli, R., Aravena, M., Boogaard, L., et al., 2020. The alma spectroscopic survey in the hubble ultra deep field: Multiband constraints on line-luminosity functions and the cosmic density of molecular gas. *The Astrophysical Journal*, 902(2):110.
- Decarli, R., Walter, F., Aravena, M., et al., 2016a. ALMA Spectroscopic Survey in the Hubble Ultra Deep Field: CO Luminosity Functions and the Evolution of the Cosmic Density of Molecular Gas. *ApJ*, 833(1):69.
- Decarli, R., Walter, F., Aravena, M., et al., 2016b. The ALMA Spectroscopic Survey in the Hubble Ultra Deep Field: Molecular Gas Reservoirs in High-redshift Galaxies. *ApJ*, 833(1):70.
- Decarli, R., Walter, F., Carilli, C., et al., 2014. A Molecular Line Scan in the Hubble Deep Field North. *ApJ*, 782:78.
- Decarli, R., Walter, F., González-López, J., et al., 2019. The ALMA Spectroscopic Survey in the HUDF: CO luminosity functions and the molecular gas content of galaxies through cosmic history. *arXiv e-prints*, arXiv:1903.09164.
- Dempsey, J.T., Friberg, P., Jenness, T., et al., 2013. SCUBA-2: on-sky calibration using submillimetre standard sources. *MNRAS*, 430(4):2534.
- Dole, H., Lagache, G., Puget, J.L., et al., 2006. The cosmic infrared background resolved by spitzer. *Astronomy & Astrophysics*, 451(2):417–429.
- Donley, J.L., Koekemoer, A.M., Brusa, M., et al., 2012. Identifying Luminous Active Galactic Nuclei in Deep Surveys: Revised IRAC Selection Criteria. *ApJ*, 748(2):142.
- Downes, A.J.B., Peacock, J.A., Savage, A., et al., 1986. The Parkes selected regions : powerful radio galaxies and quasars at high redshifts. *MNRAS*, 218:31.

- Driver, S.P., Windhorst, R.A., Ostrander, E.J., et al., 1995. The Morphological Mix of Field Galaxies to $M_I = 24.25$ mag (b J approximately 26 mag) from a Deep Hubble Space Telescope WFPC2 Image. *ApJ*, 449:L23.
- Dudzevičiūtė, U., Smail, I., Swinbank, A.M., et al., 2019. An ALMA survey of the SCUBA-2 CLS UDS field: Physical properties of 707 Sub-millimetre Galaxies. *arXiv e-prints*, arXiv:1910.07524.
- Eales, S., Dunne, L., Clements, D., et al., 2010. The Herschel ATLAS. *PASP*, 122(891):499.
- Eales, S., Lilly, S., Webb, T., et al., 2000. The Canada-UK Deep Submillimeter Survey. IV. The Survey of the 14 Hour Field. *AJ*, 120(5):2244.
- Eales, S., Smith, M.W.L., Auld, R., et al., 2012. Can Dust Emission be Used to Estimate the Mass of the Interstellar Medium in Galaxies—A Pilot Project with the Herschel Reference Survey. *ApJ*, 761(2):168.
- Engel, H., Tacconi, L.J., Davies, R.I., et al., 2010. Most Submillimeter Galaxies are Major Mergers. *ApJ*, 724(1):233.
- Fall, S.M. and Efstathiou, G., 1980. Formation and rotation of disc galaxies with haloes. *MNRAS*, 193:189.
- Fixsen, D.J., Dwek, E., Mather, J.C., et al., 1998. The Spectrum of the Extragalactic Far-Infrared Background from the COBE FIRAS Observations. *ApJ*, 508(1):123.
- Foreman-Mackey, D., Hogg, D.W., Lang, D., et al., 2013. emcee: The MCMC Hammer. *PASP*, 125(925):306.
- Franco, M., Elbaz, D., Béthermin, M., et al., 2018. GOODS-ALMA: 1.1 mm galaxy survey. I. Source catalog and optically dark galaxies. *A&A*, 620:A152.
- Frayer, D.T., Ivison, R.J., Scoville, N.Z., et al., 1998. Molecular Gas in the $Z = 2.8$ Submillimeter Galaxy SMM 02399-0136. *ApJ*, 506(1):L7.
- Frayer, D.T., Ivison, R.J., Scoville, N.Z., et al., 1999. Molecular Gas in the $z = 2.565$ Submillimeter Galaxy SMM J14011+0252. *ApJ*, 514(1):L13.
- Frayer, D.T., Reddy, N.A., Armus, L., et al., 2004. Near-Infrared Colors of Submillimeter-selected Galaxies. *AJ*, 127(2):728.

- Furusawa, H., Kosugi, G., Akiyama, M., et al., 2008. The Subaru/XMM-Newton Deep Survey (SXDS). II. Optical Imaging and Photometric Catalogs. *ApJ*, 176:1.
- Geach, J.E., Dunlop, J.S., Halpern, M., et al., 2017. The SCUBA-2 Cosmology Legacy Survey: 850 μm maps, catalogues and number counts. *MNRAS*, 465(2):1789.
- Geach, J.E. and Papadopoulos, P.P., 2012. Molecular and Atomic Line Surveys of Galaxies. I. The Dense, Star-Forming Gas Phase as a Beacon. *ApJ*, 757(2):156.
- Gehrels, N., 1986. Confidence Limits for Small Numbers of Events in Astrophysical Data. *ApJ*, 303:336.
- Gómez-Guijarro, C., Riechers, D.A., Pavesi, R., et al., 2019. Confirming Herschel Candidate Protoclusters from ALMA/VLA CO Observations. *ApJ*, 872:117.
- González-López, J., Decarli, R., Pavesi, R., et al., 2019. The ALMA Spectroscopic Survey in the HUDF: CO emission lines and 3 mm continuum sources. *arXiv e-prints*, arXiv:1903.09161.
- Gould, R.J. and Salpeter, E.E., 1963. The Interstellar Abundance of the Hydrogen Molecule. I. Basic Processes. *ApJ*, 138:393.
- Greenslade, J., Clements, D.L., Petitpas, G., et al., 2020. The nature of 500 micron risers I: SMA observations. *MNRAS*, 496(2):2315.
- Greve, T.R., Bertoldi, F., Smail, I., et al., 2005. An interferometric CO survey of luminous submillimetre galaxies. *MNRAS*, 359(3):1165.
- Groves, B.A., Schinnerer, E., Leroy, A., et al., 2015. Dust Continuum Emission as a Tracer of Gas Mass in Galaxies. *ApJ*, 799(1):96.
- Hainline, L.J., Blain, A.W., Smail, I., et al., 2011. The Stellar Mass Content of Submillimeter-selected Galaxies. *ApJ*, 740:96.
- Hale, C.L., Williams, W., Jarvis, M.J., et al., 2019. LOFAR observations of the XMM-LSS field. *A&A*, 622:A4.
- Hambly, N.C., Collins, R.S., Cross, N.J.G., et al., 2008. The WFCAM Science Archive. *MNRAS*, 384:637.
- Hatfield, P.W., Jarvis, M.J., Adams, N., et al., 2022. Hybrid photometric redshifts for sources in the COSMOS and XMM-LSS fields. *MNRAS*, 513(3):3719.

- Hauser, M.G., Arendt, R.G., Kelsall, T., et al., 1998. The COBE Diffuse Infrared Background Experiment Search for the Cosmic Infrared Background. I. Limits and Detections. *ApJ*, 508(1):25.
- Hauser, M.G. and Dwek, E., 2001. The Cosmic Infrared Background: Measurements and Implications. *Annual Review of Astronomy and Astrophysics*, 39:249.
- Healey, S.E., Romani, R.W., Taylor, G.B., et al., 2007. CRATES: An All-Sky Survey of Flat-Spectrum Radio Sources. *ApJ*, 171(1):61.
- Helou, G., Soifer, B.T., and Rowan-Robinson, M., 1985. Thermal infrared and nonthermal radio : remarkable correlation in disks of galaxies. *ApJ*, 298:L7.
- Hewett, P.C., Warren, S.J., Leggett, S.K., et al., 2006. The UKIRT Infrared Deep Sky Survey ZY JHK photometric system: passbands and synthetic colours. *Monthly Notices of the Royal Astronomical Society*, 367(2):454.
- Heywood, I., Hale, C.L., Jarvis, M.J., et al., 2020. VLA imaging of the XMM-LSS/VIDEO deep field at 1-2 GHz. *MNRAS*, 496(3):3469.
- Heywood, I., Jarvis, M.J., Hale, C.L., et al., 2022. MIGHTEE: total intensity radio continuum imaging and the COSMOS/XMM-LSS Early Science fields. *MNRAS*, 509(2):2150.
- Hill, R., Chapman, S.C., Scott, D., et al., 2018. High-resolution SMA imaging of bright submillimetre sources from the SCUBA-2 Cosmology Legacy Survey. *MNRAS*, 477(2):2042.
- Hodge, J.A. and da Cunha, E., 2020. High-redshift star formation in the Atacama large millimetre/submillimetre array era. *Royal Society Open Science*, 7(12):200556.
- Hodge, J.A., Karim, A., Smail, I., et al., 2013. An ALMA Survey of Submillimeter Galaxies in the Extended Chandra Deep Field South: Source Catalog and Multiplicity. *ApJ*, 768(1):91.
- Hodge, J.A., Swinbank, A.M., Simpson, J.M., et al., 2016. Kiloparsec-scale Dust Disks in High-redshift Luminous Submillimeter Galaxies. *ApJ*, 833(1):103.
- Hodgkin, S.T., Irwin, M.J., Hewett, P.C., et al., 2009. The UKIRT wide field camera ZYJHK photometric system: calibration from 2MASS. *Monthly Notices of the Royal Astronomical Society*, 394(2):675.
- Hogg, D.W., 2001. Confusion errors in astrometry and counterpart association. *The Astronomical Journal*, 121(2):1207.

- Hogg, D.W. and Turner, E.L., 1998. A Maximum Likelihood Method to Improve Faint-Source Flux and Color Estimates. *PASP*, 110(748):727.
- Holland, W.S., Bintley, D., Chapin, E.L., et al., 2013. SCUBA-2: the 10 000 pixel bolometer camera on the James Clerk Maxwell Telescope. *MNRAS*, 430(4):2513.
- Holland, W.S., Robson, E.I., Gear, W.K., et al., 1999. SCUBA: a common-user submillimetre camera operating on the James Clerk Maxwell Telescope. *MNRAS*, 303(4):659.
- Holmberg, E., 1958. A photographic photometry of extragalactic nebulae. *Meddelanden fran Lunds Astronomiska Observatorium Serie II*, 136:1.
- Hubble, E.P., 1926. Extragalactic nebulae. *ApJ*, 64:321.
- Hubble, E.P., 1936. *Realm of the Nebulae*.
- Hughes, D.H., Serjeant, S., Dunlop, J., et al., 1998. High-redshift star formation in the Hubble Deep Field revealed by a submillimetre-wavelength survey. *Nature*, 394:241.
- Hughes, T.M., Ibar, E., Villanueva, V., et al., 2017. VALES - III. The calibration between the dust continuum and interstellar gas content of star-forming galaxies. *MNRAS*, 468(1):L103.
- Ikarashi, S., Ivison, R.J., Caputi, K.I., et al., 2015. Compact Starbursts in $z \sim 3-6$ Submillimeter Galaxies Revealed by ALMA. *ApJ*, 810:133.
- Ikarashi, S., Kohno, K., Aguirre, J.E., et al., 2011. Detection of an ultrabright submillimetre galaxy in the Subaru/XMM-Newton Deep Field using AzTEC/ASTE. *MNRAS*, 415(4):3081.
- Ivison, R.J., Greve, T.R., Dunlop, J.S., et al., 2007. The SCUBA Half Degree Extragalactic Survey - III. Identification of radio and mid-infrared counterparts to submillimetre galaxies. *MNRAS*, 380(1):199.
- Ivison, R.J., Greve, T.R., Serjeant, S., et al., 2004. Spitzer Observations of MAMBO Galaxies: Weeding Out Active Nuclei in Starbursting Protoellipticals. *ApJ*, 154(1):124.
- Ivison, R.J., Greve, T.R., Smail, I., et al., 2002. Deep radio imaging of the SCUBA 8-mJy survey fields: submillimetre source identifications and redshift distribution. *MNRAS*, 337(1):1.
- Ivison, R.J., Lewis, A.J.R., Weiss, A., et al., 2016. The Space Density of Luminous Dusty Star-forming Galaxies at $z \gtrsim 4$: SCUBA-2 and LABOCA Imaging of Ultrared Galaxies from Herschel-ATLAS. *ApJ*, 832(1):78.

- Iverson, R.J., Magnelli, B., Ibar, E., et al., 2010. The far-infrared/radio correlation as probed by herchel. *Astronomy and Astrophysics*, 518:L31.
- Iverson, R.J., Papadopoulos, P.P., Smail, I., et al., 2011. Tracing the molecular gas in distant submillimetre galaxies via CO(1-0) imaging with the Expanded Very Large Array. *MNRAS*, 412:1913.
- Jarvis, M., Taylor, R., Agudo, I., et al., 2016. The MeerKAT International GHz Tiered Extragalactic Exploration (MIGHTEE) Survey. In *MeerKAT Science: On the Pathway to the SKA*, page 6.
- Jarvis, M.J., Bonfield, D.G., Bruce, V.A., et al., 2013. The VISTA Deep Extragalactic Observations (VIDEO) survey. *Monthly Notices of the Royal Astronomical Society*, 428(2):1281.
- Jauncey, D.L., 1968. Some Comments on a Paper Least-Squares Fit of a Gaussian to Radio Sources” by S. Von Hoerner. *ApJ*, 152:647.
- Johnson, S.P., Wilson, G.W., Wang, Q.D., et al., 2013. X-ray detections of submillimetre galaxies: active galactic nuclei versus starburst contribution. *MNRAS*, 431(1):662.
- Jones, M.H. and Lambourne, R.J.A., 2004. *An Introduction to Galaxies and Cosmology*. Cambridge University Press.
- Kaasinen, M., Scoville, N., Walter, F., et al., 2019. The Molecular Gas Reservoirs of $z \sim 2$ Galaxies: A Comparison of CO(1–0) and Dust-based Molecular Gas Masses. *ApJ*, 880(1):15.
- Kennicutt, Robert C., J., 1998. The Global Schmidt Law in Star-forming Galaxies. *ApJ*, 498(2):541.
- Kilerci Eser, E., Goto, T., and Doi, Y., 2014. Ultraluminous Infrared Galaxies in the AKARI All-sky Survey. *ApJ*, 797(1):54.
- Klaassen, P.D., Mroczkowski, T.K., Cicone, C., et al., 2020. The Atacama Large Aperture Submillimeter Telescope (AtLAST). In *Society of Photo-Optical Instrumentation Engineers (SPIE) Conference Series*, volume 11445 of *Society of Photo-Optical Instrumentation Engineers (SPIE) Conference Series*, page 114452F.
- Kleinmann, D.E. and Low, F.J., 1970. Observations of Infrared Galaxies. *ApJ*, 159:L165.
- Kreysa, E., Gemuend, H.P., Gromke, J., et al., 1998. Bolometer array development at the Max-Planck-Institut fuer Radioastronomie. In T.G. Phillips, editor, *Advanced Technology MMW*,

- Radio, and Terahertz Telescopes*, volume 3357 of *Society of Photo-Optical Instrumentation Engineers (SPIE) Conference Series*, pages 319–325.
- Lacey, C.G., Baugh, C.M., Frenk, C.S., et al., 2016. A unified multiwavelength model of galaxy formation. *MNRAS*, 462(4):3854.
- Lacy, M., Surace, J.A., Farrah, D., et al., 2021. A Spitzer survey of Deep Drilling Fields to be targeted by the Vera C. Rubin Observatory Legacy Survey of Space and Time. *MNRAS*, 501(1):892.
- Lagos, C.d.P., da Cunha, E., Robotham, A.S.G., et al., 2020. Physical properties and evolution of (sub-)millimetre-selected galaxies in the galaxy formation simulation SHARK. *MNRAS*, 499(2):1948.
- Lagos, C.d.P., Robotham, A.S.G., Trayford, J.W., et al., 2019. From the far-ultraviolet to the far-infrared - galaxy emission at $0 \leq z \leq 10$ in the SHARK semi-analytic model. *MNRAS*, 489(3):4196.
- Lagos, C.d.P., Tobar, R.J., Robotham, A.S.G., et al., 2018. Shark: introducing an open source, free, and flexible semi-analytic model of galaxy formation. *MNRAS*, 481(3):3573.
- Lawrence, A., Warren, S.J., Almaini, O., et al., 2007. The UKIRT Infrared Deep Sky Survey (UKIDSS). *MNRAS*, 379:1599.
- Lenkić, L., Bolatto, A.D., Förster Schreiber, N.M., et al., 2019. Plateau de Bure High-z Blue-Sequence Survey 2 (PHIBSS2): Search for Secondary Sources, CO Luminosity Functions in the Field, and the Evolution of Molecular Gas Density through Cosmic Time. *arXiv e-prints*, arXiv:1908.01791.
- Leung, T.K.D., Riechers, D.A., Baker, A.J., et al., 2019. The ISM Properties and Gas Kinematics of a Redshift 3 Massive Dusty Star-forming Galaxy. *ApJ*, 871(1):85.
- Liang, L., Feldmann, R., Faucher-Giguère, C.A., et al., 2018. Submillimetre flux as a probe of molecular ISM mass in high-z galaxies. *MNRAS*, 478:L83.
- Liang, L., Feldmann, R., Kereš, D., et al., 2019. On the dust temperatures of high-redshift galaxies. *MNRAS*, 489(1):1397.
- Liu, D., Schinnerer, E., Groves, B., et al., 2019a. Automated Mining of the ALMA Archive in the COSMOS Field (A3COSMOS): II. Cold Molecular Gas Evolution out to Redshift 6. *arXiv e-prints*, arXiv:1910.12883.

- Liu, T., Li, D., Eden, D., et al., 2019b. Galactic continuum surveys with the new 850 micron MKID camera at the EAO/JCMT 15-m telescope. *arXiv e-prints*, arXiv:1907.08702.
- Lonsdale, C.J., Smith, H.E., Rowan-Robinson, M., et al., 2003. SWIRE: The SIRTf Wide-Area Infrared Extragalactic Survey. *PASP*, 115:897.
- Lovell, C.C., Geach, J.E., Davé, R., et al., 2021. Reproducing submillimetre galaxy number counts with cosmological hydrodynamic simulations. *Monthly Notices of the Royal Astronomical Society*, 502(1):772.
- Low, J. and Kleinmann, D.E., 1968. Proceedings of the Conference on Seyfert Galaxies and Related Objects: 17. Infrared Observations of Seyfert Galaxies, Quasistellar Sources, and Planetary Nebulae. *AJ*, 73:868.
- Madau, P. and Dickinson, M., 2014. Cosmic Star-Formation History. *Annual Review of Astronomy and Astrophysics*, 52:415.
- Magdis, G.E., Daddi, E., Béthermin, M., et al., 2012. The Evolving Interstellar Medium of Star-forming Galaxies since $z = 2$ as Probed by Their Infrared Spectral Energy Distributions. *ApJ*, 760(1):6.
- Magnelli, B., Boogaard, L., Decarli, R., et al., 2020. The ALMA Spectroscopic Survey in the HUDF: The Cosmic Dust and Gas Mass Densities in Galaxies up to $z \sim 3$. *ApJ*, 892(1):66.
- Magnelli, B., Karim, A., Staguhn, J., et al., 2019. The IRAM/GISMO 2 mm Survey in the COSMOS Field. *ApJ*, 877(1):45.
- Magnelli, B., Lutz, D., Santini, P., et al., 2012. A Herschel view of the far-infrared properties of submillimetre galaxies. *A&A*, 539:A155.
- Mairs, S., Dempsey, J.T., Bell, G.S., et al., 2021. A Decade of SCUBA-2: A Comprehensive Guide to Calibrating 450 μm and 850 μm Continuum Data at the JCMT. *AJ*, 162(5):191.
- Masters, K.L., 2011. The hubble tuning fork - classification of galaxies [online]. <https://blog.galaxyzoo.org/2011/02/23/the-hubble-tuning-fork/>. Accessed: 2018-08-30.
- Mauduit, J.C., Lacy, M., Farrah, D., et al., 2012. The Spitzer Extragalactic Representative Volume Survey (SERVS): Survey Definition and Goals. *PASP*, 124(917):714.

- McMullin, J.P., Waters, B., Schiebel, D., et al., 2007. CASA Architecture and Applications. In R.A. Shaw, F. Hill, and D.J. Bell, editors, *Astronomical Data Analysis Software and Systems XVI*, volume 376 of *Astronomical Society of the Pacific Conference Series*, page 127.
- Meixner, M., Cooray, A., Leisawitz, D., et al., 2019. Origins Space Telescope Mission Concept Study Report. *arXiv e-prints*, arXiv:1912.06213.
- Michalowski, M.J., Dunlop, J.S., Cirasuolo, M., et al., 2012. The stellar masses and specific star-formation rates of submillimetre galaxies. *A&A*, 541:A85.
- Michałowski, M.J., Dunlop, J.S., Koprowski, M.P., et al., 2017. The SCUBA-2 Cosmology Legacy Survey: the nature of bright submm galaxies from 2 deg² of 850- μ m imaging. *MNRAS*, 469(1):492.
- Miettinen, O., Delvecchio, I., Smolčić, V., et al., 2017. An ALMA survey of submillimetre galaxies in the COSMOS field: Physical properties derived from energy balance spectral energy distribution modelling. *A&A*, 606:A17.
- Millard, J.S., Eales, S.A., Smith, M.W.L., et al., 2020. S2cosmos: Evolution of gas mass with redshift using dust emission. *Monthly Notices of the Royal Astronomical Society*, 494(1):293–315.
- Mo, H.J., Mao, S., and White, S.D.M., 1998. The formation of galactic discs. *MNRAS*, 295(2):319.
- Mocanu, L.M., Crawford, T.M., Vieira, J.D., et al., 2013. Extragalactic Millimeter-wave Point-source Catalog, Number Counts and Statistics from 771 deg² of the SPT-SZ Survey. *ApJ*, 779(1):61.
- Moster, B.P., Naab, T., and White, S.D.M., 2013. Galactic star formation and accretion histories from matching galaxies to dark matter haloes. *MNRAS*, 428(4):3121.
- Murray, S.G., Power, C., and Robotham, A.S.G., 2013. HMFcalc: An online tool for calculating dark matter halo mass functions. *Astronomy and Computing*, 3:23.
- Narayanan, D., Turk, M., Feldmann, R., et al., 2015. The formation of submillimetre-bright galaxies from gas infall over a billion years. *Nature*, 525(7570):496.
- National Aeronautics and Space Administration, 2015. Lambda cdm model of cosmology, adaptation from original nasa wmap science team image [online]. https://lambda.gsfc.nasa.gov/education/graphic_history/univ_evolution.cfm. Accessed: 2017-12-07.

- Negrello, M., Amber, S., Amvrosiadis, A., et al., 2017. The Herschel-ATLAS: a sample of 500 μm -selected lensed galaxies over 600 deg². *MNRAS*, 465(3):3558.
- Negrello, M., Hopwood, R., De Zotti, G., et al., 2010. The Detection of a Population of Submillimeter-Bright, Strongly Lensed Galaxies. *Science*, 330(6005):800.
- Neugebauer, G., Habing, H.J., van Duinen, R., et al., 1984. The Infrared Astronomical Satellite (IRAS) mission. *ApJ*, 278:L1.
- Nordon, R., Lutz, D., Saintonge, A., et al., 2013. The Far-infrared, UV, and Molecular Gas Relation in Galaxies up to $z = 2.5$. *ApJ*, 762(2):125.
- Oliver, S.J., Bock, J., Altieri, B., et al., 2012. The Herschel Multi-tiered Extragalactic Survey: HerMES. *MNRAS*, 424(3):1614.
- Oteo, I., Ivison, R.J., Dunne, L., et al., 2018. An Extreme Protocluster of Luminous Dusty Starbursts in the Early Universe. *ApJ*, 856(1):72.
- Papadopoulos, P.P. and Geach, J.E., 2012. Molecular and Atomic Line Surveys of Galaxies. II. Unbiased Estimates of their Star Formation Mode. *ApJ*, 757:157.
- Papovich, C., Dole, H., Egami, E., et al., 2004. The 24 Micron Source Counts in Deep Spitzer Space Telescope Surveys. *ApJ*, 154(1):70.
- Parshley, S.C., Kronshage, J., Blair, J., et al., 2018. CCAT-prime: a novel telescope for sub-millimeter astronomy. In H.K. Marshall and J. Spyromilio, editors, *Ground-based and Airborne Telescopes VII*, volume 10700 of *Society of Photo-Optical Instrumentation Engineers (SPIE) Conference Series*, page 107005X.
- Pavesi, R., Sharon, C.E., Riechers, D.A., et al., 2018. The CO Luminosity Density at High- z (COLDz) Survey: A Sensitive, Large-area Blind Search for Low- J CO Emission from Cold Gas in the Early Universe with the Karl G. Jansky Very Large Array. *ApJ*, 864(1):49.
- Pierre, M., Valtchanov, I., Altieri, B., et al., 2004. The XMM-LSS survey. survey design and first results. *Journal of Cosmology and Astroparticle Physics*, 2004(09):011.
- Planck Collaboration, Abergel, A., Ade, P.A.R., et al., 2011. Planck early results. XXV. Thermal dust in nearby molecular clouds. *A&A*, 536:A25.
- Planck Collaboration, Ade, P.A.R., Aghanim, N., et al., 2016. Planck 2015 results. XIII. Cosmological parameters. *A&A*, 594:A13.

- Planck Collaboration, Aghanim, N., Akrami, Y., et al., 2020. Planck 2018 results. I. Overview and the cosmological legacy of Planck. *A&A*, 641:A1.
- Polletta, M., Tajer, M., Maraschi, L., et al., 2007. Spectral Energy Distributions of Hard X-Ray Selected Active Galactic Nuclei in the XMM-Newton Medium Deep Survey. *ApJ*, 663(1):81.
- Pope, A., Aretxaga, I., Hughes, D., et al., 2019. TolTEC/LMT Extragalactic Legacy Surveys: Completing our Census of Dust-Obscured Star Formation. In *American Astronomical Society Meeting Abstracts #233*, volume 233 of *American Astronomical Society Meeting Abstracts*, page 363.20.
- Pope, A., Borys, C., Scott, D., et al., 2005. The Hubble Deep Field North SCUBA Super-map - III. Optical and near-infrared properties of submillimetre galaxies. *MNRAS*, 358(1):149.
- Pope, A., Chary, R.R., Alexander, D.M., et al., 2008. Mid-Infrared Spectral Diagnosis of Submillimeter Galaxies. *ApJ*, 675(2):1171.
- Pope, A., Scott, D., Dickinson, M., et al., 2006. The Hubble Deep Field-North SCUBA Super-map - IV. Characterizing submillimetre galaxies using deep Spitzer imaging. *MNRAS*, 370(3):1185.
- Popping, G., Pillepich, A., Somerville, R.S., et al., 2019. The ALMA Spectroscopic Survey in the HUDF: the Molecular Gas Content of Galaxies and Tensions with IllustrisTNG and the Santa Cruz SAM. *ApJ*, 882(2):137.
- Pozzetti, L., Bolzonella, M., Zucca, E., et al., 2010. zCOSMOS - 10k-bright spectroscopic sample. The bimodality in the galaxy stellar mass function: exploring its evolution with redshift. *A&A*, 523:A13.
- Privon, G.C., Narayanan, D., and Davé, R., 2018. On the Interpretation of Far-infrared Spectral Energy Distributions. I. The 850 μm Molecular Mass Estimator. *ApJ*, 867(2):102.
- Puget, J.L., Abergel, A., Bernard, J.P., et al., 1996. Tentative detection of a cosmic far-infrared background with COBE. *A&A*, 308:L5.
- Ramasawmy, J., Klaassen, P.D., Cicone, C., et al., 2022. The Atacama Large Aperture Submillimetre Telescope: key science drivers. In J. Zmuidzinas and J.R. Gao, editors, *Millimeter, Submillimeter, and Far-Infrared Detectors and Instrumentation for Astronomy XI*, volume 12190 of *Society of Photo-Optical Instrumentation Engineers (SPIE) Conference Series*, page 1219007.

- Riechers, D.A., Boogaard, L.A., Decarli, R., et al., 2020. VLA–ALMA spectroscopic survey in the Hubble Ultra Deep Field (VLA-SPECS): Total cold gas masses and CO line ratios for $z = 2\text{--}3$ main-sequence galaxies. *The Astrophysical Journal*, 896(2):L21.
- Riechers, D.A., Bradford, C.M., Clements, D.L., et al., 2013. A dust-obscured massive maximum-starburst galaxy at a redshift of 6.34. *Nature*, 496(7445):329.
- Riechers, D.A., Pavesi, R., Sharon, C.E., et al., 2019. COLDz: Shape of the CO Luminosity Function at High Redshift and the Cold Gas History of the Universe. *ApJ*, 872(1):7.
- Romero, G.E., 2020. Large Latin American Millimeter Array. *arXiv e-prints*, arXiv:2010.00738.
- Roseboom, I.G., Ivison, R.J., Greve, T.R., et al., 2012. The Herschel Multi-tiered Extragalactic Survey: SPIRE-mm photometric redshifts. *MNRAS*, 419(4):2758.
- Roseboom, I.G., Oliver, S.J., Kunz, M., et al., 2010. The Herschel Multi-Tiered Extragalactic Survey: source extraction and cross-identifications in confusion-dominated SPIRE images. *MNRAS*, 409(1):48.
- Ryden, B., 2016. *Introduction to cosmology*.
- Sandage, A., 1961. *The Hubble Atlas of Galaxies*.
- Sandage, A., Sandage, M., and Kristian, J., 1975. *Galaxies and the universe*.
- Sanders, D.B. and Mirabel, I.F., 1996. Luminous Infrared Galaxies. *Annual Review of Astronomy and Astrophysics*, 34:749.
- Sanders, R.L., Shapley, A.E., Jones, T., et al., 2021. The MOSDEF Survey: The Evolution of the Mass-Metallicity Relation from $z = 0$ to $z = 3.3$. *ApJ*, 914(1):19.
- Sargent, M.T., Béthermin, M., Daddi, E., et al., 2012. The Contribution of Starbursts and Normal Galaxies to Infrared Luminosity Functions at $z \gtrsim 2$. *ApJ*, 747(2):L31.
- Sargent, M.T., Schinnerer, E., Murphy, E., et al., 2010. No Evolution in the IR-Radio Relation for IR-luminous Galaxies at $z \gtrsim 2$ in the COSMOS Field. *ApJ*, 714(2):L190.
- Sawicki, M., Arnouts, S., Huang, J., et al., 2019. The CFHT large area U-band deep survey (CLAUDS). *MNRAS*, 489(4):5202.
- Schechter, P., 1976. An analytic expression for the luminosity function for galaxies. *ApJ*, 203:297.

- Schmidt, M., 1959. The Rate of Star Formation. *ApJ*, 129:243.
- Scott, K.S., Austermann, J.E., Perera, T.A., et al., 2008. AzTEC millimetre survey of the COSMOS field - I. Data reduction and source catalogue. *MNRAS*, 385(4):2225.
- Scoville, N., Aussel, H., Brusa, M., et al., 2007. The Cosmic Evolution Survey (COSMOS): Overview. *ApJ*, 172(1):1.
- Scoville, N., Aussel, H., Sheth, K., et al., 2014. The Evolution of Interstellar Medium Mass Probed by Dust Emission: ALMA Observations at $z = 0.3-2$. *ApJ*, 783:84.
- Scoville, N., Lee, N., Bout, P.V., et al., 2017. Evolution of interstellar medium, star formation, and accretion at high redshift. *The Astrophysical Journal*, 837(2):150.
- Scoville, N., Sheth, K., Aussel, H., et al., 2016. ISM masses and the star formation law at $z = 1$ to 6: ALMA observations of dust continuum in 145 galaxies in the COSMOS survey field. *The Astrophysical Journal*, 820(2):83.
- Scoville, N.Z., 2013. *Evolution of star formation and gas*, page 491. Cambridge University Press.
- Shim, H., Kim, Y., Lee, D., et al., 2020. NEPSC2, the North Ecliptic Pole SCUBA-2 survey: 850- μm map and catalogue of 850- μm -selected sources over 2 deg². *MNRAS*, 498(4):5065.
- Shim, H., Lee, D., Kim, Y., et al., 2022. Multiwavelength properties of 850- μm selected sources from the North Ecliptic Pole SCUBA-2 survey. *MNRAS*, 514(2):2915.
- Shu, X., Yang, L., Liu, D., et al., 2022. A Census of Optically Dark Massive Galaxies in the Early Universe from Magnification by Lensing Galaxy Clusters. *ApJ*, 926(2):155.
- Simpson, J.M., Smail, I., Dudzevičiūtė, U., et al., 2020. An ALMA survey of the brightest sub-millimetre sources in the SCUBA-2-COSMOS field. *MNRAS*, 495(3):3409.
- Simpson, J.M., Smail, I., Swinbank, A.M., et al., 2015. The SCUBA-2 Cosmology Legacy Survey: ALMA Resolves the Bright-end of the Sub-millimeter Number Counts. *ApJ*, 807:128.
- Simpson, J.M., Smail, I., Swinbank, A.M., et al., 2019. The East Asian Observatory SCUBA-2 Survey of the COSMOS Field: Unveiling 1147 Bright Sub-millimeter Sources across 2.6 Square Degrees. *ApJ*, 880(1):43.

- Simpson, J.M., Swinbank, A.M., Smail, I., et al., 2014. An ALMA Survey of Submillimeter Galaxies in the Extended Chandra Deep Field South: The Redshift Distribution and Evolution of Submillimeter Galaxies. *ApJ*, 788:125.
- Siringo, G., Kreysa, E., Kovács, A., et al., 2009. The Large APEX BOlometer CAmera LABOCA. *A&A*, 497(3):945.
- Smail, I., Ivison, R.J., and Blain, A.W., 1997. A Deep Sub-millimeter Survey of Lensing Clusters: A New Window on Galaxy Formation and Evolution. *ApJ*, 490:L5.
- Smail, I., Ivison, R.J., Blain, A.W., et al., 2002. The nature of faint submillimetre-selected galaxies. *MNRAS*, 331(2):495.
- Solomon, P.M. and Vanden Bout, P.A., 2005. Molecular Gas at High Redshift. *Annual Review of Astronomy and Astrophysics*, 43:677.
- Somerville, R.S. and Davé, R., 2015. Physical Models of Galaxy Formation in a Cosmological Framework. *Annual Review of Astronomy and Astrophysics*, 53:51.
- Speagle, J.S., Steinhardt, C.L., Capak, P.L., et al., 2014. A Highly Consistent Framework for the Evolution of the Star-Forming “Main Sequence” from $z \sim 0-6$. *ApJ*, 214:15.
- Stach, S.M., Dudzevičiūtė, U., Smail, I., et al., 2019. An ALMA survey of the SCUBA-2 Cosmology Legacy Survey UKIDSS/UDS field: source catalogue and properties. *MNRAS*, 487(4):4648.
- Stach, S.M., Smail, I., Swinbank, A.M., et al., 2018. An ALMA Survey of the SCUBA-2 Cosmology Legacy Survey UKIDSS/UDS Field: Number Counts of Submillimeter Galaxies. *ApJ*, 860(2):161.
- Stach, S.M., Swinbank, A.M., Smail, I., et al., 2017. ALMA Pinpoints a Strong Overdensity of U/LIRGs in the Massive Cluster XCS J2215 at $z = 1.46$. *ApJ*, 849:154.
- Swinbank, A.M., Simpson, J.M., Smail, I., et al., 2014. An ALMA survey of sub-millimetre Galaxies in the Extended Chandra Deep Field South: the far-infrared properties of SMGs. *MNRAS*, 438:1267.
- Swinbank, A.M., Smail, I., Chapman, S.C., et al., 2004. The Rest-Frame Optical Spectra of SCUBA Galaxies. *ApJ*, 617(1):64.

- Tacconi, L.J., Genzel, R., Neri, R., et al., 2010. High molecular gas fractions in normal massive star-forming galaxies in the young Universe. *Nature*, 463(7282):781.
- Tacconi, L.J., Genzel, R., Saintonge, A., et al., 2018. PHIBSS: Unified Scaling Relations of Gas Depletion Time and Molecular Gas Fractions. *ApJ*, 853(2):179.
- Tacconi, L.J., Genzel, R., Smail, I., et al., 2008. Submillimeter Galaxies at $z \sim 2$: Evidence for Major Mergers and Constraints on Lifetimes, IMF, and CO-H₂ Conversion Factor. *ApJ*, 680(1):246.
- Tacconi, L.J., Neri, R., Chapman, S.C., et al., 2006. High-Resolution Millimeter Imaging of Submillimeter Galaxies. *ApJ*, 640(1):228.
- Tacconi, L.J., Neri, R., Genzel, R., et al., 2013. Phibss: Molecular Gas Content and Scaling Relations in $z \sim 1-3$ Massive, Main-sequence Star-forming Galaxies. *ApJ*, 768(1):74.
- Thomson, A.P., Ivison, R.J., Simpson, J.M., et al., 2014. An ALMA survey of submillimetre galaxies in the Extended Chandra Deep Field South: radio properties and the far-infrared/radio correlation. *MNRAS*, 442(1):577.
- Thomson, A.P., Ivison, R.J., Smail, I., et al., 2012. VLA imaging of ¹²CO J = 1-0 and free-free emission in lensed submillimetre galaxies. *MNRAS*, 425:2203.
- Trayford, J.W., Camps, P., Theuns, T., et al., 2017. Optical colours and spectral indices of $z = 0.1$ eagle galaxies with the 3D dust radiative transfer code skirt. *MNRAS*, 470(1):771.
- Tremonti, C.A., Heckman, T.M., Kauffmann, G., et al., 2004. The Origin of the Mass-Metallicity Relation: Insights from 53,000 Star-forming Galaxies in the Sloan Digital Sky Survey. *ApJ*, 613(2):898.
- Tukey, J.W., 1958. Bias and confidence in not quite large samples. *Ann. Math. Statist.*, 29:614.
- Vieira, J.D., Crawford, T.M., Switzer, E.R., et al., 2010. Extragalactic Millimeter-wave Sources in South Pole Telescope Survey Data: Source Counts, Catalog, and Statistics for an 87 Square-degree Field. *ApJ*, 719(1):763.
- Viero, M.P., Moncelsi, L., Quadri, R.F., et al., 2013. HerMES: The Contribution to the Cosmic Infrared Background from Galaxies Selected by Mass and Redshift. *ApJ*, 779(1):32.
- Wakelam, V., Bron, E., Cazaux, S., et al., 2017. H₂ formation on interstellar dust grains: The viewpoints of theory, experiments, models and observations. *Molecular Astrophysics*, 9:1.

- Walter, F., Decarli, R., Aravena, M., et al., 2016. ALMA Spectroscopic Survey in the Hubble Ultra Deep Field: Survey Description. *ApJ*, 833(1):67.
- Walter, F., Decarli, R., Sargent, M., et al., 2014. A Molecular Line Scan in the Hubble Deep Field North: Constraints on the CO Luminosity Function and the Cosmic H₂ Density. *ApJ*, 782:79.
- Wang, R., Wang, W.H., Clements, D.L., et al., 2020. Submillimeter Galaxy studies in the next decade: EAO Submillimetre Futures White Paper Series, 2019. *arXiv e-prints*, arXiv:2001.07447.
- Wang, S.X., Brandt, W.N., Luo, B., et al., 2013. An ALMA Survey of Submillimeter Galaxies in the Extended Chandra Deep Field-South: The AGN Fraction and X-Ray Properties of Submillimeter Galaxies. *ApJ*, 778(2):179.
- Wang, T., Schreiber, C., Elbaz, D., et al., 2019. A dominant population of optically invisible massive galaxies in the early Universe. *Nature*, 572(7768):211.
- Wang, W.H., Lin, W.C., Lim, C.F., et al., 2017. SCUBA-2 Ultra Deep Imaging EAO Survey (STUDIES): Faint-end Counts at 450 μm . *ApJ*, 850(1):37.
- Wardlow, J.L., Cooray, A., De Bernardis, F., et al., 2013. HerMES: Candidate Gravitationally Lensed Galaxies and Lensing Statistics at Submillimeter Wavelengths. *ApJ*, 762(1):59.
- Wardlow, J.L., Smail, I., Coppin, K.E.K., et al., 2011. The LABOCA survey of the Extended Chandra Deep Field-South: a photometric redshift survey of submillimetre galaxies. *MNRAS*, 415(2):1479.
- Wei, A., Kovács, A., Coppin, K., et al., 2009. The Large Apex Bolometer Camera Survey of the Extended Chandra Deep Field South. *ApJ*, 707(2):1201.
- White, S.D.M. and Rees, M.J., 1978. Core condensation in heavy halos: a two-stage theory for galaxy formation and clustering. *MNRAS*, 183:341.
- Wilkins, S.M., Lovell, C.C., and Stanway, E.R., 2019. Recalibrating the cosmic star formation history. *MNRAS*, 490(4):5359.
- Wilson, G.W., Austermann, J.E., Perera, T.A., et al., 2008. The AzTEC mm-wavelength camera. *MNRAS*, 386(2):807.

- Wolf, M., 1908. Die Klassifizierung der kleinen Nebelflecken. *Publikationen des Astrophysikalischen Instituts Koenigstuhl-Heidelberg*, 3:109.
- Yun, M.S., Aretxaga, I., Ashby, M.L.N., et al., 2008. Spitzer IRAC infrared colours of submillimetre-bright galaxies. *MNRAS*, 389(1):333.
- Yun, M.S., Scott, K.S., Guo, Y., et al., 2012. Deep 1.1 mm-wavelength imaging of the GOODS-S field by AzTEC/ASTE - II. Redshift distribution and nature of the submillimetre galaxy population. *MNRAS*, 420(2):957.
- Zahid, H.J., Geller, M.J., Kewley, L.J., et al., 2013. The Chemical Evolution of Star-forming Galaxies over the Last 11 Billion Years. *ApJ*, 771(2):L19.
- Zavala, J.A., Aretxaga, I., Dunlop, J.S., et al., 2018. The SCUBA-2 Cosmology Legacy Survey: The EGS deep field - II. Morphological transformation and multiwavelength properties of faint submillimetre galaxies. *MNRAS*, 475:5585.
- Zavala, J.A., Casey, C.M., Manning, S.M., et al., 2021. The evolution of the ir luminosity function and dust-obscured star formation in the last 13 billion years.